Effective Dose Estimation for U.S. Army Soldiers Undergoing Multiple Computed Tomography Scans

Major (Promotable) Robert Dean Prins

Submitted in partial fulfillment of the

requirements for the degree

of Doctor of Philosophy

under the Executive Committee of the Graduate School of Arts and Sciences

COLUMBIA UNIVERSITY

2011

ABSTRACT

Effective Dose Estimation for U.S. Army Soldiers Undergoing Multiple Computed Tomography Scans

Robert Dean Prins

Diagnosing the severity of blunt trauma injuries is difficult and involves the use of diagnostic radiological scanning. The primary diagnostic radiology modality used for assessing these injuries is computed tomography (CT). CT delivers more radiation dose than other diagnostic scanning modalities. Trauma patients are at an increased risk of radiation induced cancer because of the cumulative dose effects from multiple scanning procedures. Current methods for estimating effective dose, the quantity used to describe the whole body health detriment from radiation, involves the use of published conversion coefficients and procedure specific machine parameters such as dose-length-product based on computed tomography dose index and scan length. Other methods include the use of Monte Carlo simulations based upon the specific machine geometry and radiation source. Unless the requisite machine information is known, the only means of estimating the effective dose is through the use of generic estimates that are published by scientific radiation committees and have a wide range of values. This research addressed a knowledge gap in assigning effective doses from computed tomography when machine parameters knowledge is either unknown or incomplete. The research involved the development of a new method of estimating the effective dose from CT through the use of regression models incorporating the use of patient parameters as opposed to machine specific parameters. This new method was experimentally verified using two adult anthropomorphic phantoms and optically stimulated luminescent dosimeters. The new method was then compared against a real patient population undergoing similar computed tomography scanning procedures. Utilizing statistical procedures, the new method was tested for repeatability and bias against the current conversion coefficient method. The analysis of the new method verifies that the estimation ability is similar to recent research indicating that the older conversion coefficient methods can underestimate the effective dose to the patient by up to 40%. The new method can be used as a retrospective tool for effective dose estimation from CT trauma protocols for a patient population with physical characteristics similar to the U.S. Army Soldier population.

TABLE OF CONTENTS

Table of Contents i
List of figures iv
Acknowledgments vii
Dedication ix
Preface x
    Motivation for Research x
    Significance of Research x
CHAPTER 1. Introduction 1
    United States Army Medical Care 1
        Echelons of Medical Care in the U.S. Army 1
        Radiology on the Battlefield 3
    Uniqueness of Research 7
CHAPTER 2. Preliminaries 9
    Ionizing Radiation Fundamentals 9
        Absorbed Dose 9
    Medical Use of Radiation 12
        Purpose 12
    Patient Dose 16
        Method 1 19
        Method 2 23
        Method 3 25
        Retrospective Dosimetry 28
        BMI and Effective Dose 29
        Cumulative Dose 29
    Research Hypothesis 33
CHAPTER 3. Specific Aim 1: Evaluate the range of effective doses by CT protocols from literature and retrospective patient CT studies. 36
Statement of the problem: 36
Monte Carlo Techniques 38
    Background 38
    Theory 40
        All Purpose Codes 42
        Limited Functionality 46
    Validation of Limited Functionality Codes 54
    Software Decision 55
    Protocol Specific Effective Dose 56
    Conclusion 62
CHAPTER 4. Specific Aim 2: Develop an improved model capable of predicting effective dose based upon a patient's physical characteristics (height and weight). 64
    Introduction 64
    Methodology 65
        BMI Considerations 65

Results ... 85
Uncertainties Involved in Estimating Effective Dose ... 93
Sensitivity Tables ... 94
Cervical Spine Scan Sensitivity Table ... 96
Chest Abdomen Pelvis Scan Sensitivity Table ... 98
Chest Scan Sensitivity Table ... 100
Thoracic Spine Sensitivity Table ... 102
Lumbar Spine Sensitivity Table ... 104
Conclusion ... 106
CHAPTER 5. Specific Aim 3: Verify effective dose models by measuring absorbed dose s in organs using optically stimulated luminescent dosimetry and anthropomorphic phantoms ... 108
Introduction ... 108
Theory ... 111
Optically Stimulated Luminescent Dosimetry ... 111
Anthropomorphic Phantoms ... 116
OSL Characterization ... 118
OSL Depth Response ... 124
Methodology ... 130
Results ... 135
Brain Scan ... 135
Cervical Spine Scan ... 137
Chest Abdomen Pelvis Scan ... 139
Chest Scan ... 141
Thoracic Spine Scan ... 142
Lumbar Spine Scan ... 144
Experimental Uncertainties ... 146
Brain Scan ... 146
Cervical Spine Scan ... 147
Chest Abdomen Pelvis ... 148
Chest Scan ... 150
Thoracic Spine Scan ... 151
Lumbar Spine Scan ... 152
Discussion ... 153
CHAPTER 6. Specific Aim 4: Validate the effective dose models against current DLP methods for estimating effective doses using a pilot study of representative trauma patient CT scans. ... 157
Introduction ... 157
Methods ... 159
Results ... 160
Brain Scan Comparison ... 160
Cervical Spine Scan Comparison ... 161
Chest Abdomen Pelvis Scan Comparison ... 162
Chest Scan Comparison ... 163
Thoracic Spine Scan Comparison ... 163
Lumbar Spine Scan Comparison ... 165

    Brain Scan Bland-Altman Plot 166
    Cervical Spine Bland-Altman Plot 167
    Chest Abdomen Pelvis Scan Bland-Altman Plot 168
    Chest Scan Bland-Altman Plot 169
    Thoracic Spine Scan Bland-Altman Plot 170
    Lumbar Spine Scan Bland-Altman Plot 171
  Discussion 177
CHAPTER 7. Specific Aim 5: Recommend action points for the U.S. Army based upon this research. 183
    Need for Study (Example) 184
    Recommendations 189
    Research Implications 191
    Research Needs 191
Bibliography 195

LIST OF FIGURES

Number *Page*

Figure 1. General design of a computed tomography scanning machine [33]. The x-ray tube, detector array, and data acquisition system rotates completely around the patient. 15
Figure 2. (a) Cristy-Eckerman phantom commonly used for internal radiation dosimetry [78]. (b) ADAM and EVA phantom. 22
Figure 3. a) Rando-Alderson dosimetry verification phantom. b) CIRS dosimetry verification phantom. 24
Figure 4. CTDI acrylic phantom, pencil ionization chamber, and electrometer (www.acr.org). 26
Figure 5. Graph of published articles concerning the use of Monte Carlo codes in medical physics in accordance with the above Pubmed database search terms. 39
Figure 6. Monte Carlo flowchart for photon energies less than 150 keV. Random numbers are used for sampling initial photon direction, distance between interactions, type of interacting atom within the phantom, type of interaction and scattering angle. 41
Figure 7. Screen shot of the phantom used in the ImPACT software program. The red portion represents the scanning field of view ranging from a starting point of 72.5 and having an ending point of 89. 48
Figure 8. Screen shot of the ImPACT software user input portion. A GE LightSpeed 16 scanner used to perform a head scan (shown in red). 49
Figure 9. Screen shot of the ImPACT software dose calculation portion for the user defined inputs shown in Figure 7. Remainder dose is the mean dose of the remainder organs. 50
Figure 10. Screen shot of the examination input window for PCXMC. The red box on the stylized phantom represents the scan field of view. 54
Figure 11. Representative Scans. Brain Scan (Figure 11a and Figure 11b (ImPACT)). Cervical Spine Scan (Figure 11c and Figure 11d (ImPACT)). Chest Abdomen Pelvis Scan (Figure 11e and Figure 11f (ImPACT)). Chest Scan (Figure 11g and Figure 11h (ImPACT)). Thoracic Spine Scan (Figure 11i and Figure 11j (ImPACT)). Lumbar Spine Scan (Figure 11k and Figure 11l (ImPACT)). 60
Figure 12. Phantom patient parameters. Vertical groups indicate single BMI values where height is held constant and weight varies. 70
Figure 13. Varying phantom dimensions. Figure 13a has dimensions of 175 cm and 40 kg. Figure 13b has dimensions of 175 cm and 60 kg. Figure 13c has dimensions of 175 cm and 80 kg. Figure 13d has dimensions of 175 cm and 110 kg. 71
Figure 14. Six trauma protocols ((14a) Brain Scan, (14b) Cervical Spine Scan, (14c) Chest Abdomen Pelvis Scan, (14d) Chest Scan, (14e) Thoracic Spine Scan, (14f) Lumbar Spine Scan) are presented with the left hand picture showing a representative patient scan, top right figure showing a depiction of the ImPACT phantom, and bottom right two figures showing an anterior-posterior view and right lateral view of the PCXMC phantom. 72

Figure 15. Cross-sectional view of an axial slice made up of four radiographic projections.73
Figure 16. Effects plot of the predictors plotted against effective dose. 95% confidence bands are also presented along with the fitted regression line. (16a) Brain scan, (16b) Cervical Spine Scan, and (16c) Chest Scan. 90
Figure 17. Effects plot of the predictors plotted against effective dose. 95% confidence bands are also presented along with the fitted regression line. (17a) Chest Abdomen Pelvis Scan, (17b) Thoracic Spine Scan, and (17c) Lumbar Spine Scan.93
Figure 18. Dose response according to increasing thickness of solid water slabs simulating organ depth. 94
Figure 19. Landauer Inc. nanoDot OSL dosimeter used in this research (Photo courtesy of Landauer Inc.). 109
Figure 20. Physical processes of the optically stimulated dosimeter [249]. 112
Figure 21. Light stimulation diagram describing how the OSL signal is obtained [266]. 115
Figure 22. InLight^{TM} MicroStar® System. 119
Figure 23. Results of dosimeter to ion chamber comparison when placed free-in-air. 121
Figure 24. Results of dosimeter to ion chamber comparison when placed on a phantom.121
Figure 25. Ratio of dosimeter to ion chamber angular response. 122
Figure 26. Dosimeter linearity with a coefficient of determination (R^2) value of 0.9997 between delivered dose and measured dose. 123
Figure 27. Experimental setup for assessing depth response. Figure 23a shows the detector set up without slabs of solid water. Figure 23b shows the setup with the solid water slabs on top of the blue support cushions. 125
Figure 28. Detector response at varying depths of solid water at 80 kVp. 126
Figure 29. Detector response at varying depths of solid water at 100 kVp. 126
Figure 30. Detector response at varying depths of solid water at 120 kVp. 127
Figure 31. Ratio of OSL and MOSFET detectors with the ion chamber (IC). Both detectors have a response ratio of within +/- 20%. 127
Figure 32. Ratio of the OSL orientation (OSL Flat to OSL Edge) at varying thicknesses of solid water for both 80 kVp and 100 kVp. 129
Figure 33. Representative photo of an anthropomorphic phantom on the CT scanning couch (Figure 33a) and a cross-section view of a 2.5-cm slab of the anthropomorphic phantom (Figure 33b). 132
Figure 34. Bland-Altman plot of two methods for calculating the effective dose from a brain scan. DLP-CC method represents the average of the doses from the two different conversion coefficients. 167
Figure 35. Bland-Altman plot of two methods for calculating the effective dose from a cervical spine scan. DLP-CC method represents the average of the doses from the three different conversion coefficients. 168
Figure 36. Bland-Altman plot of two methods for calculating the effective dose from a chest abdomen pelvis scan. DLP-CC method represents the average of the doses from the two different conversion coefficients. 169
Figure 37. Bland-Altman plot of two methods for calculating the effective dose from a chest scan. DLP-CC method represents the average of the doses from the three different conversion coefficients. 170

Figure 38. Bland-Altman plot of two methods for calculating the effective dose from a thoracic spine scan. DLP-CC method represents the average of the doses from the three different conversion coefficients. 171
Figure 39. Bland-Altman plot of two methods for calculating the effective dose from a lumbar spine scan. DLP-CC method represents the average of the doses from the three different conversion coefficients. 172
Figure 40. Comparison of scanning areas for the chest scan. (40a) Mathematical phantom and scanning range used to calculate the effective dose conversion coefficient [64]. (40b) Representative patient scan and mathematical phantom scanning areas used in model development. 179
Figure 41. Lifetime cancer mortality risks as a function of age at exposure based on updated atomic bomb survivor data as reported in BEIR VII [28] (Courtesy of Li et al [290]). 181
Figure 42. Hypothetical Soldier effective dose chart showing how the ERR decreases over time but is greater for a higher initial effective dose. Age-time patterns represent the radiation-associated risks for all solid cancer mortality. 189

ACKNOWLEDGMENTS

The author wishes to thank all the people who have assisted, supported, and motivated me through this amazing opportunity. My life has truly been blessed by God. As always, He is my Rock upon which to lean when times get tough. I could not have succeeded without my loving wife (Joanie) and daughter (Molly Jane) who have been incredibly supportive and understanding. I receive motivation just watching the two of them juggle their numerous tasks and yet still have time to help me with mine. I would like to thank my advisors (Marco Zaider, Larry Dauer, Greg Freyer, Ross Schmidtlein, and Cheng-Shie Wuu) for their understanding and their insight into this research. I couldn't ask for a better advisor than Larry who has provided me the logistics and knowledge necessary to complete the research within the Army's timeframe. His friendship, guidance, and support have been instrumental in my research. I will miss our commutes together. His zest for knowledge combined with his commitment to safety places him in upper level of all the Safety professionals with whom I have blessed to work. I am also extremely fortunate to have Marco as an advisor. He is truly one of the great minds of medical physics. Even though he is extremely busy with his medical physics responsibilities, he always had an open door for me when I needed advice and guidance. I owe my existence within Columbia University to Greg who has been extremely supportive in my research and development as an academician. Ross' knowledge of the science is on a plane that I will probably never be able to achieve. While we may not be office mates as we once were, I have been lucky to once again work with him. Cheng-Shie has also been incredibly supportive and understanding throughout this process. I am extremely fortunate that he has made the time to meet with me and provide me with his guidance. No research is ever completed by one person alone. I have been blessed to have an outstanding office mate (Pierre Elnajjar) whose friendship I often leaned on to get through my day. My fellow students, Megan and Allan, have been extremely supportive and helpful. Allan Just has forgotten more about statistics than I will ever know and has always been available to help with suggestions and advice. The writing group that he set up within the department provided the right amount of motivation to kick me in my rear when a kick was needed.

The Health Physics staff at Memorial Sloan Kettering Cancer Center was also instrumental in my achievement. Brian Quinn has been my research “buddy” for all my experiments. His willingness to come in and help regardless of the time of day was amazing and I could not have done any of the experiments without his assistance. Developing a passion for the research though came down to observing the experiences of one particular friend, LTC Kenny McDonald. What he has done and experienced in the Army provided me daily with the motivation that I needed. Thanks again to my loving wife, Joanie, and daughter, Molly Jane. Anything that I have done or will do is a result of their love and support.

DEDICATION

This research is dedicated to Joanie and Molly Jane for all their love and support. This research is also dedicated to the Soldiers in the United States Army who have committed and on occasion sacrificed their lives for our wonderful Country. I am truly fortunate to be given an opportunity to be a husband, a father, a leader of Soldiers, and a citizen of the United States of America.

PREFACE

Motivation for Research

In 2004, one of my dear friends, deployed to Southern Iraq in order to build a children's hospital, was severely wounded when the vehicle in which he was riding struck an improvised explosive device (IED). The explosive force of the IED caused fatalities and numerous casualties among the Soldiers in this convoy. The medical evacuation of my friend back to Walter Reed Army Medical Center (WRAMC) in Silver Spring, Maryland was relatively quick, occurring over a couple of days. Fortunately, after at least a month in intensive care and subsequent long term rehabilitation, my friend has made a remarkable recovery. While visiting my friend at WRAMC, he made the comment that doctors seemed to be constantly ordering new diagnostic scans in order to stay on top of his recovery. At that time, most of my knowledge in cumulative dose centered on the radiation dose health effects of weapons of mass destruction and radioactive isotopes. My friend and countless other heroes fighting for our Country have inspired me to learn more about the cumulative radiation dose from medical diagnostic scans. I am extremely thankful and appreciative of the dedicated Army physicians, surgeons, and medical staff for their efforts in saving the lives of these heroes.

Significance of Research

Operation Iraqi Freedom (OIF) officially began 19 March 2003 with a theater of operations primarily in the nations surrounding the Persian Gulf. Operation Enduring Freedom (OEF), 7 October 2001, included other nations in the Middle East and North Africa. Both operations are part of a greater effort termed the Global War on Terror (GWOT) by Former President George W. Bush. Since 2001, more than 1.6 million military members have deployed in support of the Global War on Terror.

Casualties and fatalities have been sustained by the service members supporting the operations. As of 7 February 2011, there have been a total of 29,136 casualties sustained in the U.S. Army [1]. Most of the fatalities on the battlefield are caused by total body disruption (blunt force trauma), severe brain injury, or hemorrhage [2]. Whereas little can be done on the battlefield when total body disruption or severe brain injury occurs, military medicine has made great strides in saving the lives of those of who have experienced hemorrhage [3]. Additionally, advances made addressing battlefield trauma have led to more Soldiers surviving traumatic wounds than in any of the previous wars [4].

Soldiers in previous wars have not had the benefit of the rapid medical evacuation abilities seen today. In Vietnam, evacuation of casualties back to a large medical center could take close to forty-five days. Today, casualties arrive back to Germany within twelve to forty-eight hours after injury and are back in the United States in four to five days. Medical advances can be inferred through the statistic that less than 5% of the casualties in Iraq die of their wounds after reaching a medical facility [5].

Blast injuries and blunt traumas have increased as the use of improvised explosive devices targeting vehicle flow increased. Victims of terrorist attacks tend to have higher injury severity scores, greater requirements for intensive care, more prolonged hospital stays, and a higher rate of mortality than other trauma victims [6]. Managing patient information on the battlefield continues to be difficult as severely wounded personnel are evacuated from the point of injury through the support combat support hospital back to Germany where greater stability care is performed [3].

Conducting medical maneuvers on the battlefield requires an extreme amount of flexibility, diligence, and competence. Medical professionals have to be capable of performing their specialty in austere conditions and still be able to ensure that all clinical medical information remains with the patient through the entire evacuation process (as needed). However, there has been a basic problem seen in the relative paucity of clinical patient information transferred with the patient to the succeeding next higher level of care.

Early in the Global War on Terrorism, there were instances of narratives being written in marker on patients' dressings to convey clinical information. In order to address this information gap, the Joint Patient Tracking Application was developed to allow users to get real-time information on the status of their injured troops [7]. However, the trauma record still doesn't show how many radiographic procedures were performed in the trauma diagnosis. Advances in diagnostic imaging have not made the management of patient imaging records easier. One combat hospital switched from film radiography to digital radiography and then back to film radiography because of increased throughput during trauma situations and the inability of outside facilities to read the compact disks with the films saved on them [8].

When failure to transfer relevant understandable radiographic information along with the patient occurs, the patient often undergoes multiple repeat diagnostic procedures covering the same area of the body. Additionally, as the level of integrated hospital care increases, the radiographic technology also increases resulting in multiple diagnostic procedures on the same area with different diagnostic modalities (standard radiographic x-ray, and computed tomography).

Increasing numbers of radiographic procedures is not unique to military medicine. Victims of trauma receive multiple diagnostic scans and thus are at an increased risk of detrimental health effects from cumulative radiation dose [9-11]. Previous methods for assigning computed tomography effective doses under these circumstances involve the use of generalized rules of thumb that are inadequate for retrospective dose analysis. This research addressed a knowledge gap in assigning effective doses from computed tomography when machine parameters knowledge is either unknown or incomplete.

CHAPTER 1. Introduction

United States Army Medical Care

The United States Army Medical Department (AMEDD) is charged with providing seamless medical care to all members of the U.S. Army regardless of location. In order to carry out this responsibility, the AMEDD has both field medical units which belong to the combatant commanders in order to coordinate the movement and control with the fighting forces, and fixed hospitals which are directly commanded by the leadership of the AMEDD. Unique challenges occur with coordination and integration of assets throughout the AMEDD.

Echelons of Medical Care in the U.S. Army

As described in the AMEDD Combat Health Support doctrine, the wartime mission of the AMEDD is to: 1) save lives, 2) clear the battlefield of casualties, 3) provide state-of-the-art care, 4) return a soldier to duty as rapidly as possible or evacuate the soldier back to a higher echelon of care for more definitive treatment, and 5) provide the most benefit to the maximum number of personnel [12]. There are five echelons of medical care within the Army ranging from battlefield medical care to fixed hospital care [13].

Echelon I – first medical care a soldier receives when wounded [13]. This level of care is considered unit-level health care and includes treatment and evacuation from the point of injury or illness to the unit’s first aid station. This echelon includes immediate lifesaving measures. Medical care is limited to self-aid, buddy aid, combat lifesaver, combat medics, and a treatment squad consisting of about ten medically trained personnel (similar to emergency medical technicians). The highest level of medical competence is usually performed by a general physician or physician's assistant capable of providing advanced trauma management.

Echelon II – supports Echelon I treatment and extends the treatment competence to include dental, laboratory, x-ray, and patient holding capabilities [13]. This level of treatment serves to examine the casualty and determine if further evacuation is needed or if the soldier can be returned to duty with the unit.

Echelon III – expands the level of care to include surgical care [13]. The surgical care can be co-located with Echelon II care in the form of forward support surgical hospitals or remain in the main base operating area. Evacuation hospitals are also found in Echelon III care.

Echelon IV – highest level of care found close to a battlefield [13]. This echelon of care serves to further stabilize patients requiring evacuation to fixed hospitals within Europe (Landstuhl Army Medical Center) prior to evacuation to Walter Reed Army Medical Center. Echelon IV facilities are staffed and equipped for general and specialized medical and surgical care.

Echelon V – definitive medical care [13]. Echelon V hospitals are fixed hospitals with extensive medical specialties providing all the necessary functions for the most definitive medical care.

Phases of medical treatment include: first aid, medical care delivered by a trained combat medic (similar to an emergency medical technician), emergency medical treatment, initial resuscitative treatment, resuscitative surgery or care, definitive treatment, convalescent care, and restorative/rehabilitative treatment.

Radiology on the Battlefield

While not as robust as at a fixed hospital, radiology on the battlefield is still fully capable of the full range of diagnostic radiology from general purpose x-rays to CT. Echelon II is the first echelon of medical care where deployed radiology units are staffed. Increasingly, CT scanners are found at Echelon II facilities where they are used to assist in determining the internal damage to a casualty. In deployed areas, combat support hospitals respond primarily to battle casualties suffered from improvised explosive devices, shrapnel, and gunshot wounds.

The number of radiographic procedures performed annually by the military mimcs the same dramatic increase as in the United States-civilian medical establishment. As a result, the annual effective dose per individual has increased as well, due primarily to the increased usage of computed tomography, interventional fluoroscopy, and nuclear medicine [14]. The National Council on Radiation Protection and Measurements (NCRP)

Report 160 states that 24% of the collective effective dose from medical scans can be attributed to computed tomography [CT] scans. Since its inception in 1972, CT usage has steadily increased due to faster computer processing, advanced techniques (i.e. helical scanning), and better detector and geometric efficiencies. Current CT machines are able to scan an entire body in under 30 seconds [14].

Military medical standards of care include the use of computed tomography scanning in initial diagnosis of traumatic injuries. For head traumas, CT scans are to be performed for any patient with a neurological score of less than 15 as assessed using the Glascow Coma Scale, prolonged loss of consciousness and/or focal neurological signs. CT scans are also used for any core body area (whole body without extremities) where bony abnormalities are present or suspected [15]. As blunt trauma injuries in OIF and OEF have increased, use of CT scanning has also increased.

Computed tomography can be used as an effective patient triage tool on the battlefield [16]. Between June 2008 and May 2009, almost 87,000 radiographic procedures were performed by U.S. Army combat support hospitals in Iraq (Echelon II through Echelon IV). However, prior to January 2009, the medical system in Iraq did not track radiographic procedures by modality. Initial modality tracking showed that from January 2009 to May 2009, out of the 33,000 procedures performed, 8,000 were CT scans [17]. At a combat support hospital in Afghanistan, more than 600 x-rays and 259 CT scans were conducted to assist with 57 surgeries on 47 admitted patients who were in 39 trauma events, all in one 38-day period in 2010 [18].

Justifying (ensuring that the benefit is greater than the risk) the use of a CT scan is important because the risk, albeit small, is measureable [19-20]. A single whole-body CT examination in a 45-year old adult would result in an estimated lifetime attributable cancer mortality risk of around 0.8% [21]. Another study performed in a hospital emergency department, determined that patients undergoing CT of the neck, chest, abdomen, or pelvis have high cumulative rates of multiple or repeat imaging. The study also determined that these patients have a heightened risk of developing cancer from cumulative CT radiation exposure [11, 22]. Whereas the risk to the individual patient is small and can be readily balanced by the medical benefits, the problem becomes greater when trauma patients undergo multiple procedures for diagnostic assessment [23].

Concerns are also noted that diagnostic procedures are repeated unnecessarily or when higher dose modalities are used instead of lower dose modalities without necessary justification [19]. These concerns have prompted the Food and Drug Administration to study whether or not tighter guidelines should be established seeking to limit the amount of radiation dose per diagnostic procedure [24].

Accurately recording all radiographic procedures is important to both assessing lifetime attributable risk to radiation induced cancer and in the physician’s justification process for determining whether or not a procedure is needed. In a battlefield trauma situation, initial medical care seeks to stabilize and save life and limb. Later, after the Soldier has been stabilized and during the rehabilitation period following the incident, assessment of the lifetime attributable risk becomes even more important to helping in the physician justification process. Different radiographic modalities provide varying degrees of diagnostic information. Trauma patients often require multiple imaging tests [9-11]. The diagnostic modality that is typically associated with high radiation dose rates is computed tomography.

However, for a particular person, determination of whether a radiographic procedure caused an increased incidence of cancer is generally not possible. Radiation induced tumors are not distinguishable from other types of tumors. Epidemiologic studies can only present the carcinogenic effect of radiation through statistical excess [25]. A means of estimating the lifetime attributable risk of radiation-induced cancer to a wounded Soldier is by thoroughly capturing and recording the accumulated effective dose. Effective dose provides an indicator of potential detriment from ionizing radiation [26]. As the long term survival rates go up, so does the risk of a radiation-induced cancer [27-28].

CTs have distinct advantages over other diagnostic imaging devices when imaging victims of severe trauma. These advantages include rapid acquisition and processing of patient images. Unlike magnetic resonance imaging, CT can acquire and process and image in less than a minute enabling rapid physician diagnosis based upon a tomographic reconstruction. Since the image can be acquired so quickly, patient movement, which reduces image quality, is significantly reduced. This is one of the reasons why MRI is not used in imaging the thoracic region of the body. The benefits (rapid diagnosis) of using CT greatly outweigh the risks (radiation induced deleterious effects in the body).

Uniqueness of Research

This research is unique from published research in that it explores the development of a patient specific methodology using patient parameters (height and weight) for determining the effective dose from specific trauma CT protocols. Current methods for determining the effective dose rely upon *a priori* knowledge of specific CT machine characteristics and a *posteriori* knowledge of dose-length product (DLP) based on machine output. The methodology of this work focuses on the use of patient parameters rather than machine specific values. Verification of the methodology was performed using *in phantom* dosimeters to measure radiation doses to specific organs. Thermoluminescent dosimeters have been primarily used to measure dose within phantoms and there is no published research concerning the use of optically stimulated luminescent dosimeters within anthropomorphic phantoms for assessing radiation dose from CT trauma protocols, therefore this study represents a unique use of this dosimetric methodology. The adult phantoms utilized in this study adhere to International Commission on Radiation Protection (ICRP) reference man and woman standards. They have been specifically milled to study specifications and are representative of the U.S. Soldier population. Finally, validation of the methodology was performed against information from a population of actual patient images collected under a Memorial Sloan-Kettering Cancer Center Institutional Review Board agreement granted for retrospective imaging studies.

This research is expected to contribute to the Biological Effects of Ionizing Radiation (BEIR) Report VII established Research Need 8, Future Medical Radiation Studies [29].

This was identified as a need for future studies to include individual dose estimates to sites of interest along with evaluations of the uncertainty in dose estimation:

"Of concern for radiological protection is the increasing use of computed tomography scans and diagnostic x-rays. Epidemiologic studies of these exposures would be particularly useful if they are feasible, particularly the following: follow-up studies of cohorts of persons receiving CT scans, especially children…The widespread use of interventional radiological procedures in the heart, lungs, abdomen, and many vascular beds, with extended fluoroscopic exposure times of patients and operators, emphasizes the need for recording of dose and later follow-up studies of potential radiation effects among these populations. There is a need to organize worldwide consortia that would use similar methods in data collection and follow-up. These consortia should record delivered doses and technical data from all x-ray or isotope-based imaging approaches including CT, positron emission tomography, and single photon emission computed tomography." [29]

CHAPTER 2. Preliminaries

Ionizing Radiation Fundamentals

Ionizing radiation, hereafter referred to as radiation, consists of neutral (neutrons, photons, neutrinos, etc.) and charged particles (electrons, positrons, protons, etc.) that carry sufficient energy to liberate electrons from atoms or molecules. Use of radiation in medicine has been explored since the early Twentieth Century [28] and whereas the concern for dose to radiation occupationally exposed workers has a long history, the long term health effects of radiation were not well understood until cohort populations (Life Span Study (Hiroshima and Nagasaki bomb survivors), radiation workers, etc.) emerged [29].

Absorbed Dose

Radiation absorbed dose is defined by the amount of average energy absorbed per unit of mass at a point in matter [30]. The SI unit of absorbed dose is Gray (Gy), which is one Joule per kilogram. The distribution of the absorbed dose within a tissue is not uniform and depends on the penetration and range of the radiation within the tissue. The dosimetric quantities described below are based upon the average absorbed dose in a specified organ or tissue.

Low Dose vs. High Dose

As an ionizing charged particle travels through a medium, energy is lost. The (unrestricted) linear energy transfer (LET) is defined as *the average energy lost by a charged particle due to electronic interactions per unit length of its trajectory* [29]. The amount of energy transferred to the medium depends upon the atomic number of the medium and on the type of radiation in terms of the LET. Typically, for low LET radiation low dose is considered less than 100 mGy. In terms of background radiation, the dose equivalent from low-LET radiation is approximately 1 mSv per year and the average background exposure in the United States can range from approximately 3 mSv to 6 mSv per year [29].

Understanding that different ionizing charged particles interacting in a tissue results in different biological effects, the International Commission on Radiation Units and Measurements (ICRU) introduced the quality factor, Q, to *weight the absorbed dose for the biological effectiveness of the particles producing the absorbed dose*, D [31]. The quality factor is based on the type and energy of the radiation at a point in a specific tissue. The product of the quality factor and the absorbed dose at a point in tissue is defined as the dose equivalent, and has units of Sievert (Sv). The International Commission on Radiological Protection (ICRP) replaced the dose equivalent concept with the quantity, equivalent dose, in 1991 to account for absorbed dose in a tissue rather than at a specific point. Equivalent dose is defined as the *absorbed dose averaged over a tissue or organ and weighted for the radiation quality that is of interest* [32]. The radiation weighting factor, w_R, used in calculating equivalent dose is analogous to the quality factor used in calculating dose equivalent when considering radiation emitted by an internal source in the body, but for external radiation the radiation weighing factor is a function of the type of radiation incident on the body and doesn't depend on the location in, or orientation of, the body [31]. The radiation weighting factor accounts for the relative biological effectiveness of the different types of radiation [20]. Equivalent dose also has units of Sievert (Sv).

Effective Dose

Effective dose is the mean low-LET *absorbed dose from a uniform whole-body irradiation that results in the same total radiation detriment as from the non-uniform, partial-body irradiation in question* [33]. The effective dose concept was introduced by the ICRP in 1975 to represent the radiation detriment for the general population or the specific population of radiation workers and to assess compliance with dose limits.

In 1991, the ICRP [32] recommended that the term effective dose be used to describe the relationship between the probability of stochastic effects and equivalent dose. Effective dose is the multiplicative result of the equivalent dose and the individual tissue weighting factors. Effective dose represents the total health detriment from uniform radiation to the whole body by summing all the tissues and organs in the body. The mathematical representation of this concept is shown in equation 1.

$$E = \sum_i D_{T,R,i} w_{R,i} w_{T,i} \tag{1}$$

The units for effective dose, E, are Sievert (Sv). The dose factor,$D_{T,R,i}$, accounts for the dose in a particular tissue from a particular type of radiation. The radiation weighting factor,$w_{R,i}$, accounts for the difference in energy imparted by each type of radiation. The tissue weighting factor,$w_{T,i}$, helps to describe how each tissue or organ responds to the radiation insult. The tissues or organs where the cells are rapidly dividing (gonad region) will be more affected by radiation than those tissues or organs where the cells are not dividing as frequently (brain) and will have a higher tissue weighting factor. Each tissue dose, radiation weighting factor, and tissue weighting factor is summed up to account for all tissues and organs involved.

Medical Use of Radiation

Purpose

Radiation is involved in medical procedures for both imaging (diagnostic) and treatment (therapy). The primary radiation used is photons.

Diagnostic

Medical imaging primarily uses x-rays to create an image of the patient's internal structure. The x-rays are created via electron interaction with (typically) a high atomic number material. This interaction occurs within an x-ray tube. Electrons are accelerated from cathode to anode made up of a high atomic number material (typically Tungsten) via a large potential difference (i.e. 120 kVp). The electrons interact with the material in the anode and produce Bremsstrahlung x-rays. Although the x-rays are emitted in an isotropic manner, the x-ray tube has a small window from which the x-rays are allowed to escape in a direction towards the patient.

The x-rays emanating from the x-ray tube are described in terms of quantity, quality, and exposure. The quantity of x-rays is the number of photons within the beam typically quantified in mAs. As the mAs is increased, the resultant image is often better because more photons are being detected by the detector but more photons are also being absorbed so that the dose to the patient increases. The quality of x-rays describes the energy spectrum of the x-rays within the beam and can be characterized in terms of the half-value layer (HVL) which is related to the potential energy difference between the cathode and the anode. The unit associated with the quality of x-rays is the electron-volt. In diagnostic radiology, the typical beam quality for a given HVL is from 40 kVp up to 140 kVp and measures the tube potential or nominal energy of the x-ray beam. The x-ray beam is a spectrum of energies. Because of the photoelectric effect, the lower energies in the spectrum will tend to be absorbed within the body contributing to the overall radiation dose without contributing to the image because of the higher absorption cross section at the lower energies for the tissue medium. Manufacturers use filters of various materials to remove lower energy x-rays from the x-ray beam but allow the higher energy x-rays to remain within the beam. Depending upon what portion of the body is being imaged, the beam quality must be higher or lower. For those portions of the body with high density tissues (e.g. bones), a higher quality (higher kVp) must be used to ensure that the x-rays have enough energy to pass through the patient without all being absorbed and thereby not contributing to the image.

Exposure is nearly proportional to the energy fluence of the x-ray beam. Together, quantity, quality, and exposure are determined by six major factors: x-ray tube target material, voltage, current, exposure time, beam filtration, and generator waveform [34].

When the x-rays interact with the patient, they are absorbed, scattered, or pass through the patient completely. Therefore, diagnostic imaging contrast is a factor of the density of the material. The areas of the body that have the greatest electron density (e.g. bone) will absorb the most x-rays and appear lighter in color than those areas which do not have a high density of material (e.g. lung) which will result in a dark color. The colors range from black (no absorption of photons) to white (total absorption of photons). Therefore, radiographic images are often referred to as negative images.

COMPUTED TOMOGRAPHY

Computed tomography (CT) has been used to make medical diagnostic images since the early 1980s and is well described in literature [34]. Increasingly, CT has been used throughout hospitals in order to rapidly acquire images aiding in patient diagnosis.

Design

Computer algorithms are capable of transforming the information from thousands of detectors into an image. The manufacture of the physical CT scanner is very important. At the most basic level, a CT scanner is made up of an x-ray tube, rotating around a patient, and x-ray detectors capable of transforming the x-ray detection into a signal to be processed to create an image (Figure 1). In most CT machines, the x-rays are emitted in the shape of a fan beam. The x-rays then undergo interactions within the patient prior to being detected by the detector array. The number of x-rays emitted by the x-ray tube is controlled by adjusting the current and the exposure time. The energy of the x-rays is controlled by adjusting the potential difference (voltage) between the cathode and the anode.

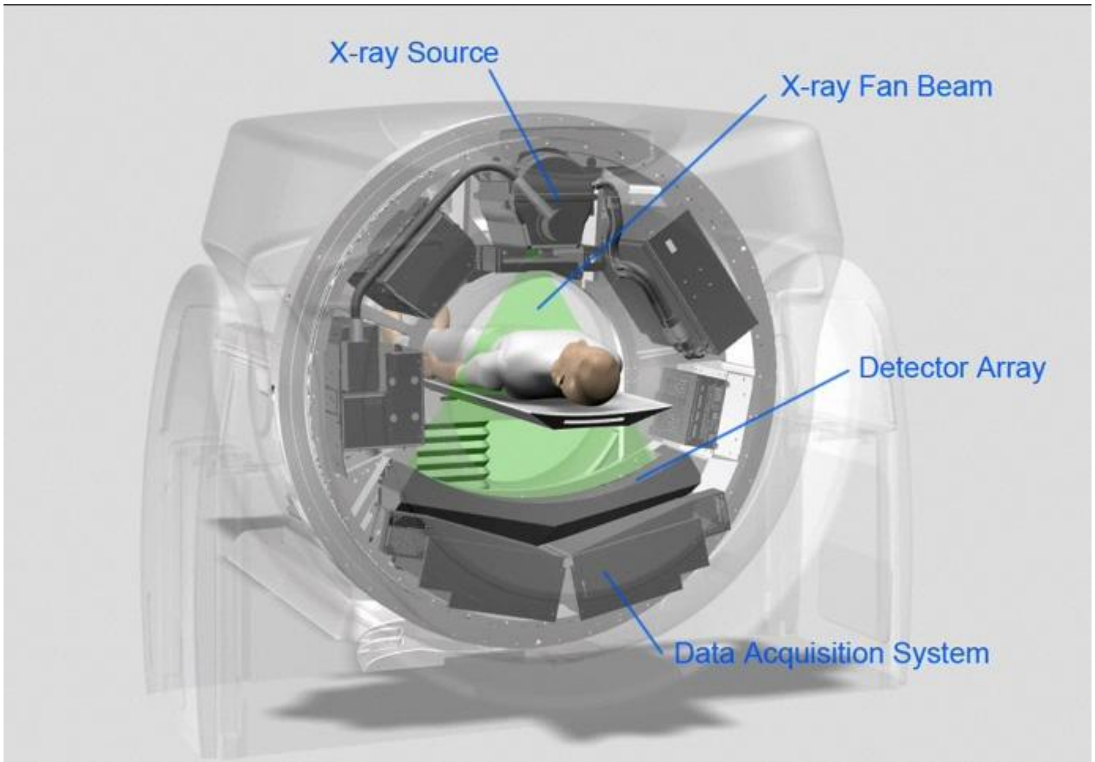

Figure 1. General design of a computed tomography scanning machine [35]. The x-ray tube, detector array, and data acquisition system rotates completely around the patient.

CT scanner detectors are made of crystals which scintillate (emit light) when interacting with radiation. Manufacturers seek to use those elements within the scintillation crystal to achieve a high degree of both absorption efficiency and scintillation efficiency precisely tuned to the spectrum of photon energies produced by the x-ray tube. The x-ray tube is often compact in geometry. A compact geometry (distance from the x-ray tube to the detector) yields a more efficient performance ratio of the scanner’s tube and generator. With all other variables being constant, a more compact geometry will use less photon current within an x-ray beam for a given study.

Tomography, meaning imaging by slices, utilizes the process of taking multiple x-ray projection images of a patient and summing their back-projections in order to create the individual slices for a three dimensional rendering of the patient over the patient scanning length [34]. Single transmission measurement through a patient made by a single detector is called a ray. A series of rays is a projection. Parallel beam geometry is a beam in which all the rays are parallel to each other. Fan beam geometry (modern CT scanners) is a beam in which all the rays diverge from each other. Acquisition of a single axial CT image (slice) may involve approximately 800 rays taken at 1,000 different projection angles for a total of 800,000 transmission measurements. Before the next slice, the table is moved (along the z-axis).

Patient Dose

Radiation dose is a result of many different CT machine parameters. Some of these parameters can be adjusted by the CT technologist in accordance with the prescribed technique protocol for each individual scanning region of the body and other parameters are non-adjustable CT machine parameters.

Non-adjustable CT machine parameters contributing to patient dose include x-ray tube filtration and focal spot size. The x-ray tube filtration serves to filter (absorb) serves to remove low-energy x-rays from the beam spectrum. These low-energy x-rays would otherwise have only contributed to the radiation dose and not the image. A measure of the filtration is the Half-Value Layer (HVL), which together with the tube potential (kVp), serves to describe the beam quality (penetrability of the beam through the patient). The HVL increases as filtration increases for a given kVp. Increasing the amount of filtration will reduce overall patient dose. The filtration has a greater effect on the absolute organ dose but little effect on the relative patient dose [36]. The focal spot size is considered a non-adjustable parameter because it is typically set by the manufacturer or medical physicist in accordance with the type of scanning procedure. Larger focal spot sizes are used for scanning when the region being scanned does not require a high degree of spatial resolution. Smaller focal spot sizes are used when a high degree of spatial resolution is required [34]. Use of smaller focal spot sizes will result in higher patient doses than use of larger focal spot sizes.

The adjustable parameters contributing to patient dose include the beam quality, beam quantity (mAs), slice thickness, gantry rotation speed, CT pitch, and perhaps most importantly patient size. Beam quality is described by the HVL and the tube potential. The adjustable parameter within beam quality is the tube potential. The tube potential is typically 120 kVp for all body regions. Tube potential is directly related to patient dose but is inversely related to image contrast. As tube potential is increased patient dose also increases [37] but image contrast is reduced due to the decreasing probability of the photoelectric effect. Beam quantity describes the number of photons resulting from the interaction of the electrons with the rotating anode. This quantity is known as tube current measured in milli-Amperes (mA). The CT technologist will adjust the mA in accordance with the different regions of the body in order to obtain an image with the least amount of noise (signal-to-noise) which varies with the square root of the number of photons.

Scanning regions with greater tissue densities (bony structures) and greater patient thicknesses will require higher mA than other scanning regions. Patient dose is directly related to the mAs. As the mAs increases, the absorbed organ dose also increases [38]. Slice thickness has a linear influence on the number of photons used to produce the image and thus have a direct relationship with patient dose. Thicker slices require more photons to produce the same image quality. However, fewer slices are needed to cover a scanning range as slice thickness is increased. Using smaller slice thicknesses can lead to more areas of the body where the slices overlap. Overlapping areas have higher doses than areas within the middle of the slice. Gantry rotation speed (revolution time) can be varied to a certain extent by the technologist. Faster rotation speeds are easier to achieve with CT machines having a smaller gantry diameter. X-ray intensity varies as the square of the distance measured from the isocenter to the x-ray tube [39]. Adjusting the CT pitch, a measure of the length of body transcribed by one full revolution of the x-ray tube divided by the slice thickness, allows a CT technologist to decrease the scanning time and indirectly the patient dose. However as the CT pitch increases, the image spatial resolution decreases [34]. Therefore most CT pitch values are near unity. Patient size also has a direct relationship with radiation dose. For a given x-ray technique, larger patients will attenuate more x-rays which reduces the number of x-rays being detected thereby reducing the image quality. In order to adjust for this, a CT technologist will increase the mA which as described above, increases the dose.

Current methods of determining the radiation dose to individual patients are largely patient generic. Measuring the radiation dose to patients from CT scans is difficult and complex.

Generally, there are three main methods of performing the measurement. The three methods are:

1. Monte Carlo simulations using mathematical phantoms [40-51].
2. Experimental measurements using physical phantoms (a tissue equivalent apparatus) and radiation detectors [52-61].
3. Calculation of organ and effective dose from CT doses index (CTDI) or dose-length product (DLP) using conversion coefficients derived via the first two methods [62-75].

Often a combination of the three methods is used to assess dose from a procedure so that comparisons can be made.

Method 1

There are several popular Monte Carlo codes available on the public domain that have been used to model radiation dose. Three of the more popular codes are Monte Carlo N-Particle (MCNP) [76], Monte Carlo N-Particle eXtended (MCNPX) [76], and Electron Gamma Shower (EGS) [77]. These codes will be explored in more detail as part of Specific Aim 1. Monte Carlo [MC] calculations employ random numbers to approach the solution to a problem. MC methods can be used to look at radiation interactions because the interactions are governed by stochastic (random) events. Therefore, MC can be applied to determine the established equivalence between the desired result and the expected behavior of the stochastic system [78]. The random numbers are used to simulate the known distribution of a variable about a given probability. Large numbers of random events can be used to form an estimate about the true solution. As more random events are used, the estimate of the solution becomes more consistent and converges to the correct solution. The behavior of the random variables adheres to the Central Limit Theorem which explains how the sum of a large number of independent random events is normally distributed as long as the expectations are finite with known variances.

Generating random numbers have been widely studied over the years and falls into three categories [79]:

1. Drawing samples from specially constructed tables,
2. Monitoring the output of a physical device or process (i.e. radioactive decay of an isotope), and
3. Calculation by a specified mathematical algorithm.

The most common random number generation today is using the third category which has been classified as a deterministic production of random numbers (also called pseudo-random). This category is limited by the period of the random number sequence. The period of the sequence occurs when a certain number of distinct elements have been produced and starts to repeat itself. This limitation can be overcome by ensuring that the period is sufficiently large through modeling a large number of random numbers.

Mathematical/Voxelized Phantoms

In order to assess the interactions of the photons in tissue and make a determination of dose, mathematical or voxelized phantoms serve as the “target of interest” within which the photons can interact.

The first mathematical phantoms replicated the human structure using a series of geometric elliptical cylinders and cones. The different shapes modeled not only the overall shape of a human but also the organs contained within the human structure. One of the initial assumptions was that all the tissue was homogeneous within an organ. As modeling ability increased, more elaborate phantoms were created to account for tissue heterogeneity. One of the first heterogeneous phantoms was created by the Medical Internal Radiation Dosimetry (MIRD) Committee of the Society of Nuclear Medicine [80]. This phantom (general dimensions of a 70 kg 170 cm reference man), commonly known as the MIRD5 phantom, consisted of a skeleton, lungs, and soft tissue as the remainder. Gradually, these phantoms were advanced to more complex geometric organ shapes and overall sizes. Two of the more famous phantoms that have been used for many years were designed by Cristy and Eckerman et al [81] (Figure 2a) at Oak Ridge National Laboratory in 1980 and Kramer et al (Figure 2b) from the National Research Center for Environment and Health (GSF) in Germany [82]. These phantoms became known as the Cristy-Eckerman phantom and the ADAM and EVA phantoms.

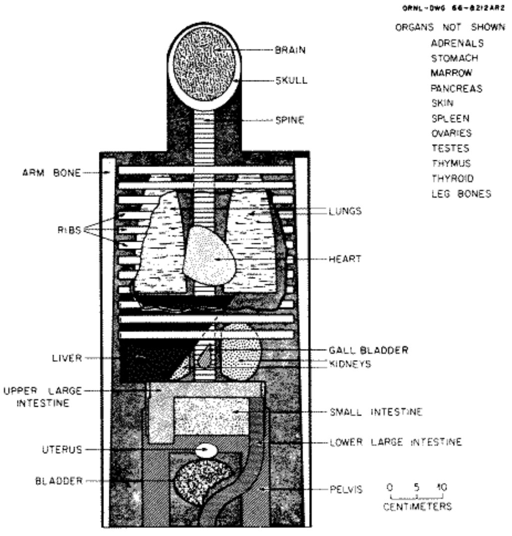

2a.

Fig. A-3. Anterior view of the principal organs in the head and trunk of the adult phantom developed by Snyder et al. (1974). Although the heart and head have been modified in this report, this schematic illustrates the simplicity of the geometries of the organs.

2b.

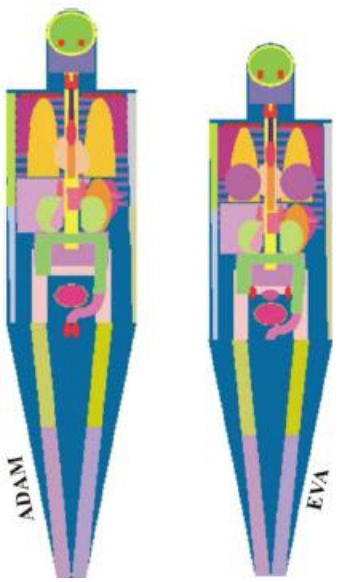

Figure 2. (a) Cristy-Eckerman phantom commonly used for internal radiation dosimetry [80]. (b) ADAM and EVA phantom.

The phantom models followed the guidance of the International Commission on Radiological Protection (ICRP) Report 23 and have been updated as appropriate according to ICRP Report 110 [83]. In ICRP Report 110, a Reference Man is defined as 176 cm tall with a mass of 73 kg. A Reference Female is 163 cm tall with a mass of 60 kg. A summary of the organs is presented below (Table 1).

Table 1. Summary of organ masses from ICRP 110 [83].

Organ	Mass of Organ (g)	
	Male	Female
Adrenals	14	13
Brain	1450	1300
Breast	25	500
Eyes	15	15
Eye Lenses	0.4	0.4
Gall Bladder	68	56
Gastro-Intestinal Tract	150	140
Heart	840	620
Kidneys	310	275
Liver	1800	1400
Lungs	1200	950
Esophagus	40	35
Ovaries		11
Pancreas	140	120
Pituitary Gland	0.6	0.6
Prostate	17	
Salivary Glands	85	70
Spleen	150	130
Testes	35	
Thymus	25	20
Thyroid	20	17

Uterus	80

Alternate uses of Monte Carlo programs include assessment of energy imparted to derive effective doses. Absorbed doses can either be calculated directly to specific locations or can be derived using energy imparted formulism.

Method 2

Measuring radiation dose via Method 2 involves the use of both physical phantoms and radiation detectors.

Physical Phantoms

Physical phantoms are also designed in accordance with ICRP 110 guidance [83]. They are often used as the comparison benchmark for computational phantoms. The physical phantoms are designed for insertion of radiation detectors and dosimeters. Each organ in the phantom will have many different locations in which the detectors and dosimeters can be placed. Because the tissue composition of the organ and surrounding areas is equivalent to a real human patient, measurements within the organ accurately reflect the radiation dose from a selected procedure. The disadvantage of physical phantoms is that their structure is rigid. However, these phantoms are very useful and can also be used for image and dosimetric verification analysis. Two of the more common developers of physical phantoms include Alderson Research Laboratories (Figure 3a) and Computerized Imaging Reference Systems (CIRS), Inc (Figure 3b).

3a. 

3b. 

Figure 3. a) Rando-Alderson dosimetry verification phantom. b) CIRS dosimetry verification phantom.

Radiation Detectors

The most common types of radiation detectors used to measure dose within a physical phantom designed to assess computed tomography scans are thermoluminescent dosimeters (TLD), metal oxide field effect transistor (MOSFET), and radiochromic film. A relatively new use for optically stimulated luminescent dosimeters (OSL) is *in phantom* organ dose assessment. OSL dosimeters will be used in this research.

TLD and OSL dosimeters operate under the same basic theory of ionizing radiation causing electrons to be trapped and when stimulated with energy recombining. The amount of electrons trapped is proportional to the radiation dose. The difference between TLDs and OSLs is primarily with the stimulation energy source. Heat is used as the stimulation source in TLDs whereas light is used as the stimulation source in OSLs. The stimulation sources are used to provide energy to the trapped electrons so that they can leave the traps.

As the electrons return to the ground state, the electrons release energy in the form of measureable luminescent light. The amount of luminescent light that is measured is proportional to the number of electrons which were trapped and is therefore proportional to the dose. MOSFET operates in accordance with semiconductor theory. Ionizing radiation within the active detection chamber of a MOSFET causes electrons to be released. The movement of electrons results in an electric charge being produced. The amount of electric charge produced is proportional to the radiation dose. Radiochromic film operates on an entirely different principle. Radiochromic film responds to different energies by different degrees of darkening. The amount of darkness relates to the amount of radiation absorbed. Radiochromic films work well in the measurement of small fields and at the edges of large fields of radiation due to its ability to measure a high dose gradient and sustain relatively high absorbed dose rates [84].

Method 3

Effective dose calculations are most often performed using CT machine produced quantitative factors derived from manufacturer listed machine values known as the computed tomography dose index (CTDI). The CTDI quantity describes the radiation dose distribution from the CT machine. The Food and Drug Administration defines the CTDI as *the integral of the dose profile along a line perpendicular to the tomographic plane divided by the product of the nominal tomographic section thickness and the number of tomograms produced in a single scan* (21CFR1020.33). CTDI is a quantity describing the average dose. CTDI is measured using a PMMA acrylic phantom and a 100-mm pencil chamber detector (Figure 4). In order to further describe how the radiation dose is distributed within the body and on the surface of the body, the weighted CTDI (CTDIw) is measured. The CTDIw is computed by summing up one-third of the CTDI measured dose inside the phantom and two-thirds of the measured CTDI value on the surface of the phantom. When the CTDIw is divided by the pitch of the CT machine, the CTDI volume (CTDIvol) is computed. CTDIvol is the quantity which the CT manufacturer provides in the dose report provided for each scan. In order to convert the average dose to effective dose a new quantity is introduced called the dose length product (DLP). The DLP is calculated by multiplying the CTDIvol by the total length of the CT scan.

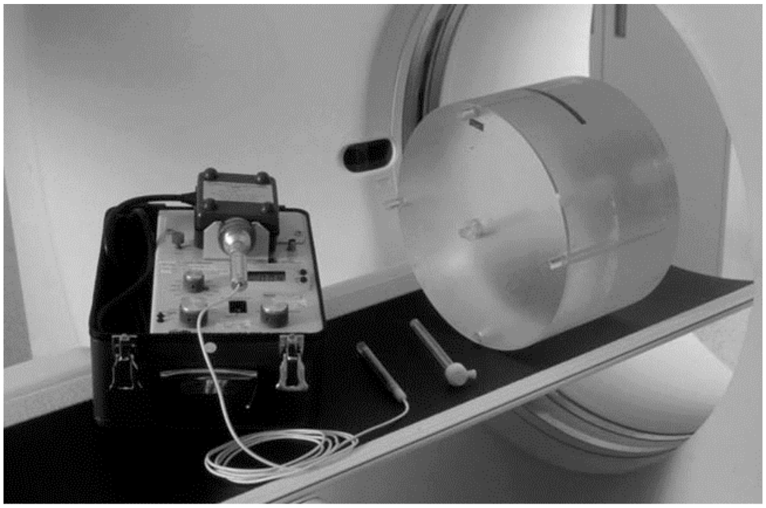

Figure 4. CTDI acrylic phantom, pencil ionization chamber, and electrometer (www.acr.org).

Use of the DLP value and conversion coefficients (different for each type of scan) is the current method of choice for determining the effective dose [72, 85]. In 2000, the European Commission published a report which developed a method to convert DLP to effective dose. This method was based off of a study in which compared a wide range of effective dose values estimated from the DLP for a wide range of scanners and ICRP tissue-weighting coefficients for a series of anatomic regions (head, neck, chest, and abdomen and pelvis). The method derived a series of coefficients for the conversion of DLP to effective dose. Many manufacturers of CT units now compute and display the DLP for each scanning procedure. Many studies have been performed which assess the validity and accuracy [86-88]. Martin et al reports the inherent relative uncertainties in estimating effective dose (using organ doses) to a reference patient to be about +/- 40% and should not be used to assess an individual patient [89].

As mentioned above, DLP can be converted to an effective dose via conversion coefficients. These conversion coefficients have been calculated from mathematical phantoms representing both adult and pediatric patients. The below table (Table 2) shows the results of a study of patient dose from computed tomography within the United Kingdom [90].

Table 2. DLP conversion coefficients. Child data normalized to CTDIw measured in the 16-cm diameter CT dosimetry phantom. Adult data for head and neck regions is normalized to CTDIw in the 16-cm diameter CT dosimetry phantom, with all other regions being normalized to a 32-cm diameter CT dosimetry phantom [90].

	Effective Dose per DLP (mSv mGy^{-1} cm^{-1})				
Region of Body	Children				Adults
	0 years	1 year	5 years	10 years	
Head	0.011	0.0067	0.0040	0.0032	0.0021
Neck	0.017	0.012	0.011	0.0079	0.0059
Chest	0.039	0.026	0.018	0.013	0.014
Abdomen/Pelvis	0.049	0.030	0.020	0.015	0.015

A survey of how DLP conversion coefficients vary in literature is presented (Table 3). Use of DLP conversion coefficients to estimate effective dose should be restricted to the same CT machine model, scanning region, and x-ray parameters (quality and quantity).

Table 3. DLP conversion coefficients from many different sources.

Region	**Jessen (1999) [68]**	**European Commission (2000) [91]**	**EC Appendix B (2004) [91]**	**EC Appendix C (2004) / NRPB-W67 (2005) [91-92]**	**Deak (2010) [75]**	**Phantom Size (cm)**
Head	0.0021	0.0023	0.0023	0.0021	0.0019	16
Head and Neck	NA	NA	NA	0.0031	NA	16
Neck	0.0048	0.0054	NA	0.0059	0.0051	16
Chest	0.014	0.017	0.018	0.014	0.0145	32
Abdomen	0.012	0.015	0.017	0.015	0.0153	32
Pelvis	0.019	0.019	0.017	0.015	0.0129	32
CAP	NA	NA	NA	0.015	NA	32

Retrospective Dosimetry

Performing a retrospective dosimetry study on patients is difficult due to the many different variables involved and the rapid evolution of CTs over the past 20 years. CT evolution has focused primarily on how the x-ray tube rotates around the body and image acquisition. Early CT machines used a step-and-shoot method which is commonly referred to as axial scanning. This method involved the 360 degree rotation of the x-ray tube along an axial plane. As technology advanced, helical scanning, with the table moving through the x-ray tube gantry as the x-ray tube rotates 360 degrees, has become much more prevalent resulting in a reduction of dose for the patient. More recent advances have reduced doses even more as “smart” capability has been added to the CT machines. Smart scanning automatically adjusting the quantity of radiation (mA) based upon the anatomic features within the field of view; more dense areas like the pelvic region will have more mA whereas less dense areas of the body like the chest region or abdomen region will have less mA. Current estimates of effective dose are listed (Table 4).

Table 4. CT effective dose estimates for given anatomical regions.

Covered Anatomy	Assigned Effective Dose per CT Examination (mSv) [11]	Effective Dose per CT (mSv)[93]	Effective Dose per CT (mSv) (Health Physics Society [94])	Yu [95]
Head,Face	2.0	1.5	2.0	1-2
Cervical Spine, Neck	2.0	NA	NA	NA
Chest, Pulmonary Embolus, Thoracic Spine	8.0	5.8	7	5-7

BMI and Effective Dose

Several studies have explored the relationship of BMI and the signal-to-noise ratio. As body size increases the noise present in an image increases [96]. Therefore, as patient size increases, machine parameters (i.e. tube current and tube potential) must also increase in order to achieve a diagnostic quality image. Obese (BMI>30) patients can experience higher radiation doses than normal sized patients [72, 85, 97].

Cumulative Dose

Ultimately, the concern over radiation lies in the not in the production, interaction, or benefits, but in how radiation may cause cancer. Biological Effects of Ionizing Radiation

(BEIR) VII predicts a baseline cancer incidence of 42% and a cancer mortality of 20% [29]. The current estimated threshold by which an increase in solid cancer incidence risk is seen is thought to be between 100 mSv and 150 mSv [98-99]. Although this threshold is much higher than any one diagnostic radiology scan, multiple recurrent scans can approach this threshold. Patients who are imaged more frequently have a higher cumulative health risk than the typical patient.

Higher radiation doses are definitely of concern when patients experience multiple computed tomography scans. Broder et al [100] estimates that the average renal colic patient presenting to an emergency room will experience 2.5 computed tomography scans. In a similar study, Katz et al [101] found that 4% of patients with suspected renal colic will undergo 3-18 computed tomography scans over a six year observation period.

The advent of computed tomography scanners in emergency rooms is a result of increased sensitivity of specific injuries [102]. Patients are undergoing more total body scans which are either used to supplement prior normal radiography scans or used as the primary diagnostic scanning medium [103]. Huda et al estimates that the average effective dose per trauma patient in a Level 1 trauma center emergency room can be as high as 40 mSv [104] per visit. Yet once the patient leaves the emergency room, the patient evaluation scanning continues.

Kim et al [10] reported that at an urban Level I trauma center, severely injured blunt-trauma patients (injury severity score greater than 30) accumulated a mean number of 70 plain radiographs, approximately 8 computed tomography scans, and almost 3 fluoroscopic studies over an average stay of more than 40 days in the surgical intensive care unit. Although the quantity of plain radiographs outnumbered the quantity of computed tomography scans, the computed tomography scans accounted for the greater portion of the overall radiation dose. Kim estimated that cumulative dose per patient was more than 100 mSv. Also noted was the variation in the number of scans each physician ordered due to a lack of an institutional policy concerning daily scans for intubated patients. Noted in the article was that dose estimation techniques did not account for variation among the patients weight.

Tien et al [105] performed a study in which dosimeters were placed on a trauma patient upon presentation to at Level I trauma center in Toronto, Canada. Study patients were separated by injury severity score so a wide variety of patient scores were represented in the study. The mean number of CT scans per patient was approximately 5 and the mean number of plain film radiographs was approximately 14. Tien suggests that approximating effective dose by counting radiological procedures underestimates the true dose. Tien's method of using dosimeters better accounts for the patient dose but the dosimeters were superficially located and thus approximations still had to take place to transform the surface dose to internal organ doses. Tien estimated that whereas the cumulative effective dose per patient was approximately 23 mSv, the cumulative equivalent dose to the thyroid was over 100 mSv.

Sodickson et al [11] performed a retrospective study at a New England hospital assessing the quantity of CTs performed over a 22 year period. The cohort numbered over 31,000 patients who underwent a diagnostic CT examination. 33% of the patients underwent more than five CT examinations, 5% underwent more than 22 examinations, and 1% underwent more than 38 examinations. In terms of cumulative effective dose, 15% of the patients received more than 100 mSv, 4% received over 250 mSv, and 1% received over 399 mSv. Most of the recurrent CTs can be explained by the patient's underlying disease and subsequent complications. However, there were 350 patients with no malignant history. In the sample medical detail provided of these patients, four patients had an abstracted medical history similar to a Soldier. Three of the patients were female (age 49, 53, and 58) with recurrent pains in the abdominal and back region. They experienced an average of 16 CT exams each (max 18, low 13). Average number of examinations by regions was 8.33 for abdominal pelvis, 1 for chest, 1 for head, 4 for spine. The lifetime attributable risk of radiation induced cancer for each of these patients was about 1.4% based upon BEIR VII methodologies. The one male patient with an abstracted medical history similar to a Soldier was for alcoholism and frequent trauma. This patient (53 years old) underwent a total of 36 CT examinations with the most frequent region scanned being the head (19) and abdomen-pelvis (6).

Diagnostic scanning of Soldiers who have experienced severe trauma doesn't necessarily end upon initial release of the Soldier from the hospital. Other factors can contribute to cumulative doses, i.e. diagnostic scanning for long-term mild traumatic disorders which might lead to alcoholism. Alcohol misuse has been documented among Soldiers returning from OIF and OEF [106-110]. Also widely documented is the link between alcohol use following trauma experiences and alcohol use as an initiator of a traumatic experience [111-113]. If we use the above mentioned male patient with abstracted medical history of alcohol and trauma, the Soldier population is at an increased risk of experiencing recurrent CT examinations and thus higher cumulative effective doses. Foreseeing increased CT examinations in the Soldier population is definitely arguable as Soldiers are deploying multiple times and have an increased incidence of post traumatic stress [111, 114-119].

As CT scans are increasingly being used in trauma diagnosis [120-122], our research is very appropriate for formulating an improved method that utilizes minimal available information, such as patient height and weight and the number and types of CT scans for estimating effective doses from different trauma scans. Additionally, since no two patients have the same size and dimensions, patient variability must be considered in developing an effective dose paradigm. In this manner, as individual organ sizes differ [123], better estimates of the effective dose can be calculated.

Research Hypothesis

A patient’s height and weight is correlated with the effective dose from computed tomography scans and such a correlation can be used to develop a model which will allow for estimating effective dose with minimal information and will result in increased accuracy of those estimates than current methods. Use of current effective dose estimating methods (dose-length-product and conversion coefficients) will significantly underestimate the accumulated radiation dose from multiple computed tomography diagnostic trauma scans.

Overall layout of the thesis is to investigate five different specific aims. Each specific aim will be a different chapter in the dissertation. Each specific aim chapter will address the methodology used to investigate the specific aim. Specific aims will address the evaluation of effective dose ranges by CT protocol, development of predictive model, verification of predictive model, validation of predictive model against real patient scans, and recommendation for the initiation of a systematic long-term Soldier study of multiple diagnostic scanning. The five specific aims are:

Specific Aim 1: Evaluate the range of effective doses by CT protocols from literature and retrospective patient CT studies.

Specific Aim 2: Develop an improved model capable of predicting effective dose based upon a patient's physical characteristics (height and weight).

Specific Aim 3: Verify effective dose models by measuring absorbed dose s in organs using optically stimulated luminescent dosimetry and anthropomorphic phantoms.

Specific Aim 4: Validate the effective dose models against current DLP methods for estimating effective doses using a pilot study of representative trauma patient CT scans.

Specific Aim 5: Recommend action points for the U.S. Army based upon this research.

Developing an accurate predictive model will allow health professionals to better determine the cumulative individual patient dose for low-dose health effect research. Studying cohorts (U.S. Army) that will routinely receive more than 100 mSv (cumulative dose) will allow researchers to establish follow-up methods for future epidemiological studies evaluating how medical x-rays and future cancers may be linked. This research is is urgently needed at this time, when the public's awareness to radiation from computed tomography scans is heightened.

CHAPTER 3. Specific Aim 1: Evaluate the range of effective doses by CT protocols from literature and retrospective patient CT studies.

Statement of the problem:

Nearly 50% of all injuries to Soldiers in Operation Iraqi Freedom and Operation Enduring Freedom were to the head/neck, abdomen, and thorax region of the body [124-126]. There are six computed tomography (CT) trauma protocols commonly used to assess and diagnose Soldier injuries from blunt trauma. These protocols are used to image the brain, cervical spine, chest, chest abdomen pelvis (whole body), thoracic spine, and lumbar spine. Each CT trauma protocol will be evaluated to estimate the effective dose per scan. The effective dose resulting from a CT scan primarily depends upon the location of the scan, the scan length, and the x-ray tube current (mA). Effective doses can vary widely from one procedure to the next as a result of differences in machine techniques, x-ray technician set-up procedures for patient scanning, and variation in patient sizes.

Table 5 lists generally accepted nominal effective doses for common diagnostic procedures. The typical nominal effective dose per CT procedures ranges from 2 mSv (CT Head) up to 20 mSv (CT Abdomen and Pelvis) for an average patient (Table 5).

Table 5. Effective doses for common radiology procedures [127].

Radiology Procedure	**Effective Dose (mSv)**	**Comparison to natural background radiation**
Abdominal Region		
CT-Abdomen and Pelvis	10-20	3-6 yrs
CT body	10	3 yrs
CT colography	10	3 yrs
Intravenous Pylegram	3	1 yr
Radiography Lower GI	8	3 yrs

Radiography Upper GI	6	2 yrs
Bone		
Radiography Spine	1.5 mSv	6 months
Radiography Extremity	0.001 mSv	less than 1 day
Central Nervous System		
CT Head	2 mSv	8 months
CT Spine	6 mSv	2 yrs
Myelography	4 mSv	16 months
Chest Region		
CT Chest	7 mSv	2 yrs
Radiography Chest	0.1 mSv	10 days
Children's Imaging		
Voiding Cystourethrogram	5-10 yr old: 1.6 mSv	6 months
	Infant: 0.8 mSv	3 months
Face and Neck		
CT sinuses	0.6 mSv	2 months
Heart		
Cardiac CT for Calcium Scoring	3 mSv	1 yr
Men's Imaging		
Bone Densitometry	0.001 mSv	less than 1 day
Women's Imaging		
Bone Densitometry	0.001 mSv	less than 1 day
Galactography	0.7 mSv	3 months
Hysterosalpingography	1 mSv	4 months
Mammography	0.7 mSv	3 months

While nominal values are useful for comparing the expected effective doses between typical procedures, they are not specific to the patient. A method other than the use of a look-up table is required to more accurately assess specific patient (or Soldier) effective doses (and associated risks) from CT procedures. Chapter 3 will explore the use of Monte Carlo techniques in estimating effective doses, assess the functionality of four different Monte Carlo codes commonly used for such a purpose, and evaluate which codes are most appropriate for meeting the goals of this present research.

Monte Carlo Techniques

Background

Over the past forty years, the use of Monte Carlo radiation transport techniques in medicine, diagnostic radiology, and radiation therapy has become widespread. The use of computers to model the interaction of photons and electrons with matter enables researchers to understand how energy is expected to be deposited in the human body under a wide variety of conditions.

In order to identify the most appropriate Monte Carlo code to use for this research, I evaluated the historical usage of Monte Carlo codes in estimating radiation doses. I performed this evaluation in a similar manner as that presented by D.W.O. Rogers in his review on the past 50 years of Monte Carlo simulations for medical physics [128], I performed a search of the Pubmed (http://www.ncbi.nlm.gov/pubmed) database to identify how many articles were published in journals since 1970 (Table 6) for the following search terms: Monte Carlo, Therapy, Diagnostic, GEANT, PCXMC, PENELOPE, EGS, and MCNP in the Title or the Abstract. I stratified the search dates into decades.

Table 6. Results of Pubmed article search related to the use of Monte Carlo techniques for radiation transport calculations.

Decade	**Diagnostic**	**Therapy**	**GEANT**	**PCXMC**	**PENELOPE**	**EGS/EGSnrc**	**MCNP**
1970-1979	4	3	0	0	0	0	0
1980-1989	33	21	0	0	0	0	0
1990-1999	61	174	5	0	2	2	55
2000-present	270	848	36	20	113	23	286

Perhaps the easiest way to visualize the growth of the use of Monte Carlo techniques within the diagnostic and therapy radiation arenas is through the use of a graph (Figure 6).

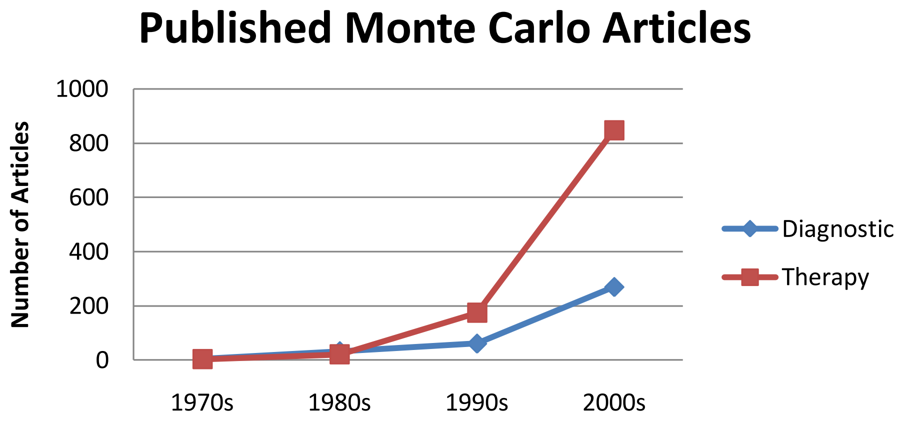

Figure 5. Graph of published articles concerning the use of Monte Carlo codes in medical physics in accordance with the above Pubmed database search terms.

As computer technology has evolved and processing speed has increased, modeling large numbers of photon and particle interactions with matter has become easier. We see that the number of articles written about Monte Carlo techniques and radiation therapy has greatly increased since the 1980s relating to the rise in radiation therapy for treating cancer. Monte Carlo techniques have also been used to simulate radiation doses from diagnostic imaging procedures.

Monte Carlo simulations use stochastic numbers to approximate a deterministic solution. This is performed by using random numbers within statistical models which are themselves applied to mathematical functions in order to model complex systems. If enough random numbers are used, the functions will then begin to converge upon calculated results that can be validated with results obtained through physical experimentation. Early Monte Carlo techniques were used to mimic well-defined problems and geometries. As the techniques improved, unknown deterministic systems were explored. In this manner, deterministic problems were solved by finding a probabilistic analog [129]. This “modern” technique was widely used to model neutron propagation through mediums during the Manhattan Project. Researchers use Monte Carlo computational experimentation to understand otherwise unfeasible or impractical realistic situations. The computational time demand is high though and powerful computers are needed to not only process the huge amounts of information but also achieve faster computational speeds. Monte Carlo coding is dependent upon user input information and models and should be validated when applicable to physical experimental results.

Theory

Most Monte Carlo software codes follow three basic steps: model a system as a probability density function, repeatedly sample from the probability density function, and finally, tally/compute the statistics of interest (i.e. energy deposition) [130]. In general, photons are emitted from a virtual point source into a solid angle defined by the field size and distance from the photon source to a mathematical phantom. The photons are then followed as they interact within the phantom according to the probability distribution of the primary physical processes that the photons may undergo. At diagnostic energies less than 150 keV, the primary physical processes are photo-electric absorption, coherent (Rayleigh) scattering, and Compton (incoherent) scattering. The probability distribution which governs the interaction possibilities is a measure of the energy of the photon and the atomic number of the medium within the phantom. Energy deposition at each interaction point is calculated and recorded. Photons will continue to be tracked through the different interactions until the photon either exits the phantom or loses enough energy that the energy of the photon is less than a lower threshold limit. Radiation dose in an organ within the phantom is calculated as the mean value of all the energy depositions within that organ. Central to the Monte Carlo process is the use of random numbers. The random numbers are used for sampling the initial photon direction, distance between interactions, type of interacting atom within the phantom, type of interaction (and subsequent energy loss), and scattering angle following an interaction. As one can see, a simulation might involve many different probability density functions and summation of huge numbers of recorded events along a photon's track (history) (Figure 6).

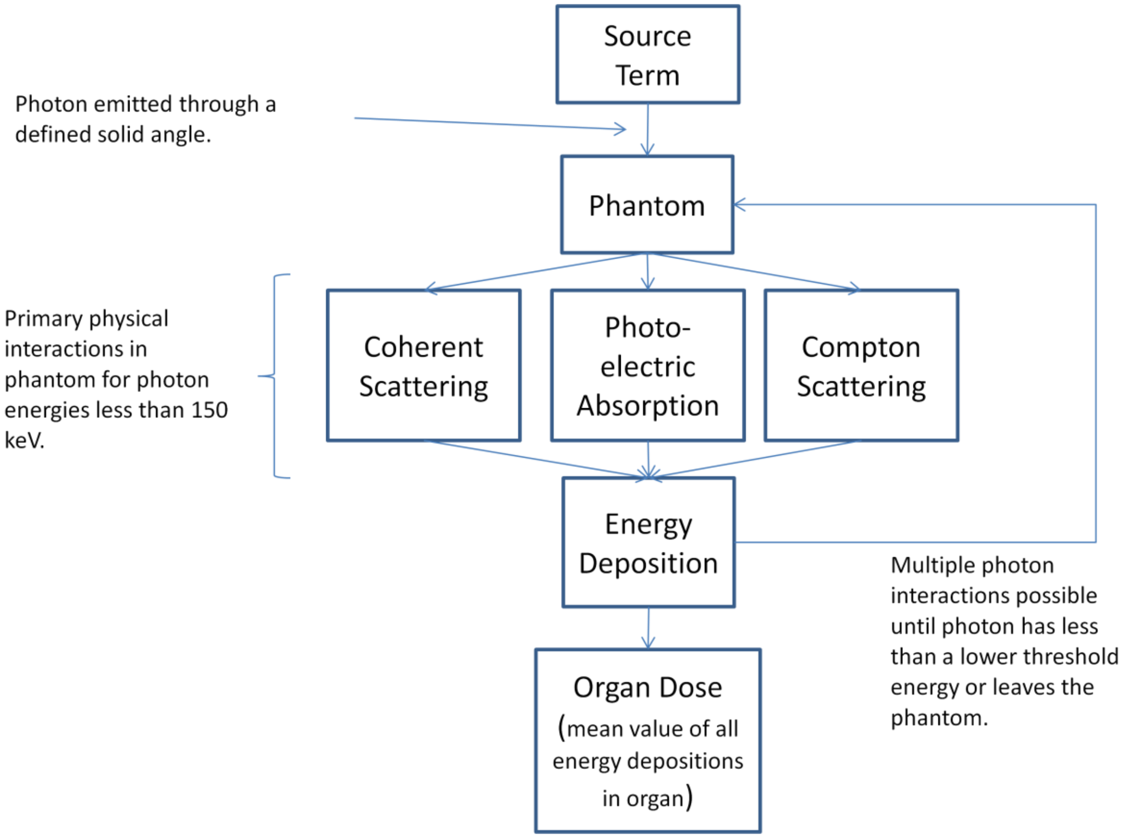

Figure 6. Monte Carlo flowchart for photon energies less than 150 keV. Random numbers are used for sampling initial photon direction, distance between interactions, type of interacting atom within the phantom, type of interaction and scattering angle.

The relative differences in determining organ and tissue doses from CT scans generally result for one of five different areas; organ dimensions, exposure parameters (spectrum and geometry), organ distance from the primary beam field of view, limitations of the Monte Carlo code concerning the x-ray source and patient modeling characteristics, and how the codes deal with basic physics parameters (photon interactions resulting from linear attenuation coefficients and elemental compositions).

All Purpose Codes

I considered two extensively used two all purpose Monte Carlo codes currently being used in medical physics, EGS and MCNP. These codes are extremely powerful and are fully capable of modeling particle interactions from very low energies to very high energies.

EGS

Background

EGS (Electron Gamma Shower) is an open source Monte Carlo code distributed, updated, and managed by the National Research Council of Canada [131-132].

EGS is based on a version of the FORTRAN computing code called MORTRAN. Originally, developed at Stanford Linear Accelerator Center (SLAC) in the early 1970s, EGS was used to study the cascade effect of nuclear disintegrations caused by high-energy particles. The original code accounted for bremsstrahlung, electron-electron scattering, ionization-loss, pair production, Compton scattering, and the photoelectric effect. Additionally, Coulombic scattering was considered. However, the lower energy limit was 0.25 MeV for photons and 1.5 MeV for electrons. The code, EGS1, was tested and found to have good agreement with internal tests at SLAC. More complex modeling geometries stimulated the advancements of newer versions of EGS. EGS soon became a program made up of many sub-programs and sub-routines. Improvements were also made for the handling of multiple scoring planes in the multiple region structures. The use of EGS for medical physics applications emerged with the fourth version of EGS, EGS4. This version of EGS added the capability of radiation transport in any element, compound, or mixture with the dynamic energy range being extended down to 1 keV. Photons and charged particles were transported randomly through a medium while undergoing physical interactions in accordance with their probability of occurrence in that medium at their energy.

Application

EGSnrc (Electron Gamma Shower National Research Council) is the current version of EGS and has been used extensively in medical physics applications. BEAMnrc, an EGS subroutine, has been used extensively to model medical linear accelerators for radiation therapy [133-142]. Another subroutine, DOSXYZnrc is used to model radiation internal dosimetry [143-144] and brachytherapy [145-148] sources. The code has been used to benchmark treatment planning systems [149-151]. Modeling ionization chambers continues to be popular with researchers [152-160]. Most of the referenced applications have been associated with megavoltage radiation beams. Very little research using EGS to model low energy radiation beams (diagnostic energies below 140 keV) has been performed although cone-beam computed tomography is seeing increased interest [56, 161-166].

Comparisons/Benchmarking

EGS has been widely compared with GEANT4, MCNP, and PENELOPE yielding good results [167-169]. EGS claims an advantage over other Monte Carlo codes in terms of computation times. Computation times are a result of the differences between how the codes handle the transport of the charged particles. Numerous studies have been performed in the development of EGS ensuring that physical processes are modeled efficiently and accurately [170-174].

Computed Tomography Modeling

Using EGS to model computed tomography beams and the resultant radiation dose is somewhat of a new research field. Previously, EGS subroutines in DOSXYZnrc have been written to convert CT images into 3-dimensional voxelized phantoms [175]. This technique has proven valuable in understanding dose to specific locations within the body and has been used in treatment planning. Validation of the modeled beam is often performed using detectors [176]. MOSFET detectors and thermoluminescent dosimeters are commonly used as the comparison base. Once validated, the code allows for a better understanding of how scattered photons contribute to dose. This can even be performed for deforming anatomy, i.e. lungs [161]. Future work in this field looks to develop tools for more accurate dose accumulation to a 3-dimensional organ integrated over time. Modeling cone-beam CT units has seen increased research in the areas of pediatric [177] and adult imaging [162-163, 178]. In general though, EGS use with CT stems more in the ability of creating voxelized phantoms which are then used for input into treatment planning systems. Although some research has been performed utilizing EGS as a code for determining radiation dose deposition from normal diagnostic CT procedures [179] more needs to be performed.

MCNP

Background

Monte Carlo N-Particle (MCNP) transport code was developed by Los Alamos National Laboratory in order to develop solutions of radiation transport problems. MCNP is capable of solving transport problems of neutrons, photons, or coupled neutron-photon systems. MCNP was originally designed for criticality safety, shielding design, design of nuclear instrumentation, calculation of material activations, radiological dose determination, spacecraft modeling, nuclear weapons design, and reactor design and analysis[180]. Similar to other general purpose Monte Carlo codes, a user can supply/define a full input file of materials and surfaces for source terms to propagate radiation through. As the radiation interacts with the various media, tallies are generated concerning the deposition of energy and histories are kept describing the total amount of energy deposited or transported through an area of interest. The output results provide information concerning the behavior of the modeled system.

Application

Since the inception of MCNP in 1980, the code has been used to extensively in modeling medical applications. The code is widely used in cancer therapy treatment planning, diagnostic imaging, and treatment beam optimization [181].

Comparisons/Benchmarking

MCNP has been compared with GEANT for the purposes of radiation detection efficiency [182-183] and low energy neutron transport, shielding, and dose calculations [184]. Similarly, MCNP and FLUKA have also been used for detector efficiencies and radiation transport studies [185-189]. MCNP compares favorably, with less than a 10% statistical deviation of the results, with the other Monte Carlo codes.

Computed Tomography Modeling

MCNP has been used for many specific applications in computed tomography dose modeling. Tzedakis et al [190-191] used MCNP to model patients of different ages and sizes using cylindrical polymethyl-methacrylate (PMMA) phantoms. MCNP has also been used as the primary radiation transport simulation code for addressing absorbed doses from CT-SPECT and microCT/PET systems [192]. In comparison research on uterine absorbed doses in pregnant women from CT scans, MCNP simulations were validated against a deterministic simulation code (TORT 3.2) and achieved agreement within experimental uncertainty with the computed exposures found to be within 35% of measured values [193].

Limited Functionality

Limited functionality or hybrid Monte Carlo programs (e.g. ImPACT and PCXMC) have been designed for explicit purposes. They are highly capable and are based off of the same fundamental principles as EGS and MCNP. However, the limitations generally arise as to the energy and type of particle that can be modeled. In medical physics applications, the limitations also involve the phantom used and the most commonly used phantom is a mathematical phantom originally designed by Cristy [194]. Although these Monte Carlo programs are not as fully functional as EGS and MCNP, if the researcher's environment fits within the confines of the limitations, these programs can be very powerful.

ImPACT

Background

ImPACT (Image Performance Assessement of CT scanners) is a widely used Monte Carlo based diagnostic radiology software program designed to simulate radiation doses from computed tomography machines. The program was developed by the National Radiation Protection Board (NRPB) of England. It has been used for estimating CT dose conversion coefficients [91, 195-198] for many general CT scanning procedures and widely used for effective dose estimation in the assessment of radiation dose health risk [67, 74, 101, 199-203]. At present, ImPACT provides an accepted standard estimate on the effective dose for a standard phantom associated with CT scanning protocols.

Purpose

ImPACT has been designed to specifically simulate photons from CT scanners in order to assess the radiation dose to specific organs within a stylized human body for the express purpose of estimating the effective dose from the diagnostic radiology CT scan.

Theory

ImPACT simulates the radiation dose in a mathematical MIRD-style phantom (Figure 7) [204]. This "adult" hermaphrodite phantom represents the human body with a variety of geometrical shapes. The different shapes approximate the various shapes and tissue densities of human organs and body structures. Due to the crudeness of the model, the program is not intended to provide precise measurements of effective dose. The program allows the user to select the approximate scanning field of view for a desired CT imaging protocol. In the figure (Figure 7), the red portion represents the scanning field of view ranging from a starting point of 72.5 up to an ending point of 89.

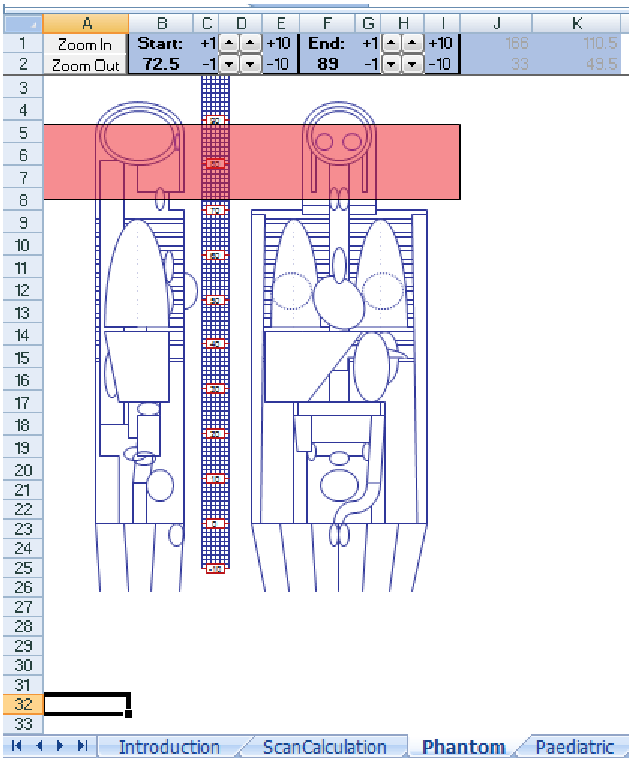

Start: 72.5

End: 89

Figure 7. Screen shot of the phantom used in the ImPACT software program. The red portion represents the scanning field of view ranging from a starting point of 72.5 and having an ending point of 89.

User inputs (Figure 8) in the ImPACT program include scanner model information, acquisition parameters, and organ weighting scheme selection (ICRP 103 [20]). Central to the program is the ability to match 23 previously coded and calculated Monte Carlo data tables (data sets) among the more than 50 different types of CT machines. The data sets were calculated using Monte Carlo methods to model the original CT machines in the NRPB survey performed in 1993. As new CT machines were manufactured an ImPACT factor was determined based upon the CTDI measured in air of the new machine compared with the CTDI measured in air of the machines for the already existing data sets. CTDI was used for the matching because it is a simple standardized means to measure the dose output from a CT scanner [205]. Therefore, comparisons can be made about the radiation dose from one machine to another.

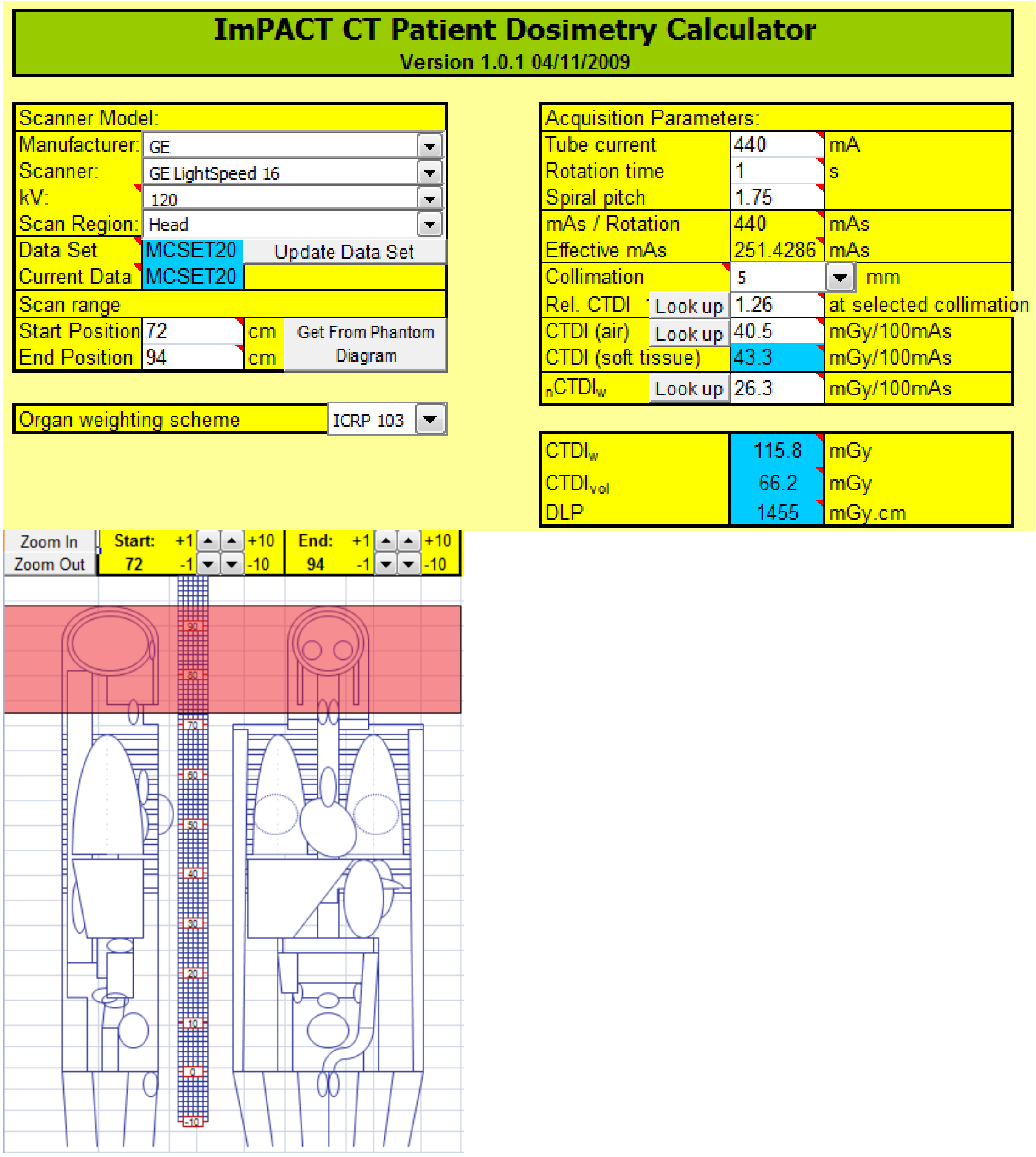

ImPACT CT Patient Dosimetry Calculator
Version 1.0.1 04/11/2009

Scanner Model:
Manufacturer: GE
Scanner: GE LightSpeed 16
kV: 120
Scan Region: Head
Data Set MCSET20
Current Data MCSET20
Scan range
Start Position 72 cm
End Position 94 cm

Organ weighting scheme ICRP 103

Acquisition Parameters:
Tube current 440 mA
Rotation time 1 s
Spiral pitch 1.75
mAs / Rotation 440 mAs
Effective mAs 251.4286 mAs
Collimation 5 mm
Rel. CTDI 1.26 at selected collimation
CTDI (air) 40.5 mGy/100mAs
CTDI (soft tissue) 43.3 mGy/100mAs
$_n$CTDI$_w$ 26.3 mGy/100mAs

CTDI$_w$ 115.8 mGy
CTDI$_{vol}$ 66.2 mGy
DLP 1455 mGy.cm

Start: 72
End: 94

Figure 8. Screen shot of the ImPACT software user input portion. A GE LightSpeed 16 scanner used to perform a head scan (shown in red).

Based on user inputs, the program calculates the radiation dose to 32 different organs. Then, using the appropriate tissue weighting factors, the effective dose is calculated using the values from the calculated organ absorbed doses (Figure 9).

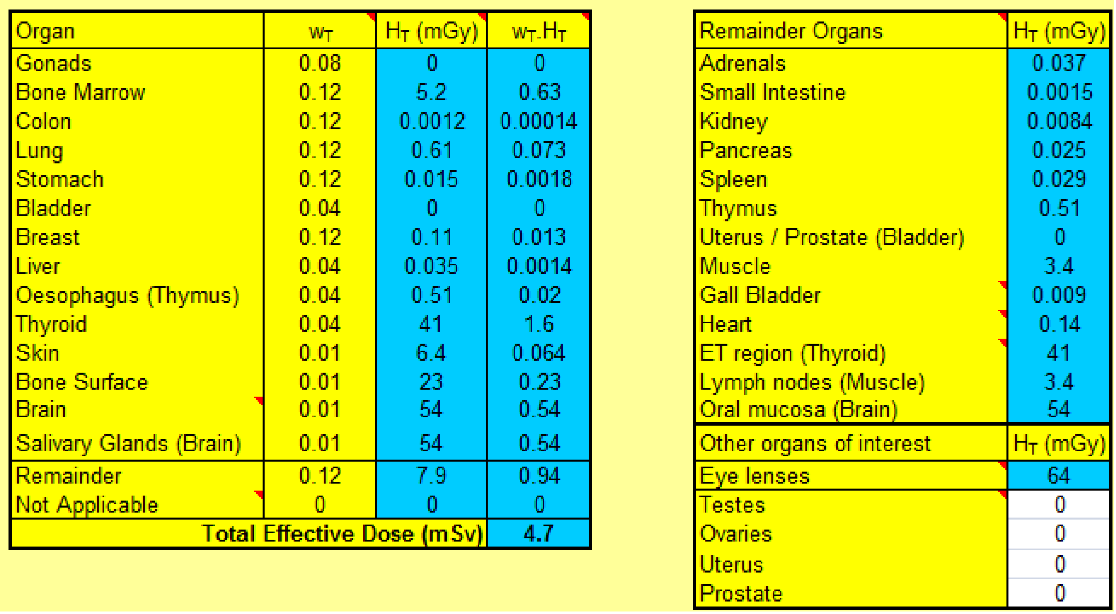

Organ	w_T	H_T (mGy)	$w_T.H_T$
Gonads	0.08	0	0
Bone Marrow	0.12	5.2	0.63
Colon	0.12	0.0012	0.00014
Lung	0.12	0.61	0.073
Stomach	0.12	0.015	0.0018
Bladder	0.04	0	0
Breast	0.12	0.11	0.013
Liver	0.04	0.035	0.0014
Oesophagus (Thymus)	0.04	0.51	0.02
Thyroid	0.04	41	1.6
Skin	0.01	6.4	0.064
Bone Surface	0.01	23	0.23
Brain	0.01	54	0.54
Salivary Glands (Brain)	0.01	54	0.54
Remainder	0.12	7.9	0.94
Not Applicable	0	0	0
		Total Effective Dose (mSv)	4.7

Remainder Organs	H_T (mGy)
Adrenals	0.037
Small Intestine	0.0015
Kidney	0.0084
Pancreas	0.025
Spleen	0.029
Thymus	0.51
Uterus / Prostate (Bladder)	0
Muscle	3.4
Gall Bladder	0.009
Heart	0.14
ET region (Thyroid)	41
Lymph nodes (Muscle)	3.4
Oral mucosa (Brain)	54
Other organs of interest	**H_T (mGy)**
Eye lenses	64
Testes	0
Ovaries	0
Uterus	0
Prostate	0

Figure 9. Screen shot of the ImPACT software dose calculation portion for the user defined inputs shown in Figure 7. Remainder dose is the mean dose of the remainder organs.

ImPACT’s simplified user interface combined with the ability to simulate many different types of CT machines has resulted in it being one of the primary tools for assessing CT effective dose among researchers in the diagnostic imaging field. A major limitation of the software is that all calculations are performed with the single mathematical phantom shown in Figure 8.

PCXMC

Background

PCXMC (PC-based program for X-ray Monte Carlo) is a Monte Carlo code originally written in 1997 at the Radiation and Nuclear Safety Authority, Finland [206-207]. The strengths of the software program are that is allows for computation of organ doses for a range of patient sizes and ages linearly interpolating organ sizes from 6 standard mathematical phantom representations (newborn, 1 year old, 5 year old, 10 year old, 15 year old, and adult) of the 1987 Cristy and Eckerman phantom models (modifications were made to include extrathoracic airways, oral mucosa, prostate and salivary glands). Organ doses are calculated from user input defining adjustable x-ray projections and examination conditions.

Purpose

The main purpose of the program is to derive the effective dose from projection radiography and fluoroscopic procedures. The effective dose is calculated in accordance with ICRP 103 tissue weighting factors and formulism. Organ doses are calculated relative to the incident air kerma at the point where the central axis of the x-ray beam enters the patient with the photon paths and interaction calculated using Monte Carlo methodologies.

Theory

Monte Carlo methodology is used to simulate photon transport and subsequent interactions between the photons and matter (Figure 6). Primary interactions considered are photoelectric absorption, coherent (Rayleigh) scattering, and incoherent (Compton) scattering. Photon information is collected at each interaction point as energy is deposited and combined into histories. The upper limit on the user defined energy of the x-ray beam is 150 keV. Within this range of energies, the kerma in tissues is approximately equivalent to the absorbed dose within the same tissues, except at the interface between bone and soft tissue [207]. Secondary electrons are approximated to be absorbed at the site of the photon interaction within tissue due to the low energy of the secondary electrons and the small range. Dose is calculated from the average values of the energy depositions, obtained from the photon histories, in the organs. Energy spectra are assumed to be an integral of monochromatic photons of specific energies up to 150 keV. The precision of the dose estimate increases and the statistical error decreases as the number of initial photons in the simulation increases. Precision is also affected by the organ dose (to low will cause high errors) and/or size of the organ.

PCXMC uses a hermaphrodite phantom to calculate the effective dose from a radiology procedure. This differs from ICRP 103 methodology for effective dose in that ICRP 103 defines the effective dose within separate reference male and female phantoms, where the equivalent organ dose is averaged and the effective dose is a weighted sum of the sex averaged organ doses [207]. Since PCXMC utilizes one hermaphrodite phantom, there is no need to perform sex averaging for the organ doses.

PCXMC allows for the user to vary the shape of the mathematical phantoms by changing the height and weight. The ability to change the shape of the mathematical phantom by changing the height and weight cannot be over-emphasized. It is well known that as the human body grows from infancy through adulthood, organs also grow. However, some organ weights also change as an adult's total body weight increases. In an autopsy study performed measuring organ sizes and mass for bodies of different ages, heights, weights, and race, Young et al [208] determined that certain organs and their associated dimensions change as a person grows. For example, the female kidneys will increase in mass as the total body weight increases up to 200 kg. Similarly, the lung mass changes increases as the body weight increases up to 150 kg and the thyroid mass increases as the body weight increases up to 125 kg. There are six standard phantoms which PCXMC uses as the base for the variation (Table 7).

Table 7. Primary dimensions of the mathematical phantoms within PCXMC.

	Weight (kg)	Total Height (cm)	Trunk Height (cm)	Trunk Thickness (cm)	Trunk Width no arms (cm)	Trunk Width w/arms (cm)	Leg Length (cm)
Newborn	3.40	50.90	21.60	9.80	10.94	12.70	16.80
1 year old	9.20	74.40	30.70	13.00	15.12	17.60	26.50
5 year old	19.00	109.10	40.80	15.00	19.64	22.90	48.00
10 year old	32.40	139.80	50.80	16.80	23.84	27.80	66.00
15 year old	56.30	168.10	63.10	19.60	29.66	34.50	78.00
Adult	73.20	178.60	70.00	20.00	34.40	40.00	80.00

As the user changes the height and weight of the phantom within PCXMC (Figure 10), the program calculates scaling factors in accordance with the primary phantom dimensions. All dimensions, including the organ sizes, are modified by the scaling factors.

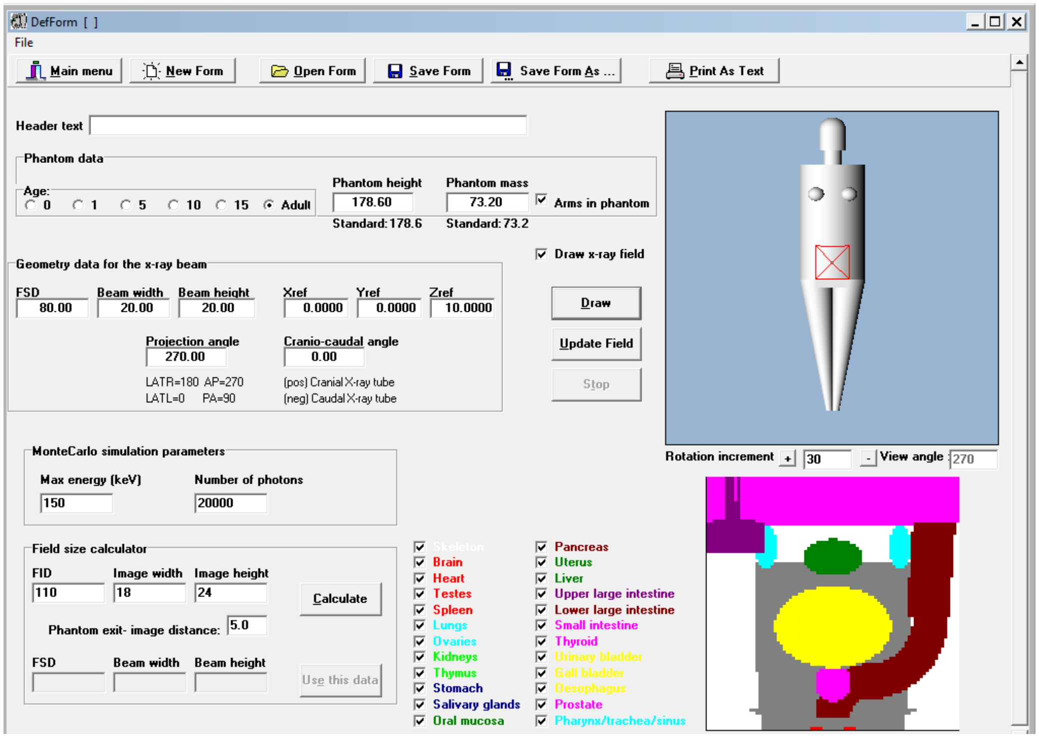

Header text:

Phantom data

Age: ○ 0 ○ 1 ○ 5 ○ 10 ○ 15 ● Adult

Phantom height: 178.60 (Standard: 178.6)

Phantom mass: 73.20 (Standard: 73.2)

☑ Arms in phantom

☑ Draw x-ray field

Geometry data for the x-ray beam

FSD	Beam width	Beam height	Xref	Yref	Zref
80.00	20.00	20.00	0.0000	0.0000	10.0000

Projection angle: 270.00

LATR=180 AP=270
LATL=0 PA=90

Cranio-caudal angle: 0.00

(pos) Cranial X-ray tube
(neg) Caudal X-ray tube

Rotation increment: 30

View angle: 270

MonteCarlo simulation parameters

Max energy (keV): 150

Number of photons: 20000

Field size calculator

FID	Image width	Image height
110	18	24

Phantom exit- image distance: 5.0

FSD	Beam width	Beam height

☑ Skeleton
☑ Brain
☑ Heart
☑ Testes
☑ Spleen
☑ Lungs
☑ Ovaries
☑ Kidneys
☑ Thymus
☑ Stomach
☑ Salivary glands
☑ Oral mucosa
☑ Pancreas
☑ Uterus
☑ Liver
☑ Upper large intestine
☑ Lower large intestine
☑ Small intestine
☑ Thyroid
☑ Urinary bladder
☑ Gall bladder
☑ Oesophagus
☑ Prostate
☑ Pharynx/trachea/sinus

Figure 10. Screen shot of the examination input window for PCXMC. The red box on the stylized phantom represents the scan field of view.

Validation of Limited Functionality Codes

Mathematical phantoms are used to provide flexibility in phantom design but may result in anatomical descriptions that are not very realistic. Comparison of recent software programs that may utilize more representative human phantoms (anthropomorphic) has been performed and has shown good agreement with PCXMC [61, 209] and ImPACT [46, 67, 210]. Such voxel image-based phantoms are more realistic anatomically but are limited in the flexibility of organ placement, shape, position, depth, and posture. University of Florida is beginning to use computational phantoms that utilize the best characteristics of the mathematical and voxel phantoms. This new class of phantoms is called a hybrid computational phantom [144, 211], but are not yet generally available to the research community. Therefore, mathematical phantoms are currently still very much in use.

ImPACT has been validated against EGS for new voxel phantom based dose assessment [52, 77]. Comparisons to CT scans often used in trauma diagnosis offer good agreement between the mathematical phantom of ImPACT and voxel phantom calculations; between -6 to 11% for chest scans, -22 to -1% for abdomen chest scans, and -4 to 11% for pelvis chest scans.

Although PCXMC is primarily designed for projection radiography, it has been used to calculate effective doses from scan projection radiography and tomosynthesis procedures where radiographic examinations are taken on a patient from the posterior-anterior (PA) and left lateral (LLAT) sides [212]. It has also been used to compare CT and conventional radiography doses from assessment of patients with arthrodesis [213]. In addition, comparisons have also been performed in order to assess absorbed doses in cardiac angiography from C-Arm computed tomography machines. Current literature shows that a CT rotation can be effectively modeled by using multiple projections per slice [36, 203, 214-215].

Software Decision

There are many different CT machines being utilized in the Army (Table 8). These machines are not only being used at fixed facilities but also in close proximity to the battlefield. As a result, a Soldier that is scanned at different facilities might be scanned with a different machine each time. Therefore, a predictive model seeking to estimate the radiation dose from a procedure should be capable of estimating the effective dose for each trauma scanning protocol for a wide variety of different CT machines. The predictive model should also be capable of predicting the effective dose for a wide variety of patient types. For this reason, I chose to use limited functionality Monte Carlo programs in order to formulate the predictive model. Use of EGS or MCNP would require knowledge of specific machine dimensions and proprietary information concerning the systems involved in the radiation delivery. In addition, such models would be machine specific and would not be capable of predicting dose across the wide variety of machines in use by the Army. Therefore, in developing my effective dose predictive model, I will utilize PCXMC (allowing for varying patient heights and weights) with the results being compared against ImPACT and with direct measurements (see chapter 5).

Table 8. Survey sample of the different computed tomography machines in use at Army medical facilities.

Manufacturer	**Type**	**Different Army Locations**
GE	LightSpeed 16	3
	LightSpeed VCT 64 Slice	1
	Discovery DST PET/CT	1
	LightSpeed VCT	1 (2 at this location)
	LightSpeed Plus	1
	LightSpeed RT	1
Toshiba	Aquilion 64	4
Philips	ACQSim	1
	Brilliance Big Bore 16	3
	Brilliance EXP	1
	MX8000	1
Siemens	Somatom Definition	1
	Symbia T6 SPECT-CT	1
	Biograph PET-CT	1
	Somatom Plus	1
Picker	PQ2000S	1
	PQ5000	1
Other	Portable CT Medtronic O-arm	1

Protocol Specific Effective Dose

In order to determine the effective dose for a given CT procedure, a retrospective study was conducted within the Memorial Sloan-Kettering Cancer Center patient archiving and communication system (PACS) under an approved Institutional Review Board (Table 9). The purpose of the study was to collect real patient retrospective data (CTDIvol, DLP, machine type, and scan range) on at least 30 patients for input into the ImPACT software in order to provide an additional comparison for the PCXMC results.

Table 9. Summary of retrospective PACS study for determining appropriate inputs in ImPACT software.

Procedure	Number of Patients	Machine Type (most commonly used)	Age (Mean, Interquartile Range)	CTDIvol (mGy) (Mean, Interquartile Range)	DLP (mGy cm) (Mean, Interquartile Range)	Scan Range (cm) (Mean, Interquartile Range)
Brain Scan	71	GE LightSpeed 16	53 (42-69)	43.32 (41.15-41.81)	679.11 (648.12-710.84)	15.67 (15.75-17.09)
Cervical Spine Scan	32	GE LightSpeed 16	59 (48-72)	26.17 (22.48-29.41)	617.91 (514.73-680.34)	23.35 (20.64-25.26)
Chest-Abdomen-Pelvis Scan	31	GE LightSpeed 16	69 (63-80)	15.06 (12.91-17.57)	1015.90 (848.80-1218.00)	67.21 (63.92-69.93)
Chest Scan	32	GE LightSpeed 16	59 (52-67)	12.19 (10.91-13.19)	470.70 (406.30-516.30)	38.61 (37.13-40.95)
Thoracic Spine Scan	53	GE LightSpeed 16	58 (47-73)	27.87 (23.11-31.81)	972.50 (811.50-1121.30)	35.17 (32.63-37.11)
Lumbar Spine Scan	64	GE LightSpeed 16	62 (48-75)	28.13 (23.69-29.41)	842.90 (710.10-970.20)	30.28 (25.73-33.60)

The PACS database patient information was randomly collected and filtered only by CT scan type. The majority of the CT machines are manufactured by General Electric (General Electric Healthcare, Waukesha, Wisconsin) and the most common model being the GE LightSpeed 16. This type is also the CT system on which the anthropomorphic verification study (Specific Aim 3) will be performed. Although there are some apparent differences (mean ages and amount of muscle mass per patient) between the MSKCC patient population and the U.S. Army Soldier population, the two populations can be compared against each other since CT scanning fields of view are set based upon anatomical landmarks [216]. The variation of patient height is seen in the variation of the patient scanning range (Table 9). The scanning length with the least amount of variation between the 1st and 3rd quartile range is the brain scan (8.5%) and the most variation occurs with the lumbar scan (31%). Arguably the most common CT scan for trauma protocols, Chest-Abdomen-Pelvis, only has a 9.4% variation (between the 1st and 3rd Quartile) in the scanning range. However, this scan will also be affected the most by patient height when comparing the minimum range (18.38 cm) and the maximum range (90.33 cm) to other scanning lengths.

As discussed previously in Chapter 2, CTDIvol is a machine specific parameter that can be used to evaluate the machine produced radiation dose characteristics in a quality assurance quality control phantom using a 100-mm detector. This parameter allows for radiation dose comparisons to be made among different types of CT machines. CTDIvol multiplied by the scanning length results in the dose-length-product (DLP). The mean of the PACS reported DLP for each CT protocol is compared against the ImPACT calculated DLP when CTDI values and other user parameters are inputted (Table 11).

The inputs for ImPACT are listed below (Table 10). These inputs were physician verified (Dr. Raymond Thornton, Department of Radiology, MSKCC) and compared with the patient images in PACS.

Table 10. ImPACT inputs based upon PACS data (most common CT model is the GE Lightspeed 16) and physician input.

Procedure	kV	Scan Region	Start Position	End Position	Tube Current	Rotation time (s)	Pitch	Collimation (mm)	CTDIvol	nCTDIw	DLP
Brain	120	Head	78	94	155	2	1.375	10	43.3	19.2	693
Cervical Spine	120	Head	64	87	155	1	1.375	10	26.1	23.2	600
CAP	120	Body	5	75	300	1	1.375	20	15.1	6.9	1054
Chest	120	Body	33	72	270	1	1.375	20	12.2	6.2	475
Thoracic Spine	120	Body	37	72	270	1	1.375	20	27.9	14.2	976
Lumbar Spine	120	Body	17	48	270	1	1.375	20	28.1	14.3	870

Representative scans are shown below comparing an actual patient scan with the scanning field of view inputted into ImPACT (Figure 11).

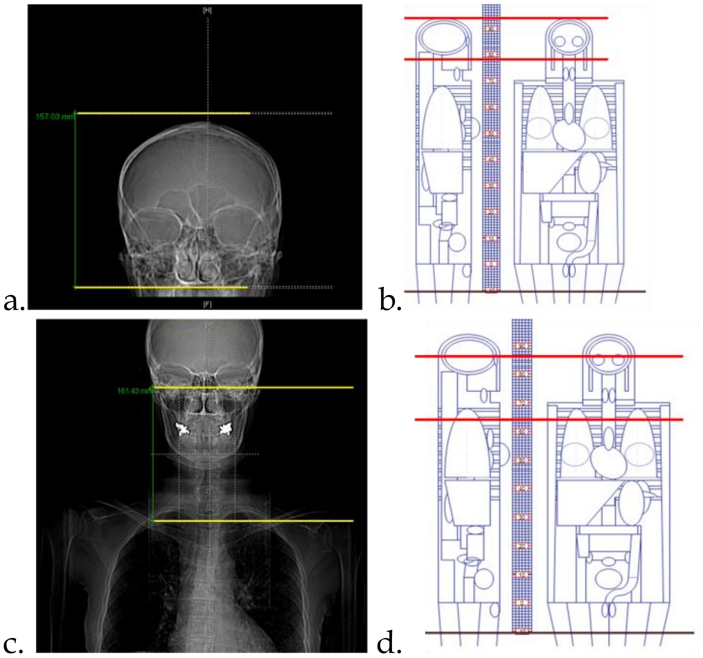

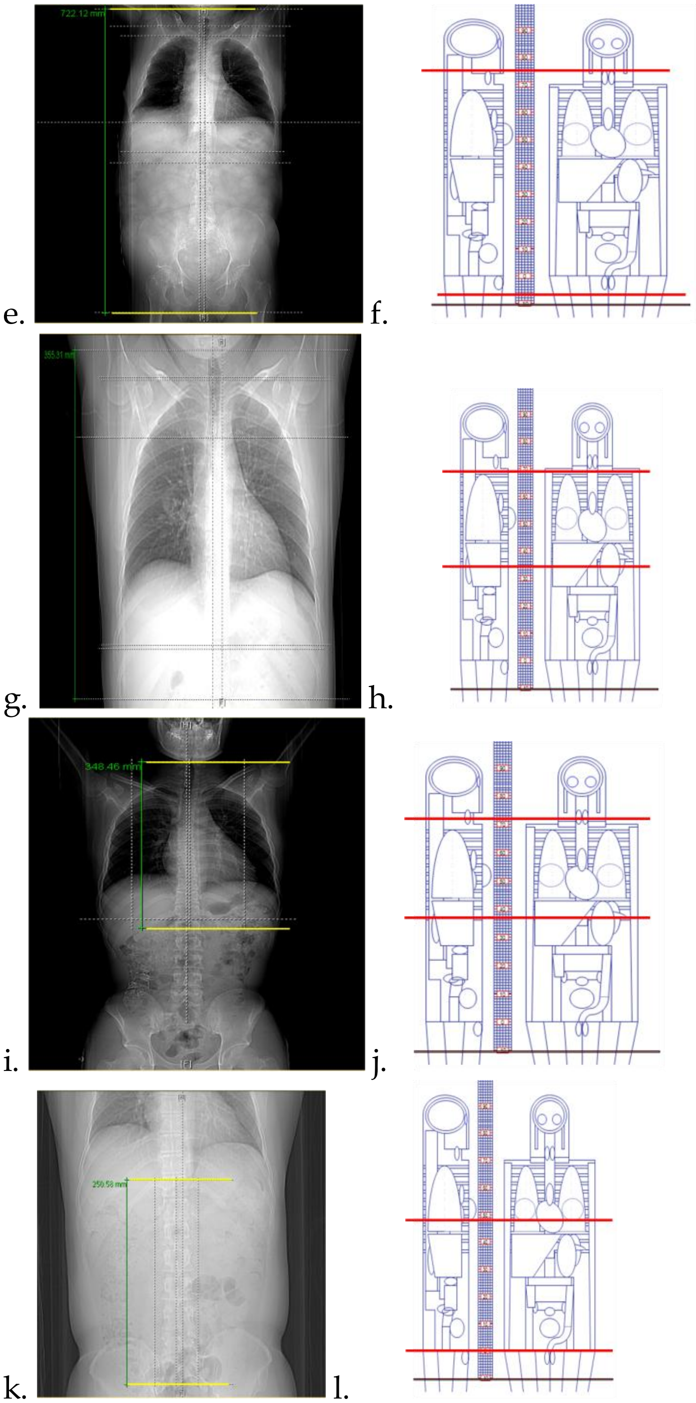

Figure 11. Representative Scans. Brain Scan (Figure 11a and Figure 11b (ImPACT)). Cervical Spine Scan (Figure 11c and Figure 11d (ImPACT)). Chest Abdomen Pelvis Scan (Figure 11e and Figure 11f (ImPACT)). Chest Scan (Figure 11g and Figure 11h (ImPACT)). Thoracic Spine Scan (Figure 11i and Figure 11j (ImPACT)). Lumbar Spine Scan (Figure 11k and Figure 11l (ImPACT)).

Table 11. Comparison between ImPACT DLP values and the mean DLP values from the patient retrospective PACS study.

Procedure	ImPACT DLP value (mGy cm)	Mean Study DLP value (mGy cm)	Absolute Percent Difference between DLP values
Brain Scan	693	679.11	2%
Cervical Spine Scan	600	617.91	3%
Chest Abdomen Pelvis Scan	1054	1015.90	4%
Chest Scan	475	470.70	1%
Thoracic Spine Scan	976	972.50	0.4%
Lumbar Spine Scan	870	842.90	3%

Since the difference between the DLP values are so small, the effective dose calculation in ImPACT will adequately describe the effective dose for the patient retrospective PACS study and can be used as a representation of the expected effective dose for each of the six trauma protocols (Table 11). Note that the effective doses are within the NRCP 160 range for the listed scans (Table 12). Effective dose for the chest abdomen pelvis scan from ImPACT is slightly higher than the listed NCRP 160 effective dose for an abdomen/pelvis scan. This is a result of the slightly longer scanning range (therefore more organs directly in the scanning field of view) of the chest abdomen pelvis scan than for the shorter scanning range of an abdomen pelvis scan.

Table 12. Effective dose per trauma protocol as calculated in ImPACT and reported in the NCRP Report 160 [14].

Procedure	Effective Dose (mSv)	Effective Dose (mSv) NCRP 160 [14]
Brain Scan	1.7	0.9 – 4 Head Scan
Cervical Spine Scan	2.4	Not listed
Chest Abdomen Pelvis Scan	27	3 – 25 Abdomen/Pelvis Scan

Chest Scan	15	4 – 18 Chest Scan
Thoracic Spine Scan	13	Not listed
Lumbar Spine Scan	11	Not listed

Conclusion

Monte Carlo programs investigate the deposition of energy (dose) in the human body from radiative particles. Many Monte Carlo programs are fully functional for modeling the transport of particles through a plethora of different mediums. Some Monte Carlo programs while more limited in functionality, are still quite capable of investigating radiation dose albeit in a more limited environment. Although EGS and MCNP are extremely powerful Monte Carlo programs, each CT machine type would have to be individually designed and modeled prior to full characterization and validation against a physical machine. While this is certainly doable over a long period of research time (many years), this is impractical for the purposes of this research. Therefore, due to the wide variety of CT machine types and manufacturers currently being used in the throughout the U.S. Army medical facilities, the decision was made to use a limited functionality Monte Carlo program specifically designed to assess only CT scans but capable of modeling the radiation dose from over 50 CT machines. Since many conversion coefficients are based upon the ImPACT software, the ImPACT effective dose calculations are useful for comparing against my predictive model effective dose per trauma procedure results. User inputs into the ImPACT software were determined based upon a retrospective CT study of patient scans and CT scanning parameters in the Memorial Sloan-Kettering Cancer Center patient archiving and communication system (Brain Scan, Cervical Spine Scan, Chest Abdomen Pelvis Scan, Chest Scan, Thoracic Spine Scan, and Lumbar Spine Scan). When the effective dose calculated by the software was compared against accepted values (NCRP 160), all values were within acceptable ranges (Table 12). Since the ImPACT software only models the effective dose based upon a single mathematical phantom in which patient dimensions (i.e. height and weight) cannot be varied, another Monte Carlo program (PCXMC) will be used to build a predictive model with which the effective dose from the six trauma scans can be determined based upon a patient's height and weight at the time of the scan (Chapter 4).

CHAPTER 4. Specific Aim 2: Develop an improved model capable of predicting effective dose based upon a patient's physical characteristics (height and weight).

Introduction

This chapter will address the development of effective dose estimation models to be used for the six different computed tomography (CT) trauma protocols discussed in the previous chapter (Chapter 3). The models will be developed from Monte Carlo simulations performed with mathematical phantoms with physical parameters common with Soldiers.

Current methods for determining the effective dose require knowledge of the CT machine's output (dose-length-product, CTDIvol, etc.) [67, 86, 203]. The machine's output is then converted to effective dose via use of a conversion coefficient developed for a specific scanning area. However, computing the effective dose without knowledge of the CT machine output is difficult and radiation professionals will often utilize National Council on Radiation Protection and Measurements (NCRP) general estimates which have a wide range and only are applicable for a few specific procedures [14]. While useful for general comparisons, application of these effective doses do not allow for patient specificity required to track cumulative radiation doses from multiple procedures. In order to track cumulative radiation from CT trauma protocols, a more patient specific methodology needs to be developed.

The U.S. Army requires that each Soldier complete a physical fitness test twice a year. The test measures upper body fitness (push-ups), lower body fitness (sit-ups), and lung stamina (two-mile run). An additional component of the physical fitness test is determining whether or not a Soldier meets certain body fat standards determined by measuring the Soldier's height, weight, and age. For Soldiers that do not meet the body fat number in accordance with their age, more advanced body fat measurements are performed beyond simple height/weight measurements. The U.S. Army therefore is indirectly tracking, on a semi-annual basis, how a Soldier's height and weight changes from the initial date of entry into military service. U.S. Army Soldiers are generally within 18 – 45 years old and can be thought of as young, healthy, and physically fit [13, 217].

The development of the methodology for the six previously mentioned CT trauma protocols (Brain, Cervical Spine, Chest/Abdomen/Pelvis, Chest, Thoracic Spine, and Lumbar Spine) will be based upon a patient's height and weight. Therefore, patient parameters (height and weight) appropriate for a typical U.S. Army Soldier population will be used as inputs into the PCXMC Monte Carlo code for effective dose determination. Regression analysis will then be used to develop the mathematical model capable of estimating the effective dose to a patient by CT trauma protocol.

Methodology

BMI Considerations

In order to ascertain the ranges of heights and weights for the typical U.S. Army Soldier population, research was conducted using Body Mass Index (BMI). BMI is a common parameter used in epidemiology studies and is calculated according the below algorithm.

$$BMI\ \left(\frac{kg}{m^2}\right) = \frac{weight\ (kg)}{height\ (m)^2} \qquad 9$$

The Center for Disease Control (CDC) separates BMI into four separate categories and defines a generalized health indicator (Table 13).

Table 13. CDC Body Mass Indicator (BMI) table.

BMI	**Definition**
< 18.5	Underweight
18.5 – 24.9	Normal
25.0 – 29.9	Overweight
> 30.0	Obese

BMI indirectly measures the overall size of the human body, thus individual organ sizes, and can be an effective indicator as to how much radiation dose a body organ will receive during a diagnostic imaging procedure [208, 218]. Even though BMI is limited by being unable to differentiate between the measures of fat content a person possesses as opposed to muscle mass. BMI measures relative weight to height and will differ between race and gender. BMI doesn't however differentiate between a physically fit person with a high BMI (for example a Soldier that is very physically fit and muscular with a high body mass) and a person who is not physically fit but with the same BMI. The U.S. Army population can be considered a physically fit population. However, BMI has been used as a mechanism for determining radiation dose.

BMI has been correlated to radiation dose for many radiology procedures [85, 219-227] and has been primarily used for cardiac procedures. As the patient's BMI increases, the x-ray tube output must also increase in order to maintain an acceptable image noise level and compensate for the increased tissue thickness. Since the tube output is a factor of the overall radiation dose, the radiation dose increases proportionally. The size of a person affects the x-ray tube output and thus has an overall effect on the amount of radiation absorbed in the body [219, 224].

There is currently no known research on correlating BMI to the effective dose from CT trauma protocols. This research will address this knowledge gap.

U.S. Army Soldiers are primarily in the Normal and Overweight category. One will initially think that a Soldier's BMI will vary according to the job with active jobs (Infantry, Special Forces, etc.) having a BMI much less than a Soldier with more of administrative job. However, across the spectrum of jobs (combat-related, combat support, or combat service support) the BMI is generally the same (Table 14). This is a result of the younger more active Soldiers having a higher degree of muscle mass and less fat as opposed to an older Soldier, who is less active, more likely to be in an administrative position, having less muscle mass, more fat, and therefore a similar BMI. For example, a study performed by Reynolds et al [228] looking into injuries and risk factors from a 100-mile road march found that 218 Soldiers (average age 21.4 years old) participating in the study, had a mean BMI of 24.5 +/- 2.6 (median = 24.1). A similar unpublished study performed by the author looking into Soldier cholesterol levels with 62 Soldiers (average age 43.5 years old) at a major command headquarters, found a mean BMI of 26.1 +/- 3 (median = 26.1). Another study showed that regardless of Army specialty, BMI is similar throughout the Army (Table 14) [229].

Table 14. Summary of studies showing how BMI is similar across the age groups in the Army regardless of job performed.

Study	Participant Type	Number	Age (std dev)	BMI
Reynolds, 1999	Infantry	218	21.4	24.5 (2.6)
Prins (Unpublished)	Administrative	62	43.5 (7.7)	26.1 (3.0)
Reynolds, 2009	Infantry	181	21.2 (1.4)	23.8 (2.5)
	Construction Engineers	125	24.1 (5.5)	25.5 (2.6)
	Combat Artillery	188	26.6 (6.0)	25.5 (4.0)
	Special Forces	162	30.5 (6.0)	25.9 (2.8)

There are many arguments against using BMI as a predictor of body fat. BMI overestimates the body fat of members of a population who are athletes and/or body builders. BMI can also underestimate the body fat of other members of a population who are elderly. Therefore, my new research methodology, henceforth to be called the Ht/Wt model, used BMI as a means of determining the height and weight of the theoretical U.S. Army population. The Ht/Wt methodology was based upon BMI's ranging from 18 (underweight) to 36 (obese). Corresponding heights and weights were calculated from the BMI values. One hundred hermaphrodite phantoms were developed for use in PCXMC simulating heights ranging from 5 feet 1 inch up to 6 feet 7 inches. Phantom weights ranged from 95 pounds up to 317 pounds. As can be observed in Table 15, the methodology for determining the number of phantoms of varying height and weight follows commonly used guidelines of ten observations for each predictor [230-231]. Extreme values are rare in a typical U.S. Army Soldier population. Table 15 shows the height/weight values for each of the 100 hermaphrodite phantoms and also shows how a single BMI can have a variety of heights and weights.

Table 15. 100 hermaphrodite phantoms based upon each BMI value.

		Body Mass Index (kg/cm^2)										
		18	20	22	24	26	28	30	32	34	36	
Height (cm)	155	43	48	53	58	62	67	72	77	82	86	Weight (kg)
	160	46	51	56	61	67	72	77	82	87	92	
	165	49	54	60	65	71	76	82	87	93	98	
	170	52	58	64	69	75	81	87	92	98	104	
	175	55	61	67	74	80	86	92	98	104	110	
	180	58	65	71	78	84	91	97	104	110	117	
	185	62	68	75	82	89	96	103	110	116	123	
	190	65	72	79	87	94	101	108	116	123	130	
	195	68	76	84	91	99	106	114	122	129	137	
	200	72	80	88	96	104	112	120	128	136	144	

Figure 12 depicts how the phantom population varies when height is plotted versus weight. The phantoms were purposefully developed so that each BMI value is represented by 10 different phantom heights.

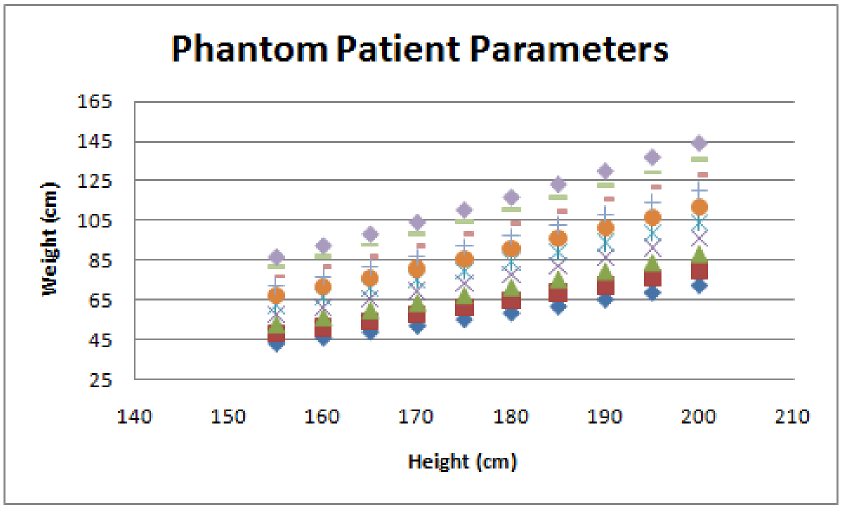

Figure 12. Phantom patient parameters. Vertical groups indicate single BMI values where height is held constant and weight varies.

Based upon the inputted height and weight, PCXMC scales the hermaphrodite mathematical phantom with a linear scaling factor for height (equation 10) and width (equation 11) [232].

$$s_z = \frac{h}{h_o} \quad 10$$

and

$$s_{xy} = \sqrt{\frac{h_o \cdot M}{h \cdot M_o}} \quad 11$$

M is the user inputted mass of the phantom. All phantom dimensions are scaled according to the two above equations and organ masses are linearly changed as a result. Figure 13 shows a typical size progression where the mathematical phantom depicts different dimensions with the red box indicating a 20-cm x 20-cm scanning field of view.

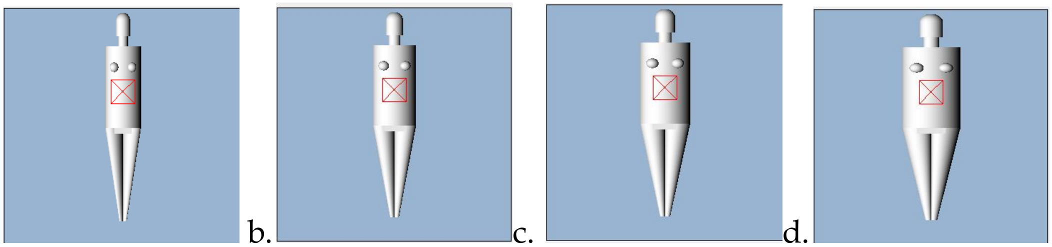

a. b. c. d.

Figure 13. Varying phantom dimensions. Figure 13a has dimensions of 175 cm and 40 kg. Figure 13b has dimensions of 175 cm and 60 kg. Figure 13c has dimensions of 175 cm and 80 kg. Figure 13d has dimensions of 175 cm and 110 kg.

A radiologist (Raymond Thornton, MD, Memorial Sloan-Kettering Cancer Center) assisted with determining the scanning ranges (upper and lower anatomical limits) for each of the six trauma protocols. This was compared against the field of view of real patient scans viewed in the PACS database. The scanning field of view for six trauma protocols (brain scan, cervical spine scan, chest abdomen pelvis scan, chest scan, thoracic spine scan, and lumbar spine scan) were compared against the patient scans is shown in Figure 14.

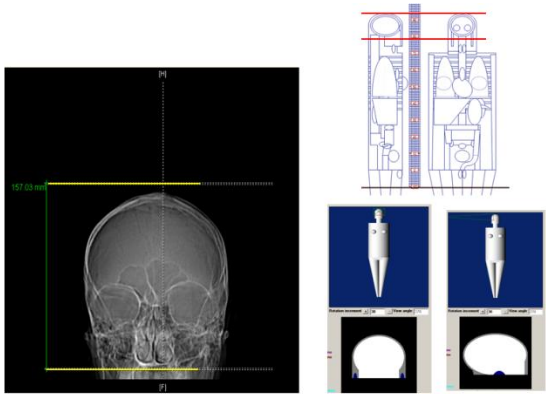

14a.

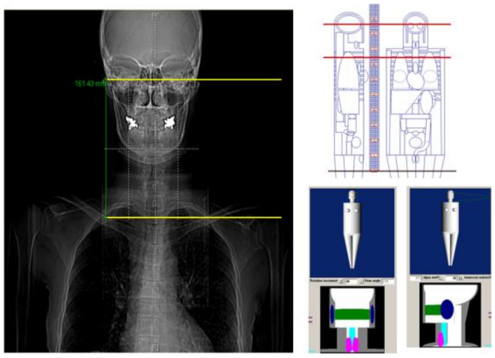

14b.

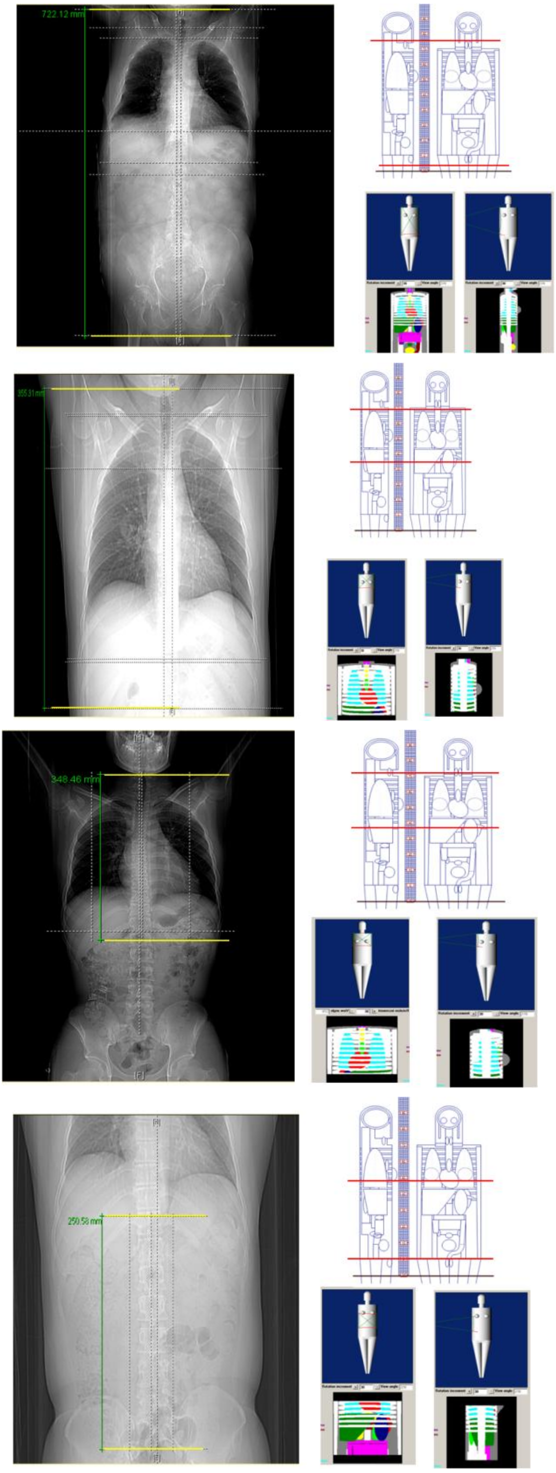

14c.

14d.

14e.

14f.

Figure 14. Six trauma protocols ((14a) Brain Scan, (14b) Cervical Spine Scan, (14c) Chest Abdomen Pelvis Scan, (14d) Chest Scan, (14e) Thoracic Spine Scan, (14f) Lumbar Spine Scan) are presented with the left hand picture showing a representative patient scan, top right figure showing a depiction of the ImPACT phantom, and

bottom right two figures showing an anterior-posterior view and right lateral view of the PCXMC phantom.

Four projections (anterior posterior (AP), posterior anterior (PA), right lateral (RLAT), and left lateral (LLAT)) simulating a 360 degree exposure were used to model a CT machine with PCXMC (Figure 15). Each projection has the same slice thickness as the desired CT axial slice. Although theoretically a researcher can use as many projections as they wish (for example 16 projections per slice), dose accumulation in that slice increases drastically. In order to equate the total effective dose (as calculated by PCXMC) to the effective dose as calculated by our accepted standard (ImPACT), calibration factors are determined and applied for the specific phantoms (height, weight, and machine output parameters). Calibration factors are a function of the number of projections. The decision was made to use the four projections described above in keeping with other published literature [214].

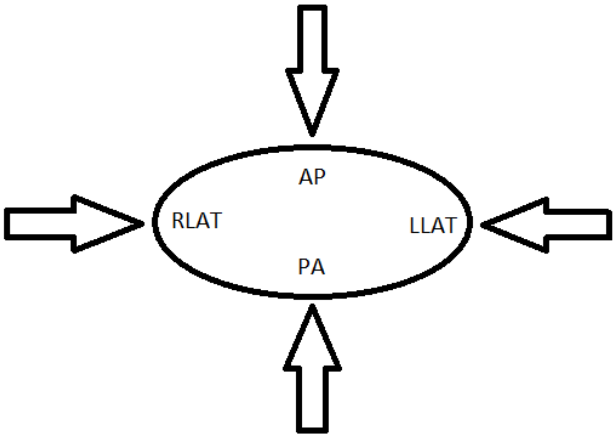

Figure 15. Cross-sectional view of an axial slice made up of four radiographic projections.

The x-ray spectrum was modeled based upon the most common CT machine in use at Memorial Sloan-Kettering Cancer Center, the General Electric (GE) LightSpeed 16. This same machine will be used to verify the code values. The GE LightSpeed 16 scans all patients at a focus-to-skin distance (FSD) of 54.1 cm. In accordance with appropriate protocols, all scans are performed at an x-ray tube energy potential of 120 kVp. The half-value layer of a scan about the body is 7.4-mm aluminum and the half-value layer of a scan about the head is 6.3-mm aluminum. The anode target angle is 7-degrees.

Entrance air kerma (air kerma measured at the surface of the phantom) values for each projection were obtained from the scans of an anthropomorphic phantom using detectors (Unfors PSD-4, SN; 162351, calibration date: 2010-01-11) placed at the center point of each scanning field-of-view at the anterior-posterior (AP), posterior-anterior (PA), left lateral (LLAT), and right lateral (RLAT) positions on the anthropomorphic phantom. Entrance air kerma values are listed in Table 16.

Table 16. Measured Entrance air kerma value (mGy) by scanning procedure for input into PCXMC.

Entrance Air Kerma (mGy)				
Scanning Procedure	Patient LLAT	Patient PA	Patient RLAT	Patient PA
Brain Scan	30.98	41.38	32.59	32.06
Cervical Spine	19.90	22.95	27.92	22.25
Ch/Ab/Pel	13.40	21.11	15.07	13.75
Chest	13.10	29.52	16.70	19.73
Thoracic Spine	6.22	6.75	6.83	7.88

Lumbar Spine	17.00	10.69	11.39	9.99

Variation in the EAK value by location is expected since the x-ray tube is rotating prior to initiation and the exact location of the x-ray tube upon activation is unknown. The variation in the EAK value is also a function of the x-ray tube current modulation adjusting for the various thicknesses of material (body, table, etc.) between the x-ray tube and the detectors. Change in x-ray tube position also results in variation of the entrance radiation dose along the z-direction for contiguous axial and helical scans. Measurements of entrance dose will be subject to entrance, exit, and scattered radiation or a combination depending upon where the entrance point is measured and the angle of the x-ray tube relative to the entrance point of the radiation beam on the patient. Comparison of the effective dose from the methodology will need to be made with the accepted standard method which does allow for changes in pitch [48].

The number of photons simulated by the Monte Carlo process is important. As the number of photons is increased, the Monte Carlo results will begin to approach physical results. However, there is a tradeoff between the number of photons and the increased computer time needed to perform the calculations. The goal is to balance the amount of photons with the computer time needed for calculations while minimizing the statistical error in the results. Published research has shown that simulations of 20,000 photons per scanning projection within the PCXMC code is adequate for estimating absorbed dose to tissues and organs and achieves an accuracy in tube output of within ±4% [36]. Increasing the number of photons results in an overall increase of computer time from days to weeks for each simulation run with only a minimal gain in percent error in estimated accuracy. The percent error was accounted for in the overall sensitivity study.

Reference Specific Aim 1, ImPACT is used as the "accepted standard" to compare the PCXMC results against. Calibration factors (Table 17) were calculated in order to correct for differences between using four projection methodology (AP, PA, LLAT, RLAT) and continuous axial scanning. Each calibration factor was calculated based upon the comparison of reference phantom within ImPACT to the mean phantom results within PCXMC. In general, good agreement without the calibration factor exists for the cervical spine scan (within 10%), chest abdomen pelvis scan (within 10%), and chest scan (within 30%). The calculated calibration factor is then applied to each of the 100 phantoms prior to regression analysis.

Table 17. Initial calculation of effective doses by accepted standard Monte Carlo program (ImPACT) and model methodology. Correction factors are presented in order to account for differences in the way the effective doses are calculated for the axial scans.

Scan	**Initial Model Mean Effective Dose (mSv)**	**Accepted Standard Effective Dose (mSv)**	**Calibration Factor**
Brain	0.809	1.7	2.1
Cervical Spine	2.223	2.4	1.08
CAP	27.57	27	0.98
Chest	19.80	15	0.76
Thoracic Spine	5.975	13	2.2
Lumbar Spine	9.224	11	1.2

Regression analysis was conducted to describe the relationship between patient dimensions (height and weight) and radiation effective dose. Linear regression is possible because effective dose (predicted outcome variable) is continuous. R is very powerful and capable of performing all the necessary regression studies. Regression analysis was performed using the open source statistical program R (www.**r**-project.org/). An R subcode, RExcel, was used to perform all R coding through Microsoft Excel. A sample of the regression language is below.

```
RegModel.1 <- lm(Effective.Dose..mSv.~Height..cm.+Weight..kg.,
data=Brain_Walkthrough_100k2)
summary(RegModel.1)
```

Microsoft Access was used to manage the PCXMC output and perform necessary database functions such as record consolidation and simple calculations prior to exporting data into Microsoft Excel for analysis by R.

Overall size of the patient has an effect on the effective dose. Perisinakis et al [46] used MCNP and ImPACT to study the effect of increasing BMI for contiguous axial CT exams and found that as the BMI increased, normalized effective dose values from contiguous axial CT exams decrease. My mathematical models for determining the effective dose from trauma scans confirms the relationship between BMI and effective dose. DeMarco et al [233] observed similar negative trends and attributed the negative trend to the protection nature of an increasing patient trunk size covering the radiosensitive tissues beneath for individuals with a high BMI. The negative trend will hold true when machine technique factors are held constant between patients of varying BMI. However, when the tube current is allowed to modulate, the effective dose is directly related to an increase in the BMI. This is due to the increasing tube current attempting to ensure that the image noise level remains constant for the same diagnostic quality. Because the absorbed dose to an organ is also directly related to the tube current, as the tube current increases, so does the overall effective dose from the scan [233].

In order to account for uncertainties in the Ht/Wt model development, an analysis has been performed following previous published literature describing sensitivities in medical physics [198, 234-236]. The sensitivity tables presented in the results section of this chapter account for the sensitivity of each portion of the overall radiation absorbed by accounting for the error in the measurement (u) or the device output and determining the sensitivity coefficient of the error on the measurement (c). This methodology as outlined for each component below is explicitly covered in an article by Gregory et al [236]. The methodology has subsequently been adapted for each individual trauma protocol.

Initial sensitivity components involve characteristics of the CT scanner. CT scanner sensitivities are published in the manufacturer documentation accompanying the machine. Very strict regulations govern the variance of the radiation output [237].

a. **Tube Current** – typical variance by manufacturer specifications is +/- 5%. This error estimate is assumed to represent the true value within a 95% confidence interval. In this case, u = a/2. So that u = 5/2. Therefore +/- 5% is considered +/-2u so the uncertainty, u, is 2.5%. The sensitivity coefficient, c, is estimated at 1 since a change in the tube current will realize an equal change in the effective dose.

b. **Exposure Time** – Manufacturer specifications states +/-5%. Therefore, u = 2.5 and c=1

c. **Tube Voltage** - Patient effective dose varies with the tube voltage as a power function, $ED \propto kVp^{2.5}$. According to the manufacturer's specification, tube voltage can vary by +/- 3%. Therefore, u = 1.5 and c = 2.5, (the effective dose difference between 120 kVp and 123.6 kVp is approximately 8 % lower as the voltage is raised by 3%, therefore if the voltage is raised by 1%, then the effective dose difference will be approximately 2.5%.

d. **Slice Width/Table Movement** - Manufacturer specifications are generally within +/- 2 mm. GE LightSpeed 16 is +/- 1mm. Therefore the u = 0.5. In accordance with CTDosimetry (ImPACT), a 0.5 mm shift will cause a change of less than 0.1%. Therefore c = 0.1

e. **CTDIair displayed/tabulated** – If the user does not specifically define the CTDIair, ImPACT uses preset tabular values. These values are based upon reported measurements in a survey that was sent out by Shrimpton [90, 238]. As mentioned in Gregory [198], the reported standard deviation was 12%. Manufacturer specifications for the normalized weighted CT dose index state that scanners of a particular model should not differ by more than +/-20% [239].

f. **CTDIair measured** – User measured values are considered to be a better estimate of the CTDIair. Assuming that the measurement device is capable of measuring the CTDIair within +/- 5%, then u = 2.5%.

The next group of sensitivity components accounts for the modeling of the x-ray production by the Monte Carlo codes.

g. **Monte Carlo Modeling** – Monte Carlo modeling is widely used to assess absorbed dose in diagnostic imaging and radiation therapy. In radiation therapy, Monte Carlo modeling is capable of predicting dose within 5% of the delivered value. Even though radiation therapy energies are much higher than diagnostic energies, the same physical principles apply to diagnostic imaging where Monte Carlo calculations are not as accurate. Because of the widespread use of Monte Carlo codes, I went with the value listed in Gregory [198], u = 2%.

h. **Photon Spectrum Modeling** – Gregory [198] states that photon spectrums in a comparison study have the greatest difference, 2%, with chest and abdominal studies and most other studies do not differ by more than 1%. Therefore,for head and cervical spine studies, u = 1% and for all other studies in this research, u= 2%.

i. **Table Attenuation** – For model development, the entrance air kerma (EAK) was measured for each trauma scan using an anthropomorphic phantom (Table 19). Table attenuation is a factor in the variance of the tube current and was measured in the entrance air kerma (EAK) study. Listed in the table below are the EAK values. EAK was measured on the center point of the scanning range at four different locations (AP, PA, LATR, LATL).

Table 18. Measured EAK values.

EAK Values (mGy)	Patient LATL	Patient PA	Patient LATR	Patient PA	Average
Brain Scan	30.98	41.38	32.59	32.06	34.76 +/- 13%
Cervical Spine	19.90	22.95	27.92	22.25	23.62 +/- 13%
Ch/Ab/Pel	13.40	21.11	15.07	13.75	16.44 +/- 20%
Chest	13.10	29.52	16.70	19.73	21.65 +/- 30%
Thoracic Spine	6.22	6.75	6.83	7.88	6.97 +/- 9%
Lumbar Spine	17.00	10.69	11.39	9.99	12.90 +/- 23%

j. **HVL** – There is +/- 10% in half-value-layer value among manufacturer's. With the GE LightSpeed 16 model, the HVL is 7.4 mmAl for a body scan and 6.3 mmAl for a head scan (both scans at 120 kVp). Gregory [198] assumes that the range in HVL among manufacturer's represents 3 standard deviations. Therefore, u = 10/3=3.3. He also sets the sensitivity coefficient, c, at 0.6.

k. **Anode Angle** – Anode angles vary by manufacturer and are often proprietary information. A sensitivity study was performed to determine how the anode angle affected the overall effective dose. There was an overall 8% difference (greatest angle to smallest angle). An inverse relationship was noted between the increasing anode angle and effective dose. Therefore, assuming that most anode angles are between 7 degrees and 16 degrees, then the uncertainty percentage, u, is 8/2 = 4 with a sensitivity coefficient, c, set at 1.

Each Monte Carlo program requires the user to input an initial estimate of the incoming radiation. Therefore, the next group of sensitivity components involves the dose input.

l. **EAK Matching** – for Model development, entrance air kerma (EAK) (mGy) was used as the dose input value. Uncertainty is % error / 2 (from the above table). All values were measured by a Unfors PSD-4 detector which was calibrated by the manufacturer. These devices adhere to the radiation device measurement specifications. Therefore, u=2.5 and c = 1.

In order to model the effective dose from a wide variety of CT machine types and manufacturers, ImPACT matches individual scanners to a data base so the sensitivity in the scanner matching must also be taken into consideration.

m. **CT Scanner Matching** – ImPACT has 23 different data sets that are used depending upon the machine model/manufacturer chosen. The chosen machine match to a data set via a calculated factor based upon CTDIair. Gregory [198] calculated the difference among the data sets to be +/-54% or 2.4% per data set. Using the GUM method for an assumed rectangular variance, u = 2.4 / sqrt(3) = 1.4%.

The Monte Carlo codes have geometrically designed mathematical phantoms (explained in Specific Aim 1) which are used to collect the dose histories and calculate the absorbed dose to the individual organ. The next sensitivity component deals with patient/phantom modeling.

n. For ImPACT organ doses, 3% uncertainty is used. Organ values are assumed to be within a 95% confidence interval of the true value. Therefore, u = 5%/2 = rounded up for greater conservatism, 3%.
o. For Model organ doses, uncertainties are listed as calculated by the PCXMC model for all 100 phantoms and then weighted (for sensitivity coefficient) according to effective dose formulism such that only the organs listed make up the total effective dose. Whereas this isn't accurate according to strict formulism (many organs are not accounted for), this does allow for comparisons to be made among the final uncertainty values.

Both the Ht/Wt model development and ImPACT involved simulating the effective dose from a CT scan by summing contiguous axial scans. In practice however, all of the trauma protocols, vice Brain Scan, are helically scanned. Therefore, error is introduced when simulating helical scans with axial scans and must be accounted for.

p. **CTDosimetry Helical Scanning** – ImPACT CTDosimetry is not capable of performing helical scanning calculations. However, adding an additional axial scan on both ends of a scanning range (axial scans) will approximate the overscanning (thus additional effective dose) which takes place with helical scanning. Axial scanning is used for Brain scans and Cervical Spine scans. Helical scans are used for all other scanning protocols. Gregory [198] assumed a standard of uncertainty of 10% for 10 rotation scans and 5% for 20 rotation scans. Modeling the uncertainty trend (exponential) using the standard uncertainties, the below uncertainties were calculated. As more rotations are used, the uncertainty in the effective dose is lowered (Table 19).

Table 19. Number of rotations per scan protocol.

Scans	Rotations (1 cm slice) + 2 rotations for helical scans		Uncertainty (%) $u = 14.253e^{-0.045 \cdot rotation}$	
	ImPACT	PCXMC	ImPACT	PCXMC
Brain	16	9.5	7	9.3
Cervical Spine	23	16	5	7
Chest Abdomen Pelvis	37	54	2.7	1.25
Chest	21	29	5.5	3.9
Thoracic Spine	19	24	6.1	4.8
Lumbar Spine	17	25	6.6	4.6

The uncertainities are propagated and combined utilizing the method of quadrature. In this method, the overall error in a theorectical measurement output, e, involving two measurements with error, m and n, is calculated as below.

$$e = \sqrt{m^2 + n^2} \qquad 13$$

Therefore, the final values on the sensitivity tables show both the overall error using tabulated values and the overall error for using measured values. The 95% confidence interval is also given.

q. **Tabulated CTDIair** – combination of Rows: 1-4,5,7-11,12-22,23-24, and 25. $u_{comb} = \sqrt{\sum_{i=1}^{N}(c_i \cdot u_i)^2}$

r. **Measured CTDIair** – combination of Rows: 1-4,6,7-11,12-22,23-24, and 25. $u_{comb} = \sqrt{\sum_{i=1}^{N}(c_i \cdot u_i)^2}$

s. 95% Confidence Interval for u_{comb} (Row 28 – Row 29)
    i. Row 28, Tabulated 95% CI for u_{comb} – 2* Row 26
    ii. Row 29, Measured 95% CI for u_{comb} – 2*Row 27

Results

Multivariable regression is a powerful tool which helps to explain the relationship between predictors and the predicted value. For multiple regression to be used though, there are certain assumptions which must be made: 1) existence – for each specific combination of values of the independent variables the dependent variable is a random variable with a certain probability distribution having finite mean and variance, 2) independence – the dependent variable observations are independent of one another, 3) linearity – the mean value of the dependent variable for each specific combination of the independent variables is a linear function, 4) homoscedasticity – the variance of the dependent variable is the same for any fixed combination of the independent variables, and 5) normality – for any fixed combination of independent variables the dependent variable is normally distributed [240]. In order to achieve a usable solution which can be widely employed, the two predictors used are height and weight either individually or within the BMI formulism. Until the capability exists to individually assess specific organ doses from a unique patient scan, these regression equations will serve to approximate the effective dose per trauma scan as derived from the phantom population explained above in the methodology.

Effective dose was modeled best by multivariable regression techniques (Table 18). This approach was primarily suggested through experience and analysis of the coefficient of determination, R^2, which was used as a measure of association between height/weight and effective dose. For four of the scans (chest abdomen pelvis, chest, lumbar spine, and thoracic spine), more than 90% of the variation in the effective dose is explained by combinations of height and weight. 96% of the variation in the effective dose is explained by combinations of height and weight for chest scans while 76% of the variation in the effective dose is explained by height and weight for brain scans. However, only 65% of the variation in the effective dose is explained by height and weight for cervical spine scans.

Table 20. Ht/Wt mathematical models for calculating the effective dose, E (mSv), by trauma scanning region. The input variables for are height (cm), height^2 (cm^2), weight (kg), and weight^2 (kg^2).

Scan Protocol	**Ht/Wt Model Regression Equation**	**R^2**
Brain	$E = 3.35 - 0.00581*\text{Height} - 0.00722*\text{Weight}$	0.76
Cervical Spine	$E = 25.7 - 0.0257*\text{Height} + 0.000724*\text{Height}^2 - 0.00711*\text{Weight}$	0.65
Ch/Ab/Pel	$E = 17.2 + 0.0628*\text{Height} - 0.102*\text{Weight}$	0.96
Chest	$E = 25.9 - 0.120*\text{Height} + 0.000456*\text{Height}^2 - 0.124*\text{Weight} + 0.000329*\text{Weight}^2$	0.96
Lumbar Spine	$E = 9.16 + 0.0418*\text{Height} - 0.0644*\text{Weight}$	0.93
Thoracic Spine	$E = 9.20 + 0.0477*\text{Height} - 0.0529*\text{Weight}$	0.90

From Table 20, we can see that for brain scans, the effective dose decreases by 0.00581 mSv and 0.00722 mSv for each unit increase in the height (cm) and weight (kg), respectively. For the other scans, the effective dose varies with height, height^2, weight, or weight^2.

The estimate of the effective dose decreases as the height and the weight increases for brain scans, cervical spine scans, and chest scans (Figure 16). The relationship between weight and the estimate of the effective dose appears to be similar for all three scans by visually inspecting the slope of the line. Weight has a steep slope for the weight indicating that the weight has more of a strong negative association with the effective dose. However, the relationship between height and the estimate of the effective dose is not similar among the three scans. Although there is still a negative association between the height and the estimate of the effective dose, the cervical spine scan and the chest scan are definitely more affected by the phantom weight than the phantom height.

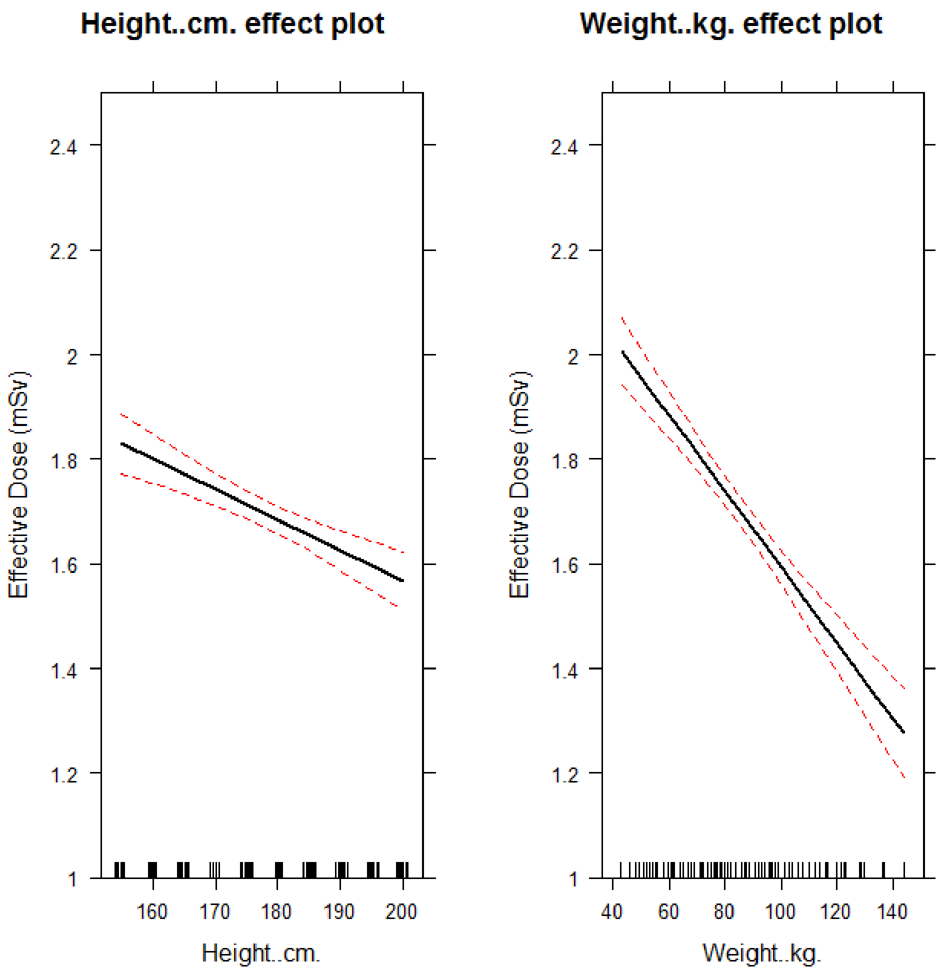
Height..cm. effect plot
Weight..kg. effect plot
Effective Dose (mSv)
2.4
2.2
2
1.8
1.6
1.4
1.2
1
160
170
180
190
200
Height..cm.
40
60
80
100
120
140
Weight..kg.

16a.

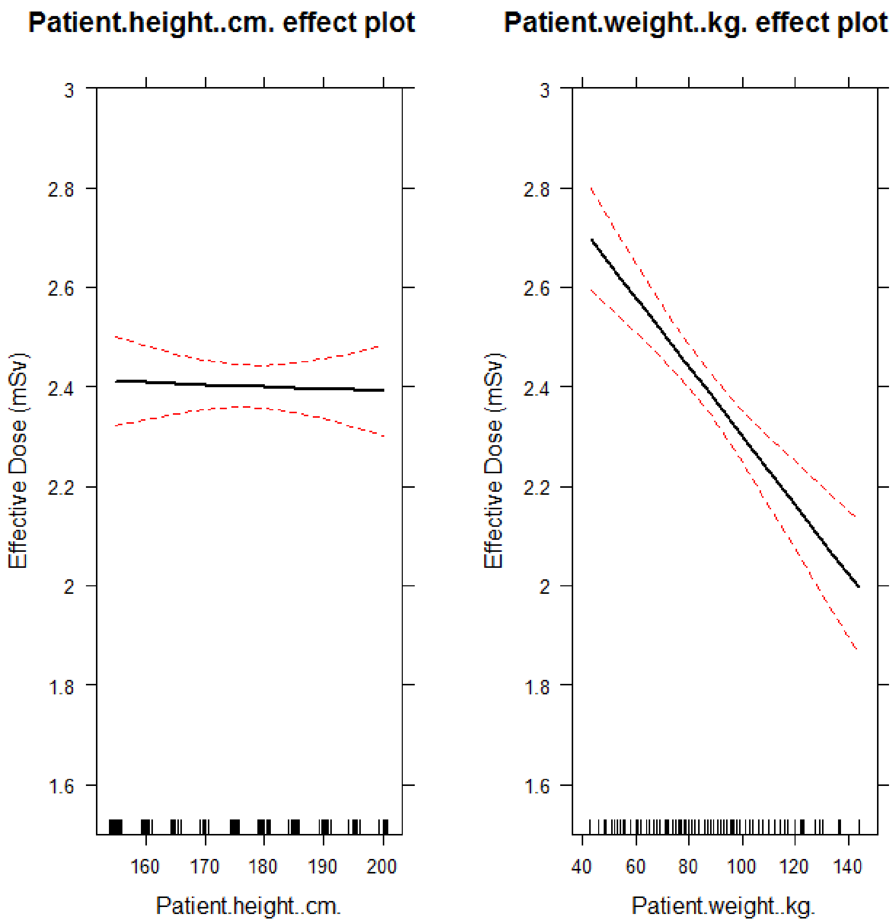
Patient.height..cm. effect plot
Patient.weight..kg. effect plot
Effective Dose (mSv)
3
2.8
2.6
2.4
2.2
2
1.8
1.6
160
170
180
190
200
Patient.height..cm.
40
60
80
100
120
140
Patient.weight..kg.

16b.

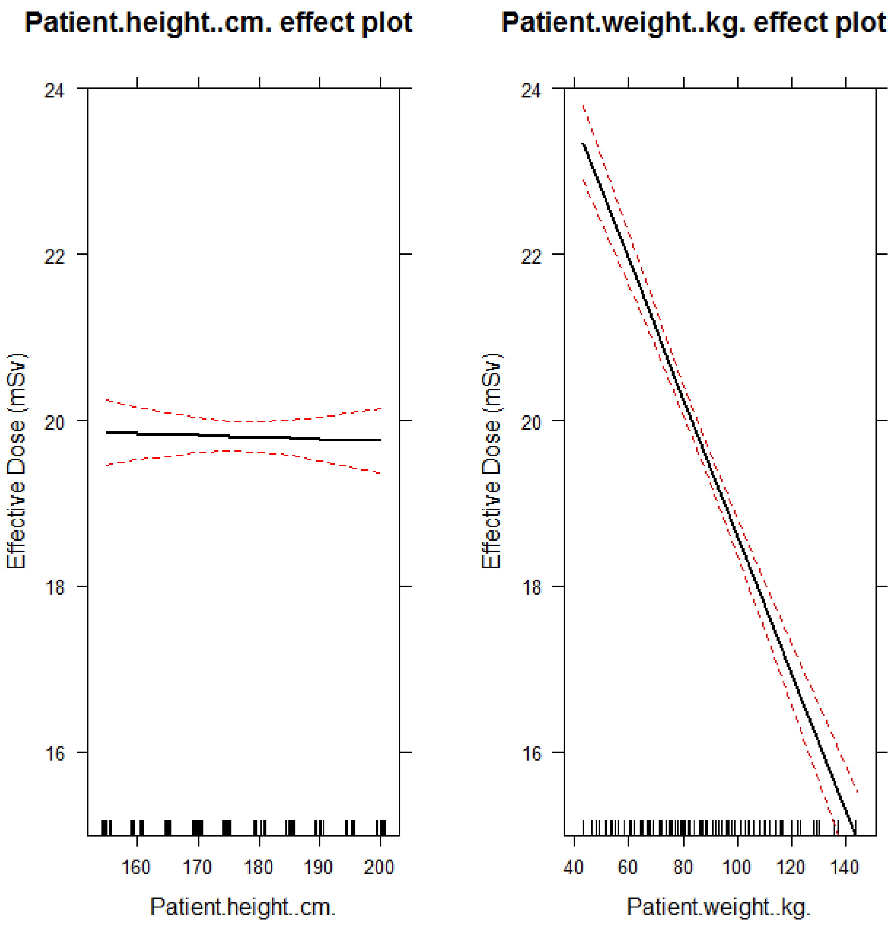

16c.

Figure 16. Effects plot of the predictors plotted against effective dose. 95% confidence bands are also presented along with the fitted regression line. (16a) Brain scan, (16b) Cervical Spine Scan, and (16c) Chest Scan.

The phantom height has a positive effect on the estimate of the effective dose for chest abdomen pelvis scans, thoracic spine scans, and lumbar spine scans (Figure 17). Conversely, the phantom weight has a negative effect on the estimate of the effective dose for the three above scans, although the range in the effective dose estimate is less for the thoracic spine and lumbar spine scans than for the chest abdomen pelvis scans.

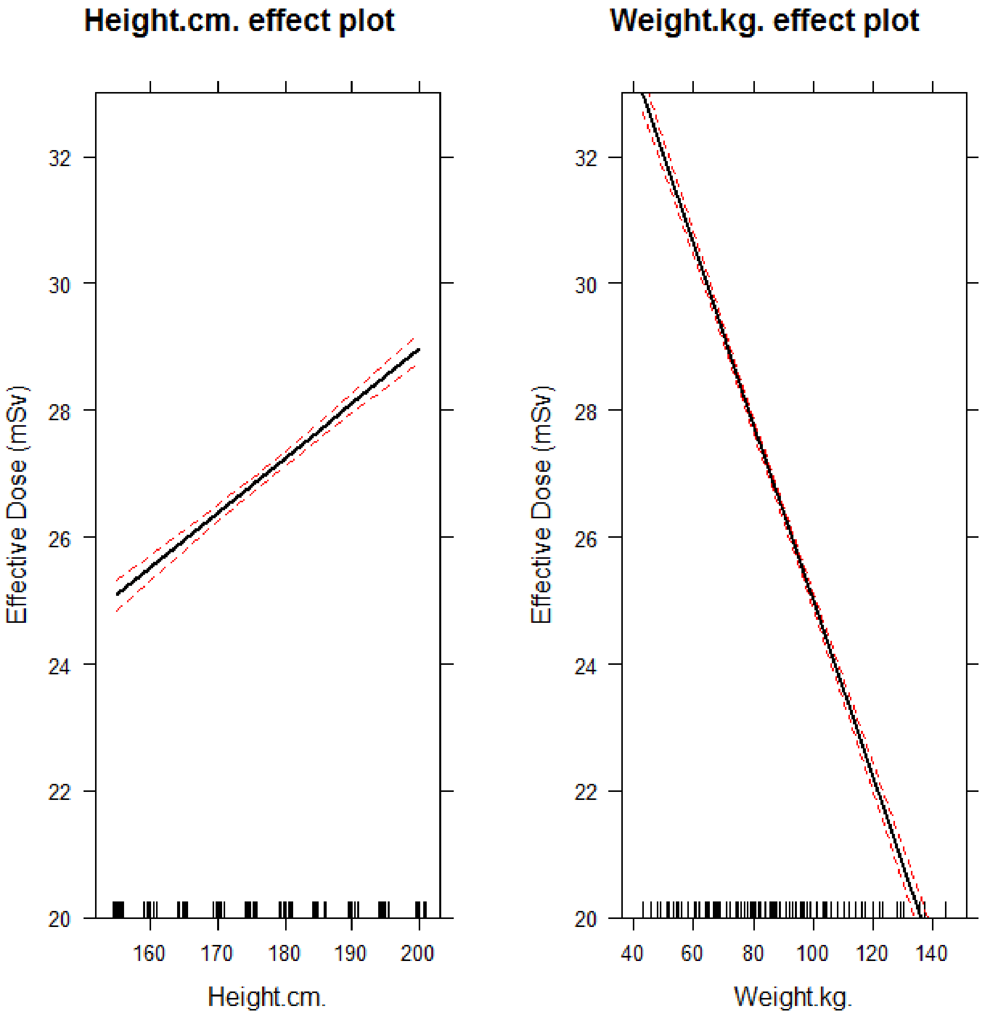
Height.cm. effect plot
Weight.kg. effect plot
Effective Dose (mSv)
32
30
28
26
24
22
20
160
170
180
190
200
Height.cm.
Effective Dose (mSv)
32
30
28
26
24
22
20
40
60
80
100
120
140
Weight.kg.

17a.

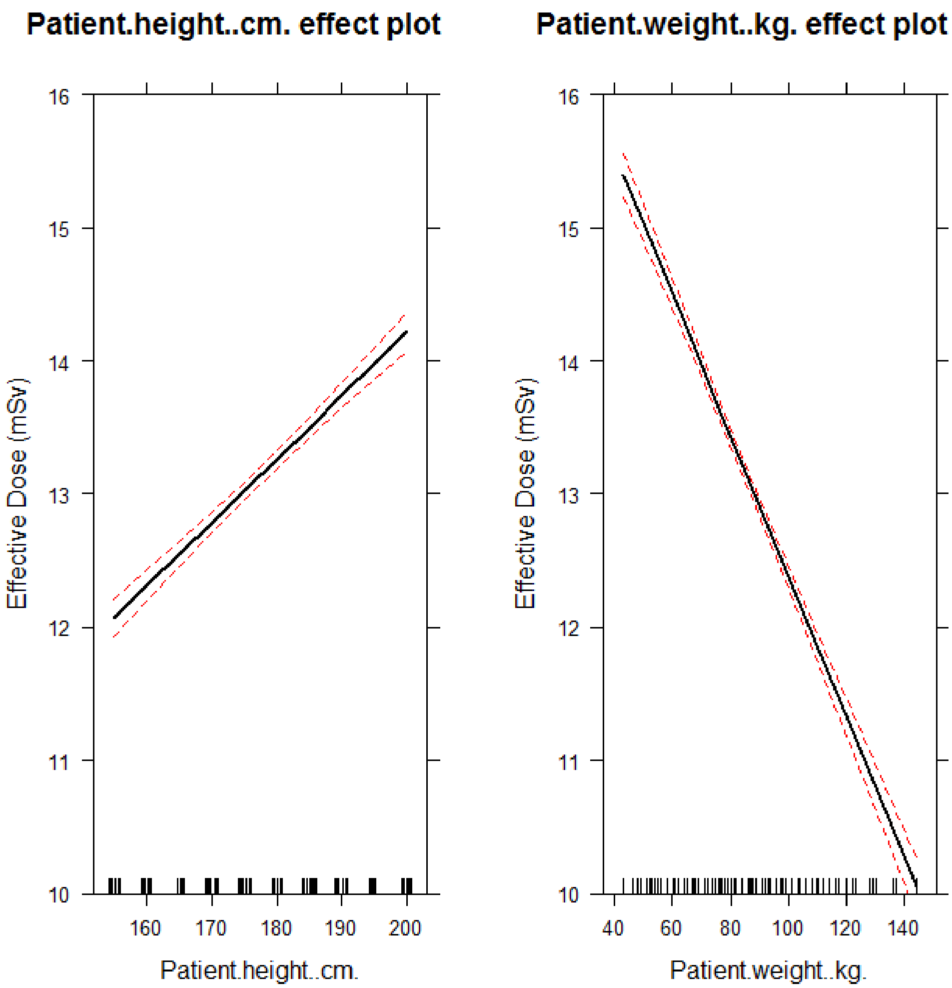
Patient.height..cm. effect plot
Patient.weight..kg. effect plot
Effective Dose (mSv)
16
15
14
13
12
11
10
160
170
180
190
200
Patient.height..cm.
Effective Dose (mSv)
16
15
14
13
12
11
10
40
60
80
100
120
140
Patient.weight..kg.

17b.

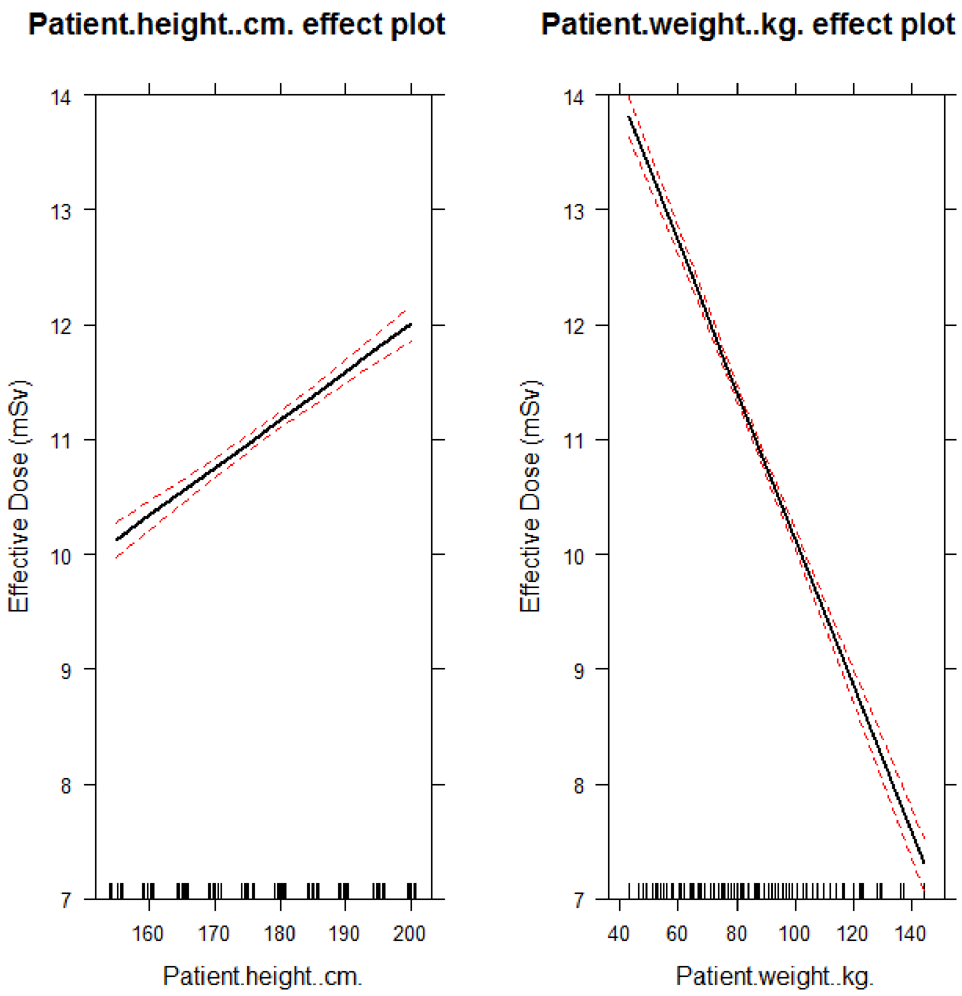

17c.

Figure 17. Effects plot of the predictors plotted against effective dose. 95% confidence bands are also presented along with the fitted regression line. (17a) Chest Abdomen Pelvis Scan, (17b) Thoracic Spine Scan, and (17c) Lumbar Spine Scan.

Uncertainties Involved in Estimating Effective Dose

The absorbed dose to an organ is dependent upon many different factors. In addition to the various machine parameters (mA, kVp, slice thickness, etc.) the depth (distance from surface) of the organ within the body and the size of the organ (including the density of the tissue) contributes to the absorbed dose quantity. As the depth increases the absorbed dose will decrease (Figure 18) exponentially. Assessing the overall absorbed dose to an organ is also made more difficult since organs are neither shaped uniformly nor are all parts of the organ at a uniform depth.

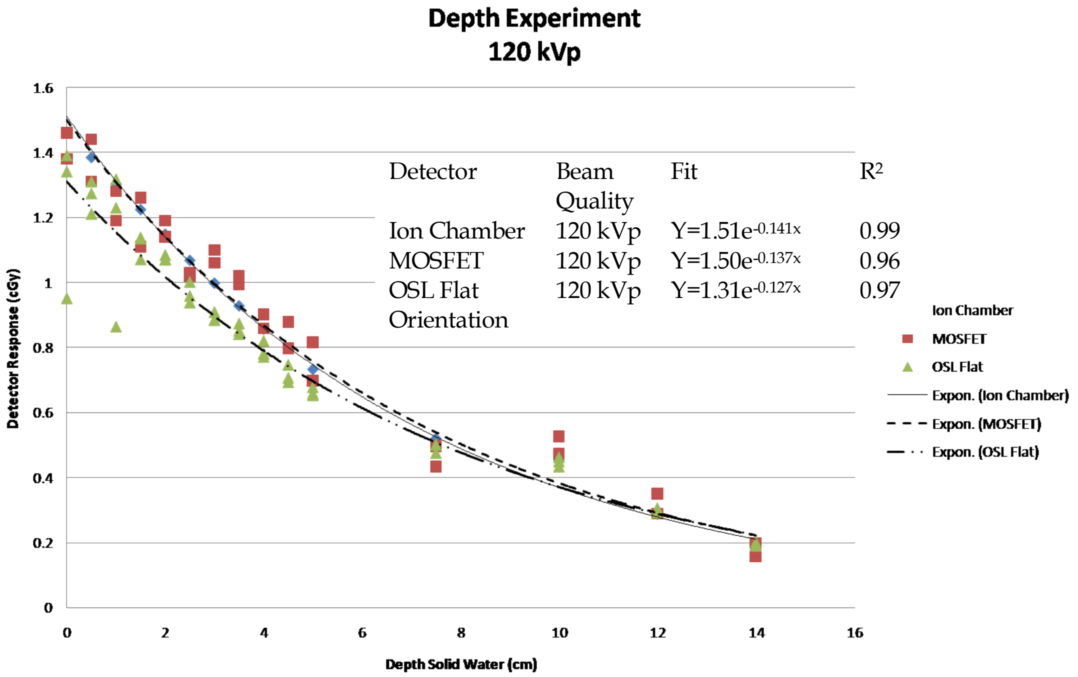

Detector	Beam Quality	Fit	R^2
Ion Chamber	120 kVp	$Y=1.51e^{-0.141x}$	0.99
MOSFET	120 kVp	$Y=1.50e^{-0.137x}$	0.96
OSL Flat Orientation	120 kVp	$Y=1.31e^{-0.127x}$	0.97

Figure 18. Dose response according to increasing thickness of solid water slabs simulating organ depth.

Sensitivity Tables

Error analysis for independent values is primarily performed using the method of propagation as discussed in Gregory et al [235-236] for propagating medical measurement uncertainties. A sensitivity table is presented for both ImPACT (Tables 21,23,25,27,29,31) and the regression model output (Tables 22,24,26,28,30,32).

Table 21. Sensitivity table for ImPACT brain scan calculations.

Category	Component	Standard Uncertainty (u)	Sensitivity Coefficient (c)	Degrees of Freedom (v)	$(c \cdot u)^2$
CT Scanner Characteristics	Tube Current	2.5	1	20	6.25
	Exposure Time	0.03	1	20	0.0009

	Tube Voltage	1.5	2.5	20	14.06
	Slice Width/Table Movement	0.5	0.1	20	2.5E-3
	CTDIair displayed/tabulated	12	1	20	144
	CTDIair measured	2.5	1	20	6.25
Modeling X-ray production	Monte Carlo Modeling	2	1	20	4
	Photon Spectrum Modeling	1	1	20	1
	Table Attenuation	2	1	20	4
	HVL	3.3	0.6	20	3.92
CT Scanner Matching	ImPACT Scanner Factor	1.4	1	20	1.96
Patient Modeling (error is not shown in software so assumption is that values are within 3%)	Adrenals/Gall Bladder				
	Brain	3	0.22	20	0.44
	Colon				
	Esophagus	3	1.76E-3	20	2.79E-5
	Kidney				
	Liver	3	1.59E-4	20	2.28E-7
	Lung	3	7.65E-4	20	5.27E-6
	Pancreas				
	Thymus	3	1.76E-3	20	2.79E-5
	Thyroid	3	0.06	20	0.032
	Uterus				
Patient Positioning	Vertical Positioning	7.4	0.3	15	4.92
	Lateral Positioning	8.4	0.18	15	2.29
Modern Scanner Matching	CTDosimetry helical Scanning (16 rotations)	7	1	20	49
Total Uncertainty Combined (u_{comb})	Tabulated CTDI$_{air}$, $u_{comb} = \sqrt{\sum_{i=1}^{N}(c_i \cdot u_i)^2}$				15
Total Uncertainty Combined (u_{comb})	Measured CTDI$_{air}$, $u_{comb} = \sqrt{\sum_{i=1}^{N}(c_i \cdot u_i)^2}$				10
	Tabulated 95% CI for U_{comb}				30
	Measured 95% CI for U_{comb}				20

Table 22. Sensitivity table for predictive Ht/Wt model brain scan calculations.

Category	Component	Standard Uncertainty (u)	Sensitivity Coefficient (c)	Degrees of Freedom (v)	$(c \cdot u)^2$
CT Scanner Characteristics	Tube Current	2.5	1	20	6.25
	Exposure Time	0.03	1	20	0.0009
	Tube Voltage	1.5	2.5	20	14.06
	Slice Width/Table Movement	1	0.2	20	0.04
	CTDIair				

	displayed/tabulated CTDIair measured				
Modeling X-ray production	Monte Carlo Modeling	2	1	20	4
	Photon Spectrum Modeling	1	1	20	1
	Table Attenuation	7	1	20	49
	HVL	3.3	0.6	20	3.92
	Anode Angle	4	1		16
Dose Input	EAK Matching	2.5	1		6.25
Patient Modeling	Adrenals/Gall Bladder*	NA			
	Brain	0.3	0.91		0.075
	Colon	NA			
	Esophagus	20	0.0054		0.012
	Kidney*	NA			
	Liver	15	6.76e-4		0.0001
	Lung	4	0.023		0.00085
	Pancreas*	NA			
	Thymus	50	0.0043		0.046
	Thyroid	12	0.057		0.47
	Uterus*	NA			
Patient Positioning	Vertical Positioning	10	.1		1
	Lateral Positioning				
Modern Scanner Matching	PCXMC helical Scanning (9 rotations)	9.5	1		90.25
Total Uncertainty Combined (u_{comb})		$u_{comb} = \sqrt{\sum_{i=1}^{N} (c_i \cdot u_i)^2}$			14
	95% CI for U_{comb}				28

Cervical Spine Scan Sensitivity Table

Table 23. Sensitivity table for ImPACT cervical spine scan calculations.

Category	Component	Standard Uncertainty (u)	Sensitivity Coefficient (c)	Degrees of Freedom (v)	$(c \cdot u)^2$
CT Scanner Characteristics	Tube Current	2.5	1	20	6.25
	Exposure Time	0.03	1	20	0.0009
	Tube Voltage	1.5	2.5	20	14.06
	Slice Width/Table Movement	1	0.2	20	0.04
	CTDIair displayed/tabulated	12	1	20	144
	CTDIair measured	2.5	1	20	6.25
Modeling X-ray production	Monte Carlo Modeling	2	1	20	4
	Photon Spectrum	1	1	20	1

	Modeling				
	Table Attenuation	2	1	20	4
	HVL	3.3	0.6	20	3.92
CT Scanner Matching	ImPACT Scanner Factor	1.4	1	20	1.96
Patient Modeling (error is not shown in software so assumption is that values are within 3%)	Adrenals/Gall Bladder	3			
	Brain	3	0.068		0.042
	Colon	3			
	Esophagus	3	0.031		0.0086
	Kidney	3			
	Liver	3	0.0018		2.92E-5
	Lung	3	0.12		0.13
	Pancreas	3			
	Thymus	3	0.031		0.0086
	Thyroid	3	0.75		5
	Uterus	3			
Patient Positioning	Vertical Positioning	7.4	0.3	15	4.92
	Lateral Positioning	8.4	0.18	15	2.29
Modern Scanner Matching	ImPACT helical Scanning (23 rotations)	5	1	20	25
Total Uncertainty Combined (u_{comb})	Tabulated CTDI$_{air}$, $u_{comb} = \sqrt{\sum_{i=1}^{N}(c_i \cdot u_i)^2}$				15
Total Uncertainty Combined (u_{comb})	Measured CTDI$_{air}$, $u_{comb} = \sqrt{\sum_{i=1}^{N}(c_i \cdot u_i)^2}$				9
	Tabulated 95% CI for U$_{comb}$				30
	Measured 95% CI for U$_{comb}$				18

Table 24. Sensitivity table for predictive Ht/Wt model cervical spine scan calculations.

Category	Component	Standard Uncertainty (u)	Sensitivity Coefficient (c)	Degrees of Freedom (v)	$(c \cdot u)^2$
CT Scanner Characteristics	Tube Current	2.5	1	20	6.25
	Exposure Time	0.03	1	20	0.0009
	Tube Voltage	1.5	2.5	20	14.06
	Slice Width/Table Movement	1	0.2	20	0.04
	CTDIair displayed/tabulated				
	CTDIair measured				
Modeling X-ray production	Monte Carlo Modeling	2	1	20	4
	Photon Spectrum Modeling	1	1	20	1
	Table Attenuation	2	1	20	4
	HVL	3.3	0.6	20	3.92

	Anode Angle	4	1	16
Dose Input	EAK Matching	2.5	1	6.25
Patient Modeling	Adrenals/Gall Bladder*			
	Brain	2.7	.078	.044
	Colon			
	Esophagus	20	.014	.078
	Kidney*			
	Liver	18	0.00064	.00013
	Lung	6.4	.026	.028
	Pancreas*			
	Thymus	35	.0079	.076
	Thyroid	10	.86	73.96
	Uterus*			
Patient Positioning	Vertical Positioning Lateral Positioning	10	.1	1
Modern Scanner Matching	PCXMC helical Scanning (16 rotations)	7	1	49
Total Uncertainty Combined (u_{comb})		$u_{comb} = \sqrt{\sum_{i=1}^{N}(c_i \cdot u_i)^2}$		13
	95% CI for U_{comb}			26

Chest Abdomen Pelvis Scan Sensitivity Table

Table 25. Sensitivity table for ImPACT chest abdomen pelvis scan calculations.

Category	Component	Standard Uncertainty (u)	Sensitivity Coefficient (c)	Degrees of Freedom (v)	$(c \cdot u)^2$
CT Scanner Characteristics	Tube Current	2.5	1	20	6.25
	Exposure Time	0.03	1	20	0.0009
	Tube Voltage	1.5	2.5	20	14.06
	Slice Width/Table Movement	1	0.2	20	0.04
	CTDIair displayed/tabulated	12	1	20	144
	CTDIair measured	2.5	1	20	6.25
Modeling X-ray production	Monte Carlo Modeling	2	1	20	4
	Photon Spectrum Modeling	1	1	20	1
	Table Attenuation	2	1	20	4
	HVL	3.3	0.6	20	3.92
CT Scanner Matching	ImPACT Scanner Factor	1.4	1	20	1.96
Patient Modeling (error is not	Adrenals/Gall Bladder	3	.054	20	.026
	Brain	3	.00049	20	2.2E-6

shown in software so assumption is that values are within 3%)	Colon	3	.19	20	.32
	Esophagus	3	.089	20	.071
	Kidney	3	.054	20	.026
	Liver	3	.074	20	.049
	Lung	3	.24	20	.52
	Pancreas	3	.054	20	.026
	Thymus	3	.089	20	.071
	Thyroid	3	.10	20	.090
	Uterus	3	.054	20	.026
Patient Positioning	Vertical Positioning	7.4	0.3	15	4.92
	Lateral Positioning	8.4	0.18	15	2.29
Modern Scanner Matching	CTDosimetry helical Scanning (37 rotations)	2.7	1	20	7.16
Total Uncertainty Combined (u_{comb})	Tabulated $CTDI_{air}$, $u_{comb} = \sqrt{\sum_{i=1}^{N}(c_i \cdot u_i)^2}$				14.00
Total Uncertainty Combined (u_{comb})	Measured $CTDI_{air}$, $u_{comb} = \sqrt{\sum_{i=1}^{N}(c_i \cdot u_i)^2}$				7.55
	Tabulated 95% CI for U_{comb}				28
	Measured 95% CI for U_{comb}				15

Table 26. Sensitivity table for predictive Ht/Wt model chest abdomen pelvis scan calculations.

Category	Component	Standard Uncertainty (u)	Sensitivity Coefficient (c)	Degrees of Freedom (v)	$(c \cdot u)^2$
CT Scanner Characteristics	Tube Current	2.5	1	20	6.25
	Exposure Time	0.03	1	20	0.0009
	Tube Voltage	1.5	2.5	20	14.06
	Slice Width/Table Movement	1	0.2	20	0.04
	CTDIair displayed/tabulated CTDIair measured				
Modeling X-ray production	Monte Carlo Modeling	2	1	20	4
	Photon Spectrum Modeling	1	1	20	1
	Table Attenuation	2	1	20	4
	HVL	3.3	0.6	20	3.92
	Anode Angle	4	1		16
Dose Input	EAK Matching	2.5	1		6.25
Patient Modeling	Adrenals/Gall Bladder*	1	.06		.0036
	Brain	1	.0002		4E-8
	Colon	2	.2		.16
	Esophagus	.3	.09		.00073
	Kidney*	1	.06		.0036

	Liver	.06	.09		2.9E-5
	Lung	.09	.3		.00073
	Pancreas*	1	.06		.0036
	Thymus	.6	.07		.0017
	Thyroid	.5	.08		.0016
	Uterus*	1	.06		.0036
Patient Positioning	Vertical Positioning Lateral Positioning	10	.1		1
Modern Scanner Matching	PCXMC helical Scanning (54 rotations)	1.25	1		1.55
Total Uncertainty Combined (u_{comb})		$u_{comb} = \sqrt{\sum_{i=1}^{N}(c_i \cdot u_i)^2}$			14
	95% CI for U_{comb}				28

Chest Scan Sensitivity Table

Table 27. Sensitivity table for ImPACT chest scan calculations.

Category	Component	Standard Uncertainty (u)	Sensitivity Coefficient (c)	Degrees of Freedom (v)	$(c \cdot u)^2$
CT Scanner Characteristics	Tube Current	2.5	1	20	6.25
	Exposure Time	0.03	1	20	0.0009
	Tube Voltage	1.5	2.5	20	14.06
	Slice Width/Table Movement	1	0.2	20	0.04
	CTDIair displayed/tabulated	12	1	20	144
	CTDIair measured	2.5	1	20	6.25
Modeling X-ray production	Monte Carlo Modeling	2	1	20	4
	Photon Spectrum Modeling	1	1	20	1
	Table Attenuation	2	1	20	4
	HVL	3.3	0.6	20	3.92
CT Scanner Matching	ImPACT Scanner Factor	1.4	1	20	1.96
Patient Modeling (error is not shown in software so assumption is that values are within 3%)	Adrenals/Gall Bladder	3	.024		.0052
	Brain	3	0.00029		7.57E-7
	Colon	3	.0087		6.81E-4
	Esophagus	3	0.087		.068
	Kidney	3	.024		.0052
	Liver	3	0.055		.027
	Lung	3	.24		.52
	Pancreas	3	.024		.0052
	Thymus	3	.087		.068
	Thyroid	3	0.055		.027
	Uterus	3	.024		.0052

Patient Positioning	Vertical Positioning	7.4	0.3	15	4.92
	Lateral Positioning	8.4	0.18	15	2.29
Modern Scanner Matching	CTDosimetry helical Scanning (21 rotations)	5.5	1	20	31
Total Uncertainty Combined (u_{comb})	Tabulated CTDI$_{air}$, $u_{comb} = \sqrt{\sum_{i=1}^{N}(c_i \cdot u_i)^2}$				15
Total Uncertainty Combined (u_{comb})	Measured CTDI$_{air}$, $u_{comb} = \sqrt{\sum_{i=1}^{N}(c_i \cdot u_i)^2}$				9
	Tabulated 95% CI for U_{comb}				30
	Measured 95% CI for U_{comb}				18

Table 28. Sensitivity table for predictive Ht/Wt model chest scan calculations.

Category	Component	Standard Uncertainty (u)	Sensitivity Coefficient (c)	Degrees of Freedom (v)	$(c \cdot u)^2$
CT Scanner Characteristics	Tube Current	2.5	1	20	6.25
	Exposure Time	0.03	1	20	0.0009
	Tube Voltage	1.5	2.5	20	14.06
	Slice Width/Table Movement	1	0.2	20	0.04
	CTDIair displayed/tabulated				
	CTDIair measured				
Modeling X-ray production	Monte Carlo Modeling	2	1	20	4
	Photon Spectrum Modeling	1	1	20	1
	Table Attenuation	2	1	20	4
	HVL	3.3	0.6	20	3.92
	Anode Angle	4	1		16
Dose Input	EAK Matching	2.5	1		6.25
Patient Modeling	Adrenals/Gall Bladder*	20	.042		.71
	Brain	23	.00028		.000041
	Colon	20	.0085		.029
	Esophagus	6	.10		.36
	Kidney*	1	.042		.0018
	Liver	3	.082		.061
	Lung	1.2	.49		.35
	Pancreas*	11	.042		.21
	Thymus	11	.13		2
	Thyroid	33	.028		.85
	Uterus*	67	.042		7.91
Patient Positioning	Vertical Positioning	10	.1		1
	Lateral Positioning				
Modern Scanner	PCXMC helical	2.9	1		15.21

Matching	Scanning (29 rotations)				
Total Uncertainty Combined (u_{comb})	$u_{comb} = \sqrt{\sum_{i=1}^{N} (c_i \cdot u_i)^2}$				8
	95% CI for U_{comb}				16

Thoracic Spine Sensitivity Table

Table 29. Sensitivity table for ImPACT thoracic spine scan calculations.

Category	Component	Standard Uncertainty (u)	Sensitivity Coefficient (c)	Degrees of Freedom (v)	$(c \cdot u)^2$
CT Scanner Characteristics	Tube Current	2.5	1	20	6.25
	Exposure Time	0.03	1	20	0.0009
	Tube Voltage	1.5	2.5	20	14.06
	Slice Width/Table Movement	1	0.2	20	0.04
	CTDIair displayed/tabulated	12	1	20	144
	CTDIair measured	2.5	1	20	6.25
Modeling X-ray production	Monte Carlo Modeling	2	1	20	4
	Photon Spectrum Modeling	1	1	20	1
	Table Attenuation	2	1	20	4
	HVL	3.3	0.6	20	3.92
CT Scanner Matching	ImPACT Scanner Factor	1.4	1	20	1.96
Patient Modeling (error is not shown in software so assumption is that values are within 3%)	Adrenals/Gall Bladder	3	.029		.0076
	Brain	3	.00033		9.80E-7
	Colon	3	.0045		.0018
	Esophagus	3	.1		.09
	Kidney	3	.029		.0076
	Liver	3	.045		.018
	Lung	3	.27		.66
	Pancreas	3	.029		.0076
	Thymus	3	.1		.09
	Thyroid	3	.063		.036
	Uterus	3	.029		.0076
Patient Positioning	Vertical Positioning	7.4	0.3	15	4.92
	Lateral Positioning	8.4	0.18	15	2.29
Modern Scanner Matching	CTDosimetry helical Scanning (19 rotations)	6.1	1	20	37
Total Uncertainty Combined (u_{comb})	Tabulated CTDI_{air}, $u_{comb} = \sqrt{\sum_{i=1}^{N} (c_i \cdot u_i)^2}$				15

Total Uncertainty Combined (u_{comb})	Measured CTDI_{air}, $u_{comb} = \sqrt{\sum_{i=1}^{N}(c_i \cdot u_i)^2}$	9
	Tabulated 95% CI for U_{comb}	30
	Measured 95% CI for U_{comb}	18

Table 30. Sensitivity table for predictive Ht/Wt model thoracic spine scan calculations.

Category	Component	Standard Uncertainty (u)	Sensitivity Coefficient (c)	Degrees of Freedom (v)	$(c \cdot u)^2$
CT Scanner Characteristics	Tube Current	2.5	1	20	6.25
	Exposure Time	0.03	1	20	0.0009
	Tube Voltage	1.5	2.5	20	14.06
	Slice Width/Table Movement	1	0.2	20	0.04
	CTDIair displayed/tabulated				
	CTDIair measured				
Modeling X-ray production	Monte Carlo Modeling	2	1	20	4
	Photon Spectrum Modeling	1	1	20	1
	Table Attenuation	2	1	20	4
	HVL	3.3	0.6	20	3.92
	Anode Angle	4	1		16
Dose Input	EAK Matching	2.5	1		6.25
Patient Modeling	Adrenals/Gall Bladder*	20	.016		.10
	Brain	15	.0036		.0029
	Colon	17	.0038		.0042
	Esophagus	5.4	.10		.29
	Kidney*	1	.016		.00026
	Liver	2.8	.039		.012
	Lung	1.1	.58		.41
	Pancreas*	11	.016		.031
	Thymus	6.3	.18		1.29
	Thyroid	19	.033		.39
	Uterus*	67	.016		1.1
Patient Positioning	Vertical Positioning Lateral Positioning	10	.1		1
Modern Scanner Matching	PCXMC helical Scanning (24 rotations)	4.8	1		23
Total Uncertainty Combined (u_{comb})	$u_{comb} = \sqrt{\sum_{i=1}^{N}(c_i \cdot u_i)^2}$				8.5
	95% CI for U_{comb}				17

Lumbar Spine Sensitivity Table

Table 31. Sensitivity table for ImPACT lumbar spine scan calculations.

Category	Component	Standard Uncertainty (u)	Sensitivity Coefficient (c)	Degrees of Freedom (v)	$(c \cdot u)^2$
CT Scanner Characteristics	Tube Current	2.5	1	20	6.25
	Exposure Time	0.03	1	20	0.0009
	Tube Voltage	1.5	2.5	20	14.06
	Slice Width/Table Movement	1	0.2	20	0.04
	CTDIair displayed/tabulated	12	1	20	144
	CTDIair measured	2.5	1	20	6.25
Modeling X-ray production	Monte Carlo Modeling	2	1	20	4
	Photon Spectrum Modeling	1	1	20	1
	Table Attenuation	2	1	20	4
	HVL	3.3	0.6	20	3.92
CT Scanner Matching	CTDosimetry Scanner Factor	1.4	1	20	1.96
Patient Modeling (error is not shown in software so assumption is that values are within 3%)	Adrenals/Gall Bladder	3	.072		.047
	Brain	3	.000014		1.76E-9
	Colon	3	.32		.92
	Esophagus	3	.0062		.00035
	Kidney	3	.072		.047
	Liver	3	.17		.26
	Lung	3	.20		.36
	Pancreas	3	.072		.047
	Thymus	3	.0062		.00035
	Thyroid	3	.00098		8.64E-6
	Uterus	3	.072		.047
Patient Positioning	Vertical Positioning	7.4	0.3	15	4.92
	Lateral Positioning	8.4	0.18	15	2.29
Modern Scanner Matching	ImPACT helical Scanning (17 rotations)	6.6	1	20	43.6
Total Uncertainty Combined (u_{comb})	Tabulated $CTDI_{air}$, $u_{comb} = \sqrt{\sum_{i=1}^{N}(c_i \cdot u_i)^2}$				15
Total Uncertainty Combined (u_{comb})	Measured $CTDI_{air}$, $u_{comb} = \sqrt{\sum_{i=1}^{N}(c_i \cdot u_i)^2}$				10
	Tabulated 95% CI for U_{comb}				30
	Measured 95% CI for U_{comb}				20

Table 32. Sensitivity table for predictive Ht/Wt model lumbar spine scan calculations.

Category	Component	Standard Uncertainty (u)	Sensitivity Coefficient (c)	Degrees of Freedom (v)	$(c \cdot u)^2$
CT Scanner Characteristics	Tube Current	2.5	1	20	6.25
	Exposure Time	0.03	1	20	0.0009
	Tube Voltage	1.5	2.5	20	14.06
	Slice Width/Table Movement	1	0.2	20	0.04
	CTDIair displayed/tabulated				
	CTDIair measured				
Modeling X-ray production	Monte Carlo Modeling	2	1	20	4
	Photon Spectrum Modeling	1	1	20	1
	Table Attenuation	2	1	20	4
	HVL	3.3	0.6	20	3.92
	Anode Angle	4	1		16
Dose Input	EAK Matching	2.5	1		6.25
Patient Modeling	Adrenals/Gall Bladder*	5.0	.085		.18
	Brain	37	1.3E-5		2.31E-7
	Colon	1.6	.25		.16
	Esophagus	5.7	.056		.10
	Kidney*	1.2	.085		.010
	Liver	.81	.16		.017
	Lung	2.0	.19		.14
	Pancreas*	2.3	.085		.038
	Thymus	.20	.0097		3.76E-6
	Thyroid	50	.00097		.0024
	Uterus*	8.6	.085		.53
Patient Positioning	Vertical Positioning	10	.1		1
	Lateral Positioning				
Modern Scanner Matching	PCXMC helical Scanning (25 rotations)	4.6	1		21
Total Uncertainty Combined (u_{comb})		$u_{comb} = \sqrt{\sum_{i=1}^{N} (c_i \cdot u_i)^2}$			8.3
	95% CI for U_{comb}				17

The greatest contribution to the overall uncertainty in the Ht/Wt model (up to 7%) came from the adaptation of axial scanning to helical scanning. However, with ImPACT, the greatest contributor to the overall uncertainty came from using tabular values for the

CTDIair (up to 13%). Since the Ht/Wt model uses direct measurement (entrance air kerma) values as initial inputs in Monte Carlo code, the Ht/Wt model did not have this large contributor. Still, the Ht/Wt model sensitivities are within statistical agreement of the sensitivities calculated for ImPACT for all six trauma protocols.

Conclusion

Regression analysis was performed in order to show the relationship between height and weight and effective dose. The goal of using height and weight as predictors is to obtain minimally confounded estimate of the effect of patient dimensions on effective dose from CT trauma protocols. These predictors can be obtained from the semi-annual physical fitness tests that every Soldier in the U.S. Army completes. Therefore, from an individual medical record, a clinician can review the results of a CT scan and by applying the patient values of height and weight, from a date near when the CT scans were performed, in the regression equation determine an estimate of the effective dose.

The regression equations will be more widely used if they are straight-forward. In this study only height and weight were used as predictors. BMI alone does not adequately express the variance in effective doses in some models as well as using BMI in conjunction with the other two predictors, height and weight. Specific machine characteristics were not assessed as predictors because this information is often not known for retrospective assessment of effective dose from CT scans. The coefficient of determination, R^2, was used to describe the variability in the calculated effective dose explained by the linear regression model.

The models explain the variability in the effective dose well for all scans except for the cervical spine scan ($R^2 = 0.65$). This lack of variability explanation is due to the cervical spine area not increasing as much by overall size as the phantoms height and weight are increased. This corresponds with what was observed in the initial patient study scanning range presented in Specific Aim 1. In the patient study, the mean scanning range of 32 patients was 23.35 cm with the 25% quartile being 20.64 cm and the 75% quartile being 25.26 cm. For all other scans, the regression equations represent the strong relationship between the effect of height and weight upon the effective dose.

The effective dose for the chest scan is more affected by weight than by height. This is explained by the location of the body which changes (increases or decreases in overall size) as a patient's weight changes. The circumference of the torso for most people will increase as a person increases in weight. As a result, we see that effective dose decreases similar to previously published research with cardiac patients [199, 225, 241-244].

Ht/Wt model verification (Specific Aim 3) will provide the confidence that both the PCXMC code is accurately describing the radiation dose to a patient from a CT scan and that the Ht/Wt modeling methodology can be used to describe the effective dose as patient dimensions change.

CHAPTER 5. Specific Aim 3: Verify effective dose models by measuring absorbed dose s in organs using optically stimulated luminescent dosimetry and anthropomorphic phantoms.

Introduction

This chapter will address the experimental verification of the estimate of the effective dose models developed in the Chapter 4. Experimental verification will be conducted by comparing organ dose measurements from anthropomorphic phantoms with organ dose values calculated using the mathematical phantoms used in Chapter 4.

Experimental dose assessments for CT scans in the diagnostic energy range are in practice typically measured with metal oxide semi-conductor field effect transistors (MOSFET) and thermoluminescent dosimeters (TLD). Both detectors are used because of their favorable characteristics with energy response, linearity, and reproducibility of irradiation. MOSFET is an electronic device which integrates radiation dose whereas TLDs incorporate a crystalline powder or chip to capture the ionizations occurring within the sensitive volume [245]. Both detectors have the key advantages of being small, good spatial resolution, and simple to use. Compared to TLDs, MOSFETs have additional significant advantages: immediate readout capability, reuse, and permanent storage of dose.

This specific aim is going to focus on the use of a more recent dosimeter, optically stimulated luminescent (OSL) material, which offers advantages similar to MOSFET detectors and is starting to achieve industry-wide use. OSL has some distinct advantages over traditional detector systems such as radiochromic dye films, plastic scintillators, TLDs, diode detectors, or MOSFET detectors [246]. Many detectors require a separate post-irradiation evaluation of the dosimeters because the readout system is not coupled directly to the detector. OSL is not restricted by the single use disadvantage of film or the limited lifetime disadvantage of MOSFET. MOSFET detectors accumulate dose and become saturated as they are used until they are unable to respond generally at accumulated doses over 200 Gy. Additionally, MOSFET lifetime will be further decreased when used in different sensitivity modes which influence their response to irradiations [247].

In order to verify that the modeled organ dose results are within expected ranges, the modeled dose results will be compared against experimental results. Patient equivalent anthropomorphic phantoms obtained from Computerized Imaging Reference Systems Inc [248] will be used. These anthropomorphic phantoms adhere to the requisite ICRP guidelines for reference man tissue equivalency [83]. These phantoms have been modified by the manufacturer based upon the requirements of this research so that internal dosimeters can be inserted into the various organ locations within the body. The internal dosimeters to be used are OSL dosimeters (Figure 19) purchased from Landauer Inc[249]. The active volume of the dosimeter is located within holders approximately 10-millimeters square.

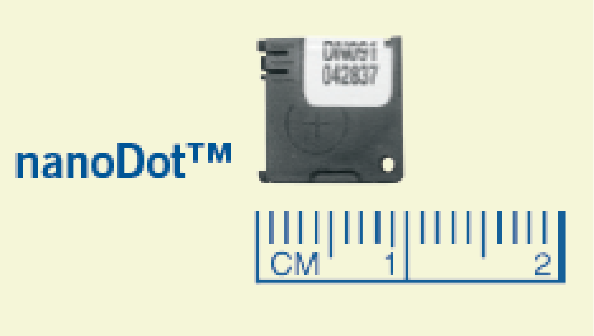

Figure 19. Landauer Inc. nanoDot OSL dosimeter used in this research (Photo courtesy of Landauer Inc.).

Characterization of the OSL dosimeters for diagnostic energies required experiments to be performed in order to assess energy dependence, linearity, reproducibility, material characteristics, and lower limits of detection. Material characteristics and composition were also experimentally assessed to determine if the geometry of the dosimeter compared to the x-ray beam direction plays a factor in absorbed dose. These experiments were important to determine the inherent dosimeter shielding.

Anthropomorphic phantoms provide realistic human equivalent dimensions and tissue/organ/muscle densities which provide realistic photon and electron scattering thus yielding realistic dose characterization [55, 250-251]. Using phantoms simulating different sexes and ages allows for a more accurate dose assessment based upon appropriate tissue simulation. Experimental measurements were conducted using the CIRS anthropomorphic phantoms and a GE LightSpeed 16 CT machine for each of the six trauma protocols (brain, cervical spine, chest abdomen pelvis, chest, thoracic spine, and lumbar spine). Anthropomorphic phantoms were used as opposed to water phantoms to simulate non-homogeneous tissue densities. The phantoms account for different elements within human tissue (carbon, oxygen, hydrogen, nitrogen, calcium, phosphorus, magnesium, aluminum, and chlorine). Tissue simulated in CIRS phantoms are average soft tissue, average bone tissue (eliminates the problem of air voids found in trabecular regions of natural bone), cartilage, spinal cord, spinal disks, lung, brain, sinus, trachea and bronchial cavities. The simulated bone tissue density matches the “age” of the phantom [248].

Theory

Optically Stimulated Luminescent Dosimetry

Use of OSL dosimeters is advantageous because: they have the ability to be read many times without the need for annealing, they display very little fading over time, and they are small in size. OSL dosimeters have been used for accident dosimetry, medical dosimetry, and natural dosimetry. The primary physical structure of the dosimeter is that of a crystal. The crystal lattice provides semiconductor-like physics where ionizing radiation causes electron-hole pairs to separate and drift to their respective junctions (n- or p-junctions). The freed electrons are of primary concern because these electrons are captured by energy traps where they stay until enough stimulated energy is provided for the electron to escape and reach the junction. This excess energy leaves the electron via luminescence as the electron drifts towards the junction. The amount of luminescence directly relates to the amount of initial radiation caused the separation of the electron-hole pair (Figure 20). The ideal dosimeter relates the trapped charge population linearly with the absorbed radiation dose in the absence of stimulation [252].

The primary distinction between OSL dosimetry and thermoluminescent (TL) dosimetry is the origin of the stimulated energy used to prompt a readable signal. With TL the stimulated energy comes from heat. As the TL dosimeter is heated up, the electrons in the traps absorb enough of the energy to leave the trap and as the electron drifts to the ground state, the excess energy provides the luminescence to be measured. There is some TL though in an OSL dosimeter, but the OSL dosimeter is primarily concerned with luminescence originating from different traps. As can be seen below (Figure 20), there are many different trap levels from which to gain information about the initial radiation via OSL.

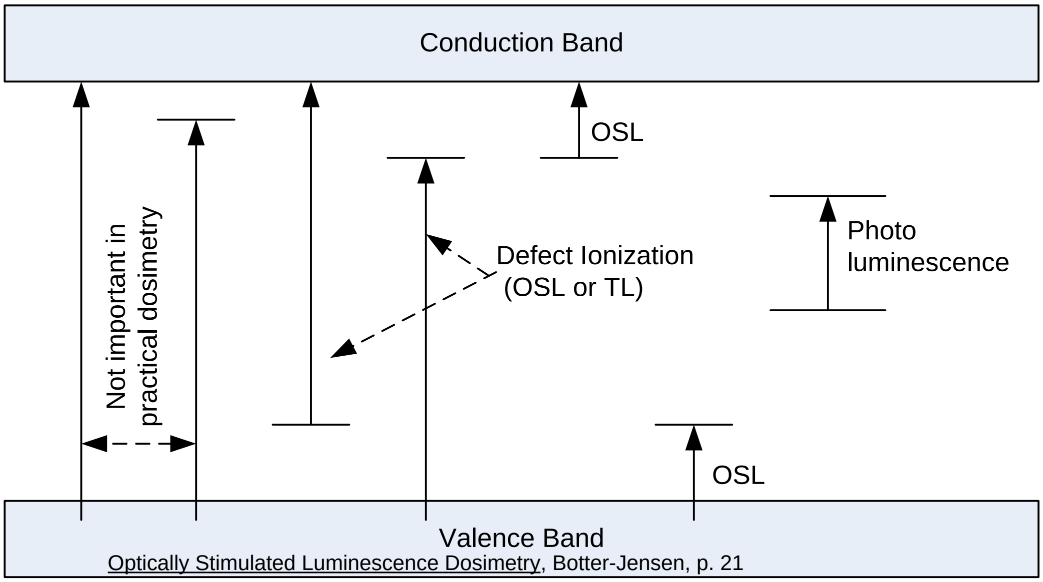

Optically Stimulated Luminescence Dosimetry, Botter-Jensen, p. 21

Figure 20. Physical processes of the optically stimulated dosimeter [252].

A distinct benefit of using OSL dosimetry is that the energy used to stimulate the electron in the trap can be tuned via different wavelengths. There are three main types of energy stimulation. The most common type is continuous wave OSL (CW-OSL). CW-OSL stimulates with a constant intensity and constant wavelength. Constant intensity refers to a constant photon flux over time. The wavelength is usually provided by a laser or more recently, a high intensity LED (light emitting diode). CW-OSL is very dependent upon temperature (having to do with the thermal trap depth, generally describing the entropy change of the system). At low temperatures, a reduced signal is observed due to competitive trapping of the released charge from a deeper trap to a shallower more stable trap which will not contribute to the luminescence. At higher temperatures, the effect of the shallow traps is negligible and the OSL signal is much higher. Intermediate temperatures yield a shifted signal peak reflecting the trapping of the charge into the shallow traps and subsequent release providing the luminescence. An ideal CW-OSL signal will approximate a simple exponential decay curve which can be approximated by first order kinetics. The signal will deviate from the exponential decay curve when re-trapping takes place into the shallow traps from deeper traps, and the presence of more than one recombination center. Linear modulated OSL (LM-OSL) keeps the constant wavelength but varies the intensity of the stimulation source in a linear manner. The OSL is monitored throughout the ramping up of the intensity. This linear ramp has an advantage over CW of resolving the trap's de-trapping rates (fast, medium, and slow). The general shape of the signal shows a linearly increasing function in proportion to the linear increase in stimulation power which is then followed by a Gaussian decrease in OSL intensity as the traps depopulate. The positioning of the signal peak reflects both the wavelength and the linear modulation rate. The resolving advantage of LM over CW eliminates the signal superposition of different trap depth depletion. Pulsed OSL (POSL) maintains the absorbed energy per pulse but varies the intensity and pulse time. An inverse relationship is used between intensity and pulse time. POSL keeps a constant wavelength throughout [246].

Scientists have found both natural-occurring crystals and have grown synthetic crystals for OSL. One of the most common naturally-occurring crystals is feldspar (located in sand). Feldspar has been used to measure background radiation found in nature and has also been used to determine the amount of radiation given off in accidents (i.e. Chernobyl) [246]. Common synthetic crystals include Al_2O_3:C, halides (KCl, KBr, NaCl, RbI, CaF_2 doped with Mn, BaF(Br, Cl, I) doped with Eu), Sulfates ($MgSO_4$, $CaSO_4$), Sulphides (MgS, SrS, CaS, BaS), and Oxides (BeO, fused quartz doped with Cu). The most commonly used synthetic material is probably Al_2O_3:C [253-267]. This synthetic material is extremely sensitive (emitted luminescence photons per unit radiation dose) to both TL and OSL. Al_2O_3:C as a TL dosimeter has a disadvantage of being extremely sensitive to heat; higher sensitivity at lower temperatures as opposed to higher temperatures. However, this temperature dependence is not of concern when used as an OSL material, and the characteristic of phototransfer of charge from deep states (traps) to shallower states is favorable. The wavelength of light used to stimulate the luminescence for Al_2O_3:C is best between 475 and 500 nm, with the peak being about 480 nm [246]. Note though that the tunable wavelengths can be used to depopulate specific traps. Environmental dosimetry is often concerned with the electrons in the shallower traps whereas medical dosimetry is concerned with the electrons in the deeper traps. Providing the necessary stimulated energy to depopulate shallow traps will not affect the charge in the deep traps. One of the ideal characteristics with OSL dosimetry is that the crystal can be read multiple times without depleting the electron traps. Zeroing the crystal is also fairly easy by thermal annealing or bleaching with stimulation light [252].

The type of OSL system that will be used in the study will be the Landauer InLight™ personal dosimetry system. This system is a continuous-wave OSL that uses bright LEDs (green wavelength) to stimulate the OSL utilizing the Al_2O_3:C crystal. The LEDs provide longer read-out capabilities as compared to pulsed OSL and has very little signal depletion.

The operational dose range for this system is up to 10 Gy with photon energies greater than 5 keV and electron energies greater than 150 keV [249, 268].

The below figure (Figure 21) illustrates the fundamental approach to reading the OSL dosimeter. The light source is filtered to the desired wavelength most optimal for luminescence and then used to stimulate the dosimeter. The luminescence within the dosimeter is then read by the photo multiplier tubes which amplify the luminescent light to be measured by the attached electronics.

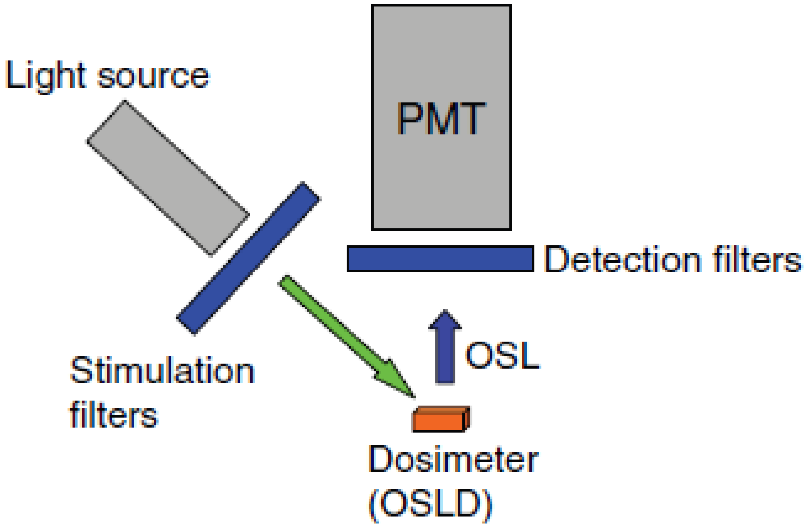

Figure 21. Light stimulation diagram describing how the OSL signal is obtained [269].

OSL and radioluminescence responses of Al_2O_3:C fiber probes have been found to increase linearly with dose rate and the absorbed dose in the radiotherapy range (0.5 – 85 Gy) with uncertainties on the order of 0.7 to 3.2% [270].

Although Al_2O_3:C is becoming the standard crystal, other materials, KBr:Eu, have shown the desired characteristics for real-time dosimetry [271]. Additionally, studies [272] have shown that OSL can be used for in vivo dosimetry on patients using a buildup cap for entrance dose measurements.

For this study, the reproducibility of the study dosimeters (Landauer Dots) was about 2.5% (within one standard deviation) with the stability of the system showing that a given batch of dosimeters can be used with a single calibration factor. A single calibration factor can also be used for dose ranges 0.5 to 4 Gy as the response from the dosimeters is linear.

OSL research is still a narrow field. AAPM annual meetings have averaged only about 3-4 presentations per year since 2005 [269]. OSL characteristics look to be promising for innovative therapy technologies such as proton therapy and heavy ion therapies but research hasn't been conducted. Additionally, OSL techniques applied to computed tomography, radio-diagnostics, fluoroscopy, and particle dosimetry are beginning to be developed.

Anthropomorphic Phantoms

Anthropomorphic phantoms have many uses in medical physics. They are designed to approximate the shape and the different tissue densities which make up the human body. Radiation detectors can often be inserted into the phantom so that the readings approximate the radiation absorbed dose at that specific location. There are many different types of anthropomorphic phantoms and some research entities even construct their own.

One of the most popular anthropomorphic phantoms used today is the Rando-Alderson phantom (Alderson Radiation Therapy Phantom, Radiology Support Devices, Inc., Long Beach, California) and has been in use for more than 30 years. These phantoms are molded of tissue-equivalent material and follow ICRU-44 standards [273]. Typically, the phantoms are ordered and designed for use with TLD dosimeters.

CIRS (Computerized Imaging Reference Systems, Norfolk, Virginia) also manufactures and designs anthropomorphic phantoms in accordance with ICRU 44 [273], ICRP 23 , and ICRP 89 specifications [248]. These phantoms can be ordered in a variety of sizes from adults down to pediatrics and have been in use since the late 1980s. For this research, we ordered an adult male (height equals 173 cm, weight equals 73 kg, thorax dimensions equal 23 cm x 32 cm) and an adult female (height equals 160 cm, weight equals 55 kg, thorax dimensions equal 20 cm x 25 cm). We specifically asked the company to make modifications to the phantoms prior to shipment so that the phantoms would accommodate a 14-mm diameter plug designed for use with a Landauer, Inc. nanoDOT dosimeter.

Researchers have regularly used anthropomorphic phantoms to experimentally verify mathematical estimates of effective dose. Hurwitz et al [274] used a CIRS female phantom for MOSFET comparison against effective dose calculations using conversion coefficients and found that the use of conversion coefficients underestimate the effective dose by up to 37%. Salvado et al [275] experimentally verified the effective dose in voxelized Rando Alderson phantoms against EGS4 simulations of a HiSpeedLX/i (GE Medical Systems, Milwaukee, Wisconsin) CT system to good agreement. Other researchers [276] have further compared the Cristy mathematical phantoms used by ImPACT with voxelized anthropomorphic phantoms and have also found that geometrical phantoms (Cristy) will also underestimate the effective dose when compared against voxelized phantoms. Comparisons between physical phantoms and computer have shown that the difference in organ dose is the smallest when either organs that are small in volume and can be easily represented by an averaged point dose estimate, or for those large organs which receive a fairly uniform absorbed dose throughout its volume, or when the organ is large but receives a properly volume averaged absorbed dose gradient [250].

OSL Characterization

The dosimeters were characterized using a special reader (MicroStar^{TM} InLight^{TM} Reader, Landauer, Inc., Glenwood, Illinois) (Figure 22) with an 80 kVp calibration. The dosimeters were exposed to diagnostic x-rays (maximum energy of 140 kVp). The dosimeters were then stimulated with a wavelength in the visible green spectrum which caused an emission of blue light which was quantified for dosimetric assessment. The dosimeters were not manipulated upon receipt and still possessed the pre-determined manufacturer specifications on radiation sensitivity.

Figure 22. InLight^{TM} MicroStar® System.

Very low energy irradiations (22 kVp – 35 kVp) were performed using a standard mammography machine (General Electric Senographe Essential 2000D, General Electric Healthcare: Chalfont St. Giles, United Kingdom) and a PMMA (poly-methyl methacrylate) mammography phantom. Low-energy irradiations (50 kVp – 140 kVp) were performed using a radiographic-fluoroscopic unit (Philips EasyDiagnost Eleva, Philips Healthcare, Andover Massachusetts) and a 20 cm x 20 cm x 20 cm Lucite phantom.

Proper calibration procedures as listed by the manufacturer were followed prior to irradiating the dosimeters. For the purposes of this study, the 80 kVp calibration set was used. Following the initial irradiation, each dosimeter was subjected to 3 sets of measurements within 24 – 72 hours.

Dosimeters were evaluated for energy response both on-phantom and free-in-air with five dosimeters were each exposed to different energies of 22, 35, 50, 80, 120 and 140 kVp. The energy response was normalized to 80 kVp. Dosimeter results were compared to results from a calibrated ion chamber (Model 10X6, Radcal Corporation, Monrovia, California) measured both on-phantom and free-in-air. Each was exposed at 22, 35, 50, 80, 120 and 140 kVp. The angular response for horizontal rotation was determined by exposing 5 dosimeters each at varying incident angles (0, 45, 90, 135 and 180 degrees) using an 80 kVp x-ray beam. Energy dependence of the dosimeter was compared against the calibrated ion chamber. The ion chamber chosen is designed for low-level radiation measurements and has a 6 cm^3 active volume with an energy dependence of plus or minus 5% in the energy range from 33 keV to 1.33 MeV.

Characterization Results

Energy dependence was shown to be within plus or minus 15% when exposed free-in-air over the diagnostic energy range between 22 to 140 kVp. The dosimeters when similarly compared with the ion chamber gave results within plus or minus 15% when exposed free-in-air (Figure 23). Energy dependence was also shown to be within plus or minus 17% when exposed on-phantom over the diagnostic energy range between 22 to 140 kVp. The dosimeters were then compared with the ion chamber and the results agreed within plus or minus 17% when exposed on-phantom (Figure 24).

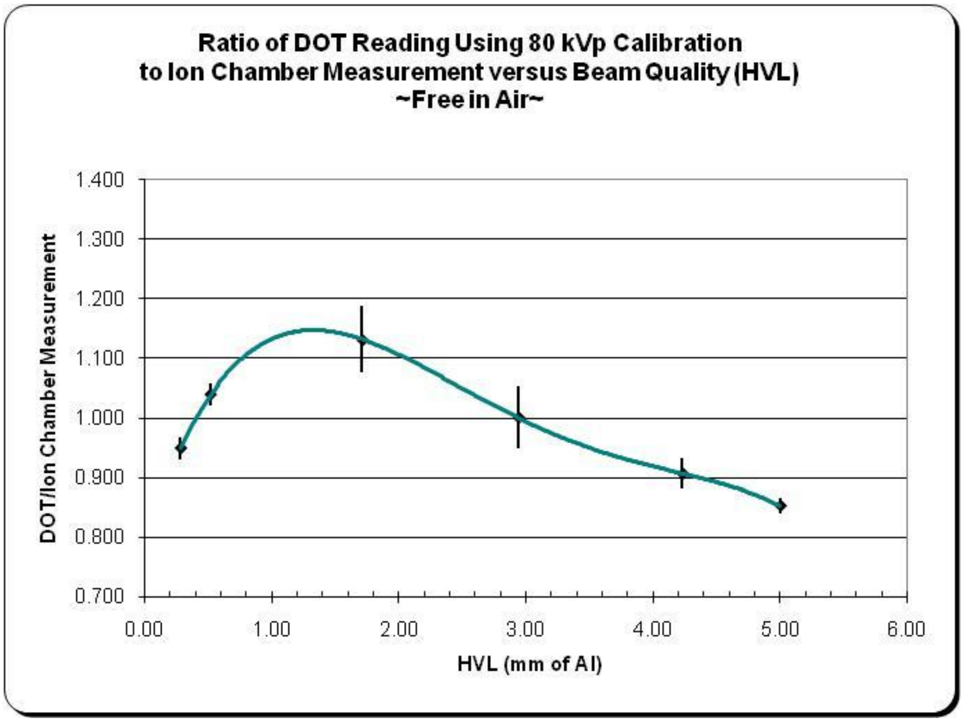

Figure 23. Results of dosimeter to ion chamber comparison when placed free-in-air.

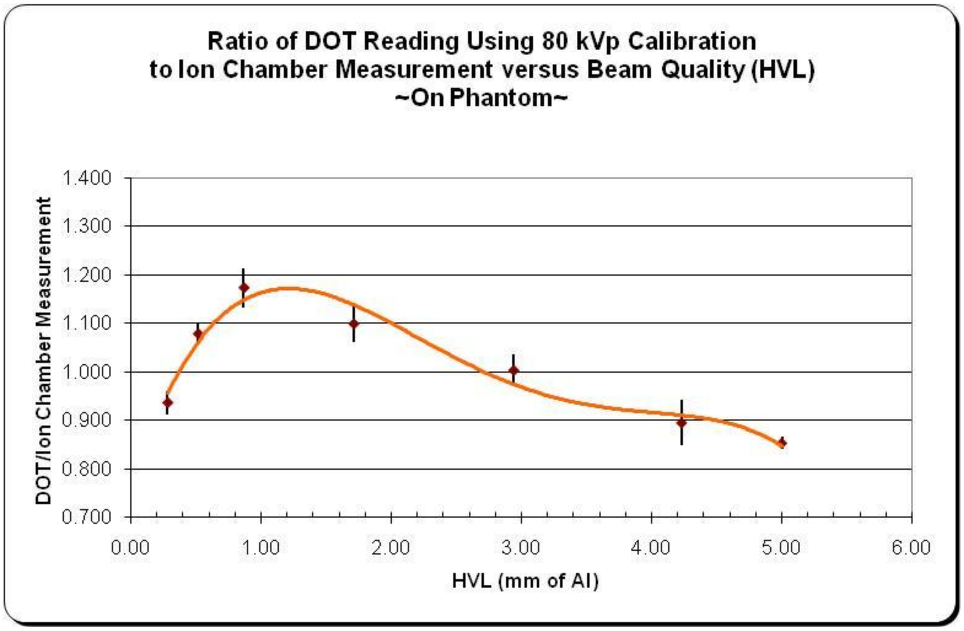

Figure 24. Results of dosimeter to ion chamber comparison when placed on a phantom.

Horizontal angular response differences at 45, 135, and 180 degrees were shown to be within 3% of the zero degree response. A 15% reduction in response was identified when the dosimeter was exposed on-edge (90 degrees) (Figure 25). As expected, the dosimeters were shown to have a linear response from 100 µGy through 20 Gy (See Figure 26) with a coefficient of determination value of 0.9997.

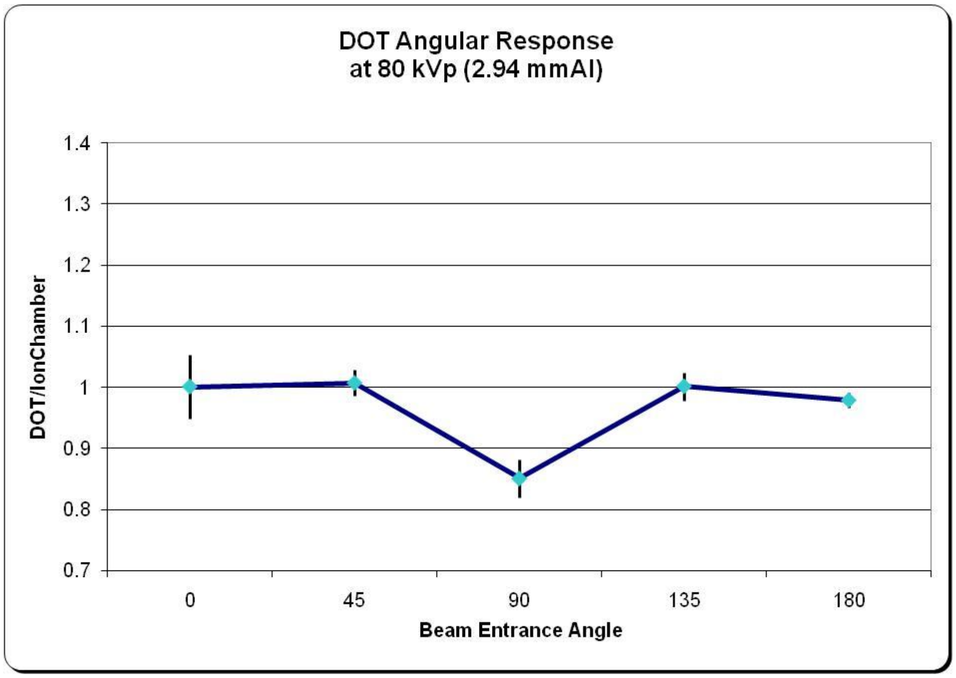

Figure 25. Ratio of dosimeter to ion chamber angular response.

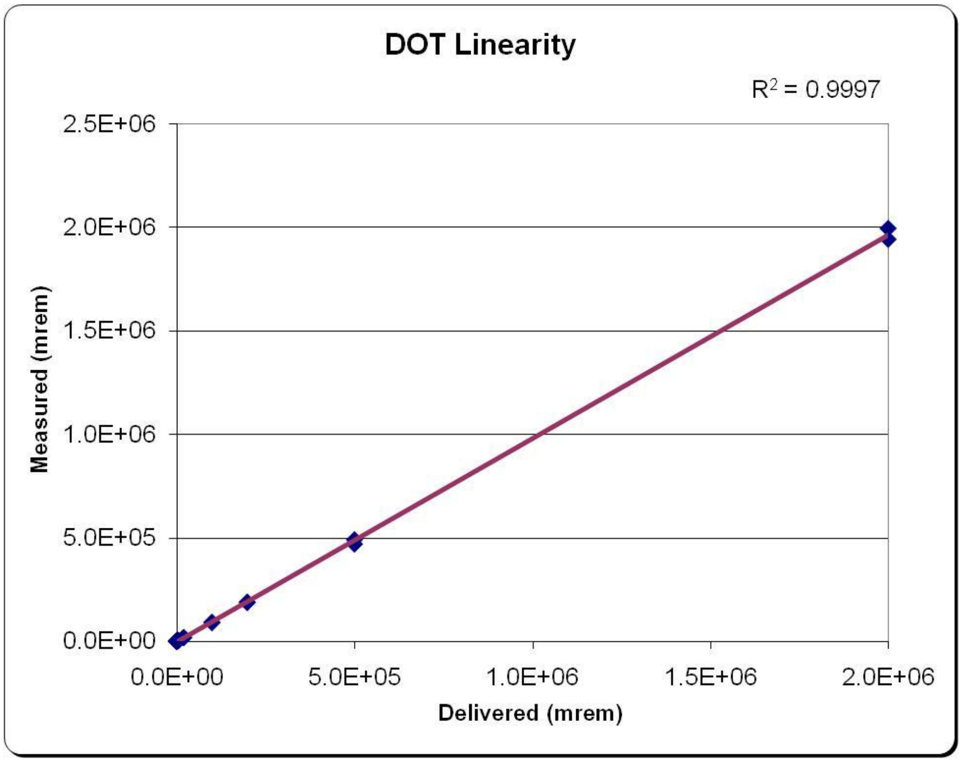

Figure 26. Dosimeter linearity with a coefficient of determination (R^2) value of 0.9997 between delivered dose and measured dose.

Discussion

The results of this study confirm the previous literature references which outlined the characterization of the dosimeters utilizing the radioisotope, ^{137}Cs [268, 277]. The dosimeters are extremely proficient at measuring low-energy x-rays produced by basic radiographic machines as proven by these measurements and confirmed in the existing literature. The unique low-profile dosimeters can be placed on equipment and personnel in radiation environments. The angular response variation was expected due to the low photon energy and the minor self-shielding of the holder material. The inherent construction of the dosimeter allows for appropriate skin dose monitoring [278]. The multiple readout, rapid analysis, and size advantages of OSL technology make the dosimeter a useful choice for passive dosimetry [279].

OSL Characterization Conclusion

The results of the basic measurements in this study show that small OSL dosimeters are suitable for patient in the low energy range (22 kVp – 140 kVp). Small size aluminum oxide OSL dosimeters and portable readers can be a convenient methodology for patient dosimetry applications across the diagnostic imaging energy range. The dosimeters can be quickly read and analyzed. OSL technology should prove extremely useful in assessing skin dose [280]. The dosimeters are linear over a large dose range and compare well with ion chamber results, having acceptable energy and angular dependence.

OSL Depth Response

In order to judge the response of the OSL with varying tissue thicknesses, a separate experiment was performed using solid water slabs to replicate varying thicknesses of tissue. Based off of the characterization experiment presented above, the OSL dosimeters were placed within a radiographic field next to both MOSFET detectors and an ion chamber (Figure 27). Three different diagnostic energies were assessed (80 kVp, 100 kVp, and 120 kVp) and the MOSFET detectors were calibrated to the beam quality HVL (7.4-mm Al) in a GE LightSpeed 16 CT machine (General Electric Medical Systems, Milwaukee, Wisconsin). Solid water slabs of varying thicknesses were used to simulate tissue. Numerical analysis and graphing was performed using Microsoft Excel.

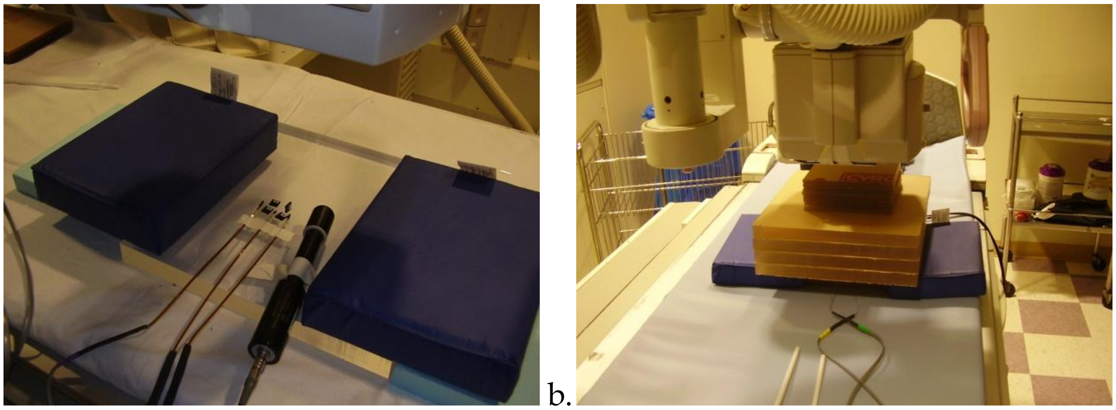

a. b.

Figure 27. Experimental setup for assessing depth response. Figure 23a shows the detector set up without slabs of solid water. Figure 23b shows the setup with the solid water slabs on top of the blue support cushions.

OSL Depth Response Results

As expected the response from all three detectors (OSL, MOSFET, and ion chamber) exponentially decreased as the solid water thickness increased (Figures 28-30). Interestingly, both detectors (OSL and MOSFET) have a similar response ratio (Figure 31) at depths up to approximately 4-cm solid water, although the OSL over-responds and the MOSFET under-responds when compared with the ion chamber. However, at thicknesses greater than 5-cm solid water, the response ratios change. Both detectors respond within +/- 20% of the calibrated ion chamber.

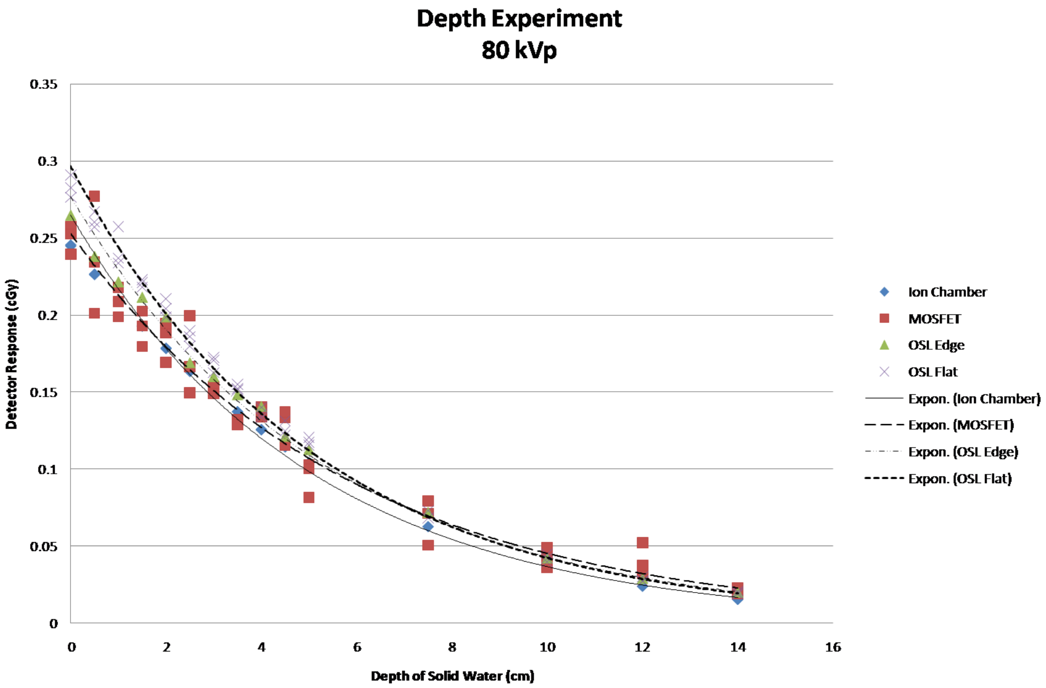

Figure 28. Detector response at varying depths of solid water at 80 kVp.

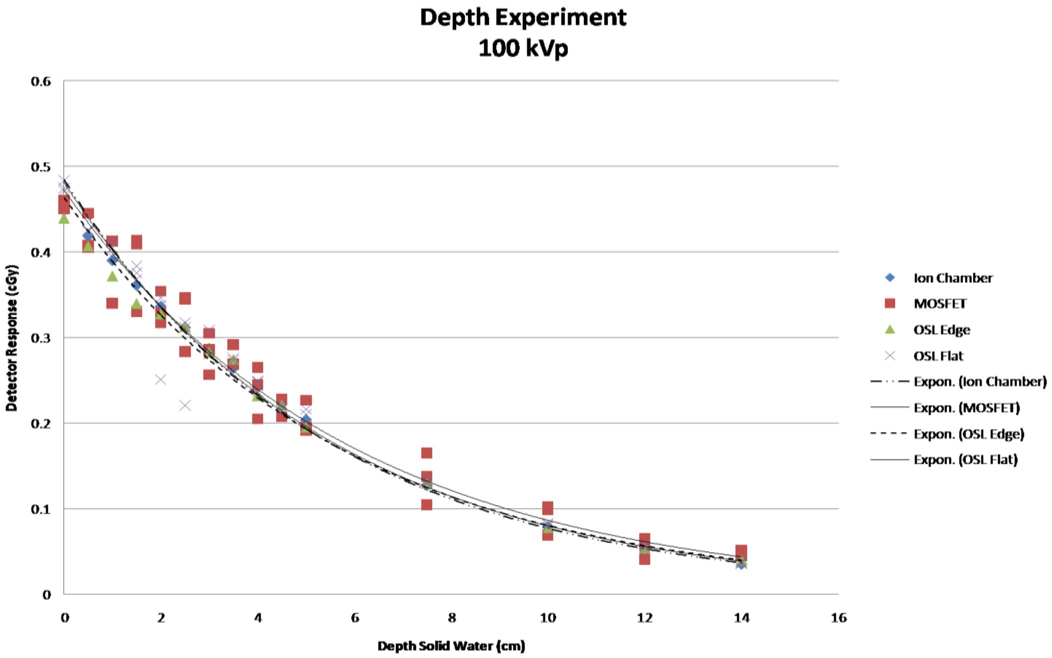

Figure 29. Detector response at varying depths of solid water at 100 kVp.

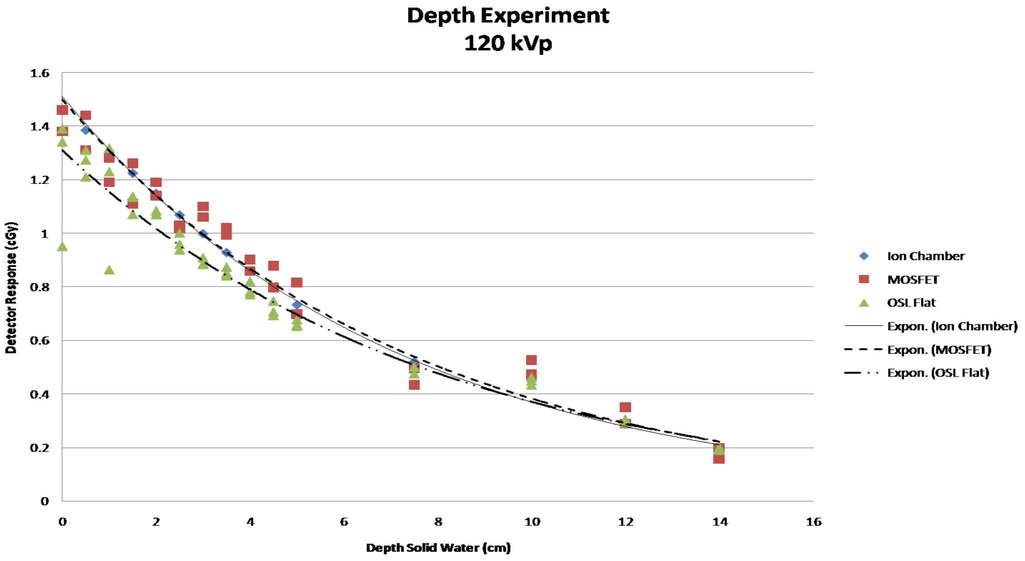

Figure 30. Detector response at varying depths of solid water at 120 kVp.

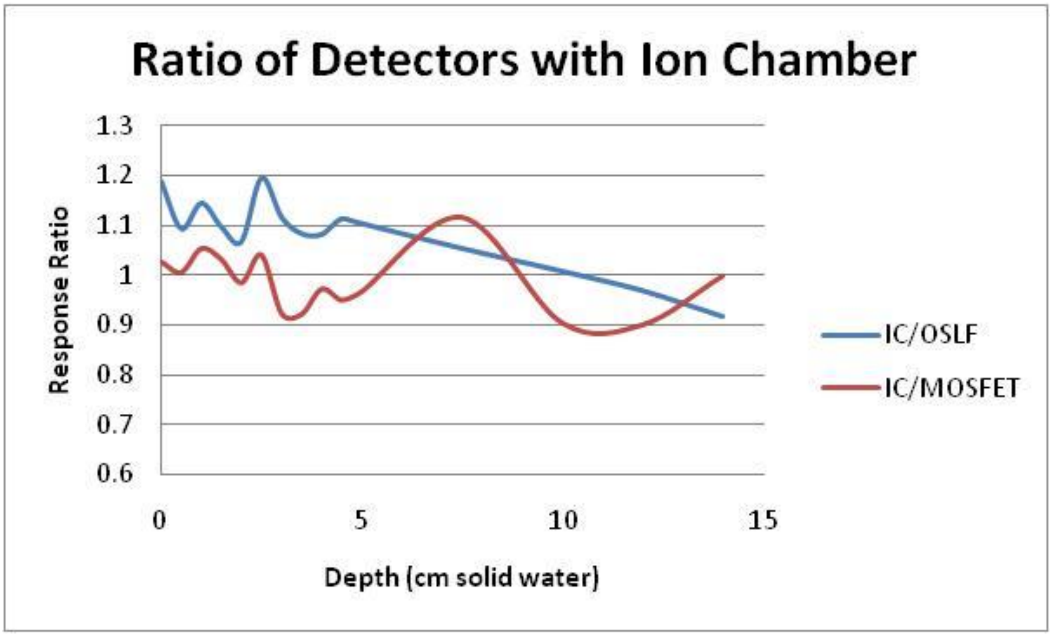

Figure 31. Ratio of OSL and MOSFET detectors with the ion chamber (IC). Both detectors have a response ratio of within +/- 20%.

Table 33 presents the fitted exponential regression equations for the three detectors and the coefficient of determination, R^2. The high coefficient of determination indicates that there is a strong relationship between the depth and the detector response and also indicates that the response of each detector would be linear when graphed on a log scale. This is in keeping with the results shown in the OSL characterization section of this chapter.

Table 33. Detector response and fitted exponential regression equations at the three experimentally assessed beam qualities. The predicted value, y, represents the detector response, and x, represents the depth (cm).

Detector	Beam Quality	Regression Equation	Correlation Coefficient, R^2
Ion Chamber	80 kVp	$y=0.2649e^{-0.198x}$	0.9971
MOSFET	80 kVp	$y=0.2526e^{-0.172x}$	0.9665
OSL Flat Orientation	80 kVp	$y=0.2967e^{-0.195x}$	0.9978
OSL Edge Orientation	80 kVp	$y=0.2768e^{-0.186x}$	0.9978
Ion Chamber	100 kVp	$y=0.4844e^{-0.183x}$	0.9970
MOSFET	100 kVp	$y=0.4733e^{-0.17x}$	0.9728
OSL Flat Orientation	100 kVp	$y=0.4821e^{-0.18x}$	0.9891
OSL Edge Orientation	100 kVp	$y=0.4636e^{-0.175x}$	0.9965
Ion Chamber	120 kVp	$y=1.5118e^{-0.141x}$	0.9862
MOSFET	120 kVp	$y=1.4995e^{-0.137x}$	0.9556
OSL Flat Orientation	120 kVp	$y=1.3109e^{-0.127x}$	0.9660

The ratio of the response of each OSL orientation (Figure 32) was shown to be within +/-12% when the dosimeter was placed along the direction of the primary beam or orthogonal to the primary beam.

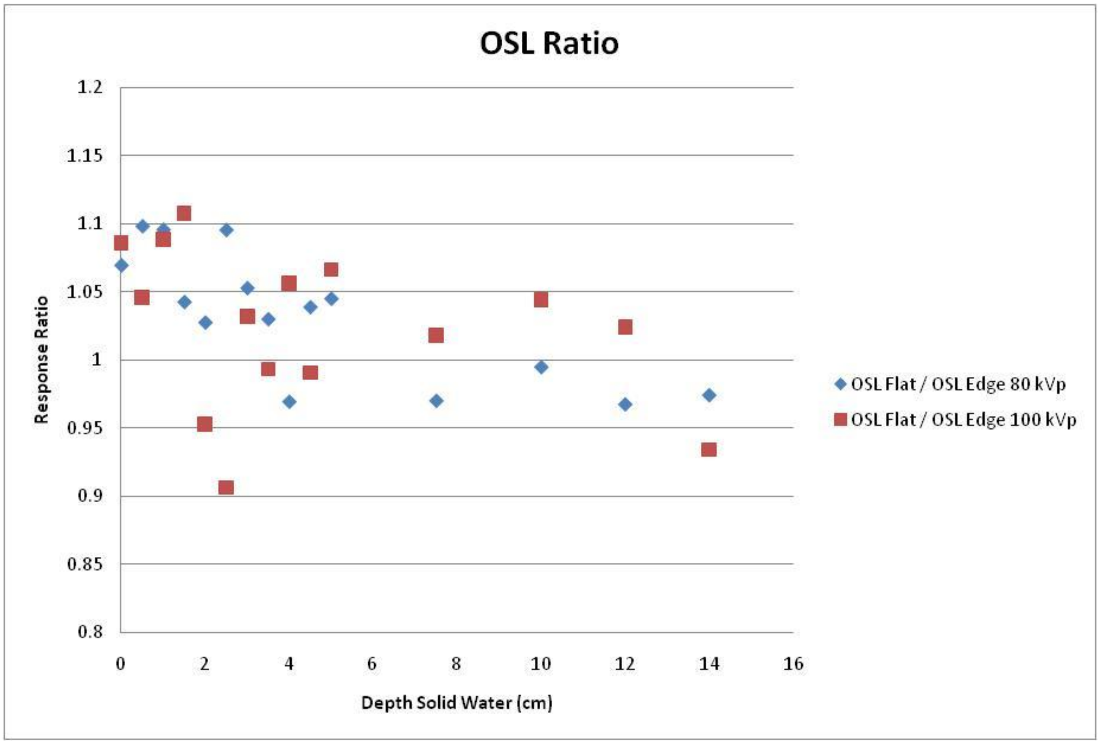

Figure 32. Ratio of the OSL orientation (OSL Flat to OSL Edge) at varying thicknesses of solid water for both 80 kVp and 100 kVp.

OSL Depth Response Discussion

The OSL responds as expected to radiation at various depths simulated by increasing thicknesses of solid water slabs. The dose response of the OSL is similar to the dose response of the more widely used MOSFET detectors. Both dose responses are within +/- 20% of the calibrated ion chamber. When the OSL nanoDot is placed within the anthropomorphic phantom, care should be taken to ensure that the dosimeter is aligned in the anthropomorphic organ plugs in the same manner for every experimental run. This will ensure that the dosimeter has a consistent response between experiments.

Responses of the OSL tend to varying more at lower diagnostic energies. For this reason, I assessed the responses of the OSL place on edge to the primary beam to the response of an

OSL placed flat (orthogonal) to the primary beam. The primary energies assessed were 80 kVp and 100 kVp. The responses were within +/- 12%.

OSL Depth Response Conclusion

OSL dosimeters have a similar response to a calibrated ion chamber when placed under increasing thicknesses of solid water simulating tissue. The overall response was exponentially decreasing as the thickness increased. The OSL response was within +/- 20 % of the ion chamber for all thicknesses of solid water. Additionally, the response did not vary more than +/- 12% when the dosimeter was placed along the direction of the primary beam or orthogonal to the primary beam. OSL can be used in an anthropomorphic phantom to assess radiation dose from a CT machine. The orientation of the OSL to the primary beam will have no significant affect on how the OSL dosimeter responds which is important when measuring the overall absorbed dose to a specific location from both primary radiation and scatter radiation.

Methodology

In order to verify the model development, the six trauma CT scans (Tables 34 and 35) were conducted on the anthropomorphic female and male phantoms with OSL dosimeters placed in different organ locations. The measured absorbed organ doses were compared against specifically modeled phantoms matching the height and weight in the PCXMC code.

Table 34. General technique factors used for the experimental measurements of the male anthropomorphic phantom (Dude). Scanning ranges are shown in Specific Aim 2.

CT Scan	Type	Tube Potential	Tube Current	Slice Thickness
Brain	Axial	120 kVp	155 mA	5 mm
Cervical Spine	Helical	120 kVp	155 mA	2.5 mm
Chest Abdomen Pelvis	Helical	120 kVp	Smart mA (220-380 mA)	5 mm
Chest	Helical	120 kVp	Smart mA (100-440 mA)	5 mm
Thoracic Spine	Helical	120 kVp	Smart mA (100-440 mA)	5 mm
Lumbar Spine	Helical	120 kVp	Smart mA (100-440 mA)	2.5 mm

Table 35. General technique factors used for the experimental measurements for the female anthropomorphic phantom (Daisy). Scanning ranges are shown in Specific Aim 2.

CT Scan	Type	Tube Potential	Tube Current	Slice Thickness
Brain	Axial	120 kVp	155 mA	5 mm
Cervical Spine	Axial	120 kVp	155 mA	2.5 mm
Chest Abdomen Pelvis	Helical	120 kVp	Smart mA (220-380 mA)	5 mm
Chest	Helical	120 kVp	Smart mA (100-440 mA)	5 mm
Thoracic Spine	Helical	120 kVp	Smart mA (100-440 mA)	5 mm
Lumbar Spine	Helical	120 kVp	Smart mA (100-440 mA)	5 mm

Phantom placement (Figure 33a) on the CT machine couch is the same as a typical human placement for CT scanning. Soft tissue plugs of appropriate density were inserted at various locations in the different slabs where organs of interest are located (Figure 33b). The anthropomorphic phantoms have been designed and manufactured in accordance with

ICRU 30 specifications for elemental composition of human tissues (Table 36) [248]. Some organs are more easily identified by their location and general shape (note the lungs (pink) in Figure 33b) than others which will take on the same color (generally gray) as normal tissue.

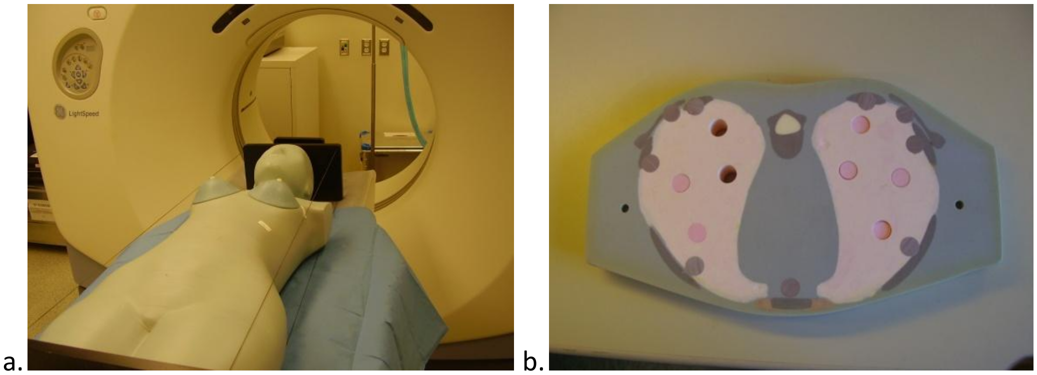

Figure 33. Representative photo of an anthropomorphic phantom on the CT scanning couch (Figure 33a) and a cross-section view of a 2.5-cm slab of the anthropomorphic phantom (Figure 33b).

Table 36. Material elemental composition for CIRS, Inc. adult anthropomorphic phantoms.

Adult Phantom Material Elemental Composition

Tissue	C	O	H	N	Ca	P	Mg	Cl	Al	Physical Density g/cc	Electron Density g/cc
Adult Bone	0.3703	0.3566	0.0483	0.0097	0.1524	0.0290	0.0619	0.0005	0.0000	1.60	5.030E+23
Soft Tissue	0.5744	0.2459	0.0847	0.0165	0.0000	0.0000	0.0762	0.0019	0.0000	1.05	3.434E+23
Spinal Cord	0.5427	0.2659	0.0736	0.0217	0.0000	0.0000	0.0937	0.0022	0.0000	1.07	3.448E+23
Spinal Disks	0.4627	0.3082	0.0675	0.0188	0.0000	0.0000	0.1407	0.0020	0.0000	1.15	3.694E+23
Lung	0.6336	0.2046	0.0832	0.0315	0.0000	0.0000	0.0000	0.0137	0.0000	0.21	6.820E+22
Brain	0.5360	0.2649	0.0816	0.0153	0.0000	0.0000	0.0998	0.0019	0.0000	1.07	3.470E+23

Determination of which organs to be measured was made by conducting a separate experiment assessing which organ doses contributed the most to the overall effective dose from each scan. There is a difference in the overall number of organ locations assessed when comparing the female phantom (Daisy) (Table 37) to the male phantom (Dude)

(Table 38). This is due to limitations on the number of soft tissue plugs (representing different organ densities) on hand at the time during the scanning experiments. When experimental scanning was conducted on Dude, more soft tissue plugs were obtained from the manufacturer and used.

Table 37. Table presenting the number of dosimeters and their locations in the female phantom (Daisy).

Organ	**Number of Dosimeters**
Adrenals / Gall Bladder	1
Bone	9
Brain	6
Colon	1
Spinal Cord	1
Esophagus	1
Eye	3 (1 in eye socket, 2 surface)
Kidney	1 (Right Kidney)
Liver	1
Lung	4
Pancreas	1
Thymus	1
Thyroid	1
Uterus	1
Total Number of Plugs	**32**

Table 38. Table presenting the number of dosimeters and their locations in the male phantom (Dude).

Organ	**Number of Dosimeters**
Heart	1
Mandible	2
Brain	6
Colon	2
T/L Spine	1
Esophagus	1
Eye	4
Kidney	2
Liver	2
Lung	8
Pancreas	1
Thymus	2
Thyroid	4
Prostate	2
Adrenals / Gall Bladder	1
Testes	2
Total Number of Plugs	**41**

All dosimeters were read in a dosimeter reader at least three times and then the readings were averaged. The dosimeter reader was calibrated using the manufacturer's 80 kVp, 2.9-mm Al HVL calibration technique. Final readings were adjusted to account for CT scanning (120 kVp) by multiplying each final reading by 115% based upon our energy response curve (Figure 24). The averaged dose to an individual organ is calculated according to the below equation (equation 13).

$$D_i = \frac{1}{n}\sum_j^n D_{i,j} \quad j = 1, \ldots n \text{ number of detectors in i-organ} \qquad 13$$

The following tables present the absorbed dose from the experimental measurements compared against those calculated using the specific dimensions of the phantoms (height and weight) as input into PCXMC. Some differences (experimental versus calculated) between the specific organ absorbed doses were expected based upon literature review [46, 59, 123, 190, 250, 281-282]. Overall, equivalent dose differences were expected to be within 30% for those organs within the primary range of the scan. Absolute percent differences are calculated according to equation 14.

$$\text{Absolute percent difference} = \left|\frac{measured - calculated}{(measured + calculated)/2}\right| * 100 \qquad 14$$

Results

Brain Scan

Table 39 lists the organ doses (mGy) for both the experimentally measured quantity and the calculated quantity for Daisy and Dude. Absorbed doses to the eyes is not able to be mathematically calculated with the PCXMC program primarily due to eyes not having an internationally agreed upon radiation sensitivity by which an equivalent dose can be calculated.

Table 39. Specific organ absorbed doses.

Organ	**Daisy**			**Dude**		
	Measured (Daisy)	**Calculated (Phantom)**	**ABS % Difference**	**Measured (Dude)**	**Calculated (Phantom)**	**ABS % Difference**

	Absorbed Dose (mGy)	**Absorbed Dose (mGy)**		**Absorbed Dose (mGy)**	**Absorbed Dose (mGy)**	
Eye	34 +/-3 (each)	NA		22.9 +/- 0.7	NA	
Brain	30 +/- 5	33.80 +/- .09	12%	21 +/- 1	17 +/- 2	21%
Thyroid	2.82 +/- .05	0.51 +/- .06	139%	0.8 +/- 0.2	0.15 +/- 0.03	137%
Lung	0.13 +/- .03	0.072 +/- .003	57%	0.2 +/- 0.1	.024 +/- 0.001	157%
Thymus	1.31 +/- .05	0.04 +/- .02	188%	0.26 +/- 0.01	0.014 +/- 0.008	180%
Esophagus	0.286 +/- .007	0.05 +/- .01	140%	0.680 +/- 0.007	0.015 +/- 0.007	191%
Liver	0.054 +/- .002	0.0062 +/- .0009	159%	0.04 +/- 0.02	0.0021 +/- 0.0007	180%

Table 40 lists the equivalent dose for each organ. Equivalent dose is determined by multiplying the absorbed dose by the ICRP 103 tissue weighting factor. Note that there is no ICRP 103 tissue weighting factor, therefore, the absorbed dose measured for the eyes is not a part of the summed equivalent dose (referred to as the modified effective dose).

Table 40. Modified effective dose per scan and the influence of the equivalent dose on the overall modified effective dose.

Organ	ICRP103 Tissue Weighting Factor	Measured Dose Equivalent (Daisy) (mSv)	Calculated Dose Equivalent (Phantom) (mSv)	ABS % Diff	Measured Dose Equivalent (Dude) (mSv)	Calculated Dose Equivalent (Phantom) (mSv)	ABS % Diff
Brain	0.01	0.30+/- 0.05	0.338 +/- 0.0009		0.21 +/- 0.01	0.17 +/- 0.02	
Esophagus	0.04	0.011 +/- 0.002	0.0020 +/- 0.0004		0.0272 +/- 0.0003	0.0006 +/- 0.0003	
Liver	0.04	.00216 +/- 0.00008	0.00025 +/- 0.00004		0.0016 +/- 0.0008	0.00008 +/- 0.00003	
Lung	0.12	0.016 +/-	0.0086		0.02 +/-	0.0029	

		0.004	+/- 0.0004		0.01	+/- 0.0001	
Thymus	0.04	0.052 +/- 0.002	0.0016 +/- 0.0008		0.0104 +/- 0.0004	0.0006 +/- 0.0003	
Thyroid	0.04	0.113 +/- 0.002	0.021+/- 0.002		0.032 +/- 0.008	0.006 +/- 0.001	
Modified Effective Dose (mSv)		0.49 +/- 0.05	0.370 +/- 0.002	28% or 12% w/brain alone	0.30 +/- 0.02	0.18 +/- 0.02	50% or 21% w/brain alone

Cervical Spine Scan

Table 41 lists the organ results for a cervical spine scan while Table 42 lists the equivalent doses and modified effective dose. The organs directly within the scanning field of view are the thyroid and lower portion of the brain. The esophagus is partially scanned.

Table 41. Cervical Spine specific organ absorbed dose.

Organ	Daisy			Dude		
	Measured (Daisy) Absorbed Dose (mGy)	Calculated (Phantom) Absorbed Dose (mGy)	ABS % Difference	Measured (Dude) Absorbed Dose (mGy)	Calculated (Phantom) Absorbed Dose (mGy)	ABS % Difference
Eye	34 +/- 2 (each)	NA		18.6 +/- 0.7	NA	
Brain	9 +/- 6 (high SD due location of dosimeters)	10.9 +/- 0.3	19%	7 +/- 4	6.5 +/- 0.2	7%
Thyroid	44.5 +/-.05	30 +/- 3	39%	21 +/- 1	28 +/- 2	29%
Lung	0.5 +/- 0.1	0.31 +/- 0.02	47%	4 +/- 3	0.83 +/- 0.04	131%
Thymus	8.0 +/- 0.2	0.26 +/- 0.09	187%	14.2 +/- 0.2	0.7 +/- 0.2	181%
Esophagus	1.83 +/- 0.02	0.5 +/- 0.1	114%	13.5 +/- 0.2	1.5 +/- 0.2	160%
Liver	0.221 +/-	0.022 +/-	164%	0.6 +/-	0.046 +/-	171%

	0.005	0.004			0.4	0.007	

Table 42. Cervical Scan modified effective dose per scan and the influence of the equivalent dose on the overall modified effective dose. The absolute percent difference between the effective dose values is lower when only considering those organs within the field-of-view (FOV) of the CT scanning range.

Organ	ICRP103 Tissue Weighting Factor	Measured Dose Equivalent (Daisy) (mSv)	Calculated Dose Equivalent (Phantom) (mSv)	ABS % Diff	Measured Dose Equivalent (Dude) (mSv)	Calculated Dose Equivalent (Phantom) (mSv)	ABS % Diff
Brain	0.01	0.09+/- 0.06	0.109 +/- 0.003		0.07 +/- 0.04	0.065 +/- 0.001	
Esophagus	0.04	0.0732 +/- 0.0008	0.020 +/- 0.004		0.540 +/- 0.008	0.060 +/- 0.008	
Liver	0.04	0.0088 +/- 0.0002	0.0009 +/- 0.0002		0.02 +/- 0.02	0.0018 +/- 0.0003	
Lung	0.12	0.06+/- 0.01	0.037 +/- 0.002		0.48 +/- 0.4	0.100 +/- 0.005	
Thymus* (cause of high % diff)	0.04	0.320 +/- 0.008	0.011 +/- 0.004		0.586 +/- 0.008	0.006 +/- 0.002	
Thyroid	0.04	1.780 +/- 0.002	1.2 +/- 0.1		0.84 +/- 0.04	1.12 +/- 0.08	
Modified Effective Dose (mSv)		2.33 +/- 0.06	1.4 +/- 0.1	50% or 37% for organs w/in FOV	2.5 +/- 0.4	1.35 +/- 0.04	60% or 15% for organs w/in FOV

The percent difference in the different methods for the modified effective dose is 50% for Daisy and 60% for Dude. When calculated using only those organs within the FOV, the percent difference is 35% for Daisy and 26% for Dude. For only those organs that lie within the scanning FOV (Thyroid, Brain, and Esophagus), the percent difference for

Dude (Measured (1.45 mSv) and Calculated (1.25 mSv)) is 15%. The percent difference for Daisy (Measured (1.94 mSv) and Calculated (1.33 mSv)) is 37%.

Chest Abdomen Pelvis Scan

Tables 43 and 44 list the absorbed doses and the modified effective dose for a chest abdomen pelvis scan. All of the organs listed in the tables are included within the primary scanning field of view except the brain (and of course the eyes).

Table 43. Organ absorbed doses for a chest abdomen pelvis scan.

Organ	Daisy			Dude		
	Measured (Daisy) Absorbed Dose (mGy)	Calculated (Phantom) Absorbed Dose (mGy)	ABS % Difference	Measured (Dude) Absorbed Dose (mGy)	Calculated (Phantom) Absorbed Dose (mGy)	ABS % Difference
Adrenals/Gall Bladder	26.90 +/- 0.03	35.9 +/- 0.3	29%	27.9 +/- 0.4	38 +/- 8	31%
Brain	0.29 +/- 0.02	0.380 +/- 0.004	27%	0.7 +/- 0.3	0.05 +/- 0.02	173%
Colon	22.3 +/- 0.7	27.5 +/- 0.7	21%	28 +/- 5	35 +/- 2	22%
Esophagus	25 +/- 1	29.4 +/- 0.1	16%	22.1 +/- 0.4	25 +/- 4	12%
Eye	0.495 +/- 0.008	NA		0.74 +/- 0.08	NA	
Kidney	24.2 +/- 0.5 (each)	42.17 +/- 0.08	14%	24.2 +/- 0.8 (each)	45 +/- 2	7%
Liver	26.0 +/- 0.2	39.20 +/- 0.03	40%	26.3 +/- 0.9	47 +/- 1	56%
Lung	27 +/- 1 (each)	45.13 +/- 0.04	18%	24 +/- 1 (each)	43 +/- 3	11%
Pancreas	25.9 +/- 0.4	32.4 +/- 0.1	22%	28.5 +/- 0.2	25 +/- 4	13%
Thymus	23.5 +/- 0.3	32.4 +/- 0.2	32%	27.0 +/- 0.5	33.3 +/- 0.5	21%
Thyroid	12.3 +/- 0.4	37.7 +/- 0.2	102%	30.2 +/- 0.8	1.4 +/- 0.7	182%
Uterus/Testes	25.6 +/- 0.1	27.0 +/- 0.1	5%	8 +/- 4	1.5 +/- 0.7	137%

Table 44. Modified effective dose for a chest abdomen pelvis scan.

Organ	ICRP103 Tissue Weighting Factor	Measured Dose Equivalent (Daisy) (mSv)	Calculated Dose Equivalent (Phantom) (mSv)	ABS % Diff	Measured Dose Equivalent (Dude) (mSv)	Calculated Dose Equivalent (Phantom) (mSv)	ABS % Diff
Brain	0.01	0.0029 +/- 0.0002	0.00380 +/- 0.00004		0.007 +/- 0.003	0.0005 +/- 0.0002	
Colon	0.12	2.68 +/- 0.08	3.30 +/- 0.08		3.4 +/- 0.6	4.2 +/- 0.2	
Esophagus	0.04	1.00 +/- 0.04	1.176 +/- 0.004		0.88 +/- 0.02	1.0 +/- 0.2	
Liver	0.04	1.040 +/- 0.008	1.568 +/- 0.001		1.05 +/- 0.04	1.88 +/- 0.04	
Lung	0.12	6.48 +/- 0.04	5.4156 +/- 0.005		5.8 +/- 0.2	5.2 +/- 0.4	
Thymus	0.04	0.94 +/- 0.01	1.296 +/- 0.008		1.08 +/- 0.02	1.33 +/- 0.02	
Thyroid	0.04	0.49 +/- 0.02	1.508 +/- 0.008		1.21 +/- 0.03	0.06 +/- 0.03	
Pancreas	0.12*	3.08 +/- 0.08	4.12 +/- 0.04		3.4 +/- 0.1	3.3 +/- 0.3	
Uterus	0.12*						
Adrenals/Gall Bladder	0.12*						
Kidney	0.12*						
Modified Effective Dose (mSv)		15.7 +/- 0.1	18.39 +/- 0.09	17%	16.7 +/- 0.6	16.9 +/- 0.6	1%

The percent difference between the modified effective doses determined using either the mathematical phantom or experimental measurement is very small, 17% for Daisy and 1% for Dude. When accounting for only those organs within the scanning field of view (all organs vice the brain), the percent difference is 16% for Daisy and stays the same for Dude at 1%.

Chest Scan

Tables 45 and 46 list the organ absorbed doses and modified effective dose for a chest scan. Organs within the scanning field of view for a chest scan include the esophagus, liver, lung, pancreas, thymus, adrenals/gall bladder, kidney, and thyroid.

Table 45. Organ absorbed doses for a chest scan.

Organ	Daisy			Dude		
	Measured (Daisy) Absorbed Dose (mGy)	Calculated (Phantom) Absorbed Dose (mGy)	ABS % Difference	Measured (Dude) Absorbed Dose (mGy)	Calculated (Phantom) Absorbed Dose (mGy)	ABS % Difference
Adrenals/Gall Bladder	4.92 +/- 0.02	3.5 +/- 0.7	34%	3.90 +/- 0.04	3.1 +/- 06	23%
Brain	0.26 +/- 0.01	0.19 +/- .04	31%	0.5 +/- 0.2	0.27 +/- 0.05	60%
Colon	0.134 +/- 0.006	0.48 +/- 0.09	113%	0.20 +/- 0.01	0.42 +/- 0.09	71%
Esophagus	12.5 +/- 0.2	16.2 +/- 0.9	26%	20.5 +/- 0.3	22 +/- 1	7%
Eye	0.29 +/- 0.02	NA		0.61 +/- 0.09	NA	
Kidney	2.16 +/- 0.03 (each)	4.2 +/- 0.4	3%	2.8 +/- 0.7 (each)	3.1 +/- 0.3	57%
Liver	11.1 +/- 0.1	13.3 +/- 0.4	18%	14 +/- 9	14.6 +/- 0.5	4%
Lung	10 +/- 4 (each)	26.0 +/- 0.3	26%	22.6 +/- 0.7 (each)	38.8 +/- 0.4	15%
Pancreas	2.43 +/- 0.03	13 +/- 1	137%	5.62 +/- 0.08	11 +/- 1	65%
Thymus	13.1 +/- 0.4	12.1 +/- 0.5	8%	27.2 +/- 0.4	32 +/- 3	16%
Thyroid	8.3 +/- 0.7	4 +/- 1	70%	25 +/- 2	6 +/- 2	123%
Uterus/Testes	0.112 +/- 0.003	0.13 +/- 0.07	15%	0.045 +/- 0.006	0.003 +/- 0.003	175%

Table 46. Modified effective dose for a chest scan.

Organ	ICRP103 Tissue Weighting Factor	Measured Dose Equivalent (Daisy) (mSv)	Calculated Dose Equivalent (Phantom) (mSv)	ABS % Diff	Measured Dose Equivalent (Dude) (mSv)	Calculated Dose Equivalent (Phantom) (mSv)	ABS % Diff
Brain	0.01	0.0026 +/- 0.0001	0.0019 +/- 0.0004		0.005 +/- 0.002	0.0027 +/- 0.0005	
Colon	0.12	0.0161 +/- 0.0007	0.0576 +/- 0.0108		0.024 +/- 0.001	0.050 +/- 0.004	
Esophagus	0.04	0.500 +/- 0.008	0.648 +/- 0.036		0.82 +/- 0.01	0.88 +/- 0.04	
Liver	0.04	0.444 +/- 0.004	0.532 +/- 0.016		0.6 +/- 0.4	0.58 +/- 0.02	
Lung	0.12	2 +/- 1	3.12 +/- 0.04		5.4 +/- 0.2	4.66 +/- 0.05	
Thymus	0.04	0.52 +/- 0.02	0.48 +/- 0.02		1.09 +/- 0.02	1.3 +/- 0.1	
Thyroid	0.04	0.332 +/- 0.001	0.16 +/- 0.04		1.00 +/- 0.08	0.24 +/- 0.08	
Pancreas	0.12*	0.354 +/- 0.002	0.62 +/- 0.04		0.4 +/- 0.2	0.5 +/- 0.1	
Uterus	0.12*						
Adrenals/Gall Bladder	0.12*						
Kidney	0.12*						
Modified Effective Dose (mSv)		4 +/- 1	5.62 +/- 0.08	34%	9.3 +/- 0.5	8.2 +/- 0.2	13%

The percent difference between the two values for the modified effective dose is 34% for Daisy and 13% for Dude. The percent difference between the two values when only accounting for those organs within the scanning field of view is 29% for Daisy and 13% for Dude.

Thoracic Spine Scan

Tables 47 and 48 list the absorbed doses and modified effective dose for a thoracic spine scan. The organs within the field of view for a thoracic spine scan include the esophagus, liver, lung, pancreas, thymus, adrenals/gall bladder, kidney, and thyroid. The scanning range for a thoracic spine scan is very similar to that of a chest scan just a little shorter.

Table 47. Organ absorbed doses for a thoracic spine scan.

Organ	Daisy			Dude		
	Measured (Daisy) Absorbed Dose (mGy)	Calculated (Phantom) Absorbed Dose (mGy)	ABS % Difference	Measured (Dude) Absorbed Dose (mGy)	Calculated (Phantom) Absorbed Dose (mGy)	ABS % Difference
Adrenals	8.9 +/- 0.2	4.0 +/- 0.8	76%	7.3 +/- 0.1	6.9 +/- 0.6	6%
Brain	0.17 +/- 0.07	0.13 +/- 0.02	27%	0.6 +/- 0.3	0.33 +/- 0.04	58%
Colon	0.36 +/- 0.009	0.12 +/- 0.02	100%	0.38 +/- 0.02	0.20 +/- 0.04	62%
Esophagus	8.8 +/- 0.2	9.3 +/- 0.5	6%	20.0 +/- 0.3	20 +/- 1	0%
Eye	0.19 +/- 0.02	NA		0.7 +/- 0.1	NA	
Kidney	7.6 +/- 0.2 (each)	0.80 +/- 0.08	180%	5 +/- 1	11.0 +/- 0.7	9%
Liver	9.3 +/- 0.2	3.6 +/- 0.1	88%	20 +/- 4	6 +/- 1	108%
Lung	9.5 +/- 0.8 (each)	17.7 +/- 0.2	8%	22.9 +/- 0.8 (each)	40.0 +/- 0.5	14%
Pancreas	7.5 +/- 0.2	2.7 +/- 0.3	94%	14.0 +/- 0.2	5.2 +/- 0.6	92%
Thymus	7.7 +/- 0.2	16 +/- 1	70%	27.4 +/- 0.5	8.8 +/- 0.3	103%
Thyroid	2.87 +/- 0.07	3.1 +/- 0.6	8%	25 +/- 3	13 +/- 2	63%
Uterus/Testes	0.44 +/- 0.01	0.03 +/- 0.02	174%	0.064 +/- 0.004	0.003 +/- 0.003	182%

Table 48. Modified effective dose for a thoracic spine scan.

Organ	ICRP103 Tissue Weighting Factor	Measured Dose Equivalent (Daisy) (mSv)	Calculated Dose Equivalent (Phantom) (mSv)	ABS % Diff	Measured Dose Equivalent (Daisy) (mSv)	Calculated Dose Equivalent (Phantom) (mSv)	ABS % Diff
Brain	0.01	0.0017 +/- 0.0007	0.013 +/- 0.002		0.006 +/- 0.003	0.0033 +/- 0.0004	
Colon	0.12	0.043 +/- 0.001	0.014 +/- 0.002		0.046 +/- 0.002	0.024 +/- 0.005	

Esophagus	0.04	0.352 +/- 0.008	0.37 +/- 0.02		0.80 +/- 0.01	0.80 +/- 0.04	
Liver	0.04	0.372 +/- 0.008	0.144 +/- 0.004		0.8 +/- 0.2	0.24 +/- 0.04	
Lung	0.12	2.3 +/- 0.1	2.12 +/- 0.02		4.8 +/- 0.5	4.80 +/- 0.06	
Thymus	0.04	0.308 +/- 0.008	0.64 +/- 0.04		1.10 +/- 0.02	0.35 +/- 0.01	
Thyroid	0.04	0.115 +/- 0.003	0.12 +/- 0.02		1.0 +/- 0.1	0.52 +/- 0.08	
Pancreas	0.12*	0.96 +/- 0.04	0.23 +/- 0.03		0.9 +/- 0.2	0.7 +/- 0.1	
Uterus	0.12*						
Adrenals/Gall Bladder	0.12*						
Kidney	0.12*						
Modified Effective Dose (mSv)		4.4 +/- 0.1	3.65 +/- 0.06	19%	9.5 +/- 0.6	7.4 +/- 0.2	25%

The percent difference between the two values for the modified effective dose is 19% for Daisy and 25% for Dude. The percent difference between the two values, measured and calculated, when only accounting for those organs within the scanning field of view is 19% for Daisy (4.41 mSv and 3.62 mSv) and 24% for Dude (9.40 mSv and 7.41 mSv).

Lumbar Spine Scan

Tables 49 and 50 list the absorbed doses and modified effective dose for a lumbar spine scan. The organs within the field of view for a lumbar spine scan include the liver, lung, pancreas, adrenals/gall bladder, kidney, and uterus/testes.

Table 49. Organ absorbed doses for lumbar spine scan.

Organ	Daisy			Dude		
	Measured (Daisy) Absorbed Dose (mGy)	Calculated (Phantom) Absorbed Dose (mGy)	ABS % Difference	Measured (Dude) Absorbed Dose (mGy)	Calculated (Phantom) Absorbed Dose (mGy)	ABS % Difference
Adrenals/Gall Bladder	18.0 +/- 0.4	20 +/- 1	11%	22.3 +/- 0.9	33 +/- 3	39%

Brain	0.0378 +/- 0.0009	0.008 +/- 0.003	130%	0.033 +/- 0.009	0.002 +/- 0.001	177%
Colon	11.6 +/- 0.3	12.8 +/- 0.2	10%	22 +/- 3	33.9 +/- 0.7	43%
Esophagus	1.36 +/- 0.03	8.7 +/- 0.5	146%	0.227 +/- 0.006	3 +/- 1	172%
Eye (each)	0.069 +/- 0.001	NA		0.07 +/- 0.01	NA	
Kidney	16.4 +/- 0.4 (each)	25.2 +/- 0.3	26%	18.7 +/- 0.8 (each)	36 +/- 1	4%
Liver	16.0 +/- 0.4	24.6 +/- 0.2	42%	13 +/- 1	26 +/- 1	67%
Lung	9.7 +/- 0.5	10.0 +/- 0.2	3%	2 +/- 1	1.9 +/- 0.3	5%
Pancreas	17.3 +/- 0.4	22.2 +/- 0.5	25%	21.1 +/- 0.3	22 +/- 3	4%
Thymus	0.39 +/- 0.01	1.5 +/- 0.3	117%	0.290 +/- 0.006	0.4 +/- 0.2	32%
Thyroid	0.190 +/- 0.005	0.14 +/- 0.07	30%	0.177 +/- 0.009	0.04 +/- 0.04	126%
Uterus/Testicles	14.8 +/- 0.4	3.5 +/- 0.3	123%	2.07 +/- 0.01	5 +/- 2	83%

Table 50. Modified effective doses for lumbar spine scan.

Organ	ICRP103 Tissue Weighting Factor	Measured Dose Equivalent (Daisy) (mSv)	Calculated Dose Equivalent (Phantom) (mSv)	ABS % Diff	Measured Dose Equivalent (Dude) (mSv)	Calculated Dose Equivalent (Phantom) (mSv)	ABS % Diff
Brain	0.01	0.000378 +/- 0.000006	0.00008 +/- 0.00003		0.00033 +/- 0.00009	0.00002 +/- 0.00001	
Colon	0.12	1.39 +/- 0.04	1.54 +/- 0.02		2.6 +/- 0.4	4.07 +/- 0.08	
Esophagus	0.04	0.054 +/- 0.001	0.35 +/- 0.02		0.0091 +/- 0.0002	0.12 +/- 0.04	
Liver	0.04	0.64 +/- 0.02	0.984 +/- 0.008		0.52 +/- 0.04	1.04 +/- 0.04	
Lung	0.12	1.16 +/- 0.06	1.20 +/- 0.02		0.5 +/- 0.1	0.23 +/- 0.04	
Thymus	0.04	0.0156 +/- 0.0004	0.06 +/- 0.01		0.0116 +/- 0.0002	0.016 +/- 0.008	

Thyroid	0.04	0.008 +/- 0.002	0.006 +/- 0.003		0.0071 +/- 0.0004	0.002 +/- 0.002	
Pancreas	0.12*	2.49 +/- 0.02	2.1 +/- 0.1		2.49 +/- 0.03	2.9 +/- 0.1	
Uterus	0.12*						
Adrenals/Gall Bladder	0.12*						
Kidney	0.12*						
Modified Effective Dose (mSv)		5.76 +/- 0.08	6.2 +/- 0.1	7%	6.1 +/- 0.4	8.4 +/- 0.1	32%

The percent difference between the two values for the modified effective dose is 7% for Daisy and 32% for Dude. The percent difference between the two values, measured and calculated, when only accounting for those organs within the scanning field of view is 0.23% for Daisy (4.29 mSv and 4.28 mSv) and 17% for Dude (3.51 mSv and 4.17 mSv).

Experimental Uncertainties

Uncertainties of the experimental study are shown below for each scanning protocol (Tables 51 – 56). The sensitivities of the organs represented are an average of the Daisy and Dude organ sensitivity. This was calculated in order to better equate to the model which is non-gender specific. The determination of the rest of the sensitivities is explained in Specific Aim 2.

Brain Scan

Table 51. Experimental sensitivity for Brain Scan.

Category	Component	Standard Uncertainty (u)	Sensitivity Coefficient (c)	Degrees of Freedom (v)	$(c \cdot u)^2$
CT Scanner Characteristics	Tube Current	2.5	1	20	6.25
	Exposure Time	0.03	1	20	0.0009
	Tube Voltage	1.5	2.5	20	14.06
	Slice Width/Table Movement	1	0.2	20	0.04

	CTDIair displayed/tabulated CTDIair measured				
Patient Modeling	Adrenals/Gall Bladder				
	Brain	10	.66		44
	Colon				
	Esophagus	7	.055		.15
	Kidney				
	Liver	21	.0045		.0089
	Lung	32	.050		2.6
	Pancreas				
	Thymus	1.5	.073		.012
	Thyroid	2.5	.17		.18
	Uterus/Testes				
Patient Positioning	Vertical Positioning				NA
	Lateral Positioning				NA
Modern Scanner Matching	CTDosimetry helical Scanning (37 rotations)				NA
Detector Uncertainties (Prins Study)	Radiation Normal Incidence	1.5	1	20	2.25
	Radiation Edges Incidence	7.5	0.2	20	2.25
	Calibration Variation	2.5	1	20	6.25
	Energy Response	8.7	1	20	75.69
	Standard Deviation of Measurement	2	1	20	4
Total Uncertainty Combined (u_{comb})	$u_{comb} = \sqrt{\sum_{i=1}^{N} (c_i \cdot u_i)^2}$				12
	95% CI for U_{comb}				24

Cervical Spine Scan

Table 52. Experimental sensitivity for Cervical Spine Scan.

Category	Component	Standard Uncertainty (u)	Sensitivity Coefficient (c)	Degrees of Freedom (v)	$(c \cdot u)^2$
CT Scanner	Tube Current	2.5	1	20	6.25

Characteristics	Exposure Time	0.03	1	20	0.0009
	Tube Voltage	1.5	2.5	20	14.06
	Slice Width/Table Movement	1	0.2	20	0.04
	CTDIair displayed/tabulated				NA
	CTDIair measured				NA
Patient Modeling	Adrenals/Gall Bladder				NA
	Brain	31	0.030		0.86
	Colon				NA
	Esophagus	0.64	0.12		0.0059
	Kidney				
	Liver	17	0.006		0.010
	Lung	12	0.11		1.7
	Pancreas				NA
	Thymus	0.98	0.19		0.035
	Thyroid	1.2	0.55		0.44
	Uterus/Testes				NA
Patient Positioning	Vertical Positioning				NA
	Lateral Positioning				NA
Modern Scanner Matching	CTDosimetry helical Scanning (rotations)				NA
Detector Uncertainties (Prins Study)	Radiation Normal Incidence	1.5	1	20	2.25
	Radiation Edges Incidence	7.5	0.2	20	2.25
	Calibration Variation	2.5	1	20	6.25
	Energy Response	8.7	1	20	75.69
	Standard Deviation of Measurement	2	1	20	4
Total Uncertainty Combined (u_{comb})		$u_{comb} = \sqrt{\sum_{i=1}^{N} (c_i \cdot u_i)^2}$			11
	95% CI for U_{comb}				22

Chest Abdomen Pelvis

Table 53. Experimental sensivity for Chest Abdomen Pelvis Scan.

Category	Component	Standard Uncertainty	Sensitivity Coefficient	Degrees of	$(c \cdot u)^2$

		(u)	(c)	Freedom (v)	
CT Scanner Characteristics	Tube Current	2.5	1	20	6.25
	Exposure Time	0.03	1	20	0.0009
	Tube Voltage	1.5	2.5	20	14.06
	Slice Width/Table Movement	1	0.2	20	0.04
	CTDIair displayed/tabulated				NA
	CTDIair measured				NA
Patient Modeling	Adrenals/Gall Bladder	0.40	0.050		4.0E-4
	Brain	12	0.00030		1.3E-3
	Colon	5.0	0.19		0.90
	Esophagus	1.0	0.06		3.6E-3
	Kidney	1.0	0.05		2.5E-3
	Liver	1.0	0.06		3.6E-3
	Lung	2.0	0.38		0.58
	Pancreas	0.60	0.050		9.0E-4
	Thymus	0.80	0.060		2.3E-3
	Thyroid	1.0	0.12		1.4E-2
	Uterus/Testes	13	0.050		0.42
Patient Positioning	Vertical Positioning				NA
	Lateral Positioning				NA
Modern Scanner Matching	CTDosimetry helical Scanning (37 rotations)				NA
Detector Uncertainties (Prins Study)	Radiation Normal Incidence	1.5	1	20	2.25
	Radiation Edges Incidence	7.5	0.2	20	2.25
	Calibration Variation	2.5	1	20	6.25
	Energy Response	8.7	1	20	75.69
	Standard Deviation of Measurement	2	1	20	4
Total Uncertainty Combined (u_{comb})		$u_{comb} = \sqrt{\sum_{i=1}^{N}(c_i \cdot u_i)^2}$			11
	95% CI for U_{comb}				22

Chest Scan

Table 54. Experimental sensitivity for Chest Scan.

Category	Component	Standard Uncertainty (u)	Sensitivity Coefficient (c)	Degrees of Freedom (v)	$(c \cdot u)^2$
CT Scanner Characteristics	Tube Current	2.5	1	20	6.25
	Exposure Time	0.03	1	20	0.0009
	Tube Voltage	1.5	2.5	20	14.06
	Slice Width/Table Movement	1	0.2	20	0.04
	CTDIair displayed/tabulated				NA
	CTDIair measured				NA
Patient Modeling	Adrenals/Gall Bladder	0.36	0.016		3.3E-5
	Brain	11	0.00059		4.2E-5
	Colon	2.4	0.0033		6.3E-5
	Esophagus	0.77	0.11		5.9E-3
	Kidney	6.6	0.016		1.1E-2
	Liver	16	0.088		2.0
	Lung	11	0.54		35
	Pancreas	0.66	0.016		1.1E-4
	Thymus	1.1	0.12		1.7E-2
	Thyroid	4.1	0.095		0.15
	Uterus/Testes	4.0	0.016		4.1E-3
Patient Positioning	Vertical Positioning				NA
	Lateral Positioning				NA
Modern Scanner Matching	CTDosimetry helical Scanning (37 rotations)				NA
Detector Uncertainties (Prins Study)	Radiation Normal Incidence	1.5	1	20	2.25
	Radiation Edges Incidence	7.5	0.2	20	2.25
	Calibration Variation	2.5	1	20	6.25
	Energy Response	8.7	1	20	75.69
	Standard Deviation of Measurement	2	1	20	4

Total Uncertainty Combined (u_{comb})		$u_{comb} = \sqrt{\sum_{i=1}^{N}(c_i \cdot u_i)^2}$			12
	95% CI for U_{comb}				24

Thoracic Spine Scan

Table 55. Experimental sensitivity for Thoracic Spine Scan.

Category	Component	Standard Uncertainty (u)	Sensitivity Coefficient (c)	Degrees of Freedom (v)	$(c \cdot u)^2$
CT Scanner Characteristics	Tube Current	2.5	1	20	6.25
	Exposure Time	0.03	1	20	0.0009
	Tube Voltage	1.5	2.5	20	14.06
	Slice Width/Table Movement	1	0.2	20	0.04
	CTDIair displayed/tabulated				NA
	CTDIair measured				NA
Patient Modeling	Adrenals/Gall Bladder	0.90	0.039		1.2E-3
	Brain	23	0.00051		1.4E-4
	Colon	1.9	0.0073		1.9E-4
	Esophagus	0.94	0.08		5.7E-3
	Kidney	5.6	0.039		0.048
	Liver	5.5	0.084		0.21
	Lung	3.0	0.51		2.3
	Pancreas	1.0	0.039		1.5E-3
	Thymus	1.1	0.093		0.010
	Thyroid	3.6	0.066		0.056
	Uterus/Testes	2.1	0.039		6.7E-3
Patient Positioning	Vertical Positioning				NA
	Lateral Positioning				NA
Modern Scanner Matching	CTDosimetry helical Scanning (rotations)				NA
Detector Uncertainties (Prins Study)	Radiation Normal Incidence	1.5	1	20	2.25
	Radiation Edges Incidence	7.5	0.2	20	2.25
	Calibration Variation	2.5	1	20	6.25

	Energy Response	8.7	1	20	75.69
	Standard Deviation of Measurement	2	1	20	4
Total Uncertainty Combined (u_{comb})		$u_{comb} = \sqrt{\sum_{i=1}^{N} (c_i \cdot u_i)^2}$			11
	95% CI for U_{comb}				22

Lumbar Spine Scan

Table 56. Experimental sensitivity for Lumbar Spine Scan.

Category	Component	Standard Uncertainty (u)	Sensitivity Coefficient (c)	Degrees of Freedom (v)	$(c \cdot u)^2$
CT Scanner Characteristics	Tube Current	2.5	1	20	6.25
	Exposure Time	0.03	1	20	0.0009
	Tube Voltage	1.5	2.5	20	14.06
	Slice Width/Table Movement	1	0.2	20	0.04
	CTDIair displayed/tabulated				NA
	CTDIair measured				NA
Patient Modeling	Adrenals/Gall Bladder	1.6	0.11		0.031
	Brain	7.4	0.000060		2.0E-7
	Colon	4.1	0.33		1.8
	Esophagus	1.2	0.0054		4.2E-5
	Kidney	1.7	0.11		0.035
	Liver	2.5	0.098		0.060
	Lung	14	0.14		3.8
	Pancreas	0.93	0.11		0.010
	Thymus	1.2	0.0023		7.6E-6
	Thyroid	1.9	0.0013		6.1E-6
	Uterus/Testes	0.80	0.11		7.7E-3
Patient Positioning	Vertical Positioning				NA
	Lateral Positioning				NA
Modern Scanner Matching	CTDosimetry helical Scanning (37 rotations)				NA
Detector Uncertainties (Prins Study)	Radiation Normal Incidence	1.5	1	20	2.25
	Radiation Edges	7.5	0.2	20	2.25

	Incidence Calibration Variation	2.5	1	20	6.25
	Energy Response	8.7	1	20	75.69
	Standard Deviation of Measurement	2	1	20	4
Total Uncertainty Combined (u_{comb})	$u_{comb} = \sqrt{\sum_{i=1}^{N}(c_i \cdot u_i)^2}$				11
	95% CI for U_{comb}				22

The experimental sensitivity for the brain scan, thoracic spine scan, and lumbar spine scan is ±12%. The experimental sensitivity for the cervical spine scan, chest abdomen pelvis scan, and chest scan is ±11%. The greatest contribution to the overall uncertainty for each of the scans is from the dosimeter energy response uncertainty, 8.7%. As expected, the scanning experimental sensitivities for the different scans are less (therefore have more precision) than the scanning sensitivities calculated by using Monte Carlo techniques. This is because experimental sensitivities reflect what is truly happening with the measurements rather than attempting to simulate reality.

Discussion

The models developed (Chapter 4) for the six CT trauma scans can be used with confidence. Experimental verification compared the scanning techniques used in the model development with the scanning techniques used on physical phantoms in a real computed tomography scanner. In all scans (vice the cervical spine scan for Daisy), the absolute percent difference between the experimentally measured modified effective dose and the calculated (same technique as that used in the model development) modified effective dose was under 30%. The 37% absolute percent difference between the two methods for calculating the modified effective dose for Daisy in the cervical spine scan was driven by the slightly higher equivalent dose to the thyroid (1.780 +/- 0.002 mSv for experimentally measured and 1.2 +/- 0.1 mSv for the calculated value) from the experimentally measured scan. This is probably due to the difference in the sizes of the thyroid between the mathematical phantom and the anthropomorphic phantom. Experimentally measured higher absorbed doses in organs as compared to calculated values are not uncommon [46, 59, 123, 190, 250, 281-282].

Values between anthropomorphic phantoms and mathematical phantoms will compare well when the organ is small in volume and can be represented by a centrally located point dose. However, when the organ is large and the dose is not uniform throughout the organ due to only a partial volume of the organ being irradiated or due to low x-ray energies, a higher absolute percent difference will be seen. But when the organ is large and the dose is fairly uniform across the organ due to the entire organ being in the scanning field-of-view, the absolute percent difference will be low [250]. This was observed in the measurement sensitivity analysis. Likewise, organs within the scanning field-of-view will generally contribute the more equivalent dose to the overall effective dose than organs not within the scanning field-of-view. Organs outside the scanning field-of-view will have a higher percent error associated with the absorbed dose.

Anthropomorphic phantoms have been used extensively to measure the radiation dose to specific locations within the human body. Researchers can design and develop their own phantoms but will often purchase the anthropomorphic phantoms from a manufacturer equipped to design, manufacture, and modify the phantoms to the researcher specifications. In my research, I purchased the anthropomorphic phantoms from CIRS (Norfolk, Virginia) modified for my specific purpose of measuring radiation dose to an exact location with optically stimulated luminescent dosimeters. The phantoms replicate reference male and reference female dimensions as defined by ICRU 44 and ICRP 23 specifications. Experiments were conducted in order to characterize the dose response of optically stimulated luminescent dosimeters designed by Landauer, Inc. These dosimeters are extremely small (approximately 1 cm x 1 cm x 0.2 cm) and can be inserted into the specifically designed tissue plugs in the anthropomorphic phantoms. Our experiments confirmed the linearity and response of the manufacturer specifications (reporting dose 10 mrad to 1500 rad, energy range 5 keV up to 20+ MeV, and an accuracy of +/- 5%) [249, 268, 283]. Additionally, our experiments also assessed the dose response of the dosimeters at varying thicknesses of solid water used to simulate increasing depths of tissue. The results confirmed that the dosimeters have an expected exponential response and when compared with a calibrated ion chamber, the response is within +/- 20% at depths down to 14 cm.

Acceptance of the verification measurements to within 30% is driven by both literature and statistical analysis. Since the measurements are assumed to be normally distributed, then about 68% of the data will lie within one standard deviation of the mean. Therefore, if two measures are within 30% of each other, then one can assume that the two measures are within one standard deviation of the true mean. There are several reasons why experimental measurements differ from the mathematical modeling. The calculated method uses a stylized mathematical Cristy phantom (Figure 10) while the measurement values were obtained using a physical anthropomorphic phantom (Figure 33). Even when Struelens et al [59] compared an MCNP voxelized Rando-Alderson phantom with a physical Rando-Alderson phantom, results were said to in agreement with most absorbed doses within the scanning field-of-view being within +/- 15% and for those organs outside the field-of-view being within +/- 30%. Struelens attributed the difference to the energy and geometrical dependence of the detectors, difference in material compositions, field sizes, and phantom positioning. Experiments performed with PCXMC and Rando-Alderson phantoms have shown strong correlation of the computed doses to experimental doses being within 30% with the primary reason for the difference being anatomic [209]. Also of note is that differences in the field size can either increase the dose (resulting from more organs being included within the field-of-view) or decreasing the dose (resulting from fewer organs being included within the field-of-view). Comparisons between two methods of calculating effective doses, experimental using TLDs and weighted CTDI methods, Cohnen et al found that excellent correlation between the two calculations could be demonstrated for differences up to 30% [284].

CHAPTER 6. Specific Aim 4: Validate the effective dose models against current DLP methods for estimating effective doses using a pilot study of representative trauma patient CT scans.

Introduction

Chapter 6 will address the comparison of effective doses estimated by use of the Ht/Wt model developed in Chapter 4 against current effective dose estimation methods. Data from a real MSKCC patient population will be used as inputs for the two methods. The two effective dose estimation methods will be statistically analyzed for repeatability and interchangeability. Finally, the two effective dose estimation methods will be applied to a hypothetical example of a CT scanning history for a Soldier who sustained traumatic injuries.

Validation of the effective dose methodology occurred with data collected in a Memorial Sloan-Kettering Cancer Center Institutional Review Board approved (approval number WA0313-10) retrospective study of patients from 2005 to 2010 who underwent CT scans of the aforementioned six scanning protocols (brain, cervical spine, chest abdomen pelvis, chest, thoracic spine, and lumbar spine). Although MSKCC patients tend to be older and have less muscle mass than the average soldier in the U.S. Army, the scanning ranges for the different scans will be very similar and are based upon anatomic locations as opposed to age, muscle mass, or gender. All patients were chosen at random and only pediatric patients were excluded due to difference in scanning machine technique factors and scanning ranges.

The statistical comparisons used in this chapter will be performed using Bland-Altman plots. Bland-Altman plots represent the difference of two measurements versus the average of the two measurements [285]. Other techniques use standard regression analysis for the two measurements, but regression analysis only shows a measure of the association (correlation) between the two measurements rather than show any information concerning agreement. Bland-Altman plots are more informative and allow us to determine how repeatable the measurements are and how well the two measurements agree.

In order to validate the Ht/Wt model developed in Chapter 4, I compared the modeled effective dose results to the current accepted method for estimating effective dose calculates the effective dose from a computed tomography scan by multiplying the dose-length-product from the scan, obtained from the individual CT dose report, with an effective dose conversion coefficient. The conversion coefficients are accepted values (AAPM [286], NCRP [14], and ICRU [287]) based upon Monte Carlo modeling of the beam characteristics, the scanning field-of-view, the photon simulation inside a patient, and the modeling of the patient themselves. Conversion coefficients are designed for specific organs and are therefore applied to each slice thickness in accordance with the location of the CT scan. Conversion coefficients typically have a higher degree of statistical uncertainty for the organs that lie outside of the scanning field-of-view than for those organs that lie within the scanning field-of-view [66, 201]. However, the effective dose contributions from these organs are generally low and are of less importance than those organs within the primary scanning field-of-view. Researchers from respected agencies (Center for Devices and Radiological Health, GSF-National Research Center for

Environment and Health, and National Radiological Protection Board) have published conversion coefficients specifically for calculating the effective dose [288].

The probability risk estimates of cancer incidence and cancer mortality can be calculated using BEIR VII methodology [29]. This methodology has been previously used to quantify the risks from CT scans [21].

Methods

Radiation doses from six different CT protocols (10 adult scans of each protocol; brain, cervical spine, chest-abdomen-pelvis, chest, thoracic spine, and lumbar spine) were collected and analyzed for dose variability. The information collected from the PACS database was age, gender, height/weight (obtained from patient electronic records), CTDI, DLP, scanning range and CT machine techniques (mA, kVp, pitch, and slice thickness). This information was used to validate the Ht/Wt models.

Previous research that we conducted showed that the variability in dose-length-product can range from 2.5-fold to 5-fold among different manufacturers and CT models when using identical technique factors. The highest variation occurred with CT scans covering the abdominal portion of the body. Other published research has shown that the effective dose can vary by 13-fold (difference between lowest effective dose and highest effective dose) with abdominal and pelvis CT scans among machines from four different institutions [289]. Our preliminary research using an anthropomorphic phantom with two different detectors on one machine showed that the effective dose (calculated from established DLP to effective dose conversion coefficients) can vary by 2-fold for brain, chest-abdomen-pelvis, and lumbar spine scans.

Results

Brain Scan Comparison

In accordance with MSKCC IRB (approval number WA0313-10), data on ten patients who underwent a brain scan were collected (Table 57). All the patients were adults. The population means +/- SD were: height 172 +/- 11 cm, weight 74 +/- 17 kg, DLP 719 +/- 18 mGy cm, and scan range 17.5 +/- 0.6 cm.

Table 57. Brain scan patient information. Ht/Wt model dose estimate, conversion coefficient model dose estimate, and comparison to nominal values for brain scans.

Height (cm)	Weight (kg)	DLP (mGy cm)	Scan Range (cm)	Predicted Effective Dose (mSv)		Effective Dose (mSv) DLP-CC method [91]		NCRP 160 ED (mSv)
				Ht/Wt Model	SD	0.0021	0.0023	
170	77	710.84	17.3	**1.80**	±0.25	**1.49**	**1.63**	Brain 0.9 - 4
172.8	59.4	710.84	18.3	**1.92**	±0.26	**1.49**	**1.63**	
173	60.5	710.84	17.0	**1.91**	±0.26	**1.49**	**1.63**	
178	65.3	752.65	18.0	**1.84**	±0.26	**1.58**	**1.73**	
179.1	84.4	752.65	18.1	**1.69**	±0.20	**1.58**	**1.73**	
193	108.9	710.84	18.3	**1.44**	±0.26	**1.49**	**1.63**	
162	60.9	710.84	17.1	**1.97**	±0.26	**1.49**	**1.63**	
165	58.7	710.84	17.0	**1.97**	±0.26	**1.49**	**1.63**	
175.3	74	710.84	17.0	**1.80**	±0.26	**1.49**	**1.63**	
153	92.7	710.84	17.0	**1.80**	±0.27	**1.49**	**1.63**	

The population average and standard deviation of predicted effective dose is 1.8 +/- 0.2 mSv. The average and standard deviation of the effective dose using the conversion coefficients for both coefficients are 1.51 +/- 0.04 mSv and 1.65 +/- 0.04 mSv respectively.

Cervical Spine Scan Comparison

Data on ten patients who underwent a cervical spine scan was collected (Table 58). All the patients were adults. The population means +/- SD were: height 166 +/- 10 cm, weight 67 +/- 15 kg, DLP 464 +/- 42 mGy cm, and scan range 21 +/- 2 cm.

Table 58. Cervical Spine patient information. Ht/Wt model dose estimate, conversion coefficient model dose estimate, and comparison to nominal values for cervical spine scans.

Height (cm)	Weight (kg)	DLP (mGy cm)	Scan Range (cm)	Predicted Effective Dose (mSv)		Effective Dose (mSv) DLP-CC method [91]			NCRP 160 ED Range (mSv)
				Ht/Wt Model	SD	0.0048	0.0054	0.0059	
174	75.9	388.99	20.36	**2.36**	±0.04	**1.87**	**2.10**	**2.30**	Not Listed
171	72.5	417.18	17.41	**2.41**	±0.04	**2.00**	**2.25**	**2.46**	
175.3	49.9	439.06	23.59	**2.54**	±0.09	**2.11**	**2.37**	**2.59**	
162	48.5	441.15	19.41	**2.72**	±0.07	**2.12**	**2.38**	**2.60**	
144	46.8	459.98	19.66	**3.37**	±0.10	**2.21**	**2.48**	**2.71**	
161	66.3	480.42	23.78	**2.62**	±0.06	**2.31**	**2.59**	**2.83**	
177	77.7	493.44	22.60	**2.34**	±0.05	**2.37**	**2.66**	**2.91**	
159.1	89.8	500.41	20.91	**2.50**	±0.08	**2.40**	**2.70**	**2.95**	
170	68	502.68	20.91	**2.45**	±0.06	**2.41**	**2.71**	**2.97**	
168.8	77.6	519.45	23.92	**2.40**	±0.05	**2.49**	**2.81**	**3.06**	

The population average and standard deviation of predicted effective dose is 2.6 +/- 0.3 mSv. The average and standard deviation of the effective dose using the conversion coefficients for the three coefficients are 2.2 +/- 0.2 mSv, 2.5 +/- 0.2 mSv, and 2.7 +/- 0.2 mSv respectively.

Chest Abdomen Pelvis Scan Comparison

Data on ten patients who underwent a chest abdomen pelvis scan was collected (Table 59). All the patients were adults. The population means +/- SD were: height 167 +/- 8 cm, weight 81 +/- 19 kg, DLP 1114 +/- 248 mGy cm, and scan range 68 +/- 4 cm.

Table 59. Chest abdomen pelvis patient information. Ht/Wt model dose estimate, conversion coefficient model dose estimate, and comparison to nominal values for chest abdomen pelvis scans.

Height (cm)	Weight (kg)	DLP (mGy cm)	Scan Length (cm)	Model Predicted Effective Dose (mSv		Standard Method Effective Dose (mSv) using Conversion Coefficient [91]		NCRP 160 ED Range (mSv)
				Ht/Wt Model	SD	0.015	0.017	
164	83.6	1414.61	67.62	**18.97**	±1.07	**21.22**	**24.05**	Chest 4 - 18 Abdomen/Pelvis 3 - 25
162.9	60.8	842.61	65.62	**21.23**	±1.07	**12.64**	**14.32**	
173	78.6	1017.59	71.01	**20.05**	±1.05	**15.26**	**17.30**	
157.5	65.8	902.81	62.48	**20.38**	±1.07	**13.54**	**15.35**	
159	63.7	951.82	61.64	**20.69**	±1.06	**14.28**	**16.18**	
180	114	1213.6	67.87	**16.88**	±1.07	**18.20**	**20.63**	
174.2	114.3	1586.81	71.09	**16.48**	±1.08	**23.80**	**26.98**	
166	68	960.56	72.60	**20.69**	±1.07	**14.41**	**16.33**	
173	84.5	1291.96	72.10	**19.45**	±1.06	**19.38**	**21.96**	
158.5	72	965.65	66.64	**19.81**	±1.07	**14.48**	**16.42**	

The population average and standard deviation of predicted effective dose is 19 +/- 2 mSv. The average and standard deviation of the effective dose using the conversion coefficients for the two coefficients is 17 +/- 3 mSv, and 19 +/- 4 mSv respectively.

Chest Scan Comparison

Data on ten patients who underwent a chest scan was collected (Table 60). All the patients were adults. The population means +/- SD were: height 169 +/- 10 cm, weight 84 +/- 15 kg, DLP 479 +/- 33 mGy cm, and scan range 13 +/- 1 cm.

Table 60. Chest scan patient information. Ht/Wt model dose estimate, conversion coefficient model dose estimate, and comparison to nominal values for chest scans.

Height (cm)	Weight (kg)	DLP (mGy cm)	Scan Length (cm)	Predicted Effective Dose (mSv)		Effective Dose (mSv) using Conversion Coefficient [91]			NCRP 160 ED Range
				Ht/Wt Model	SD	0.014	0.017	0.018	
156	108.1	428.31	12.78	**8.72**	±1.4	**6.00**	**7.28**	**7.71**	Chest Scan 4-18 mSv
172	69.6	435.29	10.4	**11.71**	±1.36	**6.09**	**7.40**	**7.84**	
181	95.6	458.5	12.78	**10.27**	±1.37	**6.42**	**7.79**	**8.25**	
157	73	471.89	12.88	**11.00**	±1.37	**6.61**	**8.02**	**8.49**	
170	75.5	473.43	12.5	**11.19**	±1.35	**6.63**	**8.05**	**8.52**	
160	85	480.79	12.53	**10.21**	±1.37	**6.73**	**8.17**	**8.65**	
183	97	492.15	12.66	**10.28**	±1.35	**6.89**	**8.37**	**8.86**	
181	100.4	496.85	12.78	**9.99**	±1.36	**6.96**	**8.45**	**8.94**	
166.5	68.1	509.16	12.38	**11.64**	±1.35	**7.13**	**8.66**	**9.16**	
161	67	538.72	14.13	**11.57**	±1.36	**7.54**	**9.16**	**9.70**	

The population average and standard deviation of predicted effective dose is 10.7 +/- 0.9 mSv. The average and standard deviation of the effective dose using the conversion coefficients for the three coefficients is 6.7 +/- 0.5 mSv, 8.1 +/- 0.6 mSv, and 8.6 +/- 0.6 mSv respectively.

Thoracic Spine Scan Comparison

Data on ten patients who underwent a thoracic spine scan was collected (Table 61). All the patients were adults. The population means +/- SD were: height 169 +/- 9 cm, weight 76 +/- 24 kg, DLP 941 +/- 174 mGy cm, and scan range 38 +/- 2 cm.

Table 61. Thoracic spine scan patient information. Ht/Wt model dose estimate, conversion coefficient model dose estimate, and comparison to nominal values for thoracic spine scans.

Height (cm)	Weight (kg)	DLP (mGy cm)	Scan Range (cm)	Predicted Effective Dose (mSv		Effective Dose (mSv) using Conversion Coefficient (Chest) [91]			NCRP 160 ED Range (mSv)
				Ht/Wt Model	SD	0.014	0.017	0.018	
177.8	109	931.52	40.3	**12.066**	±0.654	**13.04**	**15.84**	**16.77**	Not Listed
182	128.9	1213.95	41.1	**11.309**	±0.663	**17.00**	**20.64**	**21.85**	
170	59.8	1079.82	37.4	**14.440**	±0.654	**15.12**	**18.36**	**19.44**	
165	64.6	1155.71	37.7	**13.919**	±0.652	**16.18**	**19.65**	**20.80**	
165	60	651.33	38.4	**14.209**	±0.653	**9.12**	**11.07**	**11.72**	
158.6	53.7	874.82	38.4	**14.328**	±0.656	**12.25**	**14.87**	**15.75**	
176	72	773.31	36.8	**14.002**	±0.651	**10.83**	**13.15**	**13.92**	
159	74.5	972.19	35.9	**12.931**	±0.654	**13.61**	**16.53**	**17.50**	
177	70.6	947.64	34.2	**14.124**	±0.651	**13.27**	**16.11**	**17.06**	
160	61.9	811.53	38.4	**13.841**	±0.654	**11.36**	**13.80**	**14.61**	

The population average and standard deviation of predicted effective dose is 13 +/- 1 mSv. The average and standard deviation of the effective dose using the conversion coefficients for the three coefficients is 13 +/- 2 mSv, 16 +/- 3 mSv, and 17 +/- 3 mSv respectively. The average values are skewed because the second patient's BMI (38.9 kg/cm^2) is outside of the model predictive value of BMI's between 18 kg/cm^2 and 36 kg/cm^2. This type of patient results in a lower predicted effective dose. The predicted effective dose is low because the dose values are based off of a single entrance skin dose value which is used for all predicted BMIs. The high DLP value for the obese patient will reflect the adjustment made by the machine to ensure a quality diagnostic image.

Lumbar Spine Scan Comparison

Data on ten patients who underwent a lumbar spine scan was collected (Table 62). All the patients were adults. The population means +/- SD were: height 169 +/- 9 cm, weight 86 +/- 29 kg, DLP 888 +/- 173 mGy cm, and scan range 32 +/- 6 cm.

Table 62. Lumbar spine scan patient information. Ht/Wt model dose estimate, conversion coefficient model dose estimate, and comparison to nominal values for lumbar spine scans.

Height (cm)	Weight (kg)	DLP (mGy cm)	Scan Range (cm)	Predicted Effective Dose (mSv)		Effective Dose (mSv) using Conversion Coefficient (Abdomen) [91]			NRCP 160 ED Range (mSv)
				Ht/Wt Model	SD	0.012	0.015	0.017	
154	79	788.67	34.1	**8.89**	±0.70	**9.46**	**11.83**	**13.41**	Not Listed
155	62.4	949.15	32.4	**11.32**	±0.70	**11.39**	**14.24**	**16.14**	
160.6	62.2	978.96	39.0	**11.79**	±0.70	**11.75**	**14.68**	**16.64**	
157	62	762.08	25.9	**11.52**	±0.70	**9.14**	**11.43**	**12.96**	
170	68	727.48	25.2	**11.82**	±0.70	**8.73**	**10.91**	**12.37**	
167	70.5	726.22	27.2	**11.21**	±0.70	**8.71**	**10.89**	**12.35**	
180.3	98.2	967.51	34.1	**7.71**	±0.70	**11.61**	**14.51**	**16.45**	
167.5	77.1	579.19	26.7	**10.28**	±0.70	**6.95**	**8.69**	**9.85**	
151	68.9	893.42	25.2	**10.15**	±0.70	**10.72**	**13.40**	**15.19**	
175	61.4	805.92	27.4	**13.11**	±0.69	**9.67**	**12.09**	**13.70**	

The population average and standard deviation of predicted effective dose is 11 +/- 2 mSv. The average and standard deviation of the effective dose using the conversion coefficients for the three coefficients is 9 +/- 2 mSv, 12 +/- 3 mSv, and 14 +/- 3 mSv respectively. The predicted model average absolute difference to each of the conversion coefficient values is 10%, 12%, and 24%.

Determination of acceptability (agreement) was performed by analyzing the data via Bland-Altman plots. These plots show the average of the means of the two values calculated by using the two different effective dose estimation methods on the x-axis. On the y-axis, the differences between the values calculated by using the two different effective dose estimation methods are shown. This difference represents a measurement of the bias between the two effective dose estimation methodologies. A positive bias indicates that the Ht/Wt model is biased towards a higher effective dose estimation value than the DLP-CC method whereas a negative bias would indicate that the Ht/Wt model is biased towards a lower effective dose estimation value than the DLP-CC method. The 95% confidence interval of the mean of the differences illustrates the magnitude of the systematic difference. The value of zero shows the measure of equality (there is no difference between the means of the two values). If the measure of equality, zero, is not in the interval, there is a significant systematic difference. The 95% confidence interval lines (+/- 1.96 SD) show the upper and lower limits of agreement. When the values on the plot are within the mean +/- 1.96 SD and are not clinically important, the models may be used interchangeably [285, 290].

Brain Scan Bland-Altman Plot

Figure 34 shows the Bland-Altman plot for the two methods of calculating the effective dose from a brain scan. I used the average effective dose values of the two conversion coefficients. As can be seen from the plot, the Ht/Wt model has a slight positive bias in estimating the effective dose compared to the DLP-CC method. The bias is small though, indicating that there is good agreement between the two methods on average. There is no significant systematic difference because the line of equality is within the +/-1.96 SD lines. All plot values are within two standard deviations.

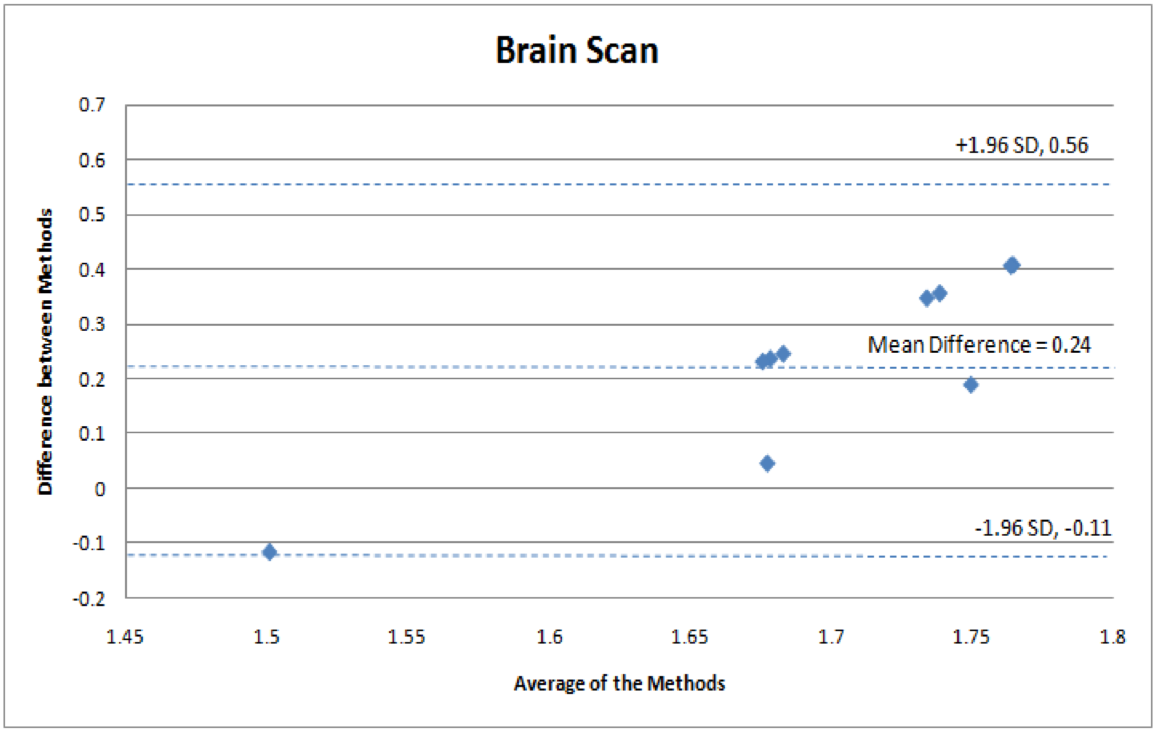

Figure 34. Bland-Altman plot of two methods for calculating the effective dose from a brain scan. DLP-CC method represents the average of the doses from the two different conversion coefficients.

Cervical Spine Bland-Altman Plot

Figure 35 shows the Bland-Altman plot for the two methods of calculating the effective dose from a cervical spine scan. I used the average effective dose values of the three conversion coefficients. As can be seen from the plot, the model has a slight positive bias compared to the average of the conversion coefficients. The bias is small though, indicating that there is good agreement between the two methods on average. There is no significant systematic difference because the line of equality is within the +/-1.96 SD lines. All plot values are within two standard deviations.

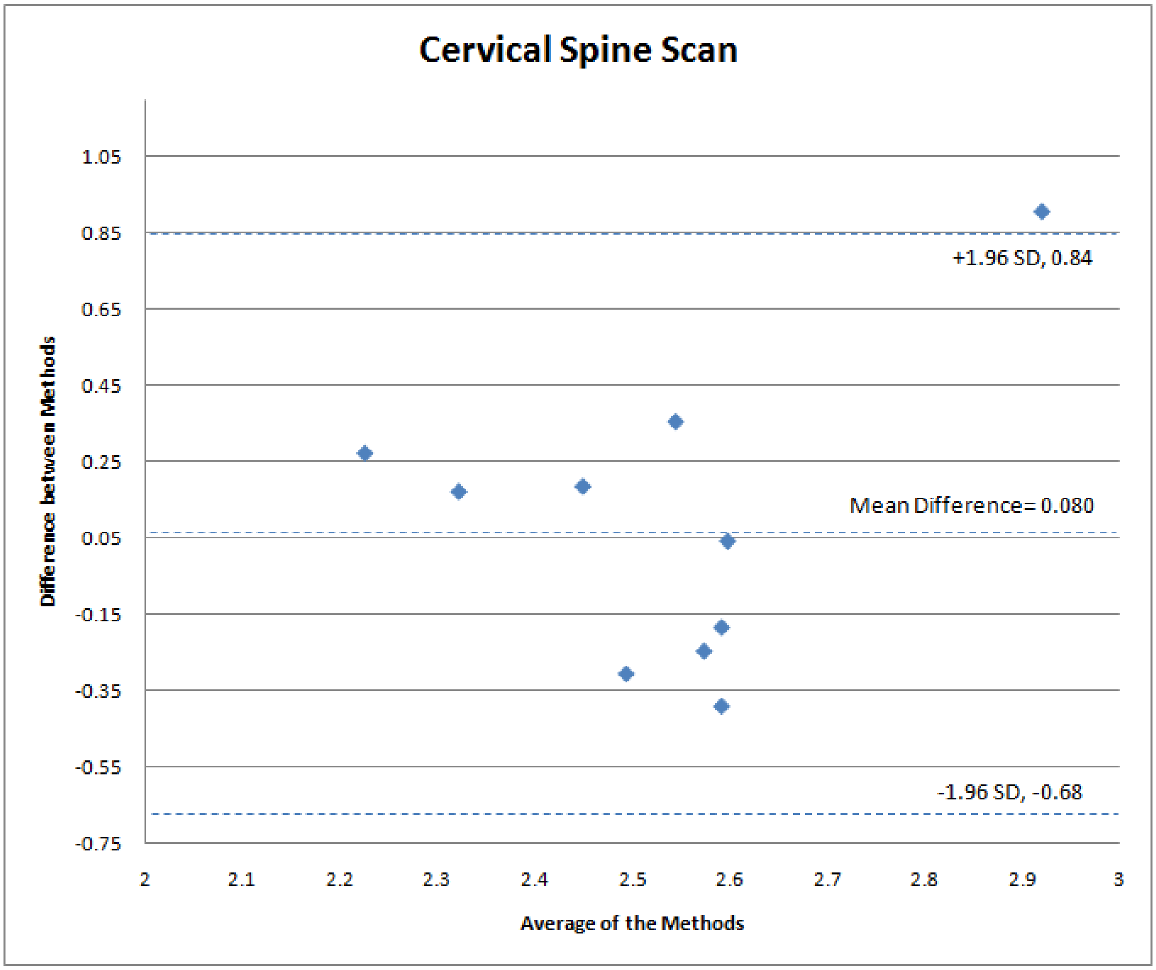

Figure 35. Bland-Altman plot of two methods for calculating the effective dose from a cervical spine scan. DLP-CC method represents the average of the doses from the three different conversion coefficients.

Chest Abdomen Pelvis Scan Bland-Altman Plot

Figure 36 shows the Bland-Altman plot for the two methods of calculating the effective dose from a chest abdomen pelvis scan. I used the average effective dose values of the two conversion coefficients. As can be seen from the plot, the model has a slight positive bias compared to the average of the conversion coefficients. The bias is large indicating that the Ht/Wt model consistently estimated higher effective doses than the DLP-CC method. This is to be expected because there is no specifically derived conversion coefficient listed for Chest Abdomen Pelvis scans only for Chest scans and Abdomen Pelvis scans. There is no significant systematic difference because the line of equality is within the +/-1.96 SD lines. All plot values are within two standard deviations.

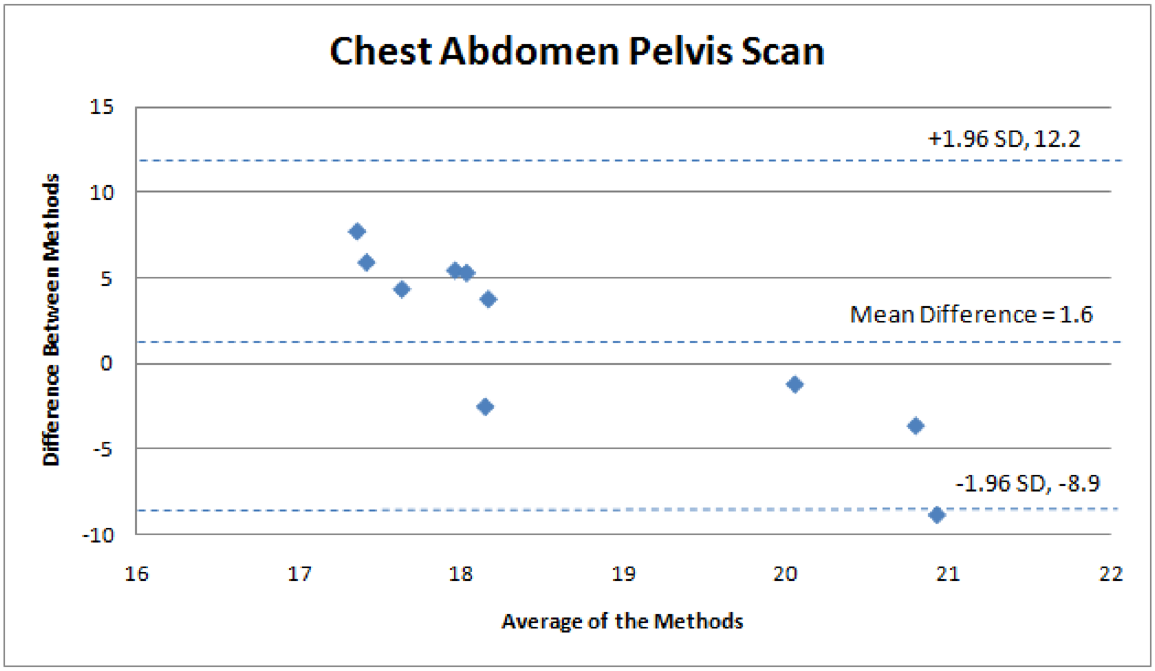

Figure 36. Bland-Altman plot of two methods for calculating the effective dose from a chest abdomen pelvis scan. DLP-CC method represents the average of the doses from the two different conversion coefficients.

Chest Scan Bland-Altman Plot

Figure 37 shows the Bland-Altman plot for the two methods of calculating the effective dose from a chest scan. I used the average estimate of the effective dose values of the three conversion coefficients to compare against the Ht/Wt model. As can be seen from the plot, the Ht/Wt model has a positive bias compared to the estimated effective dose calculated using the DLP-CC method. The 95% CI limits of agreement do not include zero so it is very unlikely that the two methods will ever agree. There is a significant systematic difference because the line of equality is not within the +/-1.96 SD lines. There is good agreement with between the two methods because the values are within the 95% CI limits of agreement.

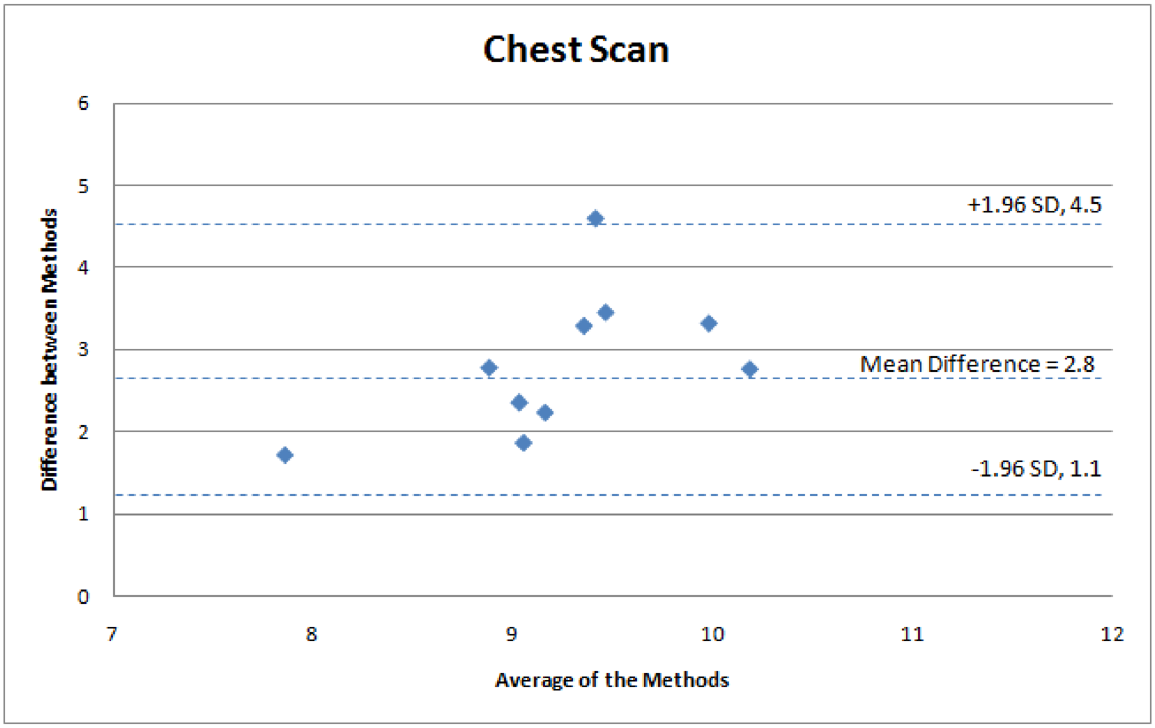

Figure 37. Bland-Altman plot of two methods for calculating the effective dose from a chest scan. DLP-CC method represents the average of the doses from the three different conversion coefficients.

Thoracic Spine Scan Bland-Altman Plot

Figure 38 shows the Bland-Altman plot for the two methods of calculating the effective dose from a thoracic spine scan. I used the average effective dose values of the three conversion coefficients. As can be seen from the plot, the model has a slight negative bias away from the model towards the conversion coefficients. There is no significant systematic difference and there is good agreement with between the two methods because the values are within +/-1.96 SD limits of agreement.

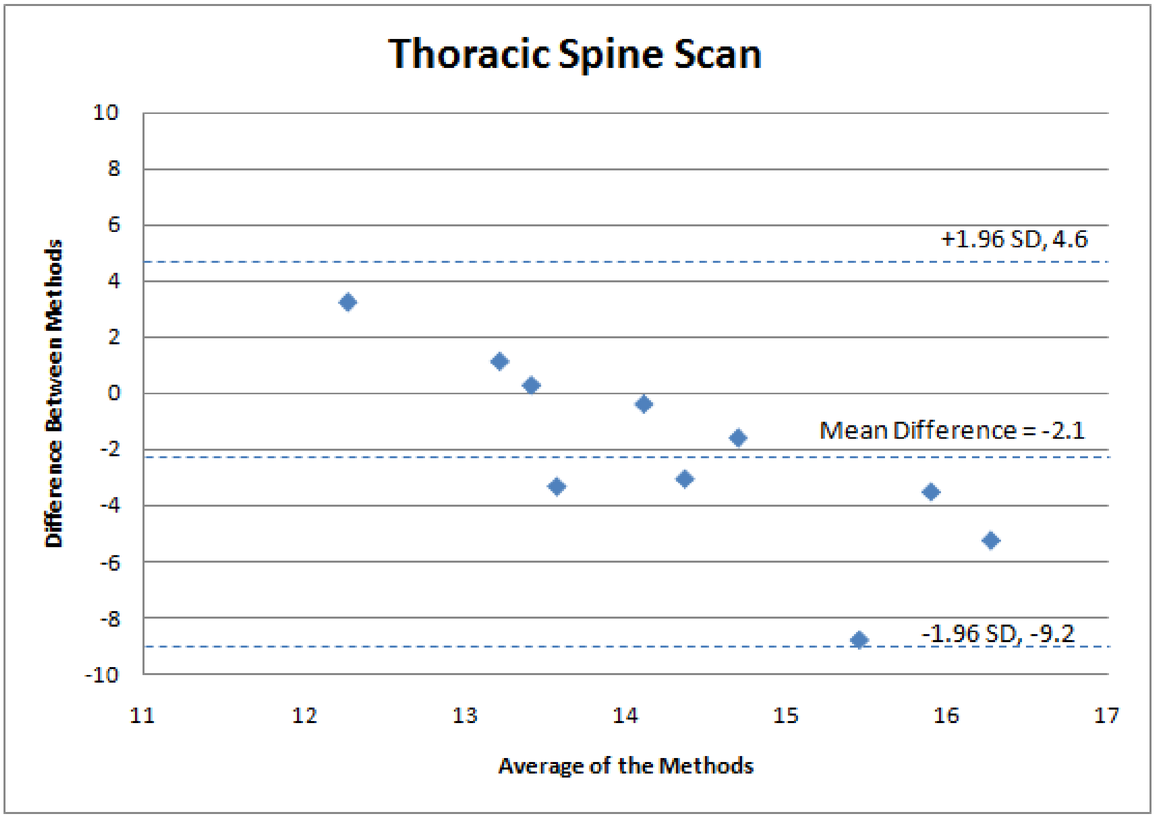

Figure 38. Bland-Altman plot of two methods for calculating the effective dose from a thoracic spine scan. DLP-CC method represents the average of the doses from the three different conversion coefficients.

Lumbar Spine Scan Bland-Altman Plot

Figure 39 shows the Bland-Altman plot for the two methods of calculating the effective dose from a lumbar spine scan. I used the average effective dose values of the three conversion coefficients. As can be seen from the plot, the model has a slight negative bias away from the model towards the conversion coefficients. There is no significant systematic difference and there is good agreement with between the two methods because the values are within +/-1.96 SD limits of agreement.

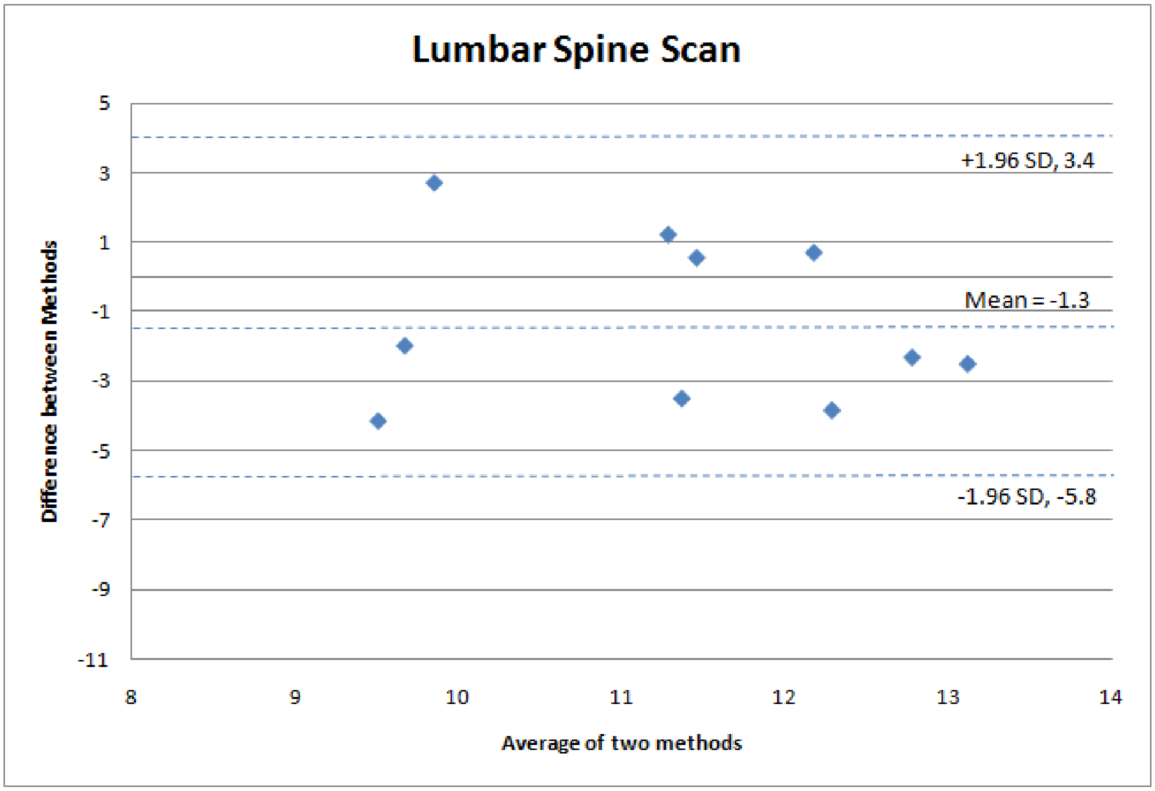

Figure 39. Bland-Altman plot of two methods for calculating the effective dose from a lumbar spine scan. DLP-CC method represents the average of the doses from the three different conversion coefficients.

The additional risk of cancer to a female and male Army Soldier of age 30 who received a chest abdomen pelvis scan is calculated using the BEIR VII methodology (Table 64). BEIR VII calculates the lifetime attributable risk (LAR) for cancer incidence and mortality according to the formulaic using tables in BEIR VII on page 311 [29].

$$LAR_{Cancer\ Incidence} = \frac{D_{Tissue}(Gy)}{0.1\ (Gy)} * \#\ of\ cases\ per\ 100{,}000\ persons\ exposed\ at\ that\ age \qquad 15$$

$$LAR_{Cancer\ Mortality} = \frac{D_{Tissue}(Gy)}{0.1\ (Gy)} * \#\ of\ cases\ per\ 100{,}000\ persons\ exposed\ at\ that\ age \qquad 16$$

Table 63. Estimation of cancer incidence and mortality from one chest abdomen pelvis CT scan.

Risk of one helical CAP scan to a reference sized Female (Daisy) and Male (Dude) Army Soldier both with age of 30 years old

Organ	Dose (mGy)		Lifetime Risk of being diagnosed with cancer in that organ		Lifetime Risk of dying of cancer in that organ	
	Daisy	*Dude*	*Daisy*	*Dude*	*Daisy*	*Dude*
Adrenals/Gall Bladder	26.90 +/- 0.03	27.9 +/- 0.4	6 in 10,000	6 in 10,000	3 in 10,000	3 in 10,000
Brain	0.29 +/- 0.02	0.7 +/- 0.3	6 in 1,000,000	1 in 100,000	3 in 1,000,000	7 in 1,000,000
Colon	22.3 +/- 0.7	28 +/- 5	2 in 10,000	4 in 10,000	8 in 100,000	4 in 10,000
Esophagus	25 +/- 1	22.1 +/- 0.4	5 in 10,000	4 in 10,000	3 in 10,000	2 in 10,000
Eye	0.50 +/- 0.02	0.74 +/- 0.08	NA	NA	NA	NA
Kidney	24.2 +/- 0.5 (each)	24.2 +/- 0.8 (each)	5 in 10,000	5 in 10,000	3 in 10,000	2 in 10,000
Liver	26.0 +/- 0.2	26.3 +/- 0.9	5 in 10,000	5 in 1,000,000	2 in 100,000	5 in 1,000,000
Lung	27 +/- 1 (each)	24 +/- 1 (each)	7 in 10,000	3 in 10,000	6 in 10,000	3 in 10,000
Pancreas	25.9 +/- 0.4	28.5 +/- 0.2	5 in 10,000	6 in 10,000	3 in 10,000	3 in 10,000
Thymus	23.5 +/- 0.3	27.0 +/- 0.5	5 in 10,000	5 in 10,000	2 in 10,000	3 in 10,000
Thyroid	12.3 +/- 0.4	30.2 +/- 0.8	5 in 100,000	3 in 10,000	1 in 10,000	3 in 100,000
Uterus/Testes	25.6 +/- 0.1	8 +/- 4	5 in 100,000	2 in 10,000	1 in 100,000	8 in 100,000

Likewise, the lifetime attributable risks can be estimated for all the trauma scans assessed (Tables 65 and 66). For those organs not specifically listed in BEIR VII Table 12D-1 and Table 12D-2 [29], the cancer incidence and cancer mortality risk is calculated using values for Other. The Daisy and Dude measured absorbed dose values (Specific Aim 3) are used for dose inputs.

Table 64. Estimation of cancer incidence and mortality for each trauma scan for a female age 30 patient.

Specific Organ Doses and Lifetime Attributable Risks to a 30-year old reference Female			
Organ	Measured (Daisy)	LAR Cancer	LAR Cancer

	Absorbed Dose (mGy)	Incidence (for those organs not explicitly listed, the category OTHER was used)	Mortality (for those organs not explicitly listed, the category OTHER was used)
Brain Scan			
Eye	34 +/-3 (each)	NA	NA
Brain	30 +/- 5	6 in 10,000	3 in 10,000
Thyroid	2.82 +/-.05	1 in 100,000	3 in 100,000
Lung	0.13 +/- .03 (each)	3 in 1,000,000	3 in 1,000,000
Thymus	1.31 +/- .05	3 in 100,000	1 in 100,000
Esophagus	0.286 +/- .007	6 in 1,000,000	3 in 1,000,000
Liver	0.054 +/- .002	5 in 100,000,000	5 in 100,000,000
Cervical Cancer			
Eye	34 +/- 2 (each)	NA	NA
Brain	9 +/- 6	2 in 10,000	9 in 100,000
Thyroid	44.5 +/-.05	2 in 10,000	5 in 10,000
Lung	0.5 +/- .1 (each)	1 in 100,000	1 in 100,000
Thymus	8.0 +/- .2	2 in 10,000	8 in 100,000
Esophagus	1.83 +/- .02	4 in 100,000	2 in 100,000
Liver	0.221 +/- .005	2 in 10,000,000	2 in 10,000,000
Chest Abdomen Pelvis Scan			
Adrenals/Gall Bladder	26.90 +/- 0.03	6 in 10,000	3 in 10,000
Brain	0.29 +/- 0.02	6 in 1,000,000	3 in 1,000,000
Colon	22.3 +/- 0.7	2 in 10,000	8 in 100,000
Esophagus	25 +/- 1	5 in 10,000	3 in 10,000
Eye	0.50 +/- 0.02 (each)	NA	NA
Kidney	24.2 +/- 0.5 (each)	5 in 10,000	3 in 10,000
Liver	26.0 +/- 0.2	5 in 10,000	2 in 100,000
Lung	27 +/- 1 (each)	7 in 10,000	6 in 10,000
Pancreas	25.9 +/- 0.4	5 in 10,000	3 in 10,000
Thymus	23.5 +/- 0.3	5 in 10,000	2 in 10,000
Thyroid	12.3 +/- 0.4	5 in 100,000	1 in 10,000
Uterus	25.6 +/- 0.1	5 in 100,000	1 in 100,000
Chest Scan			
Adrenals/Gall Bladder	4.92 +/- 0.02	1 in 10,000	5 in 100,000
Brain	0.26 +/- 0.01	5 in 1,000,000	3 in 1,000,000
Colon	0.134 +/- 0.006	1 in 1,000,000	5 in 10,000,000
Esophagus	12.5 +/- 0.2	3 in 10,000	1 in 10,000
Eye	0.29 +/- 0.02	NA	NA
Kidney	2.16 +/- 0.03 (each)	4 in 100,000	2 in 100,000

Liver	11.1 +/- 0.1	1 in 100,000	1 in 100,000
Lung	10 +/- 4 (each)	2 in 10,000	2 in 10,000
Pancreas	2.43 +/- 0.03	5 in 100,000	3 in 100,000
Thymus	13.1 +/- 0.4	3 in 10,000	1 in 10,000
Thyroid	8.3 +/- 0.7	3 in 100,000	9 in 100,000
Uterus	0.112 +/- 0.003	2 in 10,000,000	4 in 100,000,000
Thoracic Spine Scan			
Adrenals / Gall Bladder	8.9 +/- 0.2	2 in 10,000	9 in 100,000
Brain	0.17 +/- 0.07	4 in 1,000,000	2 in 1,000,000
Colon	0.36 +/- 0.009	3 in 1,000,000	1 in 1,000,000
Esophagus	8.8 +/- 0.2	2 in 10,000	9 in 100,000
Eye	0.19 +/- 0.02	NA	NA
Kidney (each)	7.6 +/- 0.2	2 in 10,000	8 in 100,000
Liver	9.3 +/- 0.2	9 in 1,000,000	8 in 1,000,000
Lung (each)	9.5 +/- 0.8	2 in 10,000	2 in 10,000
Pancreas	7.5 +/- 0.2	2 in 10,000	8 in 100,000
Thymus	7.7 +/- 0.2	2 in 10,000	8 in 100,000
Thyroid	2.87 +/- 0.07	1 in 100,000	3 in 100,000
Uterus	0.44 +/- 0.01	8 in 10,000,000	2 in 10,000,000
Lumbar Spine Scan			
Adrenals/Gall Bladder	18.0 +/- 0.4	4 in 10,000	2 in 10,000
Brain	0.0378 +/- 0.0009	8 in 10,000,000	4 in 10,000,000
Colon	11.6 +/- 0.3	1 in 10,000	4 in 100,000
Esophagus	1.36 +/- 0.03	3 in 100,000	1 in 100,000
Eye (each)	0.069 +/- 0.001	NA	NA
Kidney	16.4 +/- 0.4 (each)	3 in 10,000	2 in 10,000
Liver	16.0 +/- 0.4	2 in 100,000	1 in 100,000
Lung	9.7 +/- 0.5 (each)	2 in 10,000	2 in 10,000
Pancreas	17.3 +/- 0.4	4 in 10,000	2 in 10,000
Thymus	0.39 +/- 0.01	8 in 1,000,000	4 in 1,000,000
Thyroid	0.190 +/- 0.005	8 in 10,000,000	2 in 1,000,000
Uterus	14.8 +/- 0.4	3 in 100,000	6 in 1,000,000

Table 65. Estimation of cancer incidence and mortality for each trauma scan for a male age 30 patient.

Specific Organ Doses and Lifetime Attributable Risks to a 30-year old reference Male			
Organ	Measured (Dude) Absorbed Dose	LAR Cancer Incidence (for	LAR Cancer Mortality (for

	(mGy)	those organs not explicitly listed, the category OTHER was used)	those organs not explicitly listed, the category OTHER was used)
Brain Scan			
Eye	22.9 +/- 0.7	NA	NA
Brain	21 +/- 1	4 in 10,000	2 in 10,000
Thyroid	0.8 +/- 0.2	7 in 10,000,000	8 in 1,000,000
Lung	0.2 +/- 0.1	2 in 1,000,000	2 in 1,000,000
Thymus	0.26 +/- 0.01	5 in 1,000,000	2 in 1,000,000
Esophagus	0.680 +/- 0.007	1 in 100,000	6 in 1,000,000
Liver	0.04 +/- 0.02	9 in 100,000,000	6 in 100,000,000
Cervical Cancer			
Eye	18.6 +/- 0.7	NA	NA
Brain	7 +/- 4	1 in 10,000	7 in 100,000
Thyroid	21 +/- 1	2 in 100,000	2 in 10,000
Lung	4 +/- 3	4 in 100,000	4 in 100,000
Thymus	14.2 +/- 0.2	3 in 10,000	1 in 10,000
Esophagus	13.5 +/- 0.2	3 in 10,000	1 in 10,000
Liver	0.6 +/- 0.4	1 in 1,000,000	1 in 1,000,000
Chest Abdomen Pelvis Scan			
Adrenals/Gall Bladder	27.9 +/- 0.4	6 in 10,000	3 in 10,000
Brain	0.7 +/- 0.3	1 in 100,000	7 in 1,000,000
Colon	28 +/- 5	4 in 10,000	4 in 10,000
Esophagus	22.1 +/- 0.4	4 in 10,000	2 in 10,000
Eye	0.74 +/- 0.08	NA	NA
Kidney	24.2 +/- 0.8 (each)	5 in 10,000	2 in 10,000
Liver	26.3 +/- 0.9	5 in 1,000,000	5 in 1,000,000
Lung	24 +/- 1 (each)	3 in 10,000	3 in 10,000
Pancreas	28.5 +/- 0.2	6 in 10,000	3 in 10,000
Thymus	27.0 +/- 0.5	5 in 10,000	3 in 10,000
Thyroid	30.2 +/- 0.8	3 in 10,000	3 in 100,000
Testes	8 +/- 4	2 in 10,000	8 in 100,000
Chest Scan			
Adrenals/Gall Bladder	3.90 +/- 0.04	8 in 100,000	4 in 100,000
Brain	0.5 +/- 0.2	1 in 1,000,000	5 in 1,000,000
Colon	0.20 +/- 0.01	3 in 1,000,000	3 in 1,000,000
Esophagus	20.5 +/- 0.3	4 in 10,000	2 in 10,000
Eye	0.61 +/- 0.09	NA	NA
Kidney	2.8 +/- 0.7 (each)	6 in 100,000	3 in 100,000
Liver	14 +/- 9	3 in 1,000,000	3 in 1,000,000

Lung	22.6 +/- 0.7 (each)	2 in 10,000	2 in 10,000
Pancreas	5.62 +/- 0.08	1 in 10,000	5 in 100,000
Thymus	27.2 +/- 0.4	5 in 10,000	3 in 10,000
Thyroid	25 +/- 2	2 in 100,000	2 in 100,000
Testes	0.045 +/- 0.006	1 in 1,000,000	4 in 10,000,000
Thoracic Spine Scan			
Adrenals / Gall Bladder	7.3 +/- 0.1	1 in 10,000	7 in 100,000
Brain	0.6 +/- 0.3	1 in 100,000	5 in 1,000,000
Colon	0.38 +/- 0.02	5 in 1,000,000	5 in 1,000,000
Esophagus	20.0 +/- 0.3	4 in 10,000	2 in 10,000
Eye	0.7 +/- 0.1	NA	NA
Kidney (each)	5 +/- 1	1 in 10,000	5 in 100,000
Liver	20 +/- 4	4 in 1,000,000	4 in 1,000,000
Lung (each)	22.9 +/- 0.8 (each)	2 in 10,000	2 in 10,000
Pancreas	14.0 +/- 0.2	3 in 10,000	1 in 10,000
Thymus	27.4 +/- 0.5	5 in 10,000	3 in 10,000
Thyroid	25 +/- 3	2 in 100,000	2 in 100,000
Testes	0.064 +/- 0.004	1 in 1,000,000	6 in 10,000,000
Lumbar Spine Scan			
Adrenals/Gall Bladder	22.3 +/- 0.9	4 in 10,000	2 in 10,000
Brain	0.033 +/- 0.009	6 in 10,000,000	3 in 10,000,000
Colon	22 +/- 3	3 in 10,000	3 in 10,000
Esophagus	0.227 +/- 0.006	4 in 1,000,000	2 in 1,000,000
Eye (each)	0.07 +/- 0.01	NA	NA
Kidney	18.7 +/- 0.8 (each)	4 in 10,000	2 in 10,000
Liver	13 +/- 1	3 in 1,000,000	3 in 1,000,000
Lung	2 +/- 1	2 in 100,000	2 in 100,000
Pancreas	21.1 +/- 0.3	4 in 10,000	2 in 10,000
Thymus	0.290 +/- 0.006	6 in 1,000,000	3 in 1,000,000
Thyroid	0.177 +/- 0.009	2 in 10,000,000	2 in 10,000,000
Testes	2.07 +/- 0.01	4 in 100,000	2 in 100,000

Discussion

Although the two different methods for estimating the effective dose per scan is not consistent, the Ht/Wt model agrees with current literature which states that the DLP-CC is known to underestimate the effective dose per scan [66, 286, 291-292]. Utilizing Bland-Altman [285, 290] plots to compare two measures allows us to determine whether or not the two measures can be used interchangeably. When the values for the difference between the two methods lie within 2 standard deviations of the mean, either method can be used. Therefore, since the Bland-Altman plots for all six trauma protocols showed values for the difference between the two methods being within +/- 1.96 SD then either method can be used.

The American Association of Physicists in Medicine (AAPM) advocates the use of estimating the value of the effective dose by means of the DLP and conversion coefficients [286]. In fact, the AAPM purports that the values estimated by DLP and the calculations by more rigorous methods are consistent with maximum deviation from the mean of 15% [286]. However, this method of effective dose estimation requires knowledge of the machine technique (DLP) and ensuring that the scanning ranges of the patient and the mathematical phantom are similar. Real patient scans, especially for the chest scan, are often different than the scans on stylized mathematical phantoms due to either the anatomy of the individual patient or the CT technician's ability to localize the scan range based off of the scout images. This was observed by the strong positive bias in the Bland-Altman plot of the chest scan. The positive bias indicates that the model will systematically result in higher effective dose values for the chest scan. When we compare the scanning range for calculating the effective dose using the DLP method against our predictive model (Figure 40), we see that the positive bias is primarily due to the difference in how we account for patient variability as opposed to the machine technique variability (DLP method).

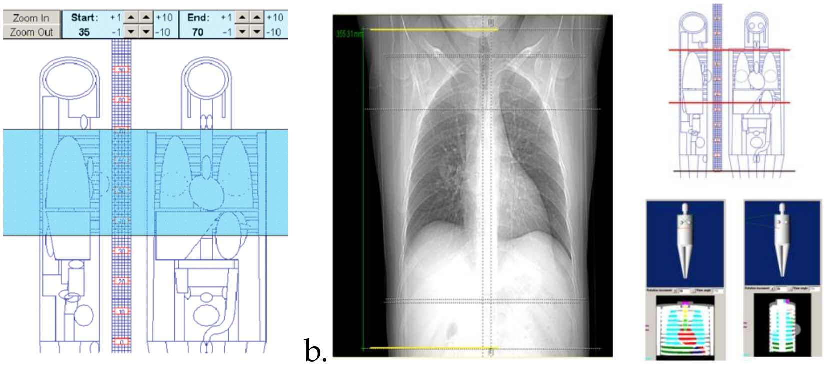

a. b.

Figure 40. Comparison of scanning areas for the chest scan. (40a) Mathematical phantom and scanning range used to calculate the effective dose conversion coefficient [66]. (40b) Representative patient scan and mathematical phantom scanning areas used in model development.

Literature shows that experimental measurements of effective dose will often be higher than DLP-conversion coefficient methods for calculating effective dose because DLP-conversion coefficient methods can underestimate the effective dose by up to 37% [274, 291-292].

Li et al [293] estimates that the use of DLP and conversion coefficients can underestimate the effective dose by 30% to 48% when compared against a hybrid computational full body computer model of an infant and 12-year old pediatric patient. Li also points out that the effective dose to both patients from an abdomen pelvis scan is nearly double that from a chest scan as a result of higher technique values (kVp and/or mA) and a larger irradiated body volume.

Part of the reason for this difference in estimation is that conversion factors are dependent upon the size of the phantom used and the scanning length [66]. DLPs also can underestimate the total energy imparted over the scanning length [286]. When scanning lengths are increased or decreased organs are either brought into the scanning field-of-view or removed from the scanning field-of-view. For scanning regions which include fewer major organs (brain scan and cervical spine scan), differences between various methods of calculating effective doses results from dimensional differences between phantoms and patients. These differences can range from 17-25% for brain CT scans to 15-19% for neck and face examinations [294].

Variations between physical phantoms and computer will yield the smallest difference in organ dose when either organs that are small in volume and can be easily represented by an averaged point dose estimate, or for those large organs which receive a fairly uniform absorbed dose throughout its volume, or when the organ is large but receives a properly volume averaged absorbed dose gradient [250].

Since the DLP-conversion coefficient method of calculating the effective dose will typically underestimate the effective dose when compared to an organ dose-based effective dose method, the Ht/Wt model is a more accurate means of assessing the estimate of the effective dose per trauma procedure based upon a patient’s height and weight at the time of the scan. Additionally, the predictive model was developed for a wide range of heights and weights. On the contrary, the DLP-conversion coefficient method depends upon machine parameters and a singular mathematical standard-sized phantom.

Ultimately, effective dose describes the relationship between the probability of stochastic effects and equivalent dose. Effective dose represents the total health detriment from uniform radiation to the whole body by summing all the tissues and organs in the body [32]. As a result of the increased use of diagnostic scans and the use of multiple scans on an individual patient, the general radiology and research community has become more aware and concerned with long term consequences of the increased doses to patients [14]. While radiation-induced cancers are not thought to be risk from general diagnostic radiology, researchers are becoming more concerned and aware of accumulated dose from multiple diagnostic scans. BEIR VII [29] can be used to calculate estimates of the probability of cancer incidence and mortality [19, 21, 295-297]. BEIR VII reports that the probability of cancer incidence decreases with age (Figure 41).

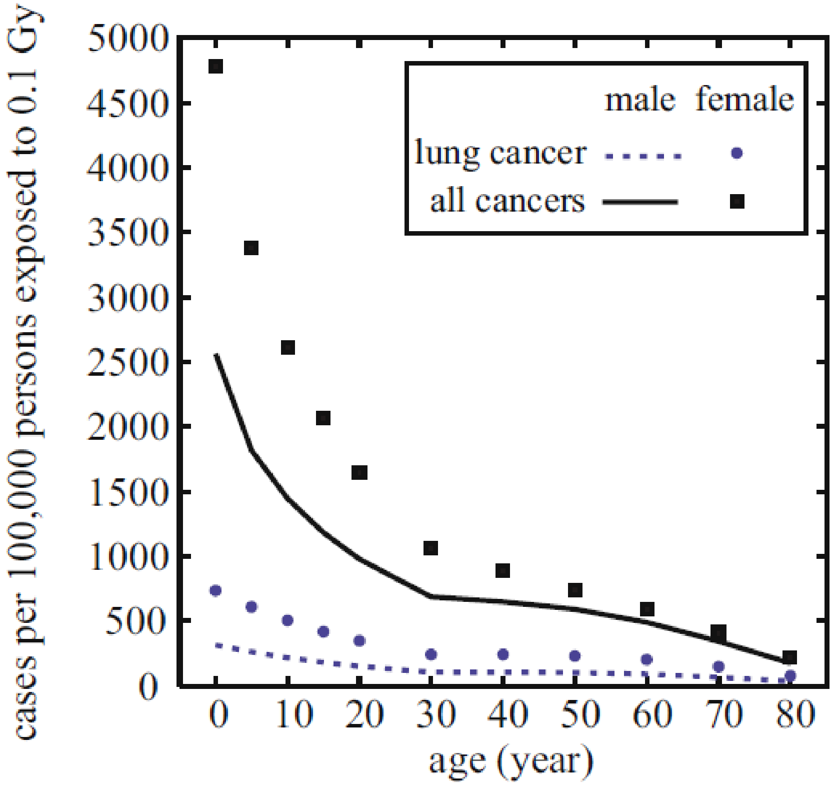

Figure 41. Lifetime cancer mortality risks as a function of age at exposure based on updated atomic bomb survivor data as reported in BEIR VII [29] (Courtesy of Li et al [293]).

Part of the reason for this decreasing susceptibility is the relatively long latency period between the health detriment and the manifestation of the disease. As a result, pediatrics will have the greatest probability of cancer (4 to 5 times) incidence than an adult. The U.S. Army population falls within the age framework older than a pediatric but young for an adult.

The American Cancer Society estimates that the risk of developing a cancer (all cancers) is 37.76 per 100 or approximately 1 in 3. Additionally, the risk of dying from a cancer is 19.58 per 100 or approximately 1 in 5 [298]. BEIR VII estimates that for a single dose of radiation, 0.1 Gy, a male of age 30 will have a 6 in 100 chance of cancer incidence (all cancers) with a 3 in 100 chance of dying from cancer (all cancers). The probability of incidence and mortality actually increases for a female receiving the same dose. This was shown in Tables 65 and 66 for a female and male Soldier respectively. The probability of incidence for all cancers increases to 10 in 100 and the probability of dying from a cancer (all cancers) increases to 5 in 100.

We can see that for each scan (Tables 65 and 66), the estimation of cancer incidence and mortality is relatively low and the benefit of the scan as opposed to the risk is very high. The next chapter will illustrate how a Soldier involved in a traumatic experience can undergo multiple scans and that the accumulation of dose is not trivial.

CHAPTER 7. Specific Aim 5: Recommend action points for the U.S. Army based upon this research.

There is concern about the potential health effect of repeated CT scan exposures and studies have shown that the lifetime cancer mortality risks from CT scans are not negligible [19, 21, 297]. The scientific community remains divided on the long-term health effects of CT radiation dose, primarily because few studies of populations exposed to CT are available. There is no debate though about how the diagnostic information from justified CT scans contributes to saving the lives of thousands of people on a daily basis.

Ultimately, reducing radiation dose to the patient is the goal while still obtaining appropriate diagnostic images. Previous dose reduction techniques have focused on adjusting for patient size and machine scanning characteristics while innovations in x-ray beam collimation, filters, image processing algorithms, automatic tube current modulation, and more efficient detector configuration have led to systemic dose reduction [299-302]. However, a common dose reduction technique, limitation of scanning length, is not a luxury that physicians have when triaging patients of whole body trauma.

Being able to establish any association between low-dose radiation and long term health effects hinges not only on the statistical model used but also on how the study is designed and employed. This is particularly important in the recommendation for a future study. U.S. Army Soldiers change duty stations frequently over the course of their career in the Armed Forces. As such, the Army Medical Department interlinks all the hospitals through a system called the Armed Forces Health Longitudinal Technology Application (AHLTA).

Currently, almost all Soldier medical records are maintained digitally in AHLTA. Military medical professionals have access to AHLTA in order to assess Soldier clinical information. There are also efforts being made towards ensuring a seamless transition of Soldier medical information from when a Soldier is on active duty to when a Soldier is seen by the Veterans Administration hospitals.

The majority of epidemiologic radiation effect studies are ecologic (based upon population comparisons) and as such causal inferences cannot be made since confounding factors or selection bias cannot be controlled. The following discussion will show how effective doses can be used in future studies. Previous radiation cohort studies involved occupationally exposed workers who potentially receive more radiation (up to 0.05 mSv per year) than the normal population yet still have relatively low exposure to radiation. Trauma patients can easily experience more than this amount of radiation [303-305].

Need for Study (Example)

The following is a hypothetical (but not atypical) scenario.

While deployed to a remote outpost in Afghanistan in support of Operation Enduring Freedom, a 25-year old male Soldier was in a tactical vehicle convoying from one location to another. Half-way through the convoy trip, the lead vehicle stopped in order to investigate an unusual section of the dirt road. Unfortunately the rest of the convoy stopped in what is referred to as a kill zone. Improvised explosive devices (IEDs) had been dug into the road where the convoy now stopped. The IEDs were remotely detonated by wireless communication signals (often in the form of cell phones) and the vehicle containing the Soldier was hit in the underbelly. Shrapnel and explosives were sent flying into and through the vehicle killing one occupant and severely injuring the Soldier and the driver of the vehicle. During the blast, the Soldier was thrown violently against the restraining harness (seat belt) and severely hit his head against both the side bullet proof window and the windshield. Other Soldiers in the convoy immediately laid down suppressive fire against the enemy and the combat medics initiated first aid to the wounded. After securing the zone by running off the enemy combatants, helicopter evacuation was called for and when arrival seemed imminent the evacuation of the wounded Soldier commenced to the forward support hospital located 40 miles away. The Soldier, while unconscious, was evacuated via the helicopter and received immediate emergency medical attention at the forward support hospital. While the Soldier’s vital signs were stabilized, the Army physicians noticed lower leg fractures and suspected severe internal bleeding. CTs were ordered in order to better assess the extent of the injuries. The Soldier received two chest-abdomen-pelvis scans (ordered to assess the internal bleeding), one cervical spine scan (ordered to assess any cervical spine damage), and since the on-site combat medics noticed cracks in the windshield and the side window, a brain scan was ordered to assess any potential brain injury. A total of four CT scans were ordered in the first 6-hours following the IED explosion. 12-hours after the explosion, the Soldier was evacuated back to Balad Air Field in Iraq where the next higher level of medical assistance could be obtained. Either the diagnostic images were too damaged in transit or they never reached the attending physicians at Balad. As a result, the physicians immediately ordered a chest-abdomen-pelvis scan, another cervical spine scan, and a brain scan. The scans were also ordered to assist in the initial diagnosis while the swelling from the internal damage obfuscated the injury extent. The Soldier was then evacuated back to Landstuhl Regional Medical Center in Kaiserslautern, Germany for further evacuation coordination could be initiated to fly the Soldier back to Walter Reed Medical Center in Silver Springs, Maryland. While at Landstuhl Regional Medical Center the Soldier received another chest-abdomen-pelvis scan in order to ensure that the internal bleeding was stabilized enough for evacuation to Walter Reed. The Soldier remained at Walter Reed Medical Center for more than 4 weeks and underwent three surgical operations designed to assist in the healing of wounds received in the lumbar spine (from shrapnel coming through the floor board in the vehicle) and the chest area (from flying debris caused by explosions coming up through the radio area). Diagnostic imaging was performed in order to assist the surgeons in their preparations and during follow-up (2 chest scans (with and without contrast), 2 lumbar spine scans (with and without contrast), and 2 brain scans (with and without contrast)). During the rehabilitation which occurred over the course of the next year three more brain scans were performed to help with assessing the traumatic brain injury and two more spinal scans were performed (one lumbar spine scan and one thoracic spine scan). A total of 19 scans were performed for this one traumatic event (seven brain scans, two cervical spine scans, four chest-abdomen-pelvis scans, two chest scans, one thoracic spine scan, and three lumbar spine scans). While the Soldier was still in the operational theater (Afghanistan and Iraq), CT machine techniques from the CT scanning machines were not collected. Scanning information from the CT machines is only known from the Landstuhl Regional Medical Center and Walter Reed Regional Medical Center. Table 67 is a list of retrospective effective doses from the computed tomography scans.

Table 66. Dose estimation for the above 19 scans.

Location	Scanning Types	Assigned Effective Dose (mSv)
Forward Support Hospital in Afghanistan	2-CAP	34 (2 x 10 (average for Ab-Pel), and 2 x 7 (average for chest))
	1-CS	6 (average for c-spine)
	1-Brain	2 (average for head)
Combat Support Hospital in Balad, Iraq	1-CAP	17 (based on above)
	1-CS	6 (same as above)
	1-Brain	2 (same as above)
Landstuhl Regional Medical Center	1-CAP	18 (based upon average of CAP patients in validation study using DLP method)
Walter Reed Regional Medical Center	2-Chest	15.6 (2 x 7.8 (average of chest patients in validation study using DLP method)
	3-Lumbar	39 (3 x 13 (average of lumbar patients in validation study using DLP method))
	5-Brain	8 (5 x 1.6 (average of Brain patients in validation study using DLP method)
	1-Thoracic	15.3 (average of thoracic patients in validation study using DLP method)
19 Total Scans		**Total Effective Dose = 123 mSv**

Assuming that the CT ranges used are similar to ranges used in the model development, and assuming that no other information is known except for the Soldier’s height and weight measured at the beginning of the deployment (6’2” (188 cm) and 200 lbs (91 kg)) and noting that the Soldier gained 10 pounds while at Walter Reed (6’2” (188 cm) and 210 lbs (96 kg)), the total effective dose is shown (Table 68).

Table 67. Ht/Wt predictive model dose estimation for the above 19 scans.

Location	Scanning Types	Ht/Wt Modeled Effective Dose (mSv)

Forward Support Hospital in Afghanistan	2-CAP	54 (2 x 27.12)
	1-CS	2.36
	1-Brain	1.6
Combat Support Hospital in Balad, Iraq	1-CAP	27.12
	1-CS	2.36
	1-Brain	1.6
Landstuhl Regional Medical Center	1-CAP	27.12
Walter Reed Regional Medical Center (assume new ht/wt)	2-Chest	21.26 (2 x 10.63)
	3-Lumbar	32.71 (3 x 10.90)
	5-Brain	7.84 (5 x 1.57)
	1-Thoracic	13.14
19 Total Scans		**Total Effective Dose ≈ 200 mSv**

The Ht/Wt model estimates an accumulated effective dose 47% higher than by estimating the effective dose using DLP-conversion coefficients and standard NCRP effective dose values. Assuming that the total effective dose from the 19 total scans over the course of one year can be modeled as a single acute dose, the BEIR VII excess relative risk (ERR) for solid cancer incidence can be modeled, where ERR *is defined as the rate of the disease in an exposed population divided by the rate of disease in an unexposed population minus 1.0* [29].

Figure 42 presents how the age-time patterns in the radiation-associated risks for all solid cancer mortality is different for a male Soldier who received an exposure of 123 mSv at age 25 opposed to that same Soldier receiving an exposure of 200 mSv at age 25. The initial ERR reflects the exposure of 200 mSv which is 62% higher than an exposure of 123 mSv.

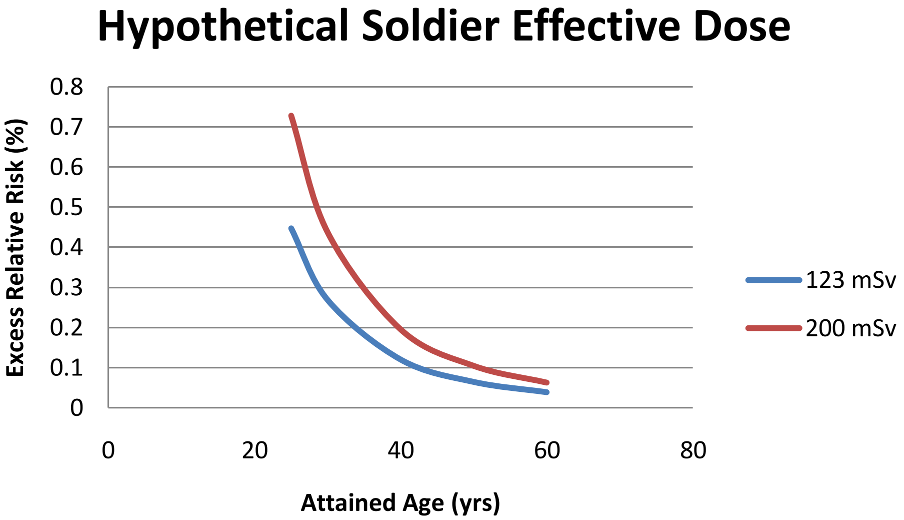

Figure 42. Hypothetical Soldier effective dose chart showing how the ERR decreases over time but is greater for a higher initial effective dose. Age-time patterns represent the radiation-associated risks for all solid cancer mortality.

The effective dose study was conducted for one hypothetical situation. However, many Soldiers have been on multiple deployments and could have sustained wounds which resulted in evacuation multiple times. This type of situation while not frequent is not rare especially with Special Operations personnel. Spinal injuries are on the rise [306] as are traumatic brain injuries [116, 307-310]. Therefore, developing and utilizing the predictive model for specific trauma scans will better estimate a patient's total effective dose than utilizing standard methods.

Recommendations

BEIR VII states that future medical radiation studies are needed to assist in understanding the effects of low-dose radiation. Organizing a population study within an Army population will help to achieve some of the aims stated in BEIR VII Research Need 8 [29]. One of the primary limitations to studying radiation-cancer as an outcome is that the latent period of cancer development can be up to 20 years. However, with a Soldier population, this study period is possible because subjects can be tracked through both the Army medical system and the Veterans Affairs hospital system.

Population studies are fairly common with research using Veterans Affairs (VA) hospitals and military subjects. In other populations, management difficulties can arise because people die, move away, or develop other medical conditions. A Soldier population may be followed with minimal disruptions as long as Soldiers are observed in an Army or VA medical facility. Difficulty will arise of a Soldier is sent to a civilian hospital for treatment and diagnostic scans are not properly inputted into the Soldier's medical records. Special procedures should be put into place to account for this common occurrence.

Medical records should be adjusted to account for the total number of diagnostic scans that are performed not just inputs for the best diagnostic scan performed. For example, if two CT scans are performed in order to get one diagnostic quality image, then there needs to be input variables for the first scan (which didn't yield a diagnostic quality image) in order to track the dose. Although the PACS system archives the patient images, there are still patient image records which do not include a dose report which reflects the scanning range, CTDIvol, and DLP. Therefore, the Ht/Wt models should be used to estimate the effective dose for appropriate scanning procedures.

Research Implications

Soldiers are receiving higher effective dose per scan than is currently being reported in literature. This has been shown in the preceding dissertation chapters. Even though it looks as though increased weight provides somewhat of a shielding effect, CT machines can automatically adjust for changes in tissue density and thickness of tissue in order to achieve a certain diagnostic picture quality. Therefore, heavier patients (thus greater cross-sectional area per slice thickness) will actually get higher doses. The Ht/Wt models do not account for higher entrance skin doses since only one entrance skin dose value was used for modeling the radiation dose of all 100 mathematical phantoms modeled. What we see from the above hypothetical example is that the predictive model predicts a total effective dose 47% higher than using standard methods. Potentially, the total effective dose may be another 10%-20% higher than the predictive model estimation. Therefore, for patients receiving multiple diagnostic CT scans, absorbed doses are indeed an area of concern and researchers should emphasize investigations of low-dose radiation effects on the human body.

Research Needs

The research predictive models could be improved upon with further research. Further research is needed to collect experimental absorbed dose information on a wide variety of CT machines and CT manufacturers. While the predictive model is an accurate estimate of the absorbed dose, further experiments will shrink errors that lead to a lack of precision. Experiments can be performed at large medical facilities which have different types of machines/manufacturers. Once absorbed dose data has been collected for both the male and female reference phantom, the predictive model should be adjusted as necessary and then validated against a patient population with the largest number of patients possible. Effective dose estimation of pediatric patients is also important since Army combat support hospitals will often treat pediatric patients from the host nation [311]. Theocharopoulus et al [197] determined that even though pediatric patients absorb less energy per scan, the effective dose is up to 24% higher than adult patients.

CHAPTER 8: Conclusion

The goal of this study was to develop predictive models for estimating the effective dose from common CT scans that are used to diagnose and assist in the rehabilitative efforts of Soldiers who have experienced traumatic injuries while serving Operation Iraqi Freedom and Operation Enduring Freedom, as well as future such activities. The hypothesis examined is the extent to which a patient's height and weight is associated with the effective dose from CT scans. My models are more accurate than current methods for estimating effective dose based upon CT machine parameters and conversion coefficients. Additionally, my models can be used as a means of estimating the effective dose when machine parameters are not known. My models support recent literature which states that current effective dose estimating methods appear to underestimate the accumulated effective doses from multiple CT diagnostic scans.

Conference presentations to appropriate professional societies are planned in order to share this research and associated results with the greater health physics community. The research results will also be presented to authorities in the U.S. Army medical system. These presentations will be conducted with the senior Army health physicists and other senior officers within the Army's Environmental, Safety, and Occupational Health community.

My research was unique in four different areas: specific focus on a U.S. Army Soldier population involved in defense of our Country through involvement in Operation Iraqi Freedom and Operation Enduring Freedom, predictive models designed to estimate the effective dose from six specific trauma protocols based off of patient heights and weights, verification of models using specifically designed anthropomorphic phantoms for use with OSL dosimeters, and validation of results against a pilot study of trauma patient representative CT scans.

Specific areas for continuation of this research include verification of the predictive models with a wider variety of CT machine types and manufacturers. Additionally, more research should be conducted into the establishment of long-term cohorts as requested in BEIR VII for low-dose medical radiation health effects.

I am extremely thankful and appreciative of the dedicated Army physicians, surgeons, and medical staff for their efforts in saving the lives of our American heroes.

Bibliography

1. Defense, Department of. [cited 2009 May 16, 2009]; Casualty Statistics]. Available from: <http://siadapp.dmdc.osd.mil/personnel/CASUALTY/castop.htm>.
2. Eastridge, B.J., et al., *Trauma system development in a theater of war: Experiences from Operation Iraqi Freedom and Operation Enduring Freedom.* J Trauma, 2006. **61**(6): p. 1366-72; discussion 1372-3.
3. Montgomery, S.P., C.W. Swiecki, and C.D. Shriver, *The evaluation of casualties from Operation Iraqi Freedom on return to the continental United States from March to June 2003.* J Am Coll Surg, 2005. **201**(1): p. 7-12; discussion 12-3.
4. Tanielian, T.J., Lisa H., *Invisible Wounds of War: Psychological and Cognitive Injuries, Their Consequences, and Services to Assist Recovery*, R.C.C.f.M.H.P. Research, Editor 2008, RAND Corporation: Santa Monica.
5. Covey, D.C., *From the frontlines to the home front. The crucial role of military orthopaedic surgeons.* J Bone Joint Surg Am, 2009. **91**(4): p. 998-1006.
6. Born, C.T., et al., *Disasters and mass casualties: II. explosive, biologic, chemical, and nuclear agents.* J Am Acad Orthop Surg, 2007. **15**(8): p. 461-73.
7. Holcomb, J.B., et al., *Understanding combat casualty care statistics.* J Trauma, 2006. **60**(2): p. 397-401.
8. Murray, C.K., et al., *Spectrum of care provided at an echelon II Medical Unit during Operation Iraqi Freedom.* Mil Med, 2005. **170**(6): p. 516-20.
9. Tien, H., et al., *Radiation exposure from diagnostic imaging in severely injured trauma patients.* J Trauma, 2007. **62**(1): p. 151-6.
10. Kim, P.K., et al., *Cumulative radiation dose caused by radiologic studies in critically ill trauma patients.* Journal of Trauma - Injury, Infection and Critical Care, 2004. **57**(3): p. 510-514.
11. Sodickson, A., et al., *Recurrent CT, cumulative radiation exposure, and associated radiation-induced cancer risks from CT of adults.* Radiology, 2009. **251**(1): p. 175-84.
12. Directorate of Combat and Doctrine Support, *Operational Branch Concept Combat Health Support*, 1994, U.S. Army Medical Department Center and School: Fort Sam Houston, Texas.
13. Army, Department of the, *Field Manual 8-10, Health Service Support in a Theater of Operations*, 1991.
14. National Council on Radiological Protection and Measurements, *Ionizing radiation exposure of the population of the united states.* NCRP Report, (160).
15. *Madigan Army Medical Center Clinical Practice Guidelines*. 2010 [cited 2010 28 October]; Available from: http://www.mamc.amedd.army.mil/Clinical/standards/list_specialty.htm.

16. Beekley, A.C., *Mass casualties in combat: lessons learned.* J Trauma, 2007. **62**(6 Suppl): p. S39-40.
17. Scott, A., *Personal Email with MAJ Andrew Scott, U.S. Army Radiation Safety Officer in Iraq*, R. Prins, Editor 2009.
18. Powell, B. *Trauma hospital in Afghanistan provides state-of-the-art medical service*. 2010 [cited 2010 25 October]; Available from: http://www.army.mil/-news/2010/10/01/45679-trauma-hospital-in-afghanistan-provides-state-of-the-art.
19. Hall, E.J. and D.J. Brenner, *Cancer risks from diagnostic radiology.* Br J Radiol, 2008. **81**(965): p. 362-78.
20. *The 2007 Recommendations of the International Commission on Radiological Protection. ICRP publication 103.* Ann ICRP, 2007. **37**(2-4): p. 1-332.
21. Brenner, D.J. and C.D. Elliston, *Estimated radiation risks potentially associated with full-body CT screening.* Radiology, 2004. **232**(3): p. 735-8.
22. Griffey, R.T. and A. Sodickson, *Cumulative radiation exposure and cancer risk estimates in emergency department patients undergoing repeat or multiple CT.* AJR Am J Roentgenol, 2009. **192**(4): p. 887-92.
23. Hall, E.J., *Lessons we have learned from our children: cancer risks from diagnostic radiology.* Pediatr Radiol, 2002. **32**(10): p. 700-6.
24. Keen, C.E., *FDA launches initiative to rein in medical radiation*, in *AuntMinnie.com*2010.
25. Hall, P.F., *Cancer risks after medical radiation.* Med Oncol Tumor Pharmacother, 1991. **8**(3): p. 141-5.
26. Mettler, F.A., Jr., et al., *Effective doses in radiology and diagnostic nuclear medicine: a catalog.* Radiology, 2008. **248**(1): p. 254-63.
27. Prokop, M., *Cancer screening with CT: dose controversy.* Eur Radiol, 2005. **15 Suppl 4**: p. D55-61.
28. Ron, E., *Cancer risks from medical radiation.* Health Phys, 2003. **85**(1): p. 47-59.
29. Council, N.R., *Health Risks from Exposure to Low Levels of Ionizing Radiation: BEIR VII Phase 2*, 2006, National Academies Press: United States of America.
30. Rossi, H.H. and M. Zaider, *Microdosimetry and Its Applications*1996, Berlin: Springer.
31. *ICRU Report 51, Quantities and Units in Radiation Protection Dosimetry*, International Commission on Radiation Units and Measurements, Editor 1993: Bethesda.
32. *Quantities used in radiological protection.* Annals of the ICRP, 1991. **21**(1-3): p. 4-11.
33. Drexler, G., et al., *Effective dose--how effective for patients?* Radiat Environ Biophys, 1993. **32**(3): p. 209-19.
34. Bushberg, J.S., J. Anthony; Leidholdt, Edwin M.; Boone, John M., *The Essential Physics of Medical Imaging*. 2nd Edition ed2001: Lippincott Williams & Wilkins. 933.

35. Analogic. *Computed Tomography Equipment*. 2010 [cited 2010 21 December]; Available from: http://www.analogic.com/products-medical-computer-tomography.htm.
36. He, W., et al., *Patient doses and projection angle in cone beam CT.* Medical Physics, 2010. **37**(5): p. 2359-2368.
37. Nikolic, B., et al., *Absorbed radiation dose in radiosensitive organs during coronary CT angiography using 320-MDCT: Effect of maximum tube voltage and heart rate variations.* American Journal of Roentgenology, 2010. **195**(6): p. 1347-1354.
38. Israel, G.M., et al., *Patient size and radiation exposure in thoracic, pelvic, and abdominal CT examinations performed with automatic exposure control.* American Journal of Roentgenology, 2010. **195**(6): p. 1342-1346.
39. *LightSpeed Series Technical Reference Manual*, G.M. Systems, Editor 2005.
40. Axelsson, B., J. Persliden, and P. Schuwert, *Dosimetry for computed tomography examination of children.* Radiation Protection Dosimetry, 1996. **64**(3): p. 221-226.
41. Zankl, M., et al., *Organ doses for children from computed tomographic examinations.* Radiation Protection Dosimetry, 1995. **57**(1-4): p. 393-396.
42. Angel, E., et al., *Monte Carlo simulations to assess the effects of tube current modulation on breast dose for multidetector CT.* Physics in Medicine and Biology, 2009. **54**(3): p. 497-511.
43. Caon, M., G. Bibbo, and J. Pattison, *An EGS4-ready tomographic computational model of a 14-year-old female torso for calculating organ doses from CT examinations.* Physics in Medicine and Biology, 1999. **44**(9): p. 2213-2225.
44. DeMarco, J.J., et al., *A Monte Carlo based method to estimate radiation dose from multidetector CT (MDCT): Cylindrical and anthropomorphic phantoms.* Physics in Medicine and Biology, 2005. **50**(17): p. 3989-4004.
45. Jarry, G., et al., *A Monte Carlo-based method to estimate radiation dose from spiral CT: From phantom testing to patient-specific models.* Physics in Medicine and Biology, 2003. **48**(16): p. 2645-2663.
46. Perisinakis, K., A. Tzedakis, and J. Damilakis, *On the use of Monte Carlo-derived dosimetric data in the estimation of patient dose from CT examinations.* Medical Physics, 2008. **35**(5): p. 2018-2028.
47. Stabin, M.G., et al. *Use of MCNP with voxel-based image data for internal dosimetry applications*. in *Monte Carlo 2005 Topical Meeting*. 2005. Chattanooga, TN.
48. Zhang, D., et al., *Variability of surface and center position radiation dose in MDCT: Monte Carlo simulations using CTDI and anthropomorphic phantoms.* Medical Physics, 2009. **36**(3): p. 1025-1038.
49. Chiavassa, S., et al., *Dosimetric comparison of Monte Carlo codes (EGS4, MCNP, MCNPX) considering external and internal exposures of the Zubal phantom to electron and photon sources.* Radiat Prot Dosimetry, 2005. **116**(1-4 Pt 2): p. 631-5.

50. Abella, V., et al., *3D dose distribution calculation in a voxelized human phantom by means of Monte Carlo method.* Applied Radiation and Isotopes, 2010. **68**(4-5): p. 709-713.
51. Li, X., et al., *Patient-specific dose estimation for pediatric chest CT.* Med Phys, 2008. **35**(12): p. 5821-8.
52. Chiou, W.K., et al., *Correlation of the dysmetabolic risk factors with different anthropometric measurements.* Endocr J, 2005. **52**(1): p. 139-48.
53. Fasola, G., et al., *Low-dose computed tomography screening for lung cancer and pleural mesothelioma in an asbestos-exposed population: baseline results of a prospective, nonrandomized feasibility trial--an Alpe-adria Thoracic Oncology Multidisciplinary Group Study (ATOM 002).* Oncologist, 2007. **12**(10): p. 1215-24.
54. Hui, C., et al., *Radiation dose from initial trauma assessment and resuscitation: review of the literature.* Can J Surg, 2009. **52**(2): p. 147-52.
55. Ioppolo, J., et al., *Diagnostic x-ray dosimetry using Monte Carlo simulation.* Phys Med Biol, 2002. **47**(10): p. 1707-20.
56. Kim, M.J., et al., *Multidetector computed tomography chest examinations with low-kilovoltage protocols in adults: effect on image quality and radiation dose.* J Comput Assist Tomogr, 2009. **33**(3): p. 416-21.
57. Mayo, J.R., et al., *CT of the chest: minimal tube current required for good image quality with the least radiation dose.* AJR Am J Roentgenol, 1995. **164**(3): p. 603-7.
58. Son, I.Y., et al., *X-ray imaging optimization using virtual phantoms and computerized observer modelling.* Physics in Medicine and Biology, 2006. **51**(17): p. 4289-4310.
59. Struelens, L., F. Vanhavere, and K. Smans, *Experimental validation of Monte Carlo calculations with a voxelized Rando-Alderson phantom: a study on influence parameters.* Phys Med Biol, 2008. **53**(20): p. 5831-44.
60. van Klaveren, R.J., et al., *Lung cancer screening by low-dose spiral computed tomography.* Eur Respir J, 2001. **18**(5): p. 857-66.
61. Zoetelief, J., et al., *Patient dosimetry for X rays used in medical imaging.* Journal of the ICRU, 2005. **5**(2): p. 1-113.
62. *Conversion coefficients for use in radiological protection against external radiation. Adopted by the ICRP and ICRU in September 1995.* Ann ICRP, 1996. **26**(3-4): p. 1-205.
63. Aldrich, J., A. Bilawich, and J. Mayo, *Radiation doses to patients receiving computed tomography examinations in British Columbia.* Can Assoc Radiol J, 2006. **57**(2): p. 79-85.
64. Aroua, A., et al., *Exposure of the Swiss population by radiodiagnostics: 2003 review.* Health Phys, 2007. **92**(5): p. 442-8.
65. Hatziioannou, K., et al., *A contribution to the establishment of diagnostic reference levels in CT.* Br J Radiol, 2003. **76**(908): p. 541-5.

66. Huda, W., K. Ogden, and M. Khorasani, *Converting dose-length product to effective dose at CT.* Radiology, 2008. **248**(3): p. 995-1003.
67. Huda, W. and K.M. Ogden, *Computing effective doses to pediatric patients undergoing body CT examinations.* Pediatric Radiology, 2008. **38**(4): p. 415-423.
68. Jessen, K.A., et al., *Dosimetry for optimisation of patient protection in computed tomography.* Appl Radiat Isot, 1999. **50**(1): p. 165-72.
69. Li, X., et al., *Patient-specific dose estimation for pediatric chest CT.* Medical Physics, 2008. **35**(12): p. 5821-5828.
70. McCollough, C.H., *CT dose: How to measure, how to reduce.* Health Physics, 2008. **95**(5): p. 508-517.
71. Smith, A., et al., *Radiation dose reduction strategy for CT protocols: successful implementation in neuroradiology section.* Radiology, 2008. **247**(2): p. 499-506.
72. Tartari, S., et al., *Low-dose unenhanced CT protocols according to individual body size for evaluating suspected renal colic: cumulative radiation exposures.* Radiol Med, 2009.
73. Thomas, K.E. and B. Wang, *Age-specific effective doses for pediatric MSCT examinations at a large children's hospital using DLP conversion coefficients: A simple estimation method.* Pediatric Radiology, 2008. **38**(6): p. 645-656.
74. Tsai, H.Y., et al., *Survey of computed tomography scanners in Taiwan: Dose descriptors, dose guidance levels, and effective doses.* Medical Physics, 2007. **34**(4): p. 1234-1243.
75. Deak, P.D., Y. Smal, and W.A. Kalender, *Multisection CT protocols: sex- and age-specific conversion factors used to determine effective dose from dose-length product.* Radiology, 2010. **257**(1): p. 158-66.
76. Los Alamos National Laboratory, *MCNPX Homepage.* [cited 2010 20 December]; Available from: https://mcnpx.lanl.gov.
77. National Research Council Canada, *EGSnrc Home Page*. 2009; Available from: http://www.irs.inms.nrc.ca/EGSnrc/EGSnrc.html.
78. Andreo, P., *Monte Carlo techniques in medical radiation physics.* Phys Med Biol, 1991. **36**(7): p. 861-920.
79. Raeside, D.E., *Monte Carlo principles and applications.* Phys Med Biol, 1976. **21**(2): p. 181-97.
80. Snyder, W.S., et al., *Estimates of absorbed fractions for monoenergetic photon sources uniformly distributed in various organs of a heterogeneous phantom.* Journal of Nuclear Medicine, 1969.
81. Cristy, M., *Mathematical phantoms representing children of various ages for use in estimates of internal dose.* Mathematical Phantoms Representing Children of Various Ages for Use in Estimates of Internal Dose, 1980.
82. Petoussi-Henss, N., et al., *The GSF family of voxel phantoms.* Physics in Medicine and Biology, 2002. **47**(1): p. 89-106.
83. *Basic anatomical and physiological data for use in radiological protection: reference values. A report of age- and gender-related differences in the anatomical and*

physiological characteristics of reference individuals. ICRP Publication 89. Ann ICRP, 2002. **32**(3-4): p. 5-265.
84. Soares, C.G., *Radiochromic film dosimetry.* Radiation Measurements, 2006. **41**(SUPPL. 1).
85. Tartari, S., et al., *Low-dose unenhanced CT protocols according to individual body size for evaluating suspected renal colic: Cumulative radiation exposures.* Protocolli TC diretta a bassa dose in funzione della corporatura del paziente nella valutazione della sospetta colica renale. Esposizione cumulativa da indagini ripetute, 2010. **115**(1): p. 105-114.
86. McCollough, C.H., *Patient dose in cardiac computed tomography.* Herz, 2003. **28**(1): p. 1-6.
87. Crawford, C.R. and K.F. King, *Computed tomography scanning with simultaneous patient translation.* Medical Physics, 1990. **17**(6): p. 967-982.
88. Nicholson, R. and S. Fetherston, *Primary radiation outside the imaged volume of a multislice helical CT scan.* British Journal of Radiology, 2002. **75**(894): p. 518-522.
89. Martin, C.J., *The application of effective dose to medical exposures.* Radiat Prot Dosimetry, 2008. **128**(1): p. 1-4.
90. Shrimpton, P.C., et al., *National survey of doses from CT in the UK: 2003.* Br J Radiol, 2006. **79**(948): p. 968-80.
91. Christner, J.A., J.M. Kofler, and C.H. McCollough, *Estimating effective dose for ct using dose-length product compared with using organ doses: Consequences of adopting international commission on radiological protection publication 103 or dual-energy scanning.* American Journal of Roentgenology, 2010. **194**(4): p. 881-889.
92. Shrimpton, P.C., et al., *Effective dose and dose-length product in CT.* Radiology, 2009. **250**(2): p. 604-5.
93. Contributors, W. *X-Ray Computed Tomography*. 2010 [cited 2010 3 May]; Available from: http://en.wikipedia.org/w/index.php?X-ray_computed_tomography&oldid=359230690.
94. Health Physics Society, *Answer to Question #4319 Category: Doses and Dose Calculations*. 2010 [cited 2010 20 December]; Available from: http://hps.org/publicinformation/ate/q4318.html.
95. Yu, L.L., Xin; Leng, Shuai; Kofler, James; Ramirez-Giraldo, Juan; Qu, Mingliang; Christner, Jodie;Fletcher, Joel; McCollough, Cynthia, *Radiation dose reduction in computed tomography: techniques and future perspective.* Imaging Medicine, 2009. **1**(1): p. 65-84.
96. Sun, Z., *Multislice CT angiography in aortic stent grafting: Relationship between image noise and body mass index.* European Journal of Radiology, 2007. **61**(3): p. 534-540.
97. Kalra, M., et al., *Strategies for CT radiation dose optimization.* Radiology, 2004. **230**(3): p. 619-28.

98. Brenner, D., et al., *Cancer risks attributable to low doses of ionizing radiation: assessing what we really know.* Proc Natl Acad Sci U S A, 2003. **100**(24): p. 13761-6.
99. Preston, D.L., et al., *Solid cancer incidence in atomic bomb survivors: 1958-1998.* Radiation Research, 2007. **168**(1): p. 1-64.
100. Broder, J., et al., *Cumulative CT exposures in emergency department patients evaluated for suspected renal colic.* J Emerg Med, 2007. **33**(2): p. 161-8.
101. Katz, S.I., et al., *Radiation dose associated with unenhanced CT for suspected renal colic: Impact of repetitive studies.* American Journal of Roentgenology, 2006. **186**(4): p. 1120-1124.
102. Sliker, C.W., K. Shanmuganathan, and S.E. Mirvis, *Diagnosis of blunt cerebrovascular injuries with 16-MDCT: Accuracy of whole-body MDCT compared with neck MDCT angiography.* American Journal of Roentgenology, 2008. **190**(3): p. 790-799.
103. Saltzherr, T.P. and J.C. Goslings, *Total body CT scan as the primary diagnostic modality in multi-trauma patients.* Primaire totale lichaams-CT bij multitraumapatiënten., 2009. **153**.
104. Huda, W., *What ER radiologists need to know about radiation risks.* Emergency Radiology, 2009. **16**(5): p. 335-341.
105. Tien, H.C., et al., *Radiation exposure from diagnostic imaging in severely injured trauma patients.* Journal of Trauma - Injury, Infection and Critical Care, 2007. **62**(1): p. 151-156.
106. Wilk, J.E., et al., *Relationship of combat experiences to alcohol misuse among U.S. soldiers returning from the Iraq war.* Drug and Alcohol Dependence, 2010. **108**(1-2): p. 115-121.
107. Wallace, A.E., E.P. Sheehan, and Y. Young-Xu, *Women, alcohol, and the military: Cultural changes and reductions in later alcohol problems among female veterans.* Journal of Women's Health, 2009. **18**(9): p. 1347-1353.
108. McCarroll, J.E., Z. Fan, and N.S. Bell, *Alcohol use in nonmutual and mutual domestic violence in the U.S. Army: 1998-2004.* Violence and Victims, 2009. **24**(3): p. 364-379.
109. Mansfield, A.J., et al., *Deployment and the use of mental health services among U.S. Army wives.* New England Journal of Medicine, 2010. **362**(2): p. 101-109.
110. Maguen, S., et al., *The impact of reported direct and indirect killing on mental health symptoms in Iraq war veterans.* Journal of Traumatic Stress, 2010. **23**(1): p. 86-90.
111. Killgore, W.D.S., et al., *Post-combat invincibility: Violent combat experiences are associated with increased risk-taking propensity following deployment.* Journal of Psychiatric Research, 2008. **42**(13): p. 1112-1121.
112. Howland, J., N.S. Bell, and I.E. Hollander, *Causes, types and severity of injury among army soldiers hospitalized with alcohol comorbidity.* Addiction, 2007. **102**(9): p. 1411-1420.

113. Boscarino, J.A., *External-cause mortality after psychologic trauma: the effects of stress exposure and predisposition.* Comprehensive Psychiatry, 2006. **47**(6): p. 503-514.

114. Mollica, R.F., *Waging a new kind of war. Invisible wounds.* Sci Am, 2000. **282**(6): p. 54-7.

115. Reger, G.M., et al., *Soldier evaluation of the virtual reality Iraq.* Telemedicine and e-Health, 2009. **15**(1): p. 101-104.

116. Ruff, R.L., S.S. Ruff, and X.F. Wang, *Headaches among Operation Iraqi Freedom/Operation Enduring Freedom veterans with mild traumatic brain injury associated with exposures to explosions.* J Rehabil Res Dev, 2008. **45**(7): p. 941-52.

117. Vanderploeg, R.D., H.G. Belanger, and G. Curtiss, *Mild Traumatic Brain Injury and Posttraumatic Stress Disorder and Their Associations With Health Symptoms.* Archives of Physical Medicine and Rehabilitation, 2009. **90**(7): p. 1084-1093.

118. Vasterling, J.J., et al., *Posttraumatic stress disorder and health functioning in a non-treatment-seeking sample of Iraq war veterans: A prospective analysis.* Journal of Rehabilitation Research and Development, 2008. **45**(3): p. 347-358.

119. Wojcik, B.E., F.Z. Akhtar, and L.H. Hassell, *Hospital admissions related to mental Disorders in U.S. Army soldiers in Iraq and Afghanistan.* Military Medicine, 2009. **174**(10): p. 1010-1018.

120. Rivas, L.A., et al., *Multislice CT in thoracic trauma.* Radiologic Clinics of North America, 2003. **41**(3): p. 599-616.

121. Huber-Wagner, S., et al., *Effect of whole-body CT during trauma resuscitation on survival: a retrospective, multicentre study.* The Lancet, 2009. **373**(9673): p. 1455-1461.

122. Epstein, O., et al., *Comparison of computed tomography and plain radiography in assessing traumatic spinal deformity.* Journal of Spinal Disorders and Techniques, 2009. **22**(3): p. 197-201.

123. Schmidt, R., et al. *Patient individual equivalent dose calculations for CT examinations*. 2009. Munich.

124. Owens, B.D., et al., *Characterization of extremity wounds in Operation Iraqi Freedom and Operation Enduring Freedom.* J Orthop Trauma, 2007. **21**(4): p. 254-7.

125. Owens, B.D., et al., *Combat wounds in operation Iraqi Freedom and operation Enduring Freedom.* J Trauma, 2008. **64**(2): p. 295-9.

126. Belmont Jr, P.J., et al., *Incidence and epidemiology of combat injuries sustained during "the surge" portion of operation iraqi freedom by a U.S. army brigade combat team.* Journal of Trauma - Injury, Infection and Critical Care, 2010. **68**(1): p. 204-210.

127. RadiologyInfo.org. *Radiation Exposure in X-ray and CT Examinations*. Patient Safety 2010 [cited 2010 1 December]; Available from: http:/www.radiologyinfo.org/en/safety/index.cfm?pg=sfty_xray.

128. Rogers, D.W., *Fifty years of Monte Carlo simulations for medical physics.* Phys Med Biol, 2006. **51**(13): p. R287-301.
129. Harrison, R.L. *Introduction to Monte Carlo simulation*. in *AIP Conference Proceedings*. 2009. Bratislava.
130. Raeside, D.E., *Monte Carlo principles and applications.* Physics in Medicine and Biology, 1976. **21**(2): p. 181-197.
131. Kawrakow, I.M.-H., E.;Rogers, D.W.O.;Tessier, F.;Walters, B.R.B., *The EGSnrc Code System: Monte Carlo Simulation of Electron and Photon Transport*, 2009, National Research Council Canada: Ottawa.
132. Bielajew, A.F.H., H.;Nelson, W.R.;Rogers, D.W.O., *History, overview and recent improvements of EGS4*, 1994, National Research Council of Canada: Ottawa.
133. Rowshanfarzad, P., et al., *Measurement and modeling of the effect of support arm backscatter on dosimetry with a Varian EPID.* Medical Physics, 2010. **37**(5): p. 2269-2278.
134. Kainz, K.K., et al., *Dose properties of a laser accelerated electron beam and prospects for clinical application.* Medical Physics, 2004. **31**(7): p. 2053-2067.
135. McCurdy, B.M.C. and S. Pistorius, *Photon scatter in portal images: Accuracy of a fluence based pencil beam superposition algorithm.* Medical Physics, 2000. **27**(5): p. 913-922.
136. McCurdy, B.M.C. and S. Pistorius, *Photon scatter in portal images: Physical characteristics of pencil beam kernels generated using the EGS Monte Carlo code.* Medical Physics, 2000. **27**(2): p. 312-320.
137. Mohan, R., C. Chui, and L. Lidofsky, *Energy and angular distributions of photons from medical linear accelerators.* Medical Physics, 1985. **12**(5): p. 592-597.
138. Petti, P.L., et al., *Investigation of buildup dose from electron contamination of clinical photon beams.* Medical Physics, 1983. **10**(1): p. 18-24.
139. Chow, J.C.L. and R. Jiang, *Monte Carlo calculation of monitor unit for electron arc therapy.* Medical Physics, 2010. **37**(4): p. 1571-1578.
140. Schmidhalter, D., et al., *Comparison of Monte Carlo collimator transport methods for photon treatment planning in radiotherapy.* Medical Physics, 2010. **37**(2): p. 492-504.
141. Vassiliev, O.N., et al., *Validation of a new grid-based Boltzmann equation solver for dose calculation in radiotherapy with photon beams.* Physics in Medicine and Biology, 2010. **55**(3): p. 581-598.
142. Pisaturo, O., et al., *A Monte Carlo-based procedure for independent monitor unit calculation in IMRT treatment plans.* Physics in Medicine and Biology, 2009. **54**(13): p. 4299-4310.
143. Strigari, L., et al., *Monte Carlo dose voxel kernel calculations of beta-emitting and Auger-emitting radionuclides for internal dosimetry: A comparison between EGSnrcMP and EGS4.* Med Phys, 2006. **33**(9): p. 3383-9.

144. Pafundi, D., et al., *An image-based skeletal dosimetry model for the ICRP reference newborn - Internal electron sources.* Physics in Medicine and Biology, 2010. **55**(7): p. 1785-1814.
145. Mourtada, F., et al., *Dosimetry characterization of a ³²P source wire used for intravascular brachytherapy with automated stepping.* Medical Physics, 2003. **30**(5): p. 959-971.
146. Selvam, T.P. and S. Bhola, *Technical Note: EGSnrc-based dosimetric study of the BEBIG C 60 o HDR brachytherapy sources.* Medical Physics, 2010. **37**(3): p. 1365-1370.
147. Chen, Z.J., P. Bongiorni, and R. Nath, *A photon spectrometric dose-rate constant determination for the advantage Pd-103 brachytherapy source.* Medical Physics, 2010. **37**(2): p. 672-674.
148. Thomson, R.M. and D.W.O. Rogers, *Monte Carlo dosimetry for i 125 and P 103 d eye plaque brachytherapy with various seed models.* Medical Physics, 2010. **37**(1): p. 368-376.
149. Gardner, J., J. Siebers, and I. Kawrakow, *Dose calculation validation of VMC++ for photon beams.* Medical Physics, 2007. **34**(5): p. 1809-1818.
150. Rawlinson, J.A., et al., *Theoretical and experimental investigation of dose enhancement due to charge storage in electron-irradiated phantoms.* Medical Physics, 1984. **11**(6): p. 814-821.
151. Babcock, K. and N. Sidhu, *The effects of dose calculation resolution on dose accuracy for radiation therapy treatments of the lung. Part I. A Monte Carlo model of the lung.* Medical Physics, 2010. **37**(2): p. 675-686.
152. Bouchard, H., et al., *Ionization chamber gradient effects in nonstandard beam configurations.* Medical Physics, 2009. **36**(10): p. 4654-4663.
153. Wulff, J., K. Zink, and I. Kawrakow, *Efficiency improvements for ion chamber calculations in high energy photon beams.* Medical Physics, 2008. **35**(4): p. 1328-1336.
154. Tessier, F. and I. Kawrakow, *Effective point of measurement of thimble ion chambers in megavoltage photon beams.* Medical Physics, 2010. **37**(1): p. 96-107.
155. Crop, F., et al., *The influence of small field sizes, penumbra, spot size and measurement depth on perturbation factors for microionization chambers.* Physics in Medicine and Biology, 2009. **54**(9): p. 2951-2969.
156. Wang, B., C.H. Kim, and X.G. Xua, *Monte Carlo modeling of a high-sensitivity MOSFET dosimeter for low- and medium-energy photon sources.* Med Phys, 2004. **31**(5): p. 1003-8.
157. Wang, B., X.G. Xu, and C.H. Kim, *Monte Carlo study of MOSFET dosemeter characteristics: dose dependence on photon energy, direction and dosemeter composition.* Radiat Prot Dosimetry, 2005. **113**(1): p. 40-6.
158. Wang, L.L.W., D.J. La Russa, and D.W.O. Rogers, *Systematic uncertainties in the Monte Carlo calculation of ion chamber replacement correction factors.* Medical Physics, 2009. **36**(5): p. 1785-1789.

159. Wang, L.L.W. and D.W.O. Rogers, *Study of the effective point of measurement for ion chambers in electron beams by Monte Carlo simulation.* Medical Physics, 2009. **36**(6): p. 2034-2042.
160. Wang, L.L.W. and D.W.O. Rogers, *The replacement correction factors for cylindrical chambers in high-energy photon beams.* Physics in Medicine and Biology, 2009. **54**(6): p. 1609-1620.
161. Poludniowski, G., et al., *An efficient Monte Carlo-based algorithm for scatter correction in keV cone-beam CT.* Physics in Medicine and Biology, 2009. **54**(12): p. 3847-3864.
162. Chow, J.C.L., *Cone-beam CT dosimetry for the positional variation in isocenter: A Monte Carlo study.* Medical Physics, 2009. **36**(8): p. 3512-3520.
163. Walters, B.R.B., et al., *Skeletal dosimetry in cone beam computed tomography.* Medical Physics, 2009. **36**(7): p. 2915-2922.
164. Bazalova, M., et al., *Correction of CT artifacts and its influence on Monte Carlo dose calculations.* Medical Physics, 2007. **34**(6): p. 2119-2132.
165. Bazalova, M., et al., *Dual-energy CT-based material extraction for tissue segmentation in Monte Carlo dose calculations.* Physics in Medicine and Biology, 2008. **53**(9): p. 2439-2456.
166. Bazalova, M., et al., *Kilovoltage beam Monte Carlo dose calculations in submillimeter voxels for small animal radiotherapy.* Medical Physics, 2009. **36**(11): p. 4991-4999.
167. Faddegon, B.A., et al., *The accuracy of EGSnrc, Geant4 and PENELOPE Monte Carlo systems for the simulation of electron scatter in external beam radiotherapy.* Physics in Medicine and Biology, 2009. **54**(20): p. 6151-6163.
168. Vilches, M., et al., *Multiple scattering of 13 and 20 MeV electrons by thin foils: A monte carlo study with GEANT, geant4, and PENELOPE.* Medical Physics, 2009. **36**(9): p. 3964-3970.
169. Pacilio, M., et al., *Monte Carlo dose calculations using MCNP4C and EGSnrc/BEAMnrc codes to study the energy dependence of the radiochromic film response to beta-emitting sources.* Physics in Medicine and Biology, 2007. **52**(13): p. 3931-3948.
170. Dunphy, P.P., E.L. Chupp, and C.M. Jensen, *Monte Carlo simulation of the response of NaI scintillator to medium energy neutrons.* Nuclear Inst. and Methods in Physics Research, A, 1993. **330**(1-2): p. 199-209.
171. Faddegon, B.A. and D.W.O. Rogers, *Comparisons of thick-target bremsstrahlung calculations by EGS4/PRESTA and ITS version 2.1.* Nuclear Inst. and Methods in Physics Research, A, 1993. **327**(2-3): p. 556-565.
172. Croft, S., *The absolute yield, angular distribution and resonance widths of the 6.13, 6.92 and 7.12 MeV photons from the 340.5 keV resonance of the ¹⁹F(p,Î±Î³)¹⁶O reaction.* Nuclear Inst. and Methods in Physics Research, A, 1991. **307**(2-3): p. 353-358.

173. del Peso, J. and E. Ros, *Fast simulation of electromagnetic showers in the ZEUS calorimeter.* Nuclear Inst. and Methods in Physics Research, A, 1991. **306**(3): p. 485-499.
174. La Russa, D.J. and D.W.O. Rogers, *Accuracy of spencer-attix cavity theory and calculations of fluence correction factors for the air kerma formalism.* Medical Physics, 2009. **36**(9): p. 4173-4183.
175. Zhong, H. and J.V. Siebers, *Monte Carlo dose mapping on deforming anatomy.* Physics in Medicine and Biology, 2009. **54**(19): p. 5815-5830.
176. Kim, S., et al., *Estimation of computed tomography dose index in cone beam computed tomography: Mosfet measurements and Monte Carlo simulations.* Health Physics, 2010. **98**(5): p. 683-691.
177. Kim, S., et al., *Estimation of absorbed doses from paediatric cone-beam CT scans: Mosfet measurements and Monte Carlo simulations.* Radiation Protection Dosimetry, 2010. **138**(3): p. 257-263.
178. Ferreira, C.C., J.W. Vieira, and A.F. Maia, *The influence of calculated CT X-ray spectra on organ absorbed dose to a human phantom.* Nuclear Instruments and Methods in Physics Research, Section B: Beam Interactions with Materials and Atoms, 2009. **267**(20): p. 3447-3455.
179. Schmidt, B. and W.A. Kalender, *A fast voxel-based Monte Carlo method for scanner- and patient-specific dose calculations in computed tomography.* Physica Medica, 2002. **18**(2): p. 43-53.
180. Trumble, E.F., *MCNP Certification Package*, 1992, Savannah River Laboratory: Aiken, SC.
181. Solberg, T.D., et al., *A review of radiation dosimetry applications using the MCNP Monte Carlo code.* Radiochimica Acta, 2001. **89**(4-5): p. 337-355.
182. Karamanis, D., *Efficiency simulation of HPGe and Si(Li) detectors in γ- and X-ray spectroscopy.* Nuclear Instruments and Methods in Physics Research, Section A: Accelerators, Spectrometers, Detectors and Associated Equipment, 2003. **505**(1-2): p. 282-285.
183. Vidmar, T., et al., *A semi-empirical model of the efficiency curve for extended sources in gamma-ray spectrometry.* Nuclear Instruments and Methods in Physics Research, Section A: Accelerators, Spectrometers, Detectors and Associated Equipment, 2001. **470**(3): p. 533-547.
184. Colonna, N. and S. Altieri, *Simulations of neutron transport at low energy: A comparison between GEANT and MCNP.* Health Physics, 2002. **82**(6): p. 840-846.
185. Yeh, Y.S., et al. *Simulating neutron propagations with FLUKA, GEANT4 and MCNP*. 2007.
186. Schlagbauer, M., et al., *Uncertainty budget for a whole body counter in the scan geometry and computer simulation of the calibration phantoms.* Radiation Protection Dosimetry, 2007. **125**(1-4): p. 149-152.

187. Pioch, C., V. Mares, and W. Rühm, *Influence of Bonner sphere response functions above 20 MeV on unfolded neutron spectra and doses.* Radiation Measurements, 2010. **45**(10): p. 1263-1267.
188. Neuhold, P., *Monte Carlo evaluations and the source normalisation problem.* Radiation Protection Dosimetry, 2005. **115**(1-4): p. 268-270.
189. Heilbronn, L., et al. *Comparisons between transport model calculations and experimental data*. 2010.
190. Tzedakis, A., et al., *Influence of z overscanning on normalized effective doses calculated for pediatric patients undergoing multidetector CT examinations.* Medical Physics, 2007. **34**(4): p. 1163-1175.
191. Tzedakis, A., et al., *The effect of z overscanning on radiation burden of pediatric patients undergoing head CT with multidetector scanners: A Monte Carlo study.* Medical Physics, 2006. **33**(7): p. 2472-2478.
192. Stabin, M.G., et al. *Use of MCNP with voxel-based image data for internal dosimetry applications*. 2005. Chattanooga, TN.
193. Hykes, J.M., et al. *Verification and validation of deterministic radiation transport numerical methods, codes, and nuclear data for estimating radiation dose to patients during CT scan*. 2009. Saratoga Springs, NY.
194. Zaidi, H. and B.M.W. Tsui, *Review of computational anthropomorphic anatomical and physiological models.* Proceedings of the IEEE, 2009. **97**(12): p. 1938-1953.
195. Atherton, J.V. and W. Huda, *Energy imparted and effective doses in computed tomography.* Medical Physics, 1996. **23**(5): p. 735-741.
196. McCollough, C.H. and B.A. Schueler, *Calculation of effective dose.* Medical Physics, 2000. **27**(5): p. 828-837.
197. Theocharopoulos, N., et al., *Estimation of effective doses to adult and pediatric patients from multislice computed tomography: A method based on energy imparted.* Medical Physics, 2006. **33**(10): p. 3846-3856.
198. Gregory, K.J., G. Bibbo, and J.E. Pattison, *On the uncertainties in effective dose estimates of adult CT head scans.* Medical Physics, 2008. **35**(8): p. 3501-3510.
199. Richards, P.J., et al., *Major trauma & cervical clearance radiation doses & cancer induction.* Injury, 2008. **39**(3): p. 347-356.
200. Pages, J., N. Buls, and M. Osteaux, *CT doses in children: A multicentre study.* British Journal of Radiology, 2003. **76**(911): p. 803-811.
201. Huda, W., *Radiation doses and risks in chest computed tomography examinations.* Proceedings of the American Thoracic Society, 2007. **4**(4): p. 316-320.
202. Martin, C.J., *Radiation dosimetry for diagnostic medical exposures.* Radiat Prot Dosimetry, 2008. **128**(4): p. 389-412.
203. Huda, W., et al., *Computing effective dose in cardiac CT.* Physics in Medicine and Biology, 2010. **55**(13): p. 3675-3684.
204. ImPACT. *CTDosimetry Spreadsheet*. 2010 [cited 2010 1 August]; Available from: http://www.impactscan.org.

205. Bauhs, J.A.V., Thomas F.; Primak, Andrew N.; McCollough, Cynthia H., *CT Dosimetry: Comparison of Measurement Techniques and Devices.* RadioGraphics, 2008. **28**: p. 8.
206. Tapiovaara, M.S.T., *PCXMC 2.0: User's Guide*, 2008, Radiation and Nuclear Safety Authority: Helsinki.
207. Tapiovaara, M.S.T., *PCXMC: A Monte Carlo program for calculating patient doses in medical x-ray examinations*, 2008, Radiation and Nuclear Safety Authority: Helsinki.
208. Young, J.F., et al., *Human organ/tissue growth algorithms that include obese individuals and black/white population organ weight similarities from autopsy data.* Journal of Toxicology and Environmental Health - Part A: Current Issues, 2009. **72**(8): p. 527-540.
209. Khelassi-Toutaoui, N., et al., *Experimental evaluation of PCXMC and prepare codes used in conventional radiology.* Radiat Prot Dosimetry, 2008. **131**(3): p. 374-8.
210. DeMarco, J.J., et al. *Estimating surface radiation dose from Multidetector CT: Cylindrical phantoms, Anthropomorphic phantoms and Monte Carlo Simulations*. in *Progress in Biomedical Optics and Imaging - Proceedings of SPIE*. 2005. San Diego, CA.
211. Lee, C., et al., *Hybrid computational phantoms of the 15-year male and female adolescent: Applications to CT organ dosimetry for patients of variable morphometry.* Medical Physics, 2008. **35**(6): p. 2366-2382.
212. Nauer, C.B., et al., *Effective doses from scan projection radiographs of the head: impact of different scanning practices and comparison with conventional radiography.* AJNR Am J Neuroradiol, 2009. **30**(1): p. 155-9.
213. Ekelund, L., et al., *Imaging of four-corner fusion (SLAC arthrodesis) of the wrist with 64-slice computed tomography.* Acta Radiologica, 2007. **48**(1): p. 76-79.
214. Fulea, D., C. Cosma, and I.G. Pop, *Monte Carlo method for radiological X-ray examinations.* Romanian Journal in Physics, 2009. **54**(7-8): p. 629-639.
215. He, W., et al., *X-ray tube current modulation and patient doses in chest CT.* Radiation Protection Dosimetry, 2011. **143**(1): p. 81-87.
216. Defense Manpower Data Center, *Active Duty Demographic Profile*. 2008 [cited 2010 15 September]; U.S. Military demographic profile as of September 2008.]. Available from: http://www.slideshare.net/pastinson/us-military-active-duty-demographic-profile-presentation.
217. Headquarters, Department of the Army, *Army Regulation 600-9, The Army Weight Control Program*, 2006, Department of the Army: Washington D.C.
218. *Body Mass Index*. 2010 [cited 2010 23 December]; Available from: http://www.cdc.gov/healthyweight/assessing/bmi/.
219. Feuchtner, G.M., et al., *Radiation dose reduction by using 100-kV tube voltage in cardiac 64-slice computed tomography: A comparative study.* European Journal of Radiology, 2010. **75**(1).

220. Krupp, N., et al., *Fluoroscopic organ and tissue-specific radiation exposure by sex and body mass index during ureteroscopy.* Journal of Endourology, 2010. **24**(7): p. 1067-1073.
221. Jiang, Y.F., et al., *Image noise and artifact in chest low-dose CT.* Chinese Journal of Radiology, 2010. **44**(1): p. 37-40.
222. Wong, J.R., et al., *Potential for Higher Treatment Failure in Obese Patients: Correlation of Elevated Body Mass Index and Increased Daily Prostate Deviations From the Radiation Beam Isocenters in an Analysis of 1,465 Computed Tomographic Images.* International Journal of Radiation Oncology Biology Physics, 2009. **75**(1): p. 49-55.
223. Patil, N., et al., *The effect of obesity on rectal dosimetry after permanent prostate brachytherapy.* Brachytherapy, 2009. **8**(2): p. 218-222.
224. Hietschold, V., et al., *Computed tomography: Influence of varying tube current on patient dose and correctness of effective dose calculations.* Computertomografie: Einfluss des variablen röhrenstroms auf die patientendosis und die genauigkeit von berechnungen der effektiven dosis, 2008. **180**(5): p. 430-439.
225. Yoshimura, N., et al., *Correlation between image noise and body weight in coronary CTA with 16-row MDCT.* Academic Radiology, 2006. **13**(3): p. 324-328.
226. Kondo, Y., *Simple method of setting proper exposure in X-ray CT examination of head and abdomen.* Nippon Hoshasen Gijutsu Gakkai Zasshi, 2005. **61**(4): p. 514-520.
227. Huppertz, A., et al., *Computed tomography for preoperative planning in minimal-invasive total hip arthroplasty: Radiation exposure and cost analysis.* European Journal of Radiology.
228. Reynolds, K.L., et al., *Injuries and risk factors in a 100-mile (161-km) infantry road march.* Preventive Medicine, 1999. **28**(2): p. 167-173.
229. Reynolds, K., et al., *A comparison of injuries, limited-duty days, and injury risk factors in infantry, artillery, construction engineers, and Special Forces soliders.* Military Medicine, 2009. **174**(7): p. 702-708.
230. Peduzzi, P., et al., *Importance of events per independent variable in proportional hazards regression analysis II. Accuracy and precision of regression estimates.* Journal of Clinical Epidemiology, 1995. **48**(12): p. 1503-1510.
231. Concato, J., et al., *Importance of events per independent variable in proportional hazards analysis I. Background, goals, and general strategy.* Journal of Clinical Epidemiology, 1995. **48**(12): p. 1495-1501.
232. Servomaa, A. and M. Tapiovaara, *Organ dose calculation in medical X ray examinations by the program PCXMC.* Radiation Protection Dosimetry, 1998. **80**(1-3): p. 213-219.
233. DeMarco, J.J., et al., *Estimating radiation doses from multidetector CT using Monte Carlo simulations: Effects of different size voxelized patient models on*

magnitudes of organ and effective dose. Physics in Medicine and Biology, 2007. **52**(9): p. 2583-2597.

234. Gregory, K.J., G. Bibbo, and J.E. Pattison, *Uncertainties in effective dose estimates of adult CT head scans: The effect of head size.* Medical Physics, 2009. **36**(9): p. 4121-4125.
235. Gregory, K.J., J.E. Pattison, and G. Bibbo, *Uncertainties of exposure-related quantities in mammographic x-ray unit quality control.* Medical Physics, 2006. **33**(3): p. 687-698.
236. Gregory, K., G. Bibbo, and J.E. Pattison, *A standard approach to measurement uncertainties for scientists and engineers in medicine.* Australasian Physical and Engineering Sciences in Medicine, 2005. **28**(2): p. 131-139.
237. U.S. Food and Drug Administration, *Radiation-Emitting Products*. 2010 [cited 2010 23 December]; Available from: http://www.fda.gov/Radiation-EmittingProducts/default.htm.
238. Shrimpton, P.C., et al., *Doses to patients from routine diagnostic X-ray examinations in England.* Br J Radiol, 1986. **59**(704): p. 749-58.
239. Brix, G.L., U.;Veit, R.;Truckenbrodt, R.;Stamm, G.; Coppenrath, E.M.;Griebel, J.;Nagel, H., *Assessment of a theoretical formalism for dose estimation in CT: an anthropomorphic phantom study.* European Radiology, 2004(14): p. 9.
240. Kleinbaum, D.G., ed. *Applied Regression Analysis and Other Multivariable Methods*. Fourth ed. 2008, Thomson Brooks Cole: USA.
241. Wielandts, J.Y., et al., *Three-dimensional cardiac rotational angiography: Effective radiation dose and image quality implications.* Europace, 2010. **12**(2): p. 194-201.
242. Gao, J.H., et al., *Dose reduction in coronary artery imaging with 64-row multi-slice helical CT with body mass index-dependent mA selection.* Chinese Journal of Radiology, 2008. **42**(8): p. 877-882.
243. Bae, K.T., et al., *Contrast enhancement in cardiovascular MDCT: Effect of body weight, height, body surface area, body mass index, and obesity.* American Journal of Roentgenology, 2008. **190**(3): p. 777-784.
244. Alkadhi, H., et al., *Radiation dose of cardiac dual-source CT: The effect of tailoring the protocol to patient-specific parameters.* European Journal of Radiology, 2008. **68**(3): p. 385-391.
245. Bower, M.W. and D.E. Hintenlang, *The characterization of a commercial MOSFET dosimeter system for use in diagnostic x ray.* Health Phys, 1998. **75**(2): p. 197-204.
246. Botter-Jensen, L., S.W. McKeever, and A.G. Wintle, *Optically Stimulated Luminescence Dosimetry*2003, New York: Elsevier. 355.
247. Danzer, J., et al. *TU-D-AUD C-09: In-Vivo Dosimetry Using Aluminum Oxide Detectors*. in *Med. Phys.* 2008. AAPM.
248. Inc., C.I.R.S. *Dosimetry Verification Phantoms*. CT & X-Ray Phantoms 2009 28 July 2009]; Available from: http://www.cirsinc.com/700_ct_xray.html.

249. Viamonte, A., et al., *Radiotherapy dosimetry using a commercial OSL system.* Medical Physics, 2008. **35**(4): p. 1261-1266.
250. Sessions, J.B., et al., *Comparisons of point and average organ dose within an anthropomorphic physical phantom and a computational model of the newborn patient.* Med Phys, 2002. **29**(6): p. 1080-9.
251. Kuon, E., et al., *Standardization of occupational dose to patient DAP enables reliable assessment of radiation-protection devices in invasive cardiology.* Rofo, 2003. **175**(11): p. 1545-50.
252. Botter-Jensen, L., S.W.S. McKeever, and A.G. Wintle, *Passive optically stimulated luminescence dosimetry*, in *Optically Stimulated Luminescence Dosimetry*2003, Elsevier. p. 101-118.
253. Yukihara, E.G., et al., *Evaluation of Al2O3:C optically stimulated luminescence (OSL) dosimeters for passive dosimetry of high-energy photon and electron beams in radiotherapy.* Med Phys, 2008. **35**(1): p. 260-9.
254. Yoshimura, E.M., *Correlation of optically stimulated luminescence and thermoluminescence of Al2O3:Fe, Mg, Cr crystals.* Nuclear Instruments and Methods in Physics Research Section A: Accelerators, Spectrometers, Detectors and Associated Equipment, 2007. **580**(1): p. 606-609.
255. Yang, X.-B., et al., *Influence of carbon on the thermoluminescence and optically stimulated luminescence of alpha -Al[sub 2]O[sub 3]:C crystals.* Journal of Applied Physics, 2008. **104**(12): p. 123112-6.
256. Whitley, V.H. and S.W. McKeever, *Linear modulation optically stimulated luminescence and thermoluminescence techniques in Al2O3:C.* Radiat Prot Dosimetry, 2002. **100**(1-4): p. 61-6.
257. West, W.G., K.J. Kearfott, and S.M. Bernal, *The sunlight OSL response of a commercially available alpha-Al2O3:C personnel dosimetry material.* Radiat Prot Dosimetry, 2006. **119**(1-4): p. 344-9.
258. Veronese, I., et al., *The use of alpha-Al2O3:C in Riso OSL single grains attachment system for assessing the spatial dose rate distribution due to incorporation of 90Sr in human teeth.* Radiat Prot Dosimetry, 2006. **119**(1-4): p. 408-12.
259. Tang, Q., et al., *TL and OSL of SrSO4 phosphors doped with Eu.* Radiat Prot Dosimetry, 2006. **119**(1-4): p. 238-43.
260. Schembri, V. and B.J. Heijmen, *Optically stimulated luminescence (OSL) of carbon-doped aluminum oxide (Al2O3:C) for film dosimetry in radiotherapy.* Med Phys, 2007. **34**(6): p. 2113-8.
261. Schembr, V., et al., *229 Optically stimulated luminescence (OSL) of carbon-doped aluminum oxide (Al203:C) for film dosimetry in radiotherapy.* Radiotherapy and Oncology, 2005. **76**(Supplement 2): p. S110-S111-S110-S111.
262. Sawakuchi, G.O., et al., *Relative optically stimulated luminescence and thermoluminescence efficiencies of Al[sub 2]O[sub 3]:C dosimeters to heavy charged particles with energies relevant to space and radiotherapy dosimetry.* Journal of Applied Physics, 2008. **104**(12): p. 124903-10.

263. Sawakuchi, G.O., et al., *Optically stimulated luminescence fluence response of Al2O3:C dosimeters exposed to different types of radiation.* Radiation Measurements, 2008. **43**(2-6): p. 450-454.
264. Oster, L., Y.S. Horowitz, and L. Podpalov, *OSL and TL in LiF:Mg,Ti following alpha particle and beta ray irradiation: application to mixed-field radiation dosimetry.* Radiat Prot Dosimetry, 2008. **128**(3): p. 261-5.
265. McKeever, S.W., et al., *Recent advances in dosimetry using the optically stimulated luminescence of Al2O3:C.* Radiat Prot Dosimetry, 2004. **109**(4): p. 269-76.
266. Homnick, J., et al. *TH-D-352-05: Optically Stimulated Luminescence (OSL) Dosimeters Can Be Used for Remote Dosimetry Services*. in *Med. Phys.* 2008. AAPM.
267. Gaza, R., E.G. Yukihara, and S.W. McKeever, *The response of thermally and optically stimulated luminescence from Al2O3:C to high-energy heavy charged particles.* Radiat Meas, 2004. **38**(4-6): p. 417-20.
268. Landauer, I., *The Power of the Dot*, in *Microstar Dosimeter Handout*.
269. Yukihara, E.G. and S.W. McKeever, *Optically stimulated luminescence (OSL) dosimetry in medicine.* Phys Med Biol, 2008. **53**(20): p. R351-79.
270. Polf, J.C., et al., *A real-time, fibre optic dosimetry system using Al2O3 fibres.* Radiat Prot Dosimetry, 2002. **100**(1-4): p. 301-4.
271. Gaza, R. and S.W. McKeever, *A real-time, high-resolution optical fibre dosemeter based on optically stimulated luminescence (OSL) of KBr:Eu, for potential use during the radiotherapy of cancer.* Radiat Prot Dosimetry, 2006. **120**(1-4): p. 14-9.
272. Viamonte, A., et al., *Radiotherapy dosimetry using a commercial OSL system.* Med Phys, 2008. **35**(4): p. 1261-6.
273. ICRU, *Tissue Substitutes in Radiation Dosimetry and Measurement (Report 44)*, International Commission on Radiation Units and Measurements (ICRU), Editor 1989: Bethesda.
274. Hurwitz, L.M., et al., *Effective dose determination using an anthropomorphic phantom and metal oxide semiconductor field effect transistor technology for clinical adult body multidetector array computed tomography protocols.* Journal of Computer Assisted Tomography, 2007. **31**(4): p. 544-549.
275. Salvado, M.L., M.; Morant, J.J.; Calzado, A., *Monte Carlo Calculation of Radiation Dose in CT Examinations Using Phantom and Patient Tomographic Models.* Radiation Protection Dosimetry, 2005. **114**(1-3): p. 5.
276. Castellano, I.A., D.R. Dance, and P.M. Evans, *CT dosimetry: getting the best from the adult Cristy phantom.* Radiat Prot Dosimetry, 2005. **114**(1-3): p. 321-5.
277. Gray, J.E., et al. *Dot Dosimeters Using Optically Stimulated Luminescent (OSL) Dosimetry Materials*. in *National Conference on Radiation Control, Crossroads in Radiation Control*. 2006. Detroit: CRCPD Publication E-06-4.

278. Jursinic, P., *Characterization of optically stimulated luminescent dosimeters, OSLDs, for clinical dosimetric measurements.* Medical Physics, Volume 34, No. 12, 2007: p. 4594-4602.

279. McKeever, S.W.S. and A.G. Wintle, *Passive optically stimulated luminescence dosimetry*, in *Optically Stimulated Luminescence Dosimetry*2003, Elsevier. p. 101-118.

280. Hamann, M., *Evaluation of a Low-dose/Slow-rotating SPECT-CT System.* Physics in Medicine and Biology, Volume 53, Number 10, 2008.

281. van Straten, M., et al., *The effect of angular and longitudinal tube current modulations on the estimation of organ and effective doses in x-ray computed tomography.* Med Phys, 2009. **36**(11): p. 4881-9.

282. Sawyer, L.J., et al., *Effective doses to patients from CT acquisitions on the GE Infinia Hawkeye: A comparison of calculation methods.* Nuclear Medicine Communications, 2008. **29**(2): p. 144-149.

283. Landauer, Inc. *MicroStar Specifications*. 2010 [cited 2010 29 September]; Available from: http://www.osldosimetry.com/documents/MicroStar_Specifications.pdf.

284. Cohnen, M., et al., *Effective doses in standard protocols for multi-slice CT scanning.* European Radiology, 2003. **13**(5): p. 1148-1153.

285. Bland, J.M.A., Douglas G., *Comparing methods of measurement: why plotting difference against standard method is misleading.* Lancet, 1995(346): p. 3.

286. *The Measurement, Reporting, and Management of Radiation Dose in CT, Report 96*, in *Report of AAPM Task Group 23 of the Diagnostic Imaging Council CT Committee*, A.A.o.P.i. Medine, Editor 2008, AAPM: College Park.

287. Measurements, I.C.o.R.U.a., *Conversion Coefficients for use in Radiological Protection against External Radiation, ICRU Report 57*, ICRU, Editor In Press: Bethesda, Maryland.

288. *Tech Report Number 457: Dosimetry in Diagnostic Radiology: An International Code of Practice*, in *Technical Reports Series*, I.A.E. Agency, Editor 2007, IAEA: Vienna.

289. Smith-Bindman, R., et al., *Radiation dose associated with common computed tomography examinations and the associated lifetime attributable risk of cancer.* Arch Intern Med, 2009. **169**(22): p. 2078-86.

290. Altman, D.G.B., J.M., *Measurement in Medicine: the Analysis of Method Comparison Studies.* The Statistician, 1983(32): p. 11.

291. Fujii, K.A., T.; Yamauchi-Kawaura, C.; Koyama, S.; Yamauchi, M.; Ko, S.; Akahane, K.; Nishizawa, K., *Radiation dose evaluation in 64-slice CT examinations with adult and paediatric anthropomorphic phantoms.* The British Journal of Radiology, 2009(82): p. 9.

292. Groves, A.M.O., K.E.; Courtney, H.M.; Yates, S.J.; Goldstone, K.E.; Blake, G.M., *16-detector multislice CT: dosimetry estimation by TLD measurement compared with Monte Carlo simulation.* The British Journal of Radiology, 2004(77): p. 4.

293. Li, X.S., Ehsan; Segars, W. Paul; Sturgeon, Gregory M.; Frush, Donald P., *Patient-specific radiation dose and cancer risk estimation in CT: Part II. Application to patients.* Medical Physics, 2011. **38**(1): p. 12
294. Adliene, D.M., S., *Discrepancy between absorbed dose estimated from phantom measurements and from estimates using data on individual head sizes in head CT examinations.* Radiation Protection Dosimetry, 2010. **139**(1-3): p. 5.
295. Fabian, T.C., *Whole-body CT in multiple trauma.* The Lancet, 2009. **373**(9673): p. 1408-1409.
296. Brenner, D.J., *Effective dose: a flawed concept that could and should be replaced.* Br J Radiol, 2008. **81**(967): p. 521-3.
297. Brenner, D.J., *Radiation risks potentially associated with low-dose CT screening of adult smokers for lung cancer.* Radiology, 2004. **231**(2): p. 440-5.
298. American Cancer Society, *Lifetime Risk of Developing or Dying from Cancer*. 2010 [cited 2010 August 25]; Available from: http://www.cancer.org/Cancer/CancerBasics/lifetime-probability-of-developing-or-dying-from-cancer.
299. Kalra, M., et al., *Strategies for CT radiation dose optimization.* Radiology, 2004. **230**(3): p. 619-28.
300. Kalra, M., et al., *Computed tomography radiation dose optimization: scanning protocols and clinical applications of automatic exposure control.* Curr Probl Diagn Radiol. **34**(5): p. 171-81.
301. Kubo, T., et al., *Radiation dose reduction in chest CT: a review.* AJR Am J Roentgenol, 2008. **190**(2): p. 335-43.
302. Li, T., et al., *Radiation dose reduction in four-dimensional computed tomography.* Med Phys, 2005. **32**(12): p. 3650-60.
303. Winslow, J.E., et al., *Quantitative assessment of diagnostic radiation doses in adult blunt trauma patients.* Ann Emerg Med, 2008. **52**(2): p. 93-7.
304. Wedegärtner, U., et al., *Diagnostic imaging in polytrauma: Comparison of radiation exposure from whole-body MSCT and conventional radiography with organ-specific CT.* Radiologische bildgebung beim polytrauma: Dosisvergleich von ganzkörper-MSCT und konventionellem röntgen mit organspezifischer CT, 2004. **176**(7): p. 1039-1044.
305. Tien, H.C., et al., *Radiation exposure from diagnostic imaging in severely injured trauma patients.* J Trauma, 2007. **62**(1): p. 151-6.
306. Schoenfeld, A.J., G.P. Goodman, and P.J. Belmont Jr, *Characterization of combat-related spinal injuries sustained by a US Army Brigade Combat Team during Operation Iraqi Freedom.* Spine Journal, 2010.
307. Wojcik, B.E., et al., *Traumatic brain injury hospitalizations of U.S. army soldiers deployed to Afghanistan and Iraq.* American journal of preventive medicine, 2010. **38**(1 Suppl).
308. Lew, H.L., et al., *Overlap of mild TBI and mental health conditions in returning OIF/OEF service members and veterans.* J Rehabil Res Dev, 2008. **45**(3): p. xi-xvi.

309. Galarneau, M.R., et al., *Traumatic brain injury during Operation Iraqi Freedom: findings from the United States Navy-Marine Corps Combat Trauma Registry.* J Neurosurg, 2008. **108**(5): p. 950-7.
310. *Invisible Wounds: Mental Health and Cognitive Care Needs of America's Returning Veterans*. 2008 17 April 2008 [cited 2010 27 August]; Available from: http://www.rand.org/pubs/research_briefs/RB9336/index1.html.
311. Spinella, P.C., M.A. Borgman, and K.S. Azarow, *Pediatric trauma in an austere combat environment.* Critical care medicine, 2008. **36**(7 Suppl).